SYNTHESIS, CHARACTERIZATION AND SUPERCONDUCTING PROPERTIES OF $SmFeAsO_{1-X}F_X$ BASED IRON PNICTIDES

Thesis submitted to the

UNIVERSITY OF KERALA

For the Award of the Degree of

DOCTOR OF PHILOSOPHY IN PHYSICS

Under the faculty of Science

By

ANOOJA J. BABU

National Institute for Interdisciplinary Science and Technology
Council of Scientific and Industrial Research
Trivandrum, India

September 2015

DECLARATION

I, Anooja J. Babu, hereby declare that the work presented in the Ph.D. thesis entitled "***Synthesis, characterization and superconducting properties of $SmFeAsO_{1-x}F_x$ based iron pnictides***" is an independent research work carried out by me for the award of degree of Doctor of Philosophy in Physics of the University of Kerala, under the guidance of Dr. U. Syamaprasad, Chief Scientist (Rtd.), Applied Superconductivity Group, Materials Science and Technology Division, CSIR - National Institute for Interdisciplinary Science and Technology (NIIST), Trivandrum. I further declare that this thesis or any part of it has not been submitted anywhere else for any other degree, diploma or other similar title.

Anooja J. Babu

Place: Trivandrum
Date: 22-09-2015

COUNCIL OF SCIENTIFIC & INDUSTRIAL RESEARCH
NATIONAL INSTITUTE FOR INTERDISCIPLINARY SCIENCE AND TECHNOLOGY
(CSIR-NIIST)
Industrial Estate P.O., Pappanamcode,
Trivandrum - 695 019
Kerala, INDIA

ISO 9001 REGISTERED

Dr. U. Syamaprasad
Chief Scientist (Rtd.)
Materials Science and Technology Division

Tel: 91-471-2741830
Fax: +91-471-2491712
E-mail: syamcsir@gmail.com

CERTIFICATE

Certified that the work embodied in the thesis entitled, "***Synthesis, characterization and superconducting properties of $SmFeAsO_{1-x}F_x$ based iron pnictides***" is an authentic record of the research work carried out by Ms. Anooja J. Babu, Applied Superconductivity Group, Materials Science and Technology Division, CSIR - National Institute for Interdisciplinary Science and Technology (NIIST), Trivandrum, under my supervision in partial fulfillment of the requirement for the degree of Doctor of Philosophy of the University of Kerala. It is further certified that no part of this thesis has been presented previously anywhere else for the award of any other degree.

U. Syamaprasad
(Research Guide)

Place: Trivandrum

Date: 22-09-2015

ACKNOWLEDGEMENTS

I would like to express my deep sense of gratitude to my supervising guide, Dr. U. Syamaprasad, Chief Scientist (Rtd.), Applied Superconductivity Group, CSIR - National Institute for Interdisciplinary Science and Technology, Trivandrum, for his timely suggestions and support during the course of my research work. Without his support I could not have completed my Ph.D. work successfully.

I would like to thank Dr. A. Ajayaghosh, Director, CSIR - NIIST; Dr. Suresh Das and Dr. B. C. Pai, former Directors, for providing all the necessary facilities to carry out this work.

I would like to thank Dr. Prabhakar Rao P., Chief Scientist & Head, Materials Science and Technology Division (MSTD), CSIR - NIIST; Dr. M. L. P. Reddy, Dr. M. T. Sebastian, and Dr. K. G. K. Warrier, former Heads of MSTD.

It is indeed a pleasure to thank Dr. Manoj Raama Varma, Senior Principal Scientist, CSIR - NIIST for his support and co-operation after the retirement of my guide.

I wish to sincerely thank Mr. P. Guruswamy, Technical Officer (Rtd.), Applied Superconductivity Group, CSIR - NIIST, for his encouragement and support.

I also extend my heartfelt thanks to Mr. M. R. Chandran, Mr. Prithviraj, Ms. Soumya and Mr. Ajeesh Paulose for extending different instrumental facilities such as SEM, XRD, and PPMS. I am also highly thankful to Mr. Sisupalan and Mr. Brahmakumar for their timely technical support for vacuum sealing of the quartz tubes.

I sincerely thank Dr. A. Sundaresan, Professor, Chemistry and Physics of Materials Unit, Jawaharlal Nehru Centre for Advanced Scientific Research (JNCASR), Bangalore; Dr. Devendra Kumar, University of Cambridge, UK; Dr. A. Bharati, IGCAR, Kalpakkam; Mr. C. K. Chandrakanth, Senior Scientist, CSIR-NIIST, Trivandrum;, for experimental equipment support, scientific discussions and collaboration. I also passionately express my gratitude & thanks to Dr. R. P. Aloysius, Senior Scientist, National Physical Laboratory, New Delhi, for his fruitful suggestions and appreciable help during his association with my research work.

It is indeed a pleasure to thank Dr. V. Biju, Head of the Department, Department of Physics, Kariavattom Campus, University of Kerala; all the faculties of Department of Physics for their timely help, valuable suggestions and academic support.

I am also grateful to the NIIST administration for extending all the timely help.

I would like to acknowledge and express my deep sense of gratitude to Kerala State Council for Science, Technology and Environment (KSCSTE) and Council for Scientific and Industrial Research (CSIR) for providing the research fellowships to carry

out this work. Apart from that, I also wish to acknowledge the funding agencies such as DST, BRNS and IPR for financial support during the various stages of my research work.

I express my sincere gratitude to my colleague and friend, Ms. Pillai Aswathy Mohan for her inspirations, sincere help, and the warmth of deep friendship during the entire course of this work. Words are insufficient to express my gratitude to her.

I also want to extend my deep gratitude to my senior colleague and friend, Dr. Neson Varghese for his timely support, valuable suggestions and sincere help throughout the research period.

I am also truly grateful to my senior colleagues Dr. P. M. Sarun, Dr. S. Vinu, Dr. Vinod, Dr. R. Shabna and Dr. A. Biju for their valuable suggestions, encouragements and useful discussions.

I owe my sincere gratitude to all my super seniors especially for their backing at various stages of my Ph.D. work.

I am also thankful to my colleagues Mr. Syju Thomas, Mr. S. Rahul, Mr. K. M. Devadas, Ms. G. R. Anuraghi, Mr. P. Anees, Mr. M. B. Basim, Mr. A. Sivaprakash, Mr. S. Santhoshkumar, Mr. K. T. Jakson, Late Mr. Rinu V. F., Mr. Maheshkumar M., Mr. Vinu S. L., Mr. Dinesh Jose and Mr. M. Firozkhan who have supported me intellectually and technically.

I thank all the members of the Magnetism group especially Dr. Senoy Thomas, Ms. Neenulekshmi P., Ms. Raji G. R., Ms. Bhagya Uthaman, Ms. Jasnamol P. P. and Mr. Rajesh for their support and valuable suggestions.

Apart from the research work, I would like to cherish and acknowledge the friendship and support of my roommates, Dr. Arya Nandan, Ms. Rakhi A.M., Ms. Sreedevi, Ms. Linsha Vazhayal, Ms. Neethu K. S. and Ms. Ramya A. N.

I wish to express sincerely my acknowledgement to all those who have contributed in different aspects for the completion of my Ph. D. work and preparation of the thesis.

At last but not the least, I wish to thank my family and my teachers for their advice and motivation in the hour of need.

Anooja J. Babu

CONTENTS

Chapter 1: Superconductivity and its applications - An overview

Chapter 2: Iron-based superconductors

Chapter 3: Preparation and characterization techniques

Chapter 4: Synthesis and characterization of $SmFeAsO_{1-x}F_x$ bulk samples with the introduction of a novel pre-processing route

Chapter 5: Effect of rare earth (RE: Gd, Ce & Y) doping at Sm^{3+} site in $SmFeAsO_{1-x}F_x$ bulk samples

Chapter 6: Effect of alkaline earth metal fluoride (CaF_2 and BaF_2) doping in Sm1111 bulk superconductor

Chapter 7: Preparation, process optimization, and characterization of Sm1111 wires

Chapter 8: Summary and conclusions

List of Figures

List of Tables

List of Abbreviations

LTS	: Low Temperature Superconductor
HTS	: High Temperature Superconductor
BCS	: Bardeen Cooper and Schrieffer
GL	: Ginzburg-Landau
YBCO	: YBaCuO
Bi-2223	: $Bi_2Sr_2Ca_2Cu_3O_{10}$
Tl-2223	: $Tl_2Ba_2Ca_2Cu_3O_{10}$
MEG	: Magneto Encephalography
SQUID	: Superconducting Quantum Interference Device
MRI	: Magnetic Resonance Imaging
LHC	: Large Hadron Collider
SMES	: Superconductive Magnetic Energy Storage
ITER	: International Thermonuclear Experimental Reactor
BNL	: Brookhaven National Laboratory
CERN	: European Organization for Nuclear Research
DESY	: Deutsches Elektronen Synchrotron
FeSC	: Iron-based Superconductor
RE	: Rare Earth element
Ch	: Chalcogen
1111	: REFeAsO
122	: BFe_2As_2 & AFe_2Se_2, A - alkaline earth metals & B - alkali metals
111	: AFeAs, A - alkaline earth metals
11	: FeCh
HP	: High Pressure
AFM	: Antiferromagnetic
2D	: Two Dimensional
3D	: Three Dimensional
ARPES	: Angle-Resolved Photoemission Spectroscopy
DFT	: Density Functional Theory
DOS	: Density of States
WHH	: Werthamer-Helfand-Hohenberg
MO	: Magneto-Optical
PIT	: Powder In Tube
IGCAR	: Indira Gandhi Centre for Atomic Research
BARC	: Bhabha Atomic Research Centre
TIFR	: Tata Institute of Fundamental Research
NPL	: National Physical Laboratory

SS	: Stainless Steel
Sm1111	: $SmFeAsO_{1-x}F_x$
SEM	: Scanning Electron Microscope
EDS	: Energy Dispersive X-ray Spectroscopy
XRD	: X-ray Diffraction
FWHM	: Full Width at Half Maximum
SEI	: Secondary Electron Imaging
LED	: Light Emitting Diode
dc	: Direct Current
ac	: Alternating Current
ARS	: Advanced Research Systems
PPMS	: Physical Property Measurement System
JNCASR	: Jawaharlal Nehru Centre for Advanced Science and Research
RRR	: Residual Resistivity Ratio
VSM	: Vibrating Sample Magnetometer
SRS	: Stanford Researh Systems
SDW	: Spin Density Wave
MPa	: Mega Pascal
BSCCO	: Bismuth Strontium Calcium Copper Oxide
OD	: Outer Diameter
ID	: Inner Diameter
Vol.%	: Volume Percentage
wt%	: Weight Percentage

List of Symbols

T_C : Critical temperature
H_C : Critical field
T : Temperature
λ : London penetration depth
e : Charge of an electron
m_e : Mass of an electron
n_s, n_n : Number of superconducting, normal electrons
n : Electron density
I_C : Critical current
J_C : Critical current density
ψ : Superconducting order parameter
ξ : Coherence length
H : Applied magnetic field
J : Current density
T : Tesla
mT : Milli tesla
H_{C1} : Lower critical field
H_{C2} : Upper critical field
H_{irr} : Irreversibility field
Φ_0 : Magnetic flux quantum
h : Planck’s constant
c : Velocity of light
k : Ginzburg-Landau parameter
Φ : Flux density
F_L : Lorentz force
Fp : Bulk pinning force
$f(p)$: Elementary pinning force
U_P : Pinning energy
L : Mean free path
J_S : Super current density
F_s : Free energy of the superconducting state
F_n : Free energy of the normal state
α, β : Expansion coefficients
A : Vector potential
2Δ : Energy gap
Θ : Debye temperature
K : Kelvin
γ : Anisotropy
D1, D2 : Diffusivity of electron band
J_{Clocal} : Intragrain critical current density

$J_{Cglobal}$: Intergrain critical current density
a, b : Sample dimensions
$\langle r \rangle$: Average grain size
ΔM : Width of the hysteresis loop
$J_C(H)$: In-field critical current density
B_C : Crossover field
Å : Angstrom unit
θ : Angle of diffraction
a, b, c : Lattice parameters
d : Inter atomic spacing
h, k, l : Miller indices of crystal planes
ρ : Resistivity
I : Current
V : Voltage
χ : *ac* susceptibility
χ', χ'' : Real and imaginary components of χ
R : Resistance
ΔT_C : Width of transition
T_{Conset} : Temperature corresponding to 90% of normal state resistivity
$T_{Coffset}$: Temperature corresponding to 10% of normal state resistivity
A : Cross-sectional area of the sample
M : Magnetization
H_{ac} : Alternating (*ac*) magnetic field
f : Frequency
f_0 : An attempt frequency
T_P : The peak position of the imaginary part
V : Volume
ρ_{300} : Normal state resistivity
ρ_{xy} : Transverse resistivity
$\mathrm{R_H}$: Hall coefficient
M_P : Paramagnetic moment
M^+ : Moments in the field-increasing branch of *M-H* curve
M^- : Moments in the field-decreasing branch of *M-H* curve

PREFACE

The phenomenon of superconductivity, in which materials conduct electric current without any resistance, has been so exciting to the scientific community. Superconductivity is exhibited by various elements, alloys, and compounds and still novel superconductors are being explored. Among them only a few are useful in terms of practical applications. Important applications of superconductors are in the development of high field magnets for instruments such as NMR, MRI, particle accelerators and in fusion reactors. Some other applications are in electrical energy storage and distribution, transportation using magnetic levitation technology and in electronics.

Recently, the superconducting world was reignited when Japanese researchers led by *Hideo Hosono* discovered a new class of iron-based superconducting material having transition temperatures relatively higher than the conventional low temperature superconductors. This discovery offered an opportunity to study the electrical and magnetic properties in a new and different system in the high temperature superconducting (HTS) class. Some of the features such as the two dimensional electronic structure, the presence of a superconducting dome in the electronic phase diagram and the anomaly in the transport property of the parental compound made iron-based superconductors similar to cuprates whereas the complex Fermi surface topology and multiband nature made them closer to magnesium diboride superconductor. Among the various classes of iron pnictides, REFeAsO (1111 type) is much promising for practical applications. The extremely high upper critical field, moderate anisotropy, relatively large critical current density and wide scope for chemical substitution make the 1111 system very promising. Among the 1111 class of superconductors, samarium based iron oxypnictide superconductor is a potential candidate due to its relatively high transition temperature T_C , large intergrain J_C, H_{C2} over 150 T and good stability in ambient conditions. These properties make it a potential material for high field applications around 30 K, where conventional superconductors cannot play a role owing to their low T_Cs.

The present work focuses on the synthesis and characterization of $SmFeAsO_{1-x}F_x$ (Sm1111) based superconductors. The main objectives are to develop a relatively simple method for good quality Sm1111 bulk superconductor, to improve its superconducting properties such as T_C, J_C and H_{C2} through substitution at different sites using selected dopants, and finally to establish the technical feasibility of making metal sheathed Sm1111 wires for conductor application. The thesis is divided into 8 chapters. The first chapter gives a brief account of the phenomenon of superconductivity, superconducting materials and their applications in various fields. The second chapter is an overview on iron-based superconductors especially their physical and superconducting properties, commonly adopted preparation techniques, and present status and relevance of iron-based superconductors. The third chapter provides details on the preparation and characterization techniques followed in this study. Chapter 4 to Chapter 7 discusses the present work in detail. Chapter 8 comprises the summary of the overall work done, the major conclusions obtained, and the future scope and directions for the present work.

Regarding the synthesis part, the main difficulties faced were the requirement of high pressure (~ 6 GPa) and high temperature (~ 1200 °C) for the synthesis of RE1111 based superconductors. This difficulty was addressed by developing a novel and a relatively simple preparation method for Sm1111 bulk superconductors which is presented in Chapter 4. The main feature of this method is the introduction of a pre-processing step by which good quality Sm1111 samples with relatively high transport J_C could be synthesized at a lower heat treatment temperature of 850 °C and ambient pressure. The pre-processing of the reaction mixture at 360-380 °C yielded a precursor having the right phase assemblage and good reactivity and thereby good quality Sm1111 samples were obtained at a relatively low temperature. The fourth chapter also discusses the effect of F variation on the structural and superconducting properties of $SmFeAsO_{1-x}F_x$ (x = 0, 0.1, 0.2, 0.3, and 0.4) superconductor. A maximum T_C of 55.3 K was attained for x = 0.4 and a transport J_C of around 750 A/cm^2 at 12 K for x = 0.3 composition. The samples with x = 0.3 also showed a magnetic J_{Clocal} of 7×10^5 A/cm^2 at 5 K and better $J_C(H)$ performance in the high field region since the defects induced due to fluorine doping enhanced the inherent vortex pinning in the system.

The studies on the impact of rare earth doping at Sm^{3+} site in $SmFeAsO_{0.7}F_{0.3}$ superconductor on both its structural and superconducting properties are incorporated in Chapter 5. Two 4f rare earth elements having ionic size smaller and larger than Sm^{3+} ion (Gd^{3+} and Ce^{3+}) and a non 4f element Y^{3+} were selected. The 4f element doping increased the T_C of the Sm1111 system irrespective of their ionic size compared to Sm^{3+} ion. Doping with the smaller Gd^{3+} resulted in lattice contraction and thereby enhanced T_C; whereas Ce^{3+} doping in Sm1111 exhibited an increase in lattice parameters, yet showed substantial enhancement in T_C. In both cases the main reason for T_C improvement was the increased charge carrier concentration of the system as confirmed by Hall Effect measurement. Very high upper critical fields above 300 T and better J_C-H performance were obtained by the simultaneous doping at oxygen and rare earth sites, through effective flux pinning. However, the doping of the non-4f element, Y^{3+} at Sm^{3+} gave a negative impact on the superconducting properties of Sm1111 system.

In Chapter 6, the combined effect of both electron and hole doping in Sm1111 system was investigated by using alkaline earth metal fluorides such as CaF_2 and BaF_2. In the modified $Sm_{1-x}A_xFeAsO_{1-2x}F_{2x}$ (A - alkaline earth metals) system F^- doping at O^{2-} site provides electrons and Ca^{2+}/Ba^{2+} at Sm^{3+} site gives holes to the system. Binary doping in Sm1111 enhanced both structural and superconducting properties of the system. Moreover, the microstructures of the samples improved tremendously using both CaF_2 and BaF_2 and hence the transport J_C of the binary doped samples increased remarkably. In addition to the enhancement of grain size, CaF_2 doped samples displayed a preferred orientation of (*00l*) planes which was quite interesting. This gives a possibility for the development of Sm1111 based conductors with higher current carrying capacity. A maximum transport J_C of 880 A/cm^2 at 12 K with a T_C of 53.8 K was achieved in the CaF_2 doped sample. BaF_2 doping also enhanced the T_C value, but the increment was only marginal as compared to the CaF_2 sample because of the relatively large ionic size of Ba^{2+}. Magnetic properties studied on binary doped Sm1111 bulk superconductors revealed that H_{C2} and $Hirr$ values improved significantly and J_C-H performance also enhanced, especially in BaF_2 doped samples due to the enhanced flux pinning resulting from the lattice mismatch created by larger ion doping at Sm^{3+} site.

Chapter 7 discusses the development of Sm1111 wires and tapes using an *in situ* PIT method wherein the precursor powder used was the pre-processed powder at 370 °C. For the wire development the sheath metal reactivity and the effect of processing temperature on the phase formation and superconducting properties were studied initially using five different candidate metals namely, Ag, Cu, Fe, Ni, and SS. Among them only Ag and Fe sheathed wires showed superconducting transitions. Secondary phases corresponding to the sheath metal were formed in the case of Cu, Ni, and SS sheathed wire samples whereas Ag and Fe were found to be chemically compatible to $SmFeAsO_{1-x}F_x$ and among them Ag was the best in terms of superconducting volume fraction and transport properties. Furthermore, both Ag and Fe sheathed wires processed at 850 °C gave the best properties. The Ag sheathed Sm1111 wire heat treated at 850 °C temperature gave a transport J_C of 4030 A/cm^2 at 12 K with a T_C around 57 K. Subsequently, selective metal addition was attempted in the superconducting core of the Ag sheathed Sm1111 wire sample for possible enhancement of transport properties. Consequently, the transport J_C of the Ag sheathed Sm1111 wire sample was successfully enhanced to 5200 A/cm^2 at 12 K by incorporation of Sn (30 wt%) into the wire sample.

List of Publications

List of Publications in SCI journals

1. ***J. B. Anooja***, P. M. Aswathy, Neson Varghese, C. K. Chandrakanth, N. Devendra Kumar, A. Sundaresan and U. Syamaprasad, "Influence of rare earth doping on the structural and electro-magnetic properties of $SmFeAsO_{0.7}F_{0.3}$ iron pnictide," ***Inorg. Chem. Front.,*** 2, 731-740 (**2015**).
2. ***J. B. Anooja***, P. M. Aswathy, Neson Varghese, Manoj Raama Varma and U. Syamaprasad, "Structural and superconducting properties of BaF_2 Doped SmFeAsO", ***Materials Science Forum-Trans Tech Publications,*** 830, 595-599 (**2015**).
3. ***J. B. Anooja***, P. M. Aswathy, Neson Varghese, R. P. Aloysius and U. Syamaprasad, "SmFeAsO superconductor with preferred crystallographic orientation and enhanced critical current density," ***J. Am. Ceram. Soc.,*** 97, 2099-2104 (**2014**).
4. ***J. B. Anooja***, P. M. Aswathy, Neson Varghese, R. P. Aloysius, and U. Syamaprasad, "Microstructure refinement and enhanced critical current density in binary doped SmFeAsO superconductor," ***AIP Conference Proceedings*** 1591, 1536-1538 (**2014**).
5. ***J. B. Anooja***, P. M. Aswathy, Neson Varghese, K. Vinod, A. Bharati and U. Syamaprasad, "Transport and magnetic properties of yttrium doped NdFeAs(O,F) superconductor," ***J. Alloys and Compd.*** 566, 43-49 (**2013**).
6. ***J. B. Anooja***, P. M. Aswathy, P. M. Sarun, U. Syamaprasad, "A novel low temperature synthesis route for $SmFeAsO_{1-x}F_x$ bulk superconductor with improved transport properties," ***J. Alloys and Compd.*** 514, 1-5 (**2012**).
7. P. M. Aswathy, ***J. B. Anooja***, Neson Varghese, C. K. Chandrakanth, N. Devendra Kumar, A. Sundaresan and U. Syamaprasad, "Rare earth (RE - Ce, Gd) modified $Nd_{1-x}RE_xFeAsO_{0.7}F_{0.3}$ superconductor with enhanced magneto-transport properties," ***RSC Adv.*** 5, 41484 (**2015**).
8. P. M. Aswathy, ***J. B. Anooja***, Neson Varghese and U. Syamaprasad, "The role of yttrium doping on the structural and superconducting properties of Sm1111 and its comparison with other (RE, Y)1111 (RE - La, Ce, and Nd) iron oxypnictides," ***J. Low Temp. Phys.*** 178, 285-294 (**2015**).
9. P. M. Aswathy, ***J. B. Anooja***, Neson Varghese, and U. Syamaprasad, "Influence of reactivity of sheath metals on the superconducting properties of $NdFeAsO_{0.6}F_{0.4}$ wires", ***Materials Science Forum-Trans Tech Publications*** 830, 557-560 (**2015**).
10. P. M. Aswathy, ***J. B. Anooja***, Neson Varghese, and U. Syamaprasad, "Enhanced transport and magnetic properties in gadolinium doped $NdFeAsO_{0.7}F_{0.3}$ superconductors," ***AIP Conference Proceedings*** 1665, 130047 (**2015**).
11. P. M. Aswathy, ***J. B. Anooja***, Neson Varghese and U. Syamaprasad, "Microstructural refinement and enhanced transport properties in binary doped NdFeAsO superconductor," ***J. Appl. Phys.*** 115, 053903 (**2014**).

12. P. M. Aswathy, ***J. B. Anooja,*** Neson Varghese and U. Syamaprasad, "$NdFeAsO_{1-x}F_x$ superconductor - impact of fluorine variation on microstructure and transport properties," ***J. Am. Ceram. Soc.,*** 96, 1176-1180 (**2013**).
13. P. M. Aswathy, ***J. B. Anooja***, P. M. Sarun and U. Syamaprasad, "An overview on iron based superconductors," ***Supercond. Sci. Technol.*** 23, 073001 (**2010**). [**Topical Review, selected for Highlights of 2010**]
14. Neson Varghese, Devadas K. M., P. M. Aswathy, ***J. B. Anooja***, Manoj Raama Varma and U. Syamaprasad, "Enhanced transport current in MgB_2 superconducting wire through metallic Fe addition", ***Materials Science Forum-Trans Tech Publications*** 830, 509-512 (**2015**).
15. K. M. Devadas, Neson Varghese, K. Vinod, S. Rahul, Syju Thomas, ***J. B. Anooja***, A. Sundaresan, S. B. Roy, and U. Syamaprasad, "Enhanced superconducting properties of MgB_2 by carbon substitution using carbon containing nano additives," ***AIP Conf. Proc.*** 1349, 913-914 (**2011**).
16. P. M. Sarun, S. Vinu, R. Shabna, ***J. B. Anooja***, P. M. Aswathy, and U. Syamaprasad, "Structural and transport properties of $(Bi_{1.6}Pb_{0.5})(Sr_{2-x}Lu_x)Ca_{1.1}Cu_{2.1}O_{8+\delta}$ superconductor," ***IEEE transactions on applied superconductivity*** 20, 61-65 (**2010**).
17. S. Vinu, P. M. Sarun, R. Shabna, P. M. Aswathy, ***J. B. Anooja***, U. Syamaprasad, "Suppression of flux-creep in (Bi,Pb)-2212 superconductor by holmium doping," ***Physica B*** 405, 4355-4359 (**2010**).

List of International/National Conference Papers

1. ***J. B. Anooja***, P. M. Aswathy, Neson Varghese, Manoj Raama Varma and U. Syamaprasad, "*Structural and Superconducting Properties of BaF_2 Doped SmFeAsO*," Presented at the International Conference on Advanced Materials and Manufacturing Process for Strategic Sectors (ICAMPS 2015), held at Trivandrum, Kerala, during May 13-15, **2015**. (Published in Trans. Tech Publications)
2. ***J. B. Anooja***, P. M. Aswathy, Neson Varghese and U. Syamaprasad, "*Magneto-Transport Properties of $SmFeAsO_{0.7}F_{0.3}$ Superconductor upon Gd Doping at Sm Site*," Presented at the International Conference on Science, Technology and Applications of Rare Earths (STAR 2015), held at Trivandrum, Kerala, during April 23-25, **2015**.
3. ***J. B. Anooja***, P. M. Aswathy, Neson Varghese and U. Syamaprasad, "*Microstructure Refinement and Enhanced Critical Current Density in Binary Doped SmFeAsO Superconductor*" Presented at the 58th DAE Solid State Physics Symposium (DAE SSPS 2013), held at Thapar University, Patiala, Punjab during December 17-21, **2013**. (Published in AIP Conf. Proc.) (**Best Poster Prize**)
4. ***J. B. Anooja***, P. M. Aswathy, Neson Varghese and U. Syamaprasad, "*Enhanced Superconducting Properties in NdFeAs(O,F) Superconductor by Yttrium Doping*" Presented at 25th Kerala Science Congress held at Technopark, Trivandrum on January 30, **2013**.
5. P. M. Aswathy, ***J. B. Anooja***, Neson Varghese, Manoj Raama Varma and U. Syamaprasad, "*Influence of Reactivity of Sheath Metals on the Superconducting Properties of $NdFeAsO_{0.6}F_{0.4}$*

Wires," Presented at the International Conference on Advanced Materials and Manufacturing Process for Strategic Sectors (ICAMPS 2015), held at Trivandrum, Kerala, during May 13-15, **2015**. (Published in Trans. Tech Publications) (**Best Poster Prize**)

6. P. M. Aswathy, ***J. B. Anooja***, Neson Varghese and U. Syamaprasad, "*Enhanced Transport and Magnetic Properties in Gadolinium Doped* $NdFeAsO_{0.7}F_{0.3}$ *Superconductors*" Presented at the 59th DAE Solid State Physics Symposium (DAE SSPS 2014), held at Vellore Institute of Technology, Vellore, Tamil Nadu, during December 16-20, **2014**. (Published in AIP Conf. Proc.)

7. P. M. Aswathy, ***J. B. Anooja***, Neson Varghese and U. Syamaprasad "*Enhanced Transport Properties in NdFeAsO Superconductor through Microstructural Refinement by* CaF_2 *Doping*," Presented at the 2nd International Conference on Advanced Functional Materials (ICAFM) held at NIIST, Thiruvananthapuram on February 19-21, 2**014**.

8. P. M. Aswathy, ***J. B. Anooja***, Neson Varghese and U. Syamaprasad, "*Impact of Fluorine Variation on the Structural and Superconducting Properties of* $SmFeAsO_{1-x}F_x$," Presented at 25th Kerala Science Congress held at Technopark, Trivandrum on January 30, **2013**.

9. P. M. Aswathy, ***J. B. Anooja***, P. M. Sarun and U. Syamaprasad, "*Effect of Pre-Processing Technique on Phase Formation, Sintering Temperature and Superconducting Properties of* $SmFeAsO_{1-x}F_x$," Presented at the Asian Conference on Applied Superconductivity and Cryogenics (ACASC) held at IUAC, New Delhi on November 16-18, **2011**.

10. Neson Varghese, K. M. Devadas, ***J. B. Anooja***, P. M. Aswathy, Manoj Raama Varma and U. Syamaprasad, "*Enhanced Transport Current in* MgB_2 *Superconducting Wire through Metallic Fe Addition*," Presented at the International Conference on Advanced Materials and Manufacturing Process for Strategic Sectors (ICAMPS 2015), held at Trivandrum, Kerala, during May 13-15, **2015**. (Published in Trans. Tech Publications)

11. K. M. Devadas, Neson Varghese, K. Vinod, S. Rahul, Syju Thomas, ***J. B. Anooja***, A. Sundaresan, S. B. Roy and U. Syamaprasad, "*Enhanced Superconducting Properties of* MgB_2 *by Carbon Substitution Using Carbon Containing Nano Additives*," Presented at the 55th DAE Solid State Physics Symposium (DAE SSPS 2010), held at Manipal on December 26-30, **2010**. (Published in AIP Conf. Proc.)

12. Neson Varghese, ***J. B. Anooja***, P. M. Aswathy, K. Vinod, S. B. Roy and U. Syamaprasad, "*Effect of Combined Addition of Nano SiC and TiC on Structural and Superconducting Properties of* MgB_2," Presented at the International Conference on Advanced Functional Materials (ICAFM) held at NIIST, Thiruvananthapuram on December 9-10, **2009**.

CHAPTER 1

SUPERCONDUCTIVITY AND ITS APPLICATIONS - AN OVERVIEW

1.1 Introduction of Superconductivity

Superconductivity, which was discovered a hundred years ago, is still an exciting field of research which includes developing novel superconductors, solving the original mechanism, and finding yet new applications. At low temperatures, the electrical resistance of certain materials completely vanishes and this phenomenon is called superconductivity, and the material is called a superconductor. The temperature at which the material becomes superconducting is called its *critical temperature* (T_C). This phenomenon was first discovered in the metal mercury (Hg) below 4.2 K by Dutch physicist Heike Kamerlingh Onnes and his co-workers in 1911 (Onnes, H. K. 1911). For his discovery, Onnes got Nobel Prize in Physics in 1913. Later, superconductivity has been observed in various elements, alloys, and compounds. The fascinating phenomenon of superconductivity develops several new applications of these materials.

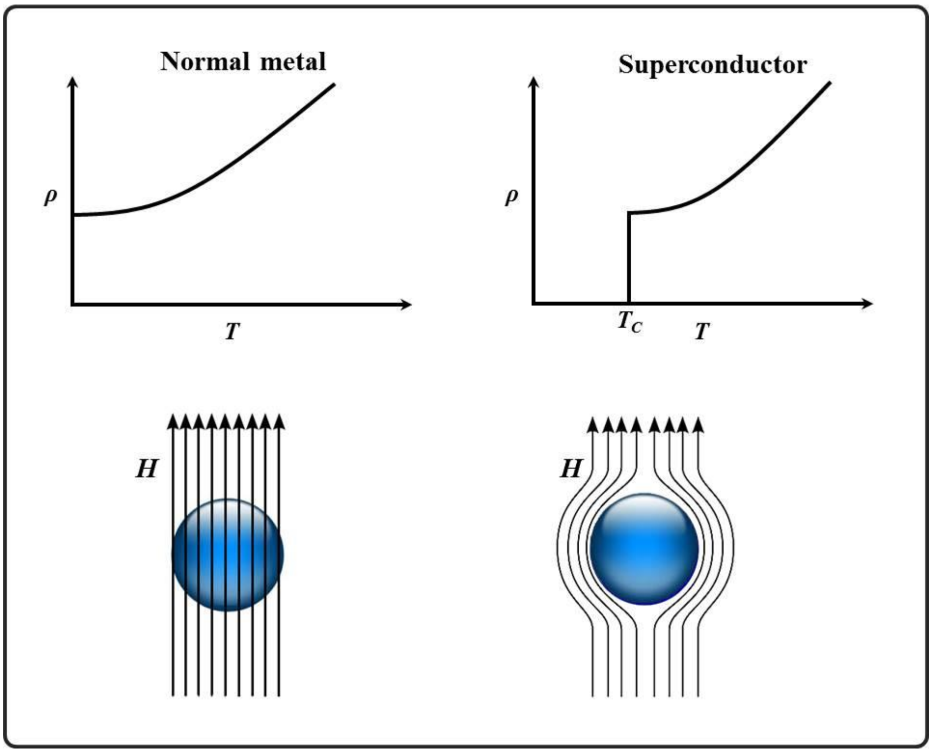

Figure 1.1: The behavior of a superconductor and a perfect conductor in terms of resistivity and magnetic field

In the superconducting state besides the disappearance of resistivity, materials expel the magnetic field. This diamagnetic phenomenon is called *Meissner effect*, noticed in 1933 in the experiments of Meissner and Ochsenfeld at Berlin (Meissner *et al.* 1933). They found that below T_C the material expels the magnetic flux inside, and this leads to the definition of a new thermodynamic state. A thermodynamic phase transition from normal to the superconducting state occurs because this phase is energetically less expensive and more ordered. The entropy of the superconducting state is less than that of the normal state and in which electrons behave coherently. A superconductor shows both zero resistance and diamagnetic nature and this combined property makes them distinct from a perfect conductor. If the material is allowed to cool and then subjected to a magnetic field, both a superconductor and a perfect conductor expel the magnetic field. But if we apply a magnetic field first and then cool, the superconductor only expels the field, and the perfect conductor remains fully permeated by the field. The behavior of a superconductor and a perfect conductor in terms of resistivity and magnetic field is given in Figure 1.1.

A superconductor expels the magnetic field only if it is below a particular value. i.e. the superconducting state cannot exist in the presence of a magnetic field greater than a critical value called *critical field* (H_C) of a superconductor. If the magnetic field is greater than H_C, the magnetic flux penetrates through the interior of the sample and the material loses its superconductivity. The critical field, H_C is temperature dependent and is given by $H_C(T) = H_C(0)[1-(T/T_C)^2]$. The magnetic field is expelled by circulating currents flowing through the surface of a superconductor called screening currents of a superconductor. Practically this screening current penetrates to a small depth from the surface called *London penetration length* (λ) (London *et al.* 1935a; London *et al.* 1935b). It can be calculated using the equation $\lambda = m_e/(\mu_0 n_s e^2)^{1/2}$, where e and m_e are the charge and mass of electron and n_s is the density of superconducting electrons (deHaas *et al.* 1925). A screening current runs only in the presence of an external field which hinders superconductivity. The surface current generates a magnetic field inside the superconductor that exactly cancels the external magnetic field causing the magnet to be repelled. This effect is too strong by which a magnet can be levitated over a superconductive material, *magnetic levitation*, and is a very popular demonstration of superconductivity.

There exists another critical parameter, destroying the superconducting state, *critical current* (I_C), which is the maximum current that a superconductor can carry. If the current passed through a superconductor exceeds I_C, it will return to the normal state even though the temperature is below its T_C. The critical current, I_C depends on the sample size also and hence it is better to express it in terms of *critical current density* (J_C). The J_C of a superconductor is the critical current conducted through the unit cross section of the material, and its unit is A/cm^2. In 1935 H. Frohlich, theoretically predicted the isotope effect, which proposed that the T_C decreases when the average isotopic mass increases (Frohlich *et al.*1950). Another striking phenomenon associated with superconductivity is *Josephson Effect* discovered in 1962 by Brian D. Josephson (Josephson, B. D. 1962). It is the phenomenon of supercurrent that flows indefinitely long without any voltage applied across two superconductors separated by a thin tunnel barrier. Superconductivity has been successfully explained by Bardeen, Cooper and Schrieffer theory (BCS theory) in1957 (Bardeen *et al.* 1957b). According to the theory, the supercurrent is carried by pairs of electrons having opposite momenta and spins; not by single electrons. Such pair of electrons is called a Cooper pair. A Cooper pair is a Bose-condensate characterized by a wave function ψ, called the *order parameter* of a superconductor. An approximate spatial dimension of the Cooper pair can be expressed in terms of c*oherence length* (ξ), and it gives the distance between two electrons in a Cooper pair (Bardeen *et al.* 1957a).

1.2 Superconducting parameters

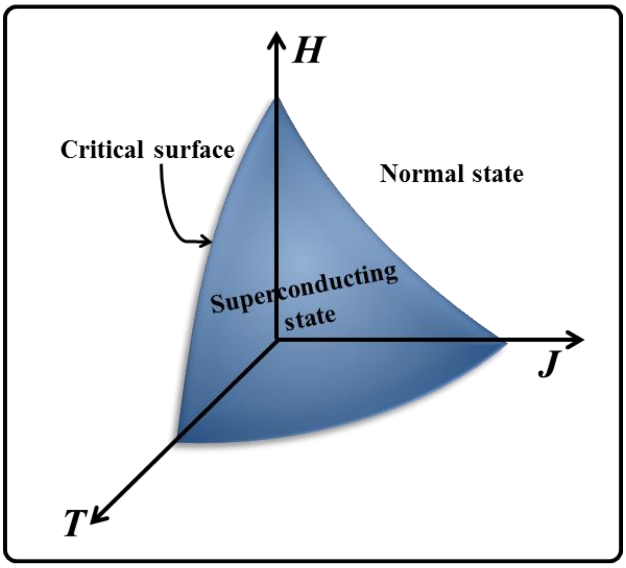

Figure 1.2: Schematic illustration of the critical surface of a superconductor

Three important parameters of a superconductor are critical temperature (T_C), critical field (H_C), and critical current density (J_C). The three parameters form a three-dimensional surface called critical surface of a superconductor as shown in Figure 1.2, and the material is superconducting only if it lies inside the critical surface. Outside the critical surface, the material becomes normal. In short in order to maintain superconductivity in a material, the applied field (*H*), the temperature (*T*) and the current density (*J*) must be kept below the critical surface.

Among these parameters, T_C and H_C of a superconductor are intrinsic properties of the material. The T_C and H_C values of superconductors vary depending on the materials from which they are made of. Critical temperature up to 133 K was reported for $HgBa_2Ca_2Cu_3O_{8+\delta}$ ceramic superconductors (Fujinami *et al.* 1998). On the basis of critical temperature, T_C superconducting materials can be classified into two groups - *Low Temperature Superconductors (LTS)* and *High Temperature Superconductors (HTS).* Generally, superconductors having T_C below the liquid nitrogen temperature (77 K) are called LTS superconductors and those having T_C > 77 K as HTS superconductors. However, superconductors with T_C > 30 K are also considered as HTS superconductors. Superconductivity in LTS can be well described using BCS phonon mediated electron pairing. Pure metals and their alloys such as Nb-Ti are some examples for LTS. A breakthrough occurred with the discovery of the cuprates based superconductor (LaBaCuO, T_C ~ 30 K) by Bednorz and Müller in 1986 and this lead to the beginning of an era of high temperature superconductors (Bednorz *et al.* 1986). Superconductivity in these materials is based on the copper-oxide planes, in which pairing is initiated by embedding them in a specific lattice. The recently discovered iron-based superconductors also belong to HTS family (Kamihara *et al.* 2008).

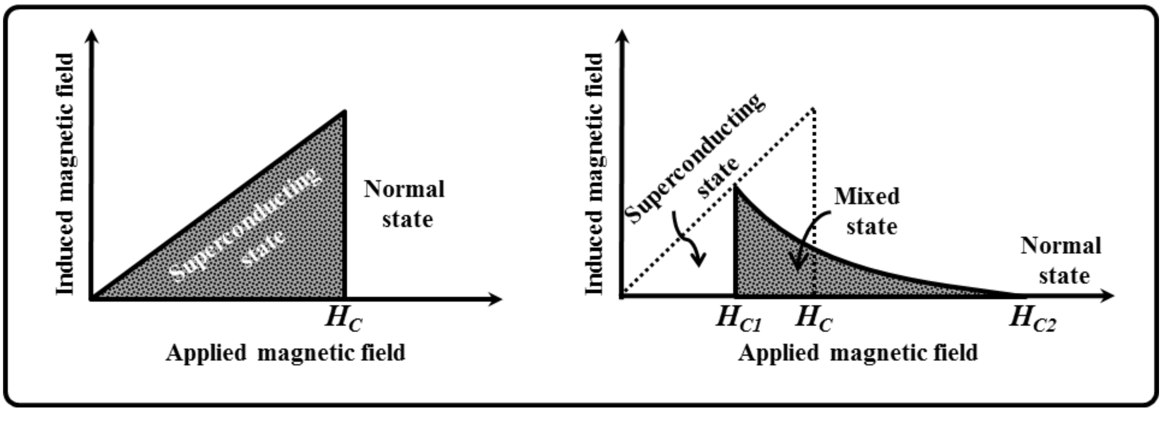

Figure 1.3: Magnetization of type-I and type-II superconductors as a function of the external magnetic field

Superconductors can be also classified into two types based on their behavior in the magnetic field as - *type-I superconductor* (soft superconductor) and *type-II superconductor* (hard superconductor) (Abrikosov, A. A. 1957). When an external field is applied to a type-I superconductor the magnetic flux is perfectly shielded from the interior of the superconductor by shielding currents along its surface up to H_C and shows a perfect diamagnetism. The shielding current exponentially decays from the surface of the superconductor and is limited to a surface layer of approximately one-tenth of a micron (Lee(b*) et al.* 2003). The elements such as lead, mercury, tin and aluminium are type-I superconductors and are usually very pure metals. The maximum fields up to which type-I superconductors can withstand are usually less than 0.1 T, and this limits their practical applications.

For a type-II superconductor the perfect diamagnetism is maintained only up to the lower critical field, H_{C1}, and then the magnetization varies continuously with the penetration of magnetic flux until the diamagnetism disappears at the upper critical field, H_{C2}, where the normal state starts. The magnetic flux penetrates the superconductor in the form of flux lines called flux vortices, and this partial diamagnetic state between H_{C1} and H_{C2} is called a mixed state (vortex state). The flux vortices in the mixed state are quantized in units of $\Phi_0 = hc/2e$, where h is Planck's constant, c is velocity of light, e is electron's charge and Φ_0 is called flux quantum (Schrieffer *et al.*1999; Abrikosov, A. A. 2004). A repulsive interaction between the flux lines eventually forms flux line bundles and consecutively a flux line lattice. The density of flux lines increases on increasing the external magnetic field and at H_{C2} the vortex cores overlap with each other; thus the material experiences a second-order phase transition into a normal state. Examples of type-II superconductors are organic, A-15, Chevrel phases, heavy fermions, fullerenes, and high temperature superconductors (cuprates and iron-based superconductors). Magnetization behavior of type-I and type-II superconductors as a function of the external magnetic field is given in Figure 1.3.

Type-II superconductors are characterized by two parameters - London penetration depth, λ, and the coherence length, ξ of the superconducting material. The lower critical field H_{C1} of a type-II superconductor mainly depends on its London penetration depth, λ, and the upper critical field H_{C2} is determined by the coherence length, ξ of the superconductor. The ratio of λ by ξ is called Ginzburg-Landau (GL) parameter, k which determines the behavior of a superconductor in the presence of an external magnetic field (Abrikosov *et al.*1957). If

$k < 1/\sqrt{2}$, positive surface energy - type-I superconductor

$k \geq 1/\sqrt{2}$, negative surface energy - type-II superconductor

Since the surface energy is negative at $k > 1/\sqrt{2}$ the appearance of normal regions in the interior of a specimen placed in a magnetic field is energetically favorable even for $H < H_{C2}$. The material remains superconducting due to lowering of their energy by creating walls between normal and superconducting regions. Therefore, the material splits into a fine-scale mixture of superconducting and normal regions, the arrangement being such as to give the maximum possible boundary area, and form a mixed state. Shubnikov was the first to suggest the fundamental nature of type-II superconductivity (1937) that a specimen placed in a magnetic field does not exhibit total flux expulsion except for very low fields (Shubnikov *et al.* 1937). In this situation, the penetration field is substantially smaller than the thermodynamic critical field H_C, but the penetration is incomplete, and superconductor is in a mixed state. Complete penetration of a flux takes place at a much higher field. At $k = 1/\sqrt{2}$, H_{C1} and H_{C2} of type-I superconductor approach one another merge at the thermodynamic critical field of type-I. Later, the work of Abrikosov in 1957 established the full consequence of a negative-surface-energy regime (Abrikosov *et al.*1957). He explained the mixed state in a superconductor with the help of Ginsburg-Landau theory by introducing a second order phase transition. However, in type-I superconductors this phase transition is a first-order in a nonzero field. According to him, in the mixed state of a superconductor, magnetic flux penetrates in the form of tubes called vortices known as Abrikosov's vortices. The Abrikosov vortices form regular vortex lattice in equilibrium conditions of the vortices. In an ideal type-II superconductor in order to minimize the potential energy arising from the mutual repulsion between the flux tubes, they are arranged in a triangular patterns and form stable vortices. The mutual-repulsion between vortices arises from the Lorentz force $J \times \Phi$ resulting from the interaction of the current density J of one vortex with the flux Φ of another vortex. For non-ideal type-II superconductors, the overall distribution of the triangular pattern is disordered and ordered only in small local regions. The distribution of vortices and the corresponding superconducting order parameter and magnetic field distributions in a type-II superconductor are shown in Figure 1.4. The vortices have a normal core of a radius of $\approx \xi$ and persistent current circulating around the core and decaying away from the vortex core at distances comparable with λ ($\lambda > \xi$).

Abrikosov also calculated H_{C1} and H_{C2} in terms of k (Schrieffer *et al.*1999) and are given by

$$H_{C1} = \frac{H_C}{k\sqrt{2}}\,(ln\,k + 0.08)$$

$$H_{C2} = H_C k\sqrt{2}$$

The upper critical field H_{C2} increases and simultaneously the lower critical field H_{C1} decreases with increasing k value. Figure 1.5 shows the plot of magnetization produced inside a superconductor with external field applied for different values of k. For $k < 1/\sqrt{2}$ we get a triangular dependence, and the material shows ideal diamagnetism below H_C and null magnetization in the normal phase. At higher values of k, the vortex phase appears and with increasing k its lower boundary (H_{C1}) decreases while its upper boundary (H_{C2}) increases.

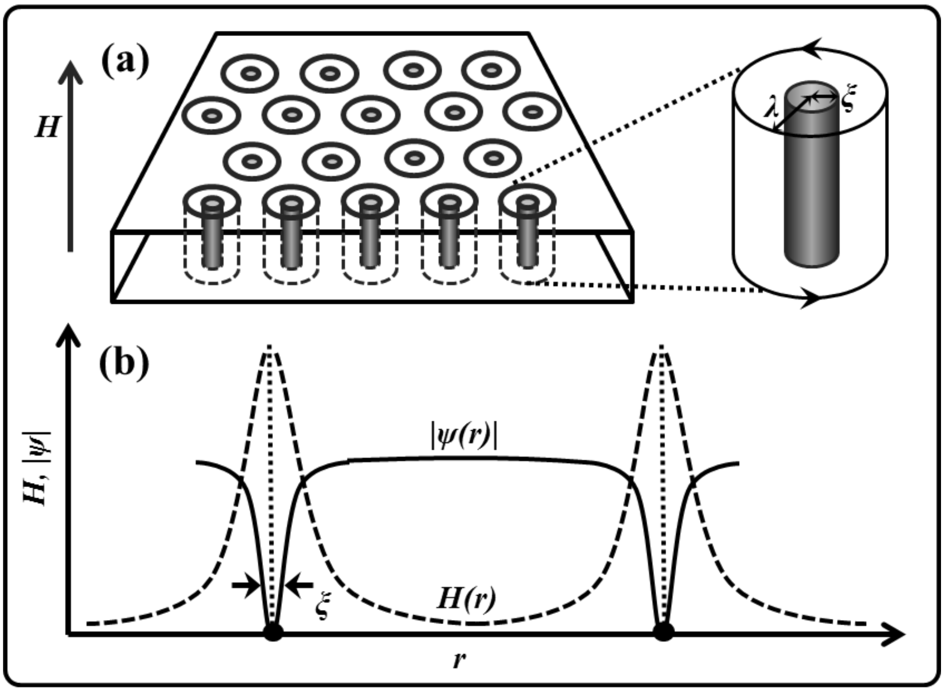

Figure 1.4: (a) Abrikosov's vortices in a type-II superconductor and (b) superconducting order parameter and magnetic field distributions around a vortex core

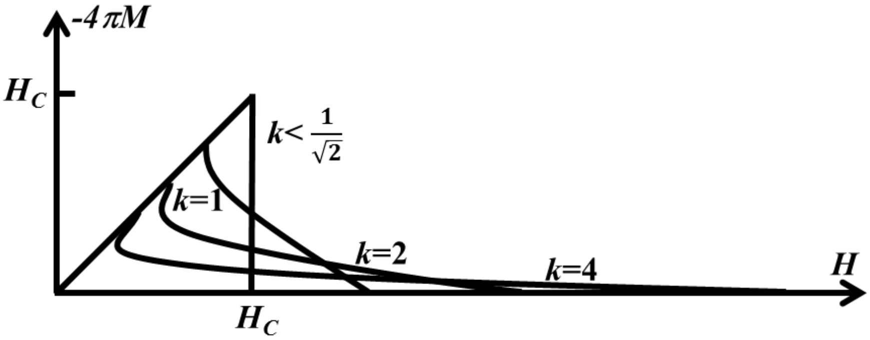

Figure 1.5: Plot of magnetization produced inside a superconductor with external field applied for different values of *k*

The critical state of type-II superconductors has also been determined by the maximum current that the superconductor can carry without energy dissipation. The current carrying property of type-II superconductors is a key parameter for the practical application of low and high temperature superconductors. If a current carrying type-II superconductor is subjected to a magnetic field (*H*), then the flux lines with in the specimen start to move in a direction perpendicular to the current and to the applied field. In the presence of a transport current density (*J*), the flux line lattice of a type-II superconductor in the mixed state experiences a Lorentz force $F_L = J \times H$. This causes vortex motion (flux flow) leading to energy dissipation, thereby inducing electrical resistance called *flux flow resistance* (Bardeen *et al.* 1965). In a homogenous superconductor without defects, this Lorentz force sets the vortices into motion, and the critical current of such an ideal superconductor becomes zero. Whereas inhomogeneous superconductor containing various types of defects like grain boundaries, dislocations, voids or second phase precipitates and the vortices get trapped by these defects. This is known as flux pinning, and the defects act as the pinning centers. Type-II superconductors with strong pinning are called hard superconductors that are relevant for power application of superconductors. Pinning centers can be intentionally introduced into the superconducting material by the addition of impurities or through radiation damage. However, some crystal defects, which are actually contained in superconducting materials, exert pinning forces which stop the vortex flow against the Lorentz forces on the vortices i.e. the pinning force (F_P) balances the Lorentz force. Hence, the critical state results from a competition between the Lorentz force acting on flux lines, pinning force, and repulsive interaction between flux lines. The pinning force favors glassy state of flux lines, whereas the repulsive interaction between vortices results in a regular flux line lattice. The orientations of *J*, *H*, F_L, and F_P in a superconducting slab are given in Figure 1.6.

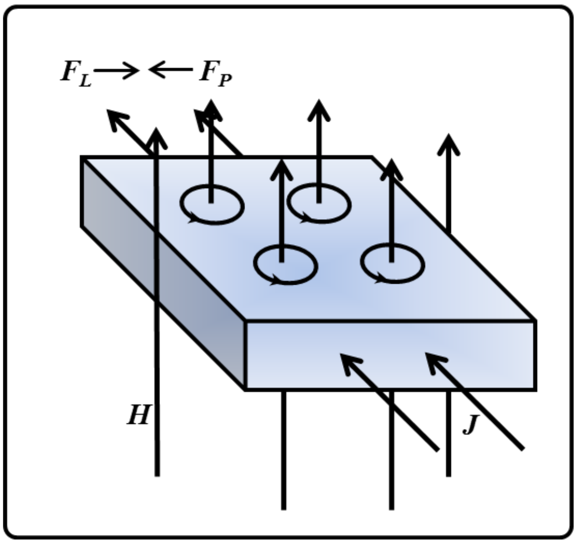

Figure 1.6: The orientations of *J*, *H*, F_L, and F_P in a superconducting slab

The interaction between the defect and the vortex is generated through various mechanisms. If the vortex stays in the superconducting region, the total energy increases by the condensation energy (energy required to nucleate a flux line within the superconductor) of the core volume since the superconducting order parameter, ψ is zero inside the vortex core. If it is located in the point defect, the condensation energy between the normal core and the defect is canceled. This energy difference gives the pinning energy U_P and $U_P = (1/2)\mu_0 H_C^2 \pi \xi^2 d$; where d is the length of the vortex that intersects with the defect. As the vortex approaches a grain boundary, its core size (ξ) is reduced due to reduced mean free path (l) since $\xi \propto l$ (Matsuhita, T. 2007; Matsumoto, K. 2010). When the vortex is located in the grain boundary, an energy gain is obtained, and this energy difference functions as the pinning energy. The maximum value of the energy change by moving the vortex across the defect is called the elementary pinning force *f(p)* and the vector sum of these elementary pinning forces gives the *bulk pinning force (F_P)* (Campbell *et al.* 1972; Larkin *et al.* 1979). F_P is determined by the product of the critical current density (J_C) and the flux density (H), $F_P = J_C \times H$. The pinning forces must be strong enough to prevent the continuous vortex motion, thereby increasing J_C. Thus, J_C increases with an increase in the pinning strength.

The pinning mechanism in superconductors has been explained by several groups. According to Blatter *et al.* (Blatter *et al.* 1994), fundamentally, two different pinning mechanisms describe the interaction of a vortex core with a pinning site - δl pinning and δT_C pinning. The δl pinning is due to scattering of the electron mean free path and the δT_C pinning is associated with a spatial scatter of the critical temperature, T_C throughout the sample. A third mechanism, which played some role in conventional superconductors, is the magnetic interaction between a flux line and a defect. This is inactive in high T_C materials due to their large values of k (Koblischka *et al.* 2000).

1.3 Fundamental theories of superconductivity

Understanding the mechanism of superconductivity has been a great challenge to theoretical physicists since the great discovery. In 1935, London brothers made significant progress in formulating a classical phenomenological theory and derived two equations which can explain the Meissner-Ochsenfeld effect (London *et al.* 1935a; London *et al.* 1935b). The complete fundamental equations for macroscopic superconductivity were formulated by Ginzburg and Landau in 1950 (Ginzburg *et al.* 1950; Ginzburg, V. L. 2004). They developed a quantum mechanical phenomenological theory of superconductivity based on the existence of a complex wave function. An adequate microscopic theory of superconductivity was not there until the introduction of BCS theory in 1957 (Landau, L. D. 1937). Bardeen, Cooper and Schrieffer proposed the formation of a Bose condensate of Cooper pairs in a superconducting ground state and the energy gap associated with this condensation (Bardeen *et al.* 1957a; Bardeen *et al.* 1957b). In this section, phenomenological and qualitative theories introduced for superconductivity are discussed in detail.

1.3.1 London's theory

In 1935, London brothers (Heinz London and Fritz London) successfully explained the Meissner-Ochsenfeld effect, only after two years from the discovery (London *et al.* 1935a; London *et al.* 1935b). They proposed a two-fluid model by which two types of charge carriers are present in the superconducting state - the normal electrons (n_n) and the superconducting electrons (n_s). The electron density $n = n_s + n_n$. They also derived two equations based on the assumption that the super current within the metal is a consequence of the movement of a part of conduction electrons that experience no friction, called super electrons. The super current density $\overrightarrow{J_S}$ is $-en_s\vec{v}$, where n_s is super electron's density. Combining equation of motion of the electron in an electric field with third Maxwell's equation, we get

$$\frac{\partial}{\partial t}\left(\frac{m_e}{n_s e^2}\vec{\nabla}\times\overrightarrow{J_S}+\vec{H}\right)=0 \qquad \textbf{..... (1.1)}$$

London assumed that the value inside the bracket becomes zero and then obtained the equation

$$\vec{\nabla}\times\overrightarrow{J_S}=\frac{n_s e^2}{m_e} \qquad \textbf{..... (1.2)}$$

The above equation is known as first London's equation. And is applicable for type-I superconductor. Equation for the magnetic field in a superconductor is obtained by using forth Maxwell's equation and is

$$\nabla^2\vec{H}-\frac{\mu_0 n_s e^2}{m_e}\vec{H}=0 \qquad \textbf{..... (1.3)}$$

This is London's second equation. The solution of this equation for a magnetic field parallel to the surface is as follows: $H_y(x)=H_0 exp(-x/\lambda_L)$, where λ_L is London's penetration depth. The solution says that the magnetic field does not vanish abruptly at the superconductor surface but penetrates into the material with exponential attenuation. Within the length λ_L, the magnetic field is reduced by a factor of 1/*e* and then vanishes deep within the superconductor. λ_L has a temperature dependence and becomes infinite at $T = T_C$ and magnetic flux fully penetrates into the superconductor.

1.3.2 Ginzburg-Landau theory

In 1950, Ginzburg and Landau proposed a macroscopic theory (GL theory) for superconductivity based on Landau theory of second-order phase transitions (Ginzburg *et al.* 1950; Ginzburg, V. L. 2004). Landau theory (Landau, L. D. 1937) says that there is a thermodynamic quantity, called an order parameter, which is zero in the symmetric (high temperature) phase and becomes continuously non-zero in the less symmetric phase. The thermodynamic wave function is $\psi = |\psi_0|\, exp(i\theta)$ and $|\psi|^2$ gives the probability of the existence of superconducting electrons. According to GL theory, at a temperature close to T_C the free energy per unit volume of a superconductor can be expanded as a Taylor series of $|\psi|^2$ where ψ is small.

$$F_s = F_n + \alpha|\psi|^2 + \beta|\psi|^4 + \cdots, \text{ where}$$

F_s - free energy of the superconducting state
F_n - free energy of the normal state
α, β - expansion coefficients

The minimum of free energy (F_s - F_n) occurs either *at* $|\psi| = 0$ or at some nonzero value of $|\psi|$.

At $|\psi| = 0$, the equilibrium state is normal
$|\psi| \neq 0$, the equilibrium state is superconducting

The variation GL free energy function, F_s - F_n, with respect to $|\psi|^2$ is shown in Figure 1.7. At $T < T_C$, $|\psi| \neq 0$ and $|\psi_0|^2 = n_s$, the density of the superconducting electron. This means that the superconducting state is stable at the temperature of T_C or less.

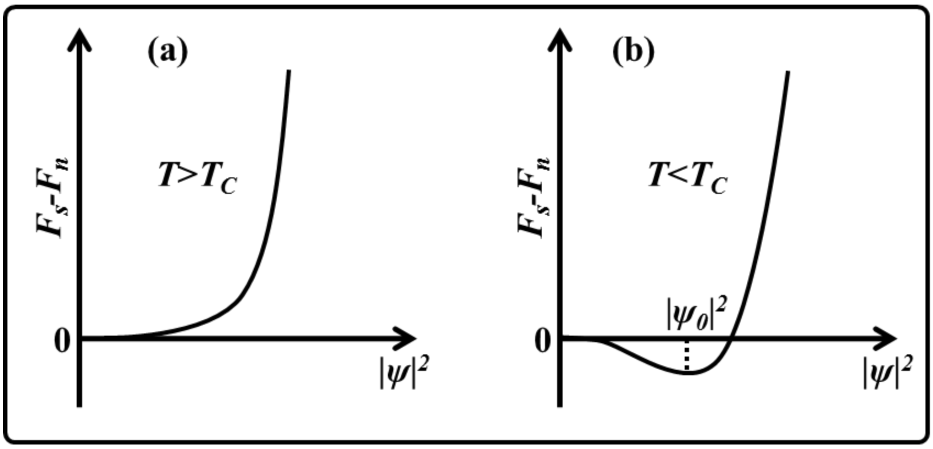

Figure 1.7: GL free energy functions F_s - F_n (a) $T > T_C$ and (b) $T < T_C$ for superconducting state and normal state

Ginzburg and Landau formulated two equations, and the solutions of these equations contain two length scales (coherence length, ξ and penetration depth, λ) which provide several features of superconductors. Coherence length (ξ) of the material is a characteristic minimum length over which the wave function can significantly change. The density of the super current carriers does not change suddenly from zero to its value in the bulk at a normal-superconductor boundary, but increases smoothly over a finite length ξ. This theory also gives the difference between type-I superconductors ($\xi > \lambda$) and type-II superconductors ($\xi < \lambda$). The coherence length of superconductor can be obtained from the formula:

$$\xi = \left(\frac{\hbar^2}{4m\alpha}\right)^{1/2}$$

Incorporating magnetic field into the free energy function we get an expression for super current j_s and is

$$j_s = \frac{e\hbar}{2mi}(\Psi^*\nabla\Psi - \Psi\nabla\Psi^*) - \frac{2e^2}{m}|\psi|^2\mathrm{A}$$

where A is the vector potential of the total field acting on Ψ.

1.3.3 BCS theory - microscopic theory of superconductivity

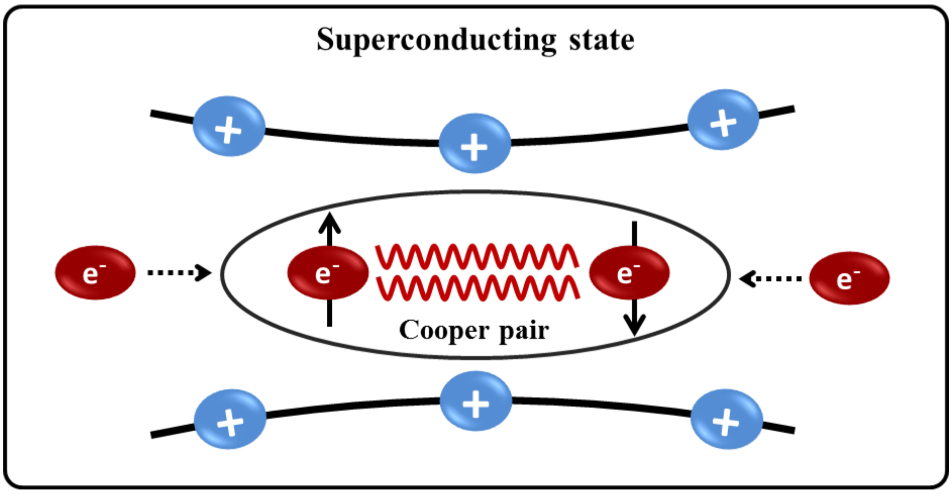

Figure 1.8: Illustration of Cooper pair formation in the superconducting state

BCS theory was the first successful theory to explain the microscopic mechanisms of superconductivity in metals and alloys. In 1957 Bardeen, Cooper, and Schrieffer published their microscopic theory of Cooper-pair formation and for this discovery they received Nobel Prize in Physics in 1972 (Bardeen *et al.* 1957a; Bardeen *et al.* 1957b). This theory is held as the standard for low temperature superconductors and explains superconductivity at temperatures close to absolute zero. The BCS theory was able to explain the basic properties of superconductors such as: (a) zero resistance of an ideal superconductor and the Meissner effect; superconductivity is essentially connected with some change in the behavior of the conduction electrons which shows up in the appearance of long-range order and an energy gap in their excitation spectrum (b) the isotope effect; the crystal lattice shows an extremely small change of properties, but nevertheless plays a very important role in establishing superconductivity because the critical temperature depends on the atomic mass (c) the second-order phase transition from a superconducting to a normal state in zero magnetic field.

The BCS theory was based on an idea that the electrons can be changed into bosons (electron pair, namely Cooper pair) by some means; thereby the total energy of the system can be lowered. The electrons are normally repelled from one another due to their identical electric charge and hence the individual electrons themselves cannot exhibit Bose condensation. But according to BCS theory, in the superconducting state the electrons feel a net attraction due to local distortion of the lattice, resulting in the formation of Cooper pairs as shown in Figure 1.8. The Cooper pair formation is the basis of BCS theory. In the superconducting state, current is carried by this Cooper pairs and not by single electrons. While a negatively charged electrons move around a positively charged ion in the lattice of the superconductor, the lattice gets distorted. This resulted in the emission of phonons and forms a trough of positive charges around the electron. A second electron is attracted towards the trough before the first electron move away or before the lattice gets back to its normal position. The forces exerted by the phonons overcome the electron's natural repulsion. In this way, two electrons bound together through a phonon mediator. The electron pairs are coherent with one another as they pass through the conductor. The electrons are screened by the phonons and are separated by some distance. When one of the electrons that makes up a Cooper pair and passes close to an ion in the crystal lattice, the attraction between the negative electron and the positive ion causes a vibration to pass from ion to ion until the other electron of the pair absorbs the vibration. The net effect is that the electron emits a phonon, and the other electron has absorbed that phonon. It is this exchange that keeps the Cooper pairs together. However, the pairs are constantly breaking and reforming. The electrons forming Cooper pair have equal and opposite momentum and spin. They can be represented by a wave function is $\psi = |\psi_0| \, exp(i\theta)$, called “BCS wave function” composed of $k\uparrow$ and $-k\downarrow$. Here $|\psi|^2$ is the density of Cooper pairs, and θ is the phase. All pairs occupy a single quantum state, the BCS ground state, whose energy is separated from the single-electron states by an energy gap (2Δ). The energy corresponding to 2Δ is necessary to break the Cooper pairs which in turn can be related to the critical temperature. The formation of Cooper pairs and the energy gap 2Δ are related to the ability of a superconductor to carry current without electrical resistance. An individual electron in the normal conducting state is scattered by the phonon and by impurities, and its direction of movement is forced to change; hence, electrical resistance is generated. However, in the superconducting state the Cooper pairs move in an ordered fashion, and the center of mass of a Cooper pair has the same value of momentum for all pairs. Due to the reduced molecular motion in the lower temperatures, Cooper pairs in the superconductor stay together. As the superconductor gains heat energy, the vibrations in the lattice become more violent and break the pairs and vanishes superconductivity.

The main conclusions of BCS theory are:

1. An attractive interaction between electrons can lead to a ground state separated from excited states by an energy gap.
2. An electron-lattice-electron interaction proceeds when one electron interacts with the lattice and deforms it; a second electron sees the deformed lattice and adjusts itself to lower its energy.
3. The penetration depth and coherence length emerge as a consequence of the BCS theory that explains the Meissner effect.
4. T_C depends on the electron density of orbitals $D(E_F)$ of one spin at the Fermi level and the electron-lattice interaction U. For $UD(E_F) << 1$, $T_C = 1.14\Theta \exp [-1/UD(E_F)]$, where Θ is the Debye temperature.
5. Magnetic flux through a superconducting ring is quantized in terms of the pair charge 2*e*.

The BCS theory has turned out to be of enormous predictive power and many of its predictions and implications like the temperature dependence of the energy gap and its relation to the critical temperature, the quantization of magnetic flux and the existence of quantum interference phenomena have been confirmed by experiment (Vonsovsky *et al.* 1982; Schrieer, J. R. 1964). BCS theory is suitable to explain the microscopic mechanisms of superconductivity in pure metals and alloys. However, the theory is not appropriate to explain the mechanisms of superconductivity in oxide superconductors. Nevertheless, other models relying on a BCS-like picture replace the phonons by other bosons, such as: plasmons, excitons and magnons, as the mediators causing the attractive interaction between a pair of electrons (Canright *et al.* 1989; Takada, Y. 1993; Kresin *et al.* 2009).

1.4 Evolution of superconductors: LTS to HTS

Soon after the discovery of superconductivity in mercury, Kamerlingh Onnes extended the list of superconducting materials by tin (T_C = 3.7 K) and lead (T_C = 7.2 K) (Hott *et al.* 2005). The same group also discovered a number of new superconducting elements such as thallium (T_C = 2.4 K), indium (T_C = 3.4 K), etc. and studied their magnetic properties. After that, Meissner concentrated his research on finding superconductors throughout the periodic table. He found superconductivity in tantalum (T_C = 4.2 K) in 1928 and thorium (T_C = 1.4 K) in 1929 and in the next year titanium (T_C = 0.4 K), vanadium (T_C = 5.3 K) and niobium (T_C = 9.2 K, the element with the highest T_C) (Goodstein *et al.* 2000). The extension to binary alloys and compounds was achieved in 1928 by de Haas and Voogd with SbSn, Sb_2Sn, Cu_3Sn and Bi_5Tl_3 (Fossheim *et al.* 2004). Shortly afterward, a Pb-Bi eutectic alloy established the first example of critical magnetic field values in the Tesla range. After 1930, there was a break in hunting for new superconducting materials around two decades. In between 1950s and 1960s, Bernd T. Matthias and John K. Hulm delivered a number of new compounds with high T_C well above 10 K as well as technically attractive H_{C2} well above 10 T. The most prominent material among these series were NbTi (T_C = 9.2 K), A15 materials (V_3Si, T_C ~ 17.5 K), A_3B type intermetallic compounds (Nb_3Sn of T_C ~ 18.3 K and Nb_3Ge of T_C ~ 23.2 K). These materials are widely used in the superconducting wire industry. Nb-Ti alloy has been the material of choice for commercial superconducting magnets. Later, a brittle Nb_3Sn intermetallic material has emerged as an excellent alternative to achieve even higher magnetic field strength. Many other metals and metal alloys were also found to be superconductors at temperatures below 23.2 K before 1973. These superconductors are known as *Low Temperature Superconductor (LTS)* materials.

In 1979, superconductivity was discovered in the magnetic material $CeCu_2Si_2$, which was the first representative of a new class of “heavy-fermion” superconductors (Steglich *et al.* 1979). In these materials Cooper pairing occurs through the magnetic mechanism; i.e. the electronic degrees of freedom which are responsible for superconductivity are directly linked with magnetic moments of partially filled f-shells of lanthanide or actinide atoms. The superconductivity below a typical T_C ~ 1 K seems to arise here from the delicate balance between the localized magnetic moments and the conduction electrons which try to neutralize these magnetic moments by spin flipping. Organic superconductors (T_C > 10 K) were discovered in 1980 (Jérome *et al.* 1980) and the origin of superconductivity in these materials are from π-electrons in stacked aromatic rings which form one or two dimensional delocalized electron systems. The restriction of the effective dimensionality and strong Coulomb repulsion effects produces superconducting transitions in these materials. In 1985, superconductivity was found in fullerides like C_{60} and C_{70} molecules at normal pressure by doping and intercalation of alkali-metal atoms ($T_C \sim 33$ K) (Tanigaki *et al.* 1991).

In 1986, J. G. Bednorz and K. A. Müller discovered cuprate based ceramic materials (LaBaCuO) that demonstrated superconducting properties as high as 35 K, for which they were acknowledged with a Nobel Prize in the following year (Bednorz *et al.* 1986). This lead to the beginning of an era of cuprate based high temperature superconductors. Till then, we believed that ceramics materials do not show superconductivity since they are normally insulators. This facilitates the possibility of finding high temperature superconductor candidates. Replacing La with Y (YBCO) Chu and others (Wu *et al.* 1987) got an incredibly high T_C of 92 K, well above liquid nitrogen temperature of 77 K. Tremendous advances were made in theoretical and experimental research and as a result the T_C reached 112 K in a Bi-based compound ($Bi_2Sr_2Ca_2Cu_3O_{10}$ or Bi-2223), 126 K in a Tl-based compound ($Tl_2Ba_2Ca_2Cu_3O_{10}$ or Tl-2223) and 135 in a Hg-based compound. The highest T_C ever reported to date is in the Hg-based compound ($HgBa_2Ca_2Cu_3O_8$) under 30 GPa pressure with $T_C = 164$ K (Gao(a) *et al.* 1994). In all cuprate based superconductors, the superconductivity occurred in the CuO_2 layer, and they belonged to non-BCS superconductors (T_C exceeds the predictions made by BCS theory). The theories behind this HTS are still not fully revealed. Most of the HTS are produced from metastable materials in which thermodynamically stable reactants are forced into forming the compound either by high pressure and temperature or by doping.

In 1990s, borocarbide superconductors of $RENi_2B_2C$ ($T_C \sim 16.5$ K) were discovered and in which phonons involve in the superconducting mechanism. However, for rare earth borocarbides the localized RE^{3+} 4f-electrons weakly interact with superconductivity associated with the 3d-electrons of the Ni_2B_2 layers (Canfield *et al.* 1998). The great astonishment in this field came in 2001 with the discovery of superconductivity up to $T_C =$ 39 K in MgB_2 by Akimitsu (Nagamatsu *et al.* 2001), a compound with low cost and abundant availability of the raw materials. Superconductivity in this material can be explained by BCS theory.

In 2006, superconductivity was discovered in an iron-containing compound LaFeOP with $T_C \sim 4$ K by Yoichi Kamihara (Hideo Hosono's research group at the Tokyo Institute of Technology) (Kamihara *et al.* 2006). In February 2008, the same group reported a T_C of 26 K in the system by replacing some of oxygen atoms with fluorine and phosphorus with arsenic (Kamihara *et al.* 2008). This discovery excited the physicists because the superconductor contains a magnetic element like iron and generally magnetism inhibits superconductivity. The T_C of iron-based superconductor rose up to 55 K by replacing La with Sm ($SmFeAsO_{1-x}F_x$) (Chen(b) *et al.* 2008; Fujioka *et al.* 2011), well above the T_C of conventional superconductors but significantly below that of the copper oxides. The exact superconducting mechanism behind them is not fully understood. The other significant characteristic of this superconductor is that there is a variety of materials having similar structures, and many new superconductors have been discovered in this family in the last five years.

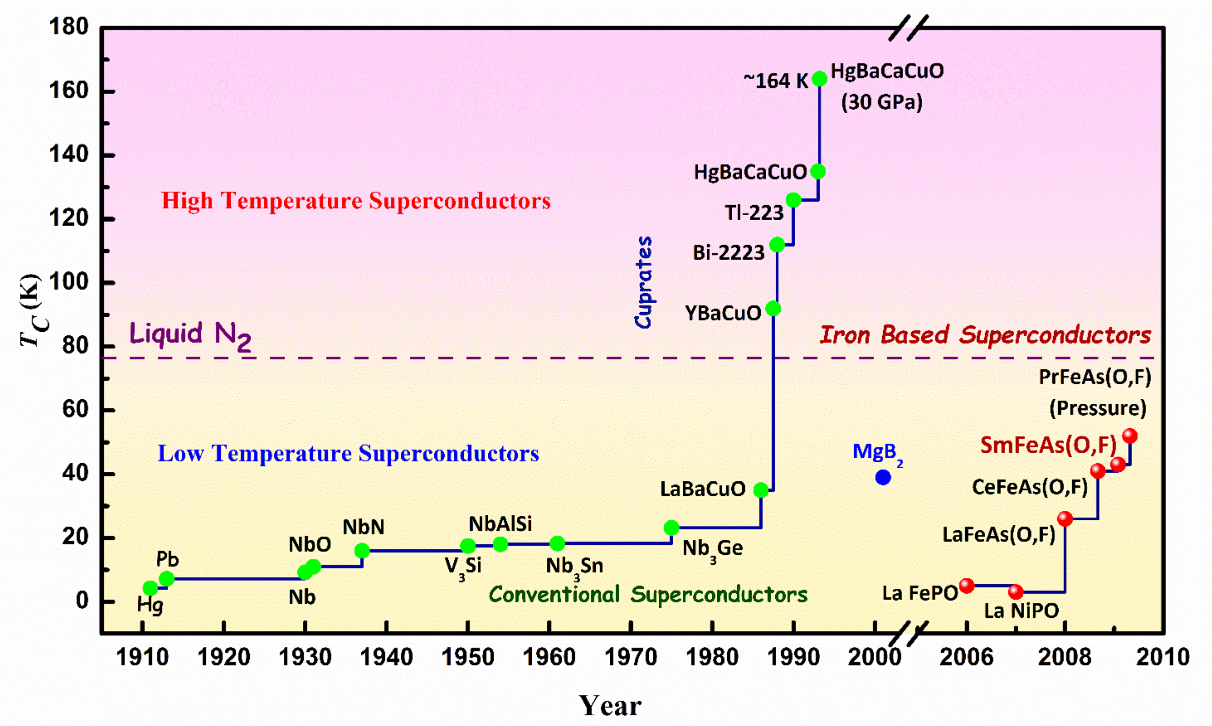

Figure 1.9: Graphical representation of evolution of superconductors in terms of critical temperature

Hundred years already passed since Onnes's discovery and over the years more than 6,000 elements, compounds, and alloys have been found to be superconductors. The evolution of superconductivity from LTS to HTS is summarized in Figure 1.9. Both the HTS and LTS materials have been used at the application level. The LTS materials like Nb-Ti and Nb_3Sn have been the choice for large-scale applications such as magnetic resonance imaging, nuclear magnetic resonance, and magnet for high energy accelerators and plasma fusion devices. YBCO and Bi-based conductors which include in the category of HTS are used for power applications.

1.5 Applications: small-scale and large-scale

At the beginning of the 21st century, superconductivity has formed the basis for new commercial products. The unusual physical properties of superconductors like zero resistance and diamagnetism resulted in some remarkable applications (Buckel *et al.* 2004; Kitazawa, K. V. 2012; Koizumi, N. 2013) in specific areas where superconducting materials can replace the conventional materials with better performance. In many fields, the superconducting technology is the only possibility for achieving the required performance. By using superconducting components, the size and weight of instruments and devices can be reduced compared to conventional techniques which are an important issue for fields like space applications. The advent of HTS has changed the dynamic of refrigeration by permitting smaller and more efficient cooling system for some applications (http://ccas-web.org/pdf/ccas_brochure_web.pdf). Design, integration of superconducting and cryogenic technologies, demonstration of systems cost benefits and long term reliability must be met before superconductivity delivers on its current promise of major societal benefits and makes substantial commercial inroads into new applications. Even though the applications of superconductivity are restricted around the liquid nitrogen temperature, those will contribute to the society since the refrigeration systems are well developed nowadays.

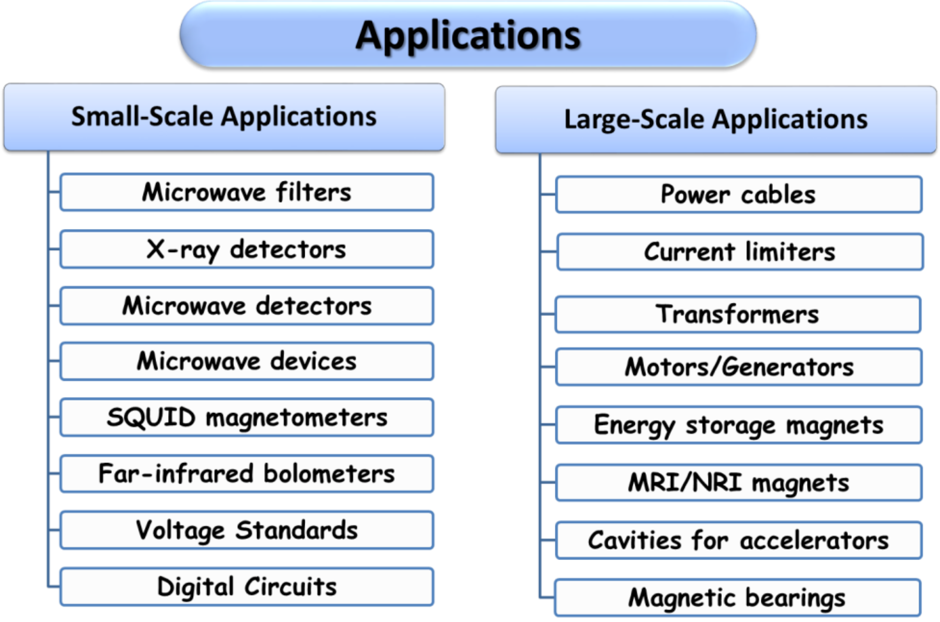

Figure 1.10: Applications of superconductors

Superconductor applications can be mainly divided into two main categories: small-scale which usually include electronic components or devices and large-scale where magnets and energy applications are of great importance (Fossheim *et al.* 2004; Daibo *et al.* 2013; http://www.conectus.org/technology.html). The major commercial applications of superconductivity in the medical diagnostic, science and industrial processing fields involve LTS materials and relatively high field magnets. Other small-scale commercial applications of superconductivity that use LTS materials include magnets for research purpose, Magneto Encephalography (MEG) based on Superconducting Quantum Interference Device (SQUID) technology used for measuring weak magnetic fields generated by the brain. The substantive commercial products incorporating HTS materials are electronic filters used in wireless base stations. About 10,000 units have been installed in wireless networks worldwide to date. The commercialization of LTS materials was done by Oxford Instruments (UK Company), and they successfully developed MRI (Magnetic Resonance Imaging) magnets. Another major LTS application is Large Hadron Collider (LHC) at CERN, the largest machine in the world using over 5000 magnets. Flowchart below (Figure 1.10) summarizes the important applications of superconductors in terms of small and large scales.

1.5.1 Small-scale applications

The major success has been achieved with small-scale devices that depend on one of the special properties of superconductors, Josephson quantum tunneling effects. Some LTS and HTS small-scale devices are now commercially available. These devices have the advantage of size and much smaller power consumption. YBCO is widely used for the HTS small-scale devices because it has a high critical temperature and can accommodate high current densities.

SQUID: The most known small-scale device is SQUID magnetometer. It contains a ring of superconductor with one or more Josephson junctions. As the current introduced into the SQUID is larger than the critical current of the Josephson junctions, a voltage appears that is proportional to the magnetic flux through the ring. The SQUID is so exceedingly sensitive that it can detect magnetic fields 100 billion times smaller than the Earth's field, and it can also detect any other physical quantity that can be converted to a magnetic flux. SQUID based technology is widely used in medical applications for mapping the magnetic fields of the human body especially in magneto encephalography. In material science and physics research, SQUID based magnetometers and susceptometers (Physical Property Measurements System) are being used for magnetic characterization of materials. LTS based SQUIDs are widely used than that based on HTS.

Microwave devices: Superconductors can also have a dramatic impact on selected passive microwave device applications because of two properties that differ greatly from those of normal metals at high frequencies. First, much lower surface resistance is available using superconductors that root lower loss and higher Q-values in superconducting microwave system components. Second, superconductors have a practically frequency independent penetration depth in the microwave frequency range that introduce no dispersion into a microwave device up to 1 THz frequency in LTS superconductors, and well above this in HTS superconductors due to their larger gap frequency. High temperature superconducting microwave components include filters, antennas, resonators, and transmission lines. HTS filters will enhance signal to noise ratio in cellular communications systems leading to reliable communication services with fewer spaced cell towers. Superconducting microwave technology offers unique advantages derived from the low microwave loss of superconducting materials and the inherent low thermal noise in cryogenically cooled components. Several microwave communication base station receiver front ends consist of superconducting components.

1.5.2 Large-scale applications

For large-scale applications both LTS and HTS have been used, among these LTS is quite common. Large-scale applications for HTS materials face a major challenge that much larger currents and lengths of superconductor are required in a working environment where the magnetic field may be several Teslas. The important large-scale applications are power transmission cables, current leads, fault current limiters, transformers, generators, motors, energy storage and magnets. In all these applications, except current limiters HTS superconductors would simply replace conventional conductors.

Power Applications: Superconductor technology will have a significant impact on the power industry since HTS wire promises to deliver more power than the copper or aluminum wires currently used. Some examples of emerging power applications are power cables, motors and generators, fault current limiters and superconducting magnetic energy storage (SMES). Most companies involved in development efforts believe that superconducting wire will transform the electric power industry in much the same way that optical fibers transformed telecommunications. HTS power cables have a broad impact on generation, transmission, and distribution. They can deliver up to five times more current than conventional power lines of the same diameter. The use of HTS wire eliminates energy loss due to electrical resistance, promising significant savings in power costs.

Motors and generators are other promising applications. Superconductivity will enable smaller, more efficient systems with significant performance enhancements. These efficiency advancements will lead to energy conservation and increased environmental protection through decreased emissions. Superconductor current limiters can effectively limit the current spikes in circuit such a way that when a large pulse of current comes through the system, the superconducting coil automatically absorbs the excess energy within milliseconds. No equipment is exposed to damage, which allows utilities to increase loads and provide more reliable service to consumers. Lockheed Martin (USA) collaborating with Southern California Edison, Intermagnetics, and Los Alamos National Laboratory demonstrated commercially viable HTS current limiters. Use of HTS transformers can also reduce the power loss during transmission, and also reduce the size and weight by half.

SMES is another technology that serves to protect modern utility grids from power interruptions. SMES offer improved performance and efficiency (98%) compared with the 90% of other utility devices, such as fuel cells. SMES technology is based on three concepts; 1. HTS materials carry current with no resistive losses, 2. electric currents produce magnetic fields, 3. magnetic fields are a form of pure energy which can be stored. SMES store energy in the magnetic field of a *dc* current that flows in a superconductor wire/tape. Energy losses are negligible, making it possible to inject and extract the current very quickly. Because the major parts in a SMES are static, wear is minimal, and reliability is high.

Transportation: Development of HTS will enable new generation transport technologies like magnetically levitated trains (Maglev). Since 1962, Japan has been working to develop Maglev train (magnetic levitation) in order to overcome the friction between the wheels and a rail of conventional trains thereby reach a commercial speed of 500 km/h and was fulfilled in March 2005. Most of the present maglev systems use YBCO material since it exhibits high magnetic irreversibility field at liquid nitrogen temperatures, and it has the ability to grow into large grains.

Superconducting Magnets: Superconducting magnets are nowadays used almost everywhere where there is a need of high magnetic fields. Typical examples include magnetic resonance imaging (MRI), high-energy particle accelerators, chemical processing, and thermonuclear fusion research. Most of these applications still rely on LTS materials because of the cost of suitable HTS materials. But in certain fields, HTS have been demonstrated. NbTi is the mostly used superconducting material for MRI magnets.

However, for high field magnets Nb_3Sn is used, and some HTS based inserts are also developed for still higher fields. With the development of cryocoolers, various kinds of cryogen-free superconducting magnets with fields of the order of 20 T are developed for practical applications. In fusion reactors, the plasma temperature needed for energy production is several million degrees, and high field superconducting magnets are required to confine the plasma. The International Thermonuclear Experimental Reactor (ITER) project is engaged in the development of fusion reactor and a large quantity of LTS superconductors. Superconducting solenoids are being used for bending and focusing of high energy particles in high-energy particle physics labs like Brookhaven National Laboratory (BNL), European Organization for Nuclear Research (CERN), Deutsches Elektronen Synchrotron (DESY) and the Fermi Laboratory. Superconducting radio frequency cavities are also finding applications in particle accelerators.

In all these cases, the superconductor must not only carry a large current with zero resistance under a high magnetic field, but it must be possible to fabricate it in long lengths with high flexibility and a high packing density. For large-scale applications, the critical current density J_C must generally be greater than 10^4 A/cm^2 (http://www.conectus.org/technology.html), and the magnet must operate well in a magnetic field from about 0.2 T for a transmission cable to about 4 T for a generator. The J_C of the high temperature superconducting materials, however, needs to be improved before they can be used extensively in commercial applications.

CHAPTER 2

IRON-BASED SUPERCONDUCTORS

2.1 The iron age in superconductivity

In 2006, scientists in Japan (Hideo Hosono group, Tokyo Institute of Technology, Japan) accidently discovered superconductivity in LaOFeP with a T_C of 4 K, a completely new type of superconductor based on iron (Kamihara *et al.* 2006). The T_C was further raised to 7 K by fluorine doping at oxygen sites (Liang *et al.* 2007). Even though this T_C was relatively low, it was very interesting because iron is famous for its ferromagnetism, and this has broken the belief that 'superconductivity does not mix with magnetism'. The use of the elements leading to magnetism, typically Fe, Ni and Co, was intentionally avoided previously in the field of superconductivity. But, superconductivity in the new materials seems to be related to magnetic behavior. Hence, the discovery of a high T_C superconductor based on iron-based compounds significantly excited the research in this field. The same group further reported another discovery in February 2008. They had replaced phosphorus with another pnictogen, arsenic, in the layered material, and the transition temperature shot up to 26 K (Kamihara *et al.* in $LaFeAsO_{0.89}F_{0.11}$ compound) (Kamihara *et al.* 2008). Actually, the discovery of relatively high T_C in an iron-containing composition triggered a wave of research and quickly pushed the transition temperature above 50 K (Wei *et al.* 2008). Even though the cuprates revealed that high temperature superconductivity was probable, the iron-based materials demonstrated that this phenomenon is not restricted to a single class of compounds. Thus, physicists found new ways of studying the superconducting mechanism behind the unconventional high temperature superconductors, an important mystery of condensed-matter physics. This also led to the beginning of an "iron age" in superconductivity and the materials science community opened a fury of activity in this area. This superconductor family was known as Pnictides in the early stage and now as 'Iron-based Superconductors (FeSC)'.

So far, iron-based superconductors have been extended to a large variety of materials and can be mainly classified into four categories according to their chemical formulae (Aswathy *et al.* 2010; Fujitsu *et al.* 2012; Ren(a) *et al.* 2009; Oh *et al.* 2011). They are 1111 (REFeAsO, RE - rare earth elements), 122 (BFe_2As_2 & AFe_2Se_2, A - alkaline earth metals & B - alkali metals), 111 (AFeAs), and 11 (FeCh, Ch - chalcogen) types. In addition to this, the intercalation of additional layers into the above categories created new materials such as 32522 ($Sr_3T_2O_5Fe_2As_2$ (T - Sc),) and 42622 ($Sr_4T_2O_6Fe_2Pn$, T - Sc, V & Pn - As, P). List of FeSCs belonging to different categories and their corresponding critical temperatures are given in Table 2.1.

Table 2.1: List of FeSCs belonging to different categories and their corresponding T_Cs

Category	Compound		T_C (K)
1111	$REFeAs(O_{1-x}F_x)$	RE=La, Ce, Nd, Sm, Gd, Y, Eu	26, 41, 50, 52, 36, 10, 11
		RE=La, Pr, Nd, Sm, Gd, Tb, Dy	43, 52, 51.9, 55, 52, 46, 45 (HP*)
	$REFeAsO_{1-x}$	RE=La, Ce, Pr, Nd, Sm, Gd, Tb, Dy, Ho, Y	31.2, 46.5, 51.3, 53, 55, 53.5, 48, 52.2, 50.3, 46.5 (HP)
	$(RE_{1-x}A_x)FeAsO$ (Gd/Tb, Th)(La, Pb)		56, 52, 10
	$RE(Fe_{1-x}A_x)AsO$	RE=La, Sm & A=Co	14.3, 15
		RE=La & A=Ni, Ir	6.5, 11.8
	$REFe(As_{1-x}A_x)O$	RE=La, Sm & A=P	10.5, 4.1
122	$(A_{1-x}B_x)$ Fe_2As_2	A=Ba & B=K	38
		A=Sr & B=Cs, K	37, 37
		A=Eu & B=K, Na	32, 34.7
		A=Ca & B=Na	20
	$A(Fe_{1-x}B_x)_2As_2$	A=Ba & B=Co	22
		A=Sr & B=Rh, Ir, Pd, Ru	21.9, 24.2, 8.7, 11.8
	$AFe_2(As_{1-x}B_x)_2$	A=Ba/Eu,, B=P	30, 26
111	AFeAs	A = Li, Na	18, 9
11	α-FeSe		8, 27 (HP)
	$Fe(Se_{1-x}A_x)$	A=Te, S	15.3, 15.5
	$(Fe_{1-x}A_x)Se$	A=Co, Ni	10, 10
	$Fe(Te_{1-x}A_x)$	A=S	10

***HP indicates High pressure synthesis**

All members of this family have layered structure in which iron atoms are arranged in a square lattice and have a similar electronic structure where the 3d electrons derived from Fe ion play an important role in superconductivity. They share several characteristics with the cuprate superconductors. They have a layered structure, the presence of competing orders, low carrier density, small coherence length and unconventional pairing. However, there are also some differences between cuprates and FeSCs. Fe-based superconductors have metallic parent compounds, their anisotropy is generally smaller and does not strongly depend on the level of doping, and their order parameter symmetry is s-wave, which is in principle not so detrimental to current transport across grain boundaries (Putti *et al.* 2010). Another motivating side of these superconductors is that they belong to a widespread class of materials where many chemical substitutions are possible. This versatility gives an opportunity to improve the superconducting properties for commercial technologies. In summary, this family has opened a new chapter in superconductor research and perhaps the most important innovation in this field for more than two decades. Besides, the fascinating richness of structural and physical properties and despite many still open issues, these materials provide new avenues for understanding the phenomenon.

2.2 Properties of iron-based superconductors

2.2.1 Physical properties

Fe-based superconductors have a layered structure similar to cuprates and in which Fe^{2+} ions are analogous to Cu^{2+} in cuprates. But in FeSCs, Fe ions are not located exactly in the same plane as As (Se) ions but are rather sandwiched by As (Se) ions, unlike CuO planes in cuprate based superconductors. Here, the Fe atoms making up the square planes are tetrahedrally coordinated by pnictogen or chalcogen atoms in these structures, and the FeAs/FeCh layer is common to the Fe-based superconductors. Similar to cuprates, this layered structure provides quasi-two-dimensional carrier transport properties. Here, the iron-pnictogen/chalcogen layer acts as conductive layer and the local structure of this layer is affected directly by the atomic (or ionic) size of metallic element such as an alkali metal, alkaline earth or rare earth element that lies between the conductive layer (or in the blocking layer) because these elements are bond to Fe ions. However, it is an antiferromagnetic (AFM) semimetal not like cuprate superconductors where the parent materials are Mott insulators (Ma *et al.* 2008). Fe^{2+} contains six electrons in its 3d orbital which play an essential role in driving the superconductivity and magnetism (Fujitsu *et al.* 2012). Furthermore, an even number of d electrons demand a band-structure of semiconductor or semimetal, i.e. the top of the valence band crosses the bottom of the conduction band (Tesanovic, Z. 2009). Moreover, Fe^{2+} magnetic ions suppress the traditional singlet s-wave electron-phonon superconductivity which makes it rather unconventional. Raman scattering studies (Min *et al.* 2013) revealed that a delicate coupling between electrons, spins, and phonons may be crucial to high T_C superconductivity in FeSCs since the parent compounds have spin-ordering.

In 1111 type, the parent compound (REFeAsO) crystallize in a tetragonal structure similar to ZrCuSiAs with a space group of *P4/nmm* at room temperature. The RE atoms (having *4mm* site symmetry) are coordinated by four As atoms and four O atoms forming distorted square antiprisms. The Fe atoms (42m) are located at the center of $FeAs_4$ tetrahedral network forming a 2D square lattice perpendicular to the *c* axis. Arsenic atoms are located at the apical sites of the tetrahedron. The structural parameters of the $FeAs_4$ tetrahedra are considered to be a contributing factor controlling the T_C, includes the bond angle of As-Fe-As (α) and the height of As with respect to the Fe planes (h). These two parameters have been extensively mentioned because the maximum T_C in FeSCs is obtained when $FeAs_4$ forms a normal tetrahedron (α = 109.5°) and h = 1.38 Å (Lee(a) *et al.* 2008; Zhao(a) *et al*. 2008; Mizuguchi *et al.* 2010). The overall T_C does not follow a unique relation to any of these parameters; rather it depends on the type of doping also (Johnston, D. C. 2010). The As-Fe-As angle in As tetrahedron varies from one family to another (Calderón *et al.* 2009). It is almost regular in the 122 family with the angles close to the ideal value, 109.47° while it is 102.8° (rather elongated) in 111 family. In 1111 family, the tetrahedron is squashed and the angle depends on the specific composition, being equal to 113.7° in LaFeAsO and 120.6° in LaFePO. The two-dimensionality of 1111 type is relatively high compared to the others, and only this group has T_C values above 50 K. The atomic structure of 1111 family consists of a stack of alternating positively charged RE-O layers and negatively charged Fe-As layers along the *c* axis and the distance between the Fe-As layers corresponds to the length of the *c* axis. The RE-O layer plays as an insulating charge reservoir layer while the Fe-As layer acts as the conducting active block. The structure of REFeAsO comprises sheets of Fe^{2+} ions in between ionic blocks of $REOAs^{2-}$. The valence state of each atom is RE^{3+}, Fe^{2+}, As^{3-} and O^{2-}. The 122 and 111 types also have similar structures resembling the 1111 type while the ‘blocking layer’ which separates is different: alkaline-earth metals for the 122 type family and alkali metals for the 111 type. The 122 type has a $ThCr_2Si_2$ type crystal lattice with a space group of *I4/mmm*, and 111 type has Cu_2Sb type structure (Rotter *et al.* 2008; Wang(c) *et al.* 2008). The 11 type materials have the simplest structure among iron-based superconductors, in which iron chalcogenide layers are simply stacked together (Hsu *et al.* 2008). However, the real crystalline status is much more complicated because the occupation of Fe^{2+} ions within the interstitial site suppresses superconductivity severely (McQueen *et al.* 2009). The crystal structure of different categories of iron-based superconductors is shown in Figure 2.1.

The calculated Fermi surface for LaFeAsO is shown in Figure 2.2. It consists of two electron cylinders, two hole cylinders and a 3D hole pocket (Singh *et al.* 2008). This has been resulting from five bands which cross the Fermi level. The electron and hole cylinders along k_z direction replicate a quasi-two-dimensional nature of the atomic structure. The two hole type cylinders pass along the Γ-Z high-symmetry line of the Brillouin zone and the other two electron type along the M-A line. The 3D hole pocket is a distorted sphere centered at the Z high-symmetry point. Polarization dependent ARPES (Angle-resolved photoemission spectroscopy) studies and band calculations further showed that the hole and electron pockets involve all five Fe 3d orbitals (Zhang(c) *et al.* 2011a). The density functional theory (DFT) calculations in LaFeAsO also show that the electronic structure is similar to that of LaFePO (Singh *et al.* 2008). The states near the Fermi level have dominantly Fe d orbitals while states above the Fermi level are mixtures of p orbital of oxygen, hybridized Fe d and pnictogen p orbitals. This explicitly says that the electronic structure of FeSCs is dominated by the Fe 3d. The DFT and dynamical mean field theory calculations done on LaFeAsO predict a steep and negative slope of the density of states (DOS) at the Fermi level (Aichhorn *et al.* 2009). In 111 type and 122 type the sizes of the electron and hole pockets are comparable, while the huge hole pocket in 1111 type is due to the charge redistribution on its surface (Yang(c) *et al.* 2010). Therefore, the electronic structure of iron-based superconductors exhibits multiband and multi-orbital nature unlike the single band Fermi surface of cuprates.

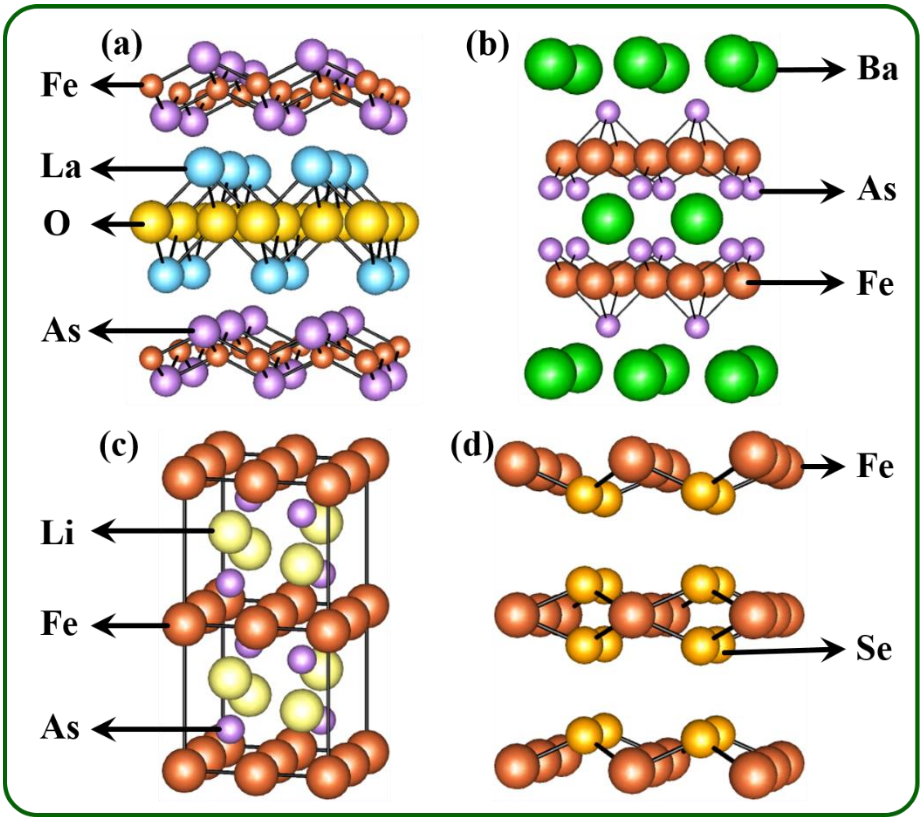

Figure 2.1: Crystal structure of the four categories of iron pnictides (a) 1111 type (b) 122 type (c) 111 type and (d) 11 type

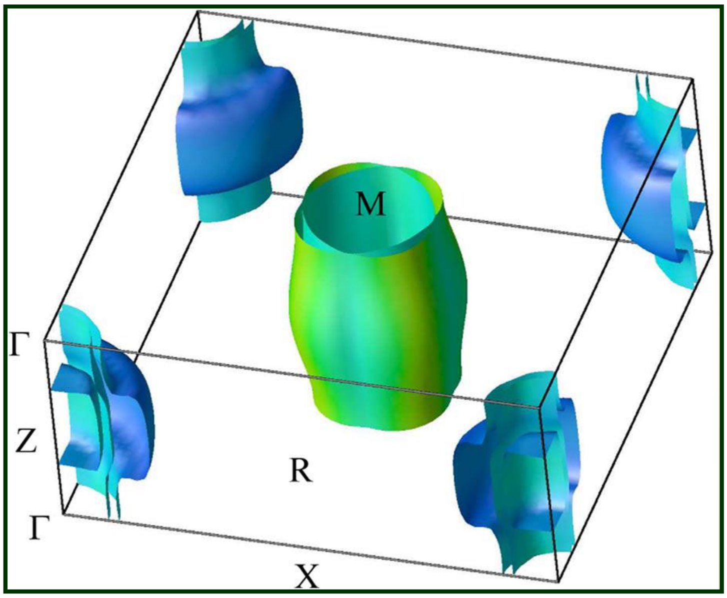

Figure 2.2: Fermi surface of LaFeAsO shaded by velocity [darker (blue) is low velocity]. The symmetry points are Γ = (0, 0, 0), Z = (0, 0, 1/2), X = (1/2, 0, 0), R = (1/2, 0, 1/2), M = (1/2, 1/2, 0), A = (1/2, 1/2, 1/2)

An early calculation based on an Andreev spectroscopy says that FeSCs have a single energy gap (Chen(b) *et al.* 2008). Later, ARPES studies in $Ba_{0.6}K_{0.4}Fe_2As_2$ revealed two superconducting energy gaps that are nearly isotropic without nodes (Ding(a) *et al.* 2008). A large gap of the order of 12 meV attributing from strong pairing interactions originates from the inter-band interactions between the nested hole and electron Fermi surface. Another gap is observed on the large hole-type Fermi surface which is of the order of 6 meV. In hole doped 122 type single crystals, the Fermi surface consists of an inner hole-like pocket, an outer hole-like pocket, both centered at the Brillouin zone center, and a small electron-like Fermi surface. The local density approximation band structure calculation predicted a more pronounced 3D electronic structure in the 122 family and a transition from 3D to 2D has also been observed at temperatures above the structural transition temperature (Liu(a), C. 2009). This suggests that high temperature superconductivity does not just exist in systems with low dimensional electronic structures such as cuprates. The pairing mechanism for the iron-based superconductors is a spin fluctuation mechanism with a sign reversal in the order parameter (Mazin *et al.* 2009). The suggested order parameters have s-wave symmetry but different signs on the electron pockets and hole pockets, i.e. s± symmetry. This is completely different from the d_{x2-y2} symmetry and s-wave symmetry widely accepted for the copper oxide superconductors and MgB_2, respectively. However, pairing mechanism based on orbital fluctuation says that s-wave order parameters without sign reversal, s++ symmetry exist in FeSCs (Kontani *et al.* 2010).

Table 2.2: Summary on physical properties of FeSCs in comparison with other superconductors

Features	Iron-based	MgB_2	Cuprates
Parent material	Antiferromagnetic semi metal	Metal	Mott insulator
Orbitals composing	Fe 3d	B $2p_\sigma$, $2p_\pi$	Cu $3d_{x2-y2}$ O $2p_\sigma$
Fermi level	5 bands	2 bands	single band
Pairing symmetry	s±, s++	s	$3d_{x2-y2}$
Proposed pairing mechanism	Spin fluctuation Orbital fluctuation	Phonon	Spin fluctuation (phonon, polaron)
Coherence length (nm)	2-10	5-12	1.5

Theoretical calculations (Boeri, *et al.* 2008) indicate that electron-phonon coupling is not sufficient to explain superconductivity in the whole family of iron-based superconductors. However, superconductivity and magnetism in iron-based superconductors show a strong sensitivity to the crystal lattice. These results indicate that electron-phonon interaction plays some role in the superconducting mechanism by affecting the magnetic properties (Bang, Y. 2009). In order to understand the magnetic properties, first-principles calculations were performed by many groups (Yin *et al.* 2008; Moon *et al.* 2009). Extensive studies were conducted to find the possibility of magnetically mediated superconductivity in terms of localized spins and itinerant electrons. Magnetism in iron-based superconductors may have both itinerant electron and local moment characters. In this point of view, many theories and models have been proposed in which itinerant electrons and localized moments coexist in iron-based superconductors, and they play some roles in magnetism (Kou *et al.* 2009). The antiferromagnetic ordering in the undoped parent compound itinerantly results from the Fermi surface nesting and is suppressed by doping. Doping reduces the degree of Fermi surface nesting and in turn suppresses the magnetic instability. The nesting vector (π, π) separating the electron and hole Fermi surface is same as an antiferromagnetic ordering wave vector except for some 11 type iron-based superconductors (Ma(a) *et al.* 2009). The Fermi surface nesting is considered closely related to the superconducting phenomena since it is suppressed in the superconducting phase. The electronic states whose energies are much lower than Fermi level are strongly spin-polarized while the states around Fermi level are normal-metal-like. In FeSCs, the stripe AFM configuration is the only stable ground state due to the presence of the magnetic frustration caused by the nearest neighbor exchange and the next nearest neighbor exchange among localized Fe^{2+} moments. The magnetic stripe phase breaks the tetragonal symmetry, removes the frustration, and causes a structural distortion. In 11 type, double-stripe-type magnetic ordering is present which corresponds to a wavevector of (π, 0) (Ma(a) *et al.* 2009). Meanwhile, DFT calculations predict that the ground state of FeSe has the single-stripe-type antiferromagnetic order, similar to those in LaFeAsO and $BaFe_2As_2$. In LaFeAsO, the magnetic structure of the oxypnictides lies in the *ab* plane that consists of chains of parallel Fe spins that are coupled antiferromagnetically in the orthogonal direction with an ordered moment of less than 1 μB (Yildirim, T. 2008). The measured magnetic moment is also much smaller than the moment of metallic Fe which is supposed to be due to magnetic frustration and/or spin fluctuations. In 122 type, AFM order lies along the *a* axis of the *ab* plane and have a multiorbital nature (Huang *et al.* 2008). The antiferromagnetic spin fluctuation and the multiband are two factors to drive the system into the superconducting state.

Table 2.2 summarizes the physical properties of iron-based superconductors in comparison with those of copper oxide superconductors and MgB_2.

2.2.2 Superconducting properties

Table 2.3: Superconducting properties of FeSCs in comparison with other superconductors

Material		T_C (Max) (K)	H_{C2} (at 4.2 K) (T)	J_C (at 4.2 K, 0 T) (A/cm^2)	γ
Iron-based	**1111**	55	100-300	10^6	5-10
	122	39	70-135	10^6	1.5-2
	11	16	50	10^5	1.5-1.9
Cuprates		134	>100	10^6 (YBCO) 10^7 (BSSCO)	5-7(YBCO) 50-90(BSSCO)
MgB_2		39	30-40	10^6	1.5-5
NbTi		9	11-12	10^6	-
Nb_3Sn		18	25-29	10^6	-

The performance of a superconductor is characterized by several parameters like the critical temperature (T_C), critical current density (J_C), upper critical field (H_{C2}) and anisotropy (γ). A large H_{C2} and small anisotropy are unique properties of iron-based superconductors. The H_{C2} of FeSC is higher than that of MgB_2 but is smaller than that of a typical cuprate (Fujitsu *et al.* 2012; Tarantini *et al.* 2011; Gurevich, A. 2011; Ishida *et al.* 2009; Putti *et al.* 2010; Ma(b), Y. 2012). But the anisotropic ratio of H_{C2} of FeSC is smaller than that of MgB_2 or cuprates. The upper critical field H_{C2} of a type II superconducting material is an intrinsic property and can be calculated using the one band Werthamer-

Helfand-Hohenberg (WHH) formula $H_{C2}(0\ \mathrm{K}) = -0.693T_C\ [\mathrm{d}H_{C2}/\mathrm{d}T]_{TC}$, where $[\mathrm{d}H_{C2}/\mathrm{d}T]_{TC}$ is obtained from the slope of the curve H_{C2} versus T at T_C. The first magnetoresistance measurements in polycrystalline La-1111 up to 45 T indicated a μ_0H_{C2} value larger than 60 T (Hunte *et al.* 2008). The H_{C2} values increase when we replace La with other rare earth elements having a smaller ionic radius, a similar trend as observed in T_C (Jaroszynski *et al.* 2008a). H_{C2} values above 100 T were estimated in bulk $SmFeAsO_{0.85}F_{0.15}$ with T_C of 46 K (Senatore *et al.* 2008) and $NdFeAsO_{0.82}F_{0.18}$ with T_C of 51 K (Wang(d) *et al.* 2009). This H_{C2} value shows a remarkable increase compared to that expected from WHH method. This points out that H_{C2} values extrapolated using the WHH model is not valid for the low temperature range and this behavior is similar to that observed in MgB_2 in the dirty limit (Yuan *et al.* 2009). These results suggest that superconductivity in 1111 results from two bands and that enhancement in H_{C2} value can be interpreted by a two-gap scenario. In addition to WHH method, H_{C2} can also be calculated using the Ginzburg-Landau relation $H_{C2} = H_{C2}(0)(1-t^2)/(1+t^2)$, where $t = T/T_C$ is the reduced temperature. The $H_{C2}(0)$ determined using GL theory was higher than that using WHH extrapolation in La1111 system (Zhu *et al.* 2008). Measurements based on microwave surface impedance technique and pulsed field up to 55 T using a tunnel diode oscillator also agree with the GL theory (Narduzzo *et al.* 2008).

To verify the above results, measurements in single-crystal are highly desired. First single crystal studies were done by Jia *et al.* (Jia *et al.* 2008) in $NdFeAsO_{0.82}F_{0.18}$ with T_C = 47 K and the upper critical fields determined based on the WHH extrapolations were even $H_{C2}{\parallel}ab(0\ \mathrm{K})$ = 304 T and $H_{C2}{\parallel}c(0\ \mathrm{K})$ = 62-70 T. Further studies by Jaroszynski et al. (Jaroszynski *et al.* 2008b) on single crystals of $NdFeAsO_{0.7}F_{0.3}$ at very high magnetic field up to 60 T also showed 100-200 T field scale of H_{C2}. Though, their studies show a spin-dependent positive magneto-resistance for $H_{C2}{\parallel}c$ due to the presence of paramagnetic Nd^{3+} ions. The presence of paramagnetic phase significantly reduces $H_{C2}(0)$ as compared to that based on WHH extrapolations to low temperatures. The extrapolation based on GL theory also neglects the paramagnetic limitations and could overestimate the actual $H_{C2}(0)$. The extrapolated H_{C2} values are two or three times higher than this limit that indicate a considerable enhancement of the Pauli-limited field by the strong coupling effect (Joa *et al.* 2009). Pauli-limited field of a superconductor is the field at which the free energy in the normal state becomes equal to the condensation energy of the superconductor. At the sufficiently large magnetic field, the superconductivity is destroyed by orbital and spin pair breaking which leads to the flattening of $H{\parallel}ab$ at a lower temperature range. In the case of

As deficient RE1111 systems enhanced local exchange field acting on the superconducting charge carriers caused by an increasing alignment of localized extrinsic magnetic moments in the vicinity of arsenic vacancies may also suppress H_{C2} at lower temperature and higher magnetic field (Fuchs *et al.* 2009). Studies on 11 type also support with the Pauli paramagnetic limiting effects, in addition to orbital effects arising with different anisotropies of the Fermi velocities for the two bands, in Fe-based superconductors (Lei *et al.* 2010).

Measurements on single crystals have also shown that the temperature dependencies of $H_{C2}\|ab$ and $H_{C2}\|c$ can be different and deviating from the WHH behavior especially in the case of $H_{C2}\|c$ (Jaroszynski *et al.* 2008b). The temperature dependence of $H_{C2}\|c$ exhibits a significant upward curvature while it is less pronounced for $H_{C2}\|ab$. This behavior of H_{C2} in iron-based superconductors can be explained by the two band model, similar to MgB_2 superconductor (Singh *et al.* 2008; Gurevich, A. 2003). According to that, superconductivity arises from nearly 2D electron band with in-plane diffusivity, D1, and a more isotropic heavy hole band with smaller diffusivity, D2. If D1/D2 << 1, we get an upward curvature or if D1/D2 ~ 1 H_{C2} exhibit WHH behavior. However, 122 and 11 type shows a downward curvature of H_{C2} in both directions with respect to temperature (Yuan *et al.* 2009; Fang *et al.* 2003). $H_{C2}\|ab$ at lower temperature exhibits stronger flattening than $H_{C2}\|c$, so that both curves merge at lower temperature (Yuan *et al.* 2009). The different behavior of these systems is associated with distinctive Fermi surface topology present in these materials which permit orbital limiting of the upper critical field at all field orientation. The behavior of H_{C2} near T_C is limited by orbital effects for which $\gamma(T)$ is controlled by the anisotropy of the electron mass m. As temperature decreases, the contribution of nearly isotropic paramagnetic effects increases, and $\gamma(T)$ decreases toward 1. The paramagnetic effect is more pronounced in 11 type as a result of their small Fermi energies and large effective masses (Tarantini *et al.* 2011). The wide-ranging behavior of H_{C2} with temperature in different categories of iron-based superconductors can be explained by using the theory of clean multiband superconductivity (Gurevich, A. 2010). This theory considered the effect of pairing symmetries, orbital and paramagnetic pair-breaking, and the instability arising due to Zeeman splitting. According to this theory, the s± pairing enhances the orbitally limited H_{C2} for different Fermi velocities which result in an upward curvature in $H_{C2}(T)$ at intermediate temperatures. This behavior is different from the conventional s++ pairing in MgB_2 superconductor for which the upturn occurs at low temperatures. If the Fermi energy is too low, the paramagnetic effects become prominent and eliminate the upward curvature and get flattening in $H_{C2}(T)$ behavior.

The anisotropy parameter $\gamma(T) = H_{C2}{\parallel}ab/H_{C2}{\parallel}c$ also depends on temperature. For $NdFeAsO_{0.82}F_{0.18}$ single crystals, the anisotropy value is nearly 5 which is even below that for YBCO single crystals (Jia *et al.* 2008). Yet, members of the 122 family show nearly isotropic H_{C2} values and the γ value decreases with decreasing temperature. The γ value changes from 2 to 1 while going from T_C down to 4.2 K (Yuan *et al.* 2009). The irreversibility field (H_{irr}), a factor which limits the application of superconductors, is also relatively high (higher than that of MgB_2) that makes the new superconductor promising for magnetic field applications.

The critical current density of a superconductor is also an important parameter in the application point of view. J_C can be calculated from the magnetic hysteresis loop using Bean critical current model (Bean, C.P. 1962). By which $J_{Cglobal} = 20\Delta M/\mathrm{a}(1\text{-a}/3\text{b})$, where a and b are sample dimensions perpendicular to the applied field and ΔM is the width of the hysteresis loop, and $J_{Clocal} = 30\Delta M/\langle r\rangle$, where $\langle r\rangle$ is the average grain size. J_{Clocal} (intragrain) is mainly controlled by vortex pinning while $J_{Cglobal}$ (intergrain) is ruled by connections across grain boundaries and voids present in the sample. The value of intergrain current density in FeSCs is found to be more than one order of magnitude larger at 4.2 K than for early results on randomly oriented polycrystalline cuprates. The J_C of the order of $\sim 2 \times 10^6$ A/cm^2 at 4.2 K is reported in single crystals of Sm1111 sample (Zhigadlo *et al.* 2008).

Magneto-optical (MO) studies in Sm1111 and Nd1111 polycrystalline samples by Yamamoto *et al.* (Yamamoto *et al.* 2008b) revealed that there exist two distinct scales of current due to the granular nature of iron pnictides. The presence of FeAs wet phase at the grain boundaries and other material inhomogeneities significantly reduce the intergrain current flow in iron pnictide compounds. The strong granularity in polycrystalline samples restricted the $J_{Cglobal}$ to the values of the order of 10^3 A/cm^2 at 4.2 K in self-field. Low density, grain boundary-wetting FeAs phase, cracks and phase inhomogeneities are the main sources responsible for current blocking in polycrystalline materials, which suppress the order parameter at grain boundaries. MO imaging and remanent field analysis of samples had shown that the intergranular current had a superconducting-normal-superconducting like temperature dependence. The $J_{Cglobal}$ in the sample is limited by the proximity coupled conductive As-Fe phase and/or by the intrinsic weak coupling. This is strongly supported by the very strong fall off of J_C even in 0.1 T field. The size of the sample is another important factor which limits the $J_{Cglobal}$, but J_{Clocal} is size independent. The field of penetration within the sample is proportional to the $J_{Cglobal} \times$ (sample size). However, the J_{Clocal} depends on the preparation methods; its value is found to be larger for Powder In Tube (PIT) wires than bulk ones (Otabea *et al.* 2009). But $J_{Cglobal}$ is more or less identical for both types. The Sm1111, 122 and 11 type wires made in the early stages by the *ex situ* PIT method exhibited poor grain connectivity and had relatively low J_C of ~ 10-10^3 A/cm^2 at (4.2 K, 1 T) as the grain boundaries in these wires are likely covered by second phases (Putti *et al.* 2010). But further developments in this area can more or less eliminate the problems arising from chemical granularity, porosity, and other extrinsic factors. It is expected that optimization of the synthesis process will raise J_C values closer to the intrinsic intragrain current density of the oxypnictide phase, which has been evaluated to be of the order of 10^6 A/cm^2 (Ma(b) *et al.* 2009b).

The field dependence of the critical current density in iron-based superconductor is superior to that of MgB_2 and high T_C cuprate superconductors. The J_C of FeSCs is almost constant with increasing field up to 7 T at 4.2 K. But the J_C values display an abrupt decrease when the magnetic field is below 1 T and after that become nearly field independent. In the Nd1111 sample, the J_C drops only by a factor of 2-6 when the field changes from 1 to 9 T for temperature below 30 K (Wang(d) *et al.* 2009). The $J_C(H)$ behavior can be explained by the collective vortex pinning theory; J_C is field independent when the applied field is below a particular field, called the crossover field B_C. Below B_C, the sample is in the single vortex pinning regime and above B_C a transition from the single vortex pinning regime to the small-bundle-pinning regime takes place. The temperature dependence of J_C also shows a crossover from 3D Josephson coupled pancake vortices to 2D pancakes. The field and temperature dependence of J_C values are similar to that observed in YBCO superconductor. Both of these materials exhibit similar properties like nm-scale coherence length, the exceptionally high H_{C2} values and pinning associated with atomic-scale defects resulting from chemical doping (Putti *et al.* 2010). The $J_C(T, H)$ performance can be improved by introducing pinning centers of the order of coherence length. FeSCs have a short coherence length which makes it possible to achieve strong pinning and high critical current densities. The J_C of $BaFe_2As_2$ thin film has been enhanced by the incorporation of oxide nanopillars (Zhang(c) *et al.* 2011b). This $J_C(H)$ performance is promising for the use of oxypnictide superconductors in high field application. The above results show that iron-based superconductors exhibited extremely high H_{C2}, low anisotropy, and rather large J_C values, independent of the field at low temperatures, indicating possibilities for magnet applications at 20-30 K, where the niobium based superconductors cannot play a role owing to their lower T_Cs (Ma(b), Y. 2012).

2.3 Preparation techniques of iron-based superconductors

The extraordinarily rich crystal chemistry of iron pnictide system has expanded the synthesis route of these materials to more diverse techniques. Several methods have been used to prepare oxypnictides that include solid state method, high pressure method and flux method (Aswathy *et al.* 2010; Sefat, A. S. 2013; Ma(b) *et al.* 2009b). Due to the air sensitivity of the reactants (rare-earths, alkali metals, alkaline-earth metals), reactant toxicity (arsenic, selenium) and volatility at reaction temperatures (sublimation point of As is around 600 °C), and the desire to form products without oxygen (in 122, 111, 11 type) and to have the metal in low nominal oxidation state (Fe^{2+}), the synthesis of FeSC is more difficult compared to that of the cuprates (Sefat, A. S. 2013). For the above reasons, chemical reactions are performed in an inert gas filled glove box, with only a few parts per million partial pressure levels of O_2 and H_2O. In addition, the materials are also air sensitive during sintering temperatures thereby the samples are regularly placed in evacuated silica ampoules for heat treatment. Significant pressures can build up in sealed tubes and so care should be taken to avoid minor explosions.

Solid state method (ambient pressure method) is a conventional way of producing polycrystalline samples. The first reported iron-based superconductor $LaFeAsO_{1-x}F_x$ was synthesized using the solid state method (Kamihara *et al.* 2008). This route has been used for the preparation of all of the four categories of FeSCs with two-step method or single step PIT method. For the preparation of 1111 type compounds, usually a two-step method is used. It consists of a synthesis of REAs or FeAs starting from pure elements followed by synthesis of the oxypnictide via reacting REAs with stoichiometric amounts of Fe, Fe_2O_3/REO_3 and iron fluorides (FeF_2, FeF_3) powders. The binary compounds are obtained after pre-sintering of RE powder with As pieces at 500 °C/12 h and then at 850 °C/2 h for REAs; Fe powder with As pieces at 900 ^oC/24 h for FeAs, in evacuated quartz tubes. Later, the final compound was prepared by stoichiometric mixing of the binary products with the remaining chemicals in an inert atmosphere and pressed into pellets. The pellets were wrapped in Ta foil, sealed in an evacuated quartz tube and sintered at 1150-1250 ^oC for 40-60 h. In order to simplify the fabrication process, an alternative one step PIT method is also used for iron-based superconductors (Ma(b) *et al.* 2009a). The PIT method involves a simple procedure as follows; thoroughly mixing all the starting materials one time, packing the powders in metal tubes (Ta or Fe tubes), and sintering at 1160-1180 °C for 45 h. The major merits of this fabrication method are safety and convenience. The 122 type can be synthesized by stoichiometric mixing of the elements, placed inside an alumina crucible, sealed in a silica tube in partial pressure of argon, and then heated at 600 °C for 15 h (Sefat, A. S. 2013). Then the samples are reground, pelletized and sintered again at 650 °C and then at 750 °C by following the above procedures (Rotter *et al.* 2008). For 11 type, stoichiometric amounts of selenium and iron powders are mixed, ground, pelletized, and then annealed several times in evacuated silica tubes up to 700 °C (Hsu *et al.* 2008).

Other methods used to prepare polycrystalline pnictides samples is the high pressure method in which the use of pressure allows considerable shortening of reaction times and reduces evaporation of volatile elements. A short sintering period and effective maintenance of fluorine in high pressure capsule make this method superior to solid state synthesis. In this method, for 1111 type, the binary compound and the remaining stoichiometric powders are sealed in boron nitride crucibles and sintered in a high pressure synthesis apparatus under a pressure of 6 GPa at 1250 °C for 2 h (Jaroszynski *et al.* 2008a). The main drawbacks of this method are: difficulty to operate, small product yield due to small sample space, and the reduced reaction times often results in the formation of impurity phases such as rare earth oxides, arsenides, and fluorides. But, the high pressure method is the only effective way to synthesize oxygen deficient $ReFeAsO_{1-\delta}$ samples (Ren(a) *et al.* 2008a). The high pressure synthesized samples have higher T_C compared to that of solid state method. Moreover, this method advances the percentage of fluorine doping in 1111 system, doping level up to 0.6 is attained in La1111, which is six times higher than the ambient one (Lu *et al.* 2008). Also, superconductivity above 40 K was realized in heavy rare earth elements (Tb, Dy etc.) based 1111 systems by using this method, T_C of these materials is comparable to that of the light rare earth based compounds synthesized by the solid state reaction.

For the synthesis of single-crystalline FeSCs, flux method is widely used. Jia et al. produced $NdFeAsO_{0.82}F_{0.18}$ single crystals using this technique initially (Jia *et al.* 2008). This method is efficient in lowering the processing temperature, and growing high-quality single crystals. The crystals of 1111 and 11 (few mm size on a side) have been grown using NaCl salt as flux. The procedure is as follows: a homogeneous mixture with molar ratio of polycrystalline 1111:NaCl = 1:20 are sealed in a tantalum tube under partial argon atmosphere, sealed in an evacuated silica tube and then the sealed tube is subjected to heat treatment at 1150 °C for 24 h, afterwards cooled to 600 °C. However, KCl salt was used as a flux for $FeSe_x$ crystals and heated up to 850 °C and slowly cooled to the solidification temperature of the salts. In addition to the above methods, there exist other methods like Bridgman method and Ammonothermal method for the synthesis of 122 selenides (e.g., $K_xFe_{2-y}Se_2$; $T_C \sim 30$ K) (Sefat, A. S. 2013).

From the viewpoint of practical applications, it is necessary to convert these bulk materials into wire and tape forms. The one step PIT method is an effective and fast method for developing iron-based superconducting wires (Ma(b) *et al.* 2009a; Ma(b) *et al.* 2009b). Iron pnictide wires are fabricated by filling stoichiometric amounts of RE, As, REF_3, Fe, and Fe_2O_3 powders into metal tubes under Ar atmosphere. The tubes are then swaged and drawn to wires and finally given a heat treatment under Ar. A suitable metal tube (sheath material) which does not degrade the superconducting properties is a necessity to prepare wires. Continuous efforts are being made by several groups to develop methods to prepare good quality iron-based superconducting wires.

2.4 Doping effect on superconducting properties

Most of the parent materials of iron-based superconductors do not show superconductivity and become superconductors only by partial substitution at different sites, especially at oxygen site in 1111 and at alkaline earth metal site in 122 types (Fujitsu *et al.* 2012; Hao *et al.* 2013; Johrendt D. 2011). It is surprising that the doping even up to 50% within Fe_2As_2 layers does not destroy superconductivity while in the case of cuprate based systems any change made in the Cu-O layer will destroy the superconductivity. That is; both direct and indirect doping is possible in these materials. The substitution in the conduction layer (at Fe or As site) is called direct doping and that in the blocking layer is called indirect doping. The indirect doping is found to have more advantages in achieving a higher T_C than the direct doping. In these categories, the superconductivity occurs in their tetragonal phase and not in the orthorhombic phase due to the antiferromagnetic ordering in the orthorhombic phase. With doping, the tetragonal-orthorhombic transition temperature decreases and is accompanied by the suppression of the antiferromagnetic state and superconductivity emerges in succession. The phase diagram (doping dependence of T_C) of FeAs superconductors has a dome-like structure similar to cuprates. i.e. the critical temperature increases, reaches a maximum, and then decreases as the dopant levels increases. However, recent reports in $LaFeAsO_{1-x}H_x$ reveals that the superconducting region forms a double dome structure composed of the conventional narrow superconducting dome located around x = 0.08 with a maximum T_C = 29 K and an additional wide superconducting dome located around x = 0.35 with a maximum T_C = 36 K (Hosono *et al.* 2013).

Superconductivity can be induced in FeSCs either by electron doping or hole doping or isoelectronic (non-charge-carrier) doping. In both electron and hole doping, the structural and magnetic phase transition becomes suppressed by doping. The ground state of the parent compounds possess antiferromagnetic long-range order, which typically competes with superconductivity. The first report on superconductivity in $LaFeAsO_{1-x}F_x$ is an example of electron doping in which F doping at O site brings extra electron carriers and disorder into the Fe-As layer (Kamihara *et al.* 2008). In addition, the lattice constants decrease systematically with nominal F content that in turn develops an inner chemical pressure. Also, the distance between $(LaO)^{\delta+}$ and $(FeAs)^{\delta-}$ layers prominently decreases, proposing that the electron doping enhances polarization and Coulomb interaction between the layers. A more effective carrier doping method in 1111 type was also found in high pressure synthesis in that superconductivity can be directly obtained by making oxygen vacancies, without adding any extra element (Ren(a) *et al.* 2008a). Recently, it has been observed that hydrogen doping at oxygen site is an alternative technique for high concentration electron doping. The substitution limit of hydrogen in REFeAsO ($x = 0.5$) is much higher than that of fluorine ($x = 0.2$), the hydrogen substitution technique provides an effective pathway for high-density electron doping (Hosono *et al.* 2013). Hole doping was first reported in 122 system ($BaFe_2As_2$) by potassium doping and obtained a critical temperature of 38 K (Rotter *et al.* 2008). Doping by other alkali metals like sodium and cesium in alkaline earth metal site also induces superconductivity in 122 system. Hole doping of 1111 system has been realized in La1111 by Sr doping at La site ($La_{1-x}Sr_xOFeAs$) with T_C = 25 K (Wen *et al.* 2008). The element Pb has also been reported to result in superconductivity when used for doping at the La site (Che *et al.* 2008). But hole doping using Ca^{2+} ions in LaFeAsO at the lanthanide site did not show superconductivity and is attributed to the greater ionic radius mismatch between the La^{3+} ion and Ca^{2+} ion. Another effective indirect doping method which can also induce superconductivity with T_C above 50 K in 1111 system was done by using 5f elements like thorium (Th) and uranium (U) on RE site (Wang(a) *et al.* 2008). Electron doping in $BaFe_2As_2$ is also possible by direct substitution of cobalt (Co) for iron and the phase diagram of Co doped material appears to be analogous to that of potassium doping, only the superconducting dome is narrower and the highest T_C is about 25 K (Sefat *et al.* 2008a). The direct electron doping in iron pnictides is possible by using other 3d transition metal elements of Co and Ni at the Fe site. The other 3d transition metals such as Cr, Mn, Cu, etc. are not able to induce superconductivity. However, the 5d transition metal of Ir doping by partially replacing Fe and P doping at the As site are effective in inducing superconductivity; yet have a lower T_C.

Apart from one site doping, the co-doping method is an excellent way to enhance T_C, which can simultaneously introduce two dopants into the two sites of the RE-O layer, causing larger distortion. Higher T_C values were reported in several mixed rare earth oxypnictides; eg.: La doped iron oxypnictide $SmFeAs_{0.95}La_{0.05}O_{0.85}F_{0.15}$ with T_C of 57.3 K (highest recorded T_C in FeScs) (Wei *et al.* 2008), $La_{1-x}Sm_xFeAsO_{0.85}$ with T_C ~ 55 K (Yi *et al.* 2008b), T_C up to 47.5 K in $Ce_{1-x}Gd_xFeAsO_{0.84}F_{0.16}$ (Yang(a) *et al.* 2008), Ce doped series of $La_{1-x}Ce_xFeAsO_{0.9}F_{0.1}$ with T_C = 28.78 K (Che *et al.* 2008). In short, chemical doping at any crystallographic site is effective to induce superconductivity. Doping brings structural modifications such as a reduction in cell volume, a decrease in distance between layers, and an increase in distance between RE^{3+} and F^- which enhances spin and charge density fluctuations.

2.5 Present status and relevance of iron-based superconductors

The exceptional properties and distinct dissimilarities from existing superconductors like cuprates and conventional superconductors have made iron-based superconductors a new class of high temperature superconductors and that received much attention of the superconducting world. They have properties intermediate between the LTS materials like NbTi and Nb_3Sn and the cuprates like YBCO and Bi-2212 or Bi-2223. Their properties bridge a conceptual gap between conventional superconductors and the high T_C cuprates. La1111 have properties similar to conventional MgB_2, but the other high T_C oxypnictides are like cuprates. Also, the relationships between the magnetism and the superconductivity in iron-based materials attract the interest of many physicists. In addition, the discovery of superconductivity in $LaFeAsO_{1-x}F_x$ has triggered multiple discoveries of the extended families of FeSCs. The physics and chemistry behind iron pnictides may bring more revelations and perhaps give clues for a better understanding of high temperature superconductivity or even the discovery of new high T_C materials. The field of iron-based superconductors grows rapidly, and that makes superconductivity research more lively and attractive. Research in the area of FeSCs was started with Japanese Group (Kamihara *et al.* 2006); later a great deal of work was contributed by the Chinese scientists. After that, many works were reported from all over world mainly from USA, Germany, Australia, Italy, Iran, Switzerland and France. In India, research on iron-based superconductors have been reported from IGCAR, BARC, TIFR, and NPL.

Extensive studies performed in iron-based superconductors have revealed that their properties are preferable for applications such as high H_{C2} values comparable to those for the copper oxide high T_C superconductors, superior $J_C(H)$ performance and smaller anisotropy. Even the highest T_C pnictides, Sm- and Nd-1111, have anisotropies much smaller than typical cuprates (γ ~ 30) (Putti *et al.* 2010). But the presence of toxic elements such as As or Se in FeSCs with a high T_C is a serious issue that prevents many researchers from this field and hence experiment must be conducted in a well-controlled environment. Besides, the bulk synthesis of iron pnictides, both wire and thin film, is also ahead at the international level. However, the synthesis methods for bulk, wire, thin film, and tape forms yet need to be optimized to obtain a significant transport J_C. The advantage for the practical application of FeSCs is confirmed by converting them into film and wire/tape forms. Katase et al. (Katase *et al.* 2011) successfully prepared high-quality cobalt doped $BaFe_2As_2$ epitaxial films grown on (*001*)-tilt $(La,Sr)(Al,Ta)O_3$ and MgO bicrystal substrates by pulsed laser deposition. The grain boundary properties of the film was studied using the current-voltage characteristics of the bicrystal grain boundary junctions and it is clarified that a transition from a strongly coupled grain boundary behavior to a weak link behavior is higher than that of cuprates. In addition, the orientation angle dependence of J_C at the grain boundaries is lower than that of cuprates that will avoid the need for controlling the in-plane orientation for FeSCs tapes; thereby reduce the fabrication cost.

Even though the magnetic J_C of the order of 10^6 A/cm^2 has been obtained, transport J_C achieved in 1111 type based wires is only of the order of 10^3 A/cm^2 at 4.2 K (Wang(b) *et al.* 2010). This value is much lower than that of wires and tapes made from MgB_2, high T_C cuprates, NbTi and Nb_3Sn (10^5-10^6 A/cm^2 at 4.2 K). The wide difference between the transport J_C and the magnetic J_C arising due to the factors such as the presence of inevitable impurity phase of FeAs, strong reactivity of rare earths with most of the sheath metals at elevated temperatures, occurrence of cracks, porosity, inherent granularity etc. However, in the past two years the transport J_C of iron-based superconducting wires has rapidly increased. At 4.2 K, 122 wire has achieved transport J_C of 10^5A/cm^2 in self-field and even 1.4×10^4A/cm^2 in a field of 14 T, respectively (Gao(b) *et al.* 2012). The $SmFeAsO_{1-x}F_x$ tape prepared through both one-step PIT method and *ex situ* PIT method reached a transport J_C of the order of 10^3 A/cm^2 at 4.2 K in self-field (Wang(a) *et al.* 2012; Fujioka *et al.* 2011). Although many technical challenges are to be addressed, the extremely high H_{C2} up to 300 T, ever found in any other class of superconductors together with relatively large J_C of the order of 10^6 A/cm^2 at 4.2 K and moderately high T_C make iron-based superconductors highly promising for future applications.

2.6 Objectives of the present work

The prospect of applied superconductivity has dramatically changed with the discovery of superconductivity in iron-based compounds in 2008. This has opened up new avenues which enable the superconducting property to be tailored suiting to different requirements. The extremely high upper critical field, moderate anisotropy, relatively large critical current density and wide scope for chemical substitution makes 1111 type system highly promising for practical applications. In 1111 family Sm-based iron oxypnictide superconductor is a potential candidate due to it's relatively high transition temperature, large intergrain J_C, an H_{C2} over 150 T and its good stability in ambient conditions. These properties make it a potential material for high field applications around 30 K, where conventional superconductors cannot play a role owing to their low T_Cs.

The use of superconductors for technological applications calls for their conversion into flexible wires or tapes with desired properties. Based on the applications, superconductors require stabilization using a normal metal cladding for electrical, thermal, and mechanical protection. Moreover, the transport properties of these wires are to be studied at different magnetic fields to gain information on their weak-link and flux pinning behavior. But, it is difficult to fabricate these compounds in the form of flexible conductors with the desired dimensions as they are mechanically hard and brittle. The demand for high temperature, high pressure and inert atmosphere for obtaining phase pure material with improved superconducting properties also makes wire making of iron pnictides more challenging. Challenges such as the volatility and toxicity of arsenic, the strong affinity of rare earths towards oxygen and the reactivity of the rare earths with most of the sheath metals at elevated temperatures are also to be addressed in order to develop the superconductors in the form of wires/tapes for practical application. Moreover, the synthesis of phase pure material with improved superconducting properties demands high sintering temperature, high pressure, and inert atmosphere. However, PIT method using either *in situ* (heat treatment of the starting powders) or *ex situ* (sintering of already reacted powders) methods is an effective method to fabricate iron-based superconducting wires. The thesis aims to investigate various aspects of synthesizing Sm1111 superconductors in the form of bulk conductors and to establish enhanced transport properties in metal sheathed superconducting wires for technological applications.

The main objectives of the thesis are given below.

1. To develop a relatively simple method to synthesize Sm1111 bulk superconductors
2. Investigate the substitutional effects in Sm1111 superconductor at different sites to improve T_C, J_C, and H_{C2}
3. To establish the technical feasibility of making iron-based superconducting wires in Sm1111 system for technological applications

CHAPTER 3

PREPARATION AND CHARACTERIZATION TECHNIQUES

3.1 Introduction

This chapter summarizes the preparation method adopted for the present work and various experimental methods used for the structural and superconducting characterization of the samples. Iron-based superconductors are only prepared by a limited number of research groups around the world, due to the very complicated synthesis route and the toxicity and volatility of arsenic (Kamihara *et al.* 2006; Chen(c) *et al.* 2008; Ren(a) *et al.* 2008a; Martinelli *et al.* 2008). The synthesis of phase pure iron pnictides is very difficult, and its synthesis route is not yet optimized. The presence of impurity phases like FeAs significantly affects the superconducting properties; especially this blocks the supercurrent flow throughout the material and limits their applicability range (Kametani *et al.* 2009a). General preparation methods adopted in the present work both for bulk and wire samples, and their characterization techniques are briefly described here.

3.2 Preparation of iron-based superconductors

Both bulk and wire samples were prepared in the present study. There exist many methods for the preparation of iron pnictide superconductors (Chen(c) *et al.* 2008, Ren(a) *et al.* 2008b; Jia *et al.* 2008). Important among them are solid state reaction method, high pressure method, flux method, etc. The details of these methods including their merits and demerits have been already discussed in Chapter 2. Among them the solid state method is the simplest, convenient and low cost method for both bulk and wire sample preparation and hence the same was used in the present work for the preparation of iron pnictides superconductors both in bulk and wire forms. Synthesis of bulk samples was done using single step-two stage solid state reaction, by introducing a novel pre-processing step. However, wire samples were prepared using Powder In Tube (PIT) method (Jia *et al.* 2008; Ma(b) *et al.* 2011). The ingredients chosen for the preparation of $SmFeAsO_{1-x}F_x$ are Sm, Fe, As, Fe_2O_3 and FeF_2 powders (M/s Alfa Aesar, purity 99.99%). Here, high purity Sm rod was filed under inert atmosphere in a glove box so as to get Sm powder without oxidation.

Because of the toxicity and low vaporization temperature of arsenic/phosphorus elements and the high reactivity of rare earth, alkali, and alkaline earth metals, the synthesis of iron-based compounds is a challenging task and requires careful handling from different angles. All preparation processes need to be carried out in a well-conditioned inert gas atmosphere glove box to avoid oxygen and water vapor. Thus, a glove box that can maintain a vacuum or an inert atmosphere was exclusively used in the present work. It is a stainless steel assembly with a main chamber and an antechamber. The frontal portion of the main chamber has a glass window with a provision for two neoprene gloves. The antechamber can be evacuated up to a level of 10^{-3} mbar. The main chamber is partially evacuated and then flushed with high purity argon gas. This is repeated several times automatically to ensure high purity argon atmosphere in the main chamber. The evacuation of both the chambers is done using a two-stage rotary vacuum pump. The pressure levels in both the chambers are monitored by Pirani gauges and are displayed on digital and analogue meters.

The samples are usually sealed inside an evacuated quartz tube during the heat treatment procedure in order to avoid oxidation and volatile loss of As and F. However, during heat treatment there is a remote chance of the leakage of arsenic vapor by an accidental breakage of quartz tubes. So, adequate provision is made in the furnace to flush out any toxic gasses above the building top in the event of a breakage of the sealed quartz tube.

3.2.1 Preparation of bulk samples

Starting from the first report of iron-based superconductor by Kamihara et al. (Kamihara *et al.* 2006) solid state reaction method at ambient pressure is the generally used method to synthesis polycrystalline samples. It is a much simpler method compared to high pressure synthesis, another method used for pnictides synthesis. In the present work, the solid state reaction method was used for the synthesis of $SmFeAsO_{1-x}F_x$ bulk superconducting samples (Chen(c) *et al.* 2008). The schematic representation of the main steps involved in the preparation procedure is given in Figure 3.1. The preparation procedure mainly consists of three steps - mixing and grinding, pelletization and vacuum sealing, and sintering at a suitable temperature. In the first step, all the ingredients were weighed according to the calculated stoichiometric ratio using an electronic balance (Metller AE240, Greifensee, Switzerland). Then, the weighed ingredients were thoroughly mixed and ground using Agate mortar and pestle in a glove box under Ar atmosphere. Homogeneously mixed powder were compacted into rectangular pellets with dimensions of 15 × 5 × 2 mm^3, under a pressure of 500 MPa using a hydraulic press (Herzog TP 20P) in the second step. The pellets were sealed inside evacuated quartz tubes to avoid oxidation and volatile loss. Finally, the sealed tubes were subjected to heat treatment at suitable temperatures in a programmable muffle furnace having stability and accuracy better than ±1 °C controlled using a Eurotherm-2404 temperature controller.

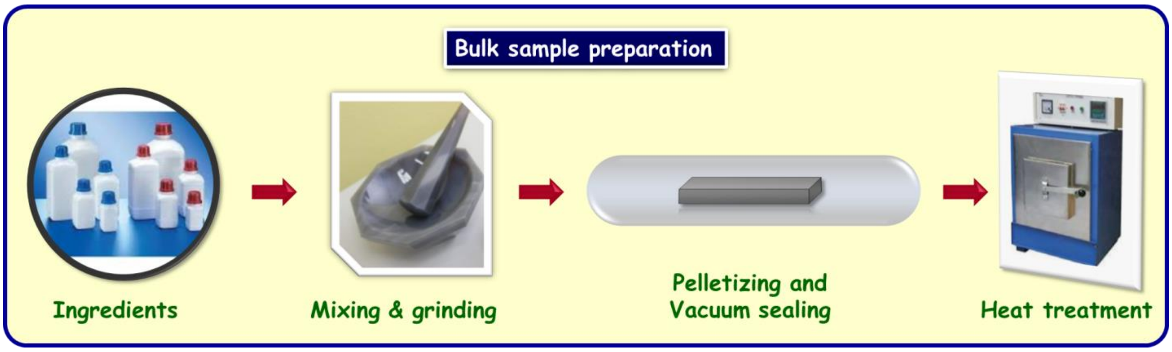

Figure 3.1: Schematic representation of preparation method used for $SmFeAsO_{1-x}F_x$ bulk samples

In the present study, bulk samples were prepared using the above method with an additional pre-processing stage before the final high temperature synthesis (Anooja *et al.* 2012). This method was developed by our group and described herein as a single step-two stage solid state reaction. By introducing the novel pre-processing stage, the final processing temperature could be reduced drastically. Details of this preparation technique used for bulk samples throughout this work will be discussed in Chapter 4.

3.2.2 Preparation of wire samples

Conventional Power In Tube (PIT) method was used for making $SmFeAsO_{1-x}F_x$ wires (Jia *et al.* 2008). The PIT process takes advantage of the low material costs and the relatively simple deformation techniques employed. The main steps involved in a PIT process is schematically illustrated in Figure 3.2. Generally, a mixture of a stoichiometric amount of ingredients was used as a precursor powder. In the present work, the powder preprocessed at 370°C was used as precursor. The details of the processing steps are given in Chapter 7. After homogeneous mixing, the powder was filled in a suitable metal tube having desired dimension and mechanically compacted. The ends of the tubes were sealed by inserting copper studs and further crimpled mechanically. The powder filled tubes were then subjected to groove rolling and reduced into desired dimension. The long length composite wires were cut into small pieces and then the ends of the wires were pressed and capped using stainless steel (SS) caps and finally given a heat treatment under high purity argon atmosphere. After heat treatment, short length samples were cut for various structural and superconducting characterizations.

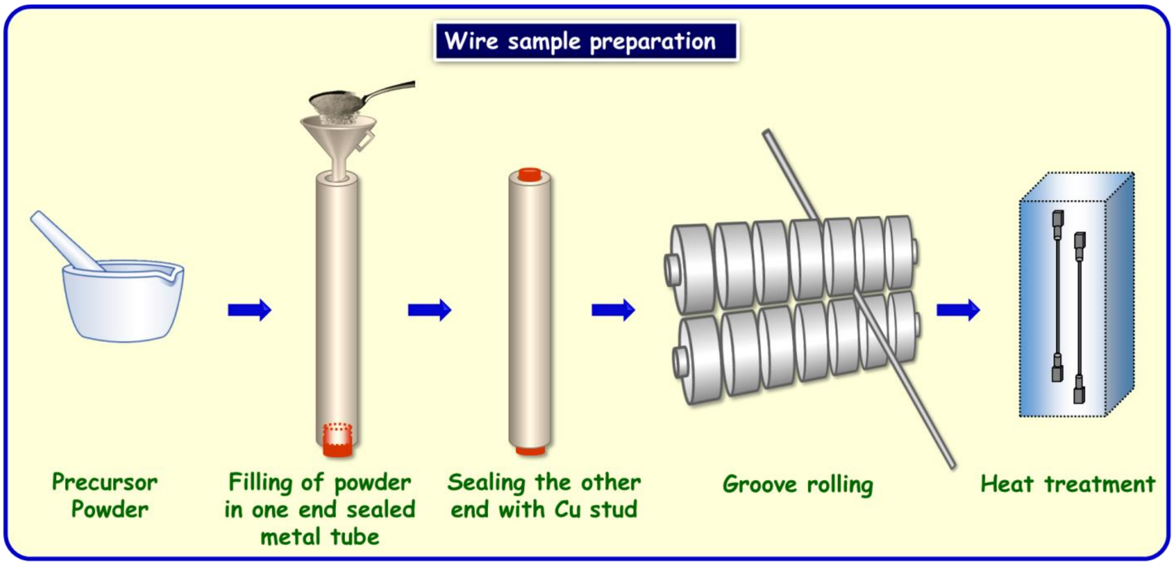

Figure 3.2: Schematic representation of preparation method used for $SmFeAsO_{1-x}F_x$ wire samples

3.3 Characterization techniques used in the present study

The various characterization techniques that have been used for this thesis work are presented in this section. This section has been mainly divided into two - structural characterization techniques and superconducting characterization techniques.

3.3.1 Structural characterization techniques

Structural characterization of the samples for phase identification, determination of the crystal structure, calculation of the crystal lattice parameters, strain, grain size, etc. was done by using the x-ray diffraction technique. Microstructural characterization techniques used in the present study include scanning electron microscopy (SEM), energy dispersive spectroscopy (EDS) and optical microscopy. Grain morphology and grain size were examined by SEM, and elemental analysis of the sample was done by EDS. The optical images of the wire samples were taken using an optical microscope for analyzing their cross-sectional features.

3.3.1.1 Powder x-ray diffraction (XRD)

X-ray diffraction technique is an analytical tool extensively used for phase identification and unit cell dimension estimation of a crystalline material. Each crystalline material has its one unique x-ray diffraction pattern that may be used as a “fingerprint” for its identification. By analyzing XRD data, we can identify different phases present in the sample and estimate the phase assemblage quantitatively. The principle behind the working of x-ray diffractometer is that “the *d* spacing between the crystal lattice act as 3D diffraction gratings for x-ray wavelengths. Constructive interference of x-rays diffracted from the crystal forms XRD pattern obeying the Bragg's equation. A crystal can be considered as an ordered arrangement of atoms. When a beam of electromagnetic radiation is incident on a crystal, then all atoms in the path of the beam scatter the x-rays simultaneously. In general, the scattered x-rays interfere, essentially canceling each other out. In certain specific directions, the scattered x-rays are in-phase and interfere constructively. To yield useful information about the structure of the material, the wavelength of the incident rays should be of the same order of magnitude as the interatomic spacing in the crystal structure. X-rays are used to produce the diffraction pattern because their wavelength λ is typically the same order of magnitude (1-100 Å) as the spacing d between planes in the crystal. The directions of possible diffractions depend only on the size and shape of the unit cell. The intensities of the diffracted waves depend on the kind and arrangement of atoms in the crystal structure. W.L. Bragg developed an equation for diffraction by treating this diffraction mathematically as reflection from the diffracting planes. According to this any crystal can be considered as a set of equidistant parallel planes that pass through all of the atoms in the crystal, called "Bragg" planes. For a crystal, many different sets of such planes are possible and are labeled with a set of integers (*hkl*), called the Miller indices. Bragg showed that for an x-ray of wavelength λ and angle of incidence θ with respect to a Bragg plane, scattered waves from the various ions lying in a single Bragg plane will be coherent if the angle of reflection equals the angle of incidence. Scattering in this direction from successive planes a distance d apart will also be coherent and will interfere constructively if $2d\sin\theta = n\lambda$, where n is an integer. This equation is called Bragg's equation.

Generally, an x-ray diffractometer consists of an x-ray source, a sample holder, and a detector. The source is a cathode ray tube (x-ray tube) which is capable of producing a beam of monochromatic x-rays. A current is applied to the heating filament within the tube thereby emitting electrons and a high voltage, typically 15-60 kilovolts, is applied to the tube. This high voltage accelerates the electrons, which then hits a target and produces x-rays. The wavelength of these x-rays produced is characteristic of the target used. These x-rays are collimated and directed onto the sample placed inside the sample holder. A detector detects the diffracted x-ray signal; the signal is then processed either by a microprocessor or electronically, converting the signal to a count rate. In summary, x-ray diffraction technique comprises - (1) production, (2) diffraction and (3) detection. A schematic representation of the basic components of a typical x-ray diffractometer is shown in Figure 3.3.

In the present study, powder XRD analysis of the samples was conducted by an automated x-ray diffractometer (PANalytical X'pert Pro, Model No: PW 3040/60). It consists of an x-ray source (CuKα radiation, λ = 1.540566 Å) on the incident beam side and a monochromator and a proprietary detector, X' celerator at the diffracted beam side. This instrument has θ-θ Bragg-Brentano geometry with the fully automated operation and data acquisition. Generally, scans were performed under a tube voltage of 40 KV and current of 30 mA, and scanning angle (2θ) ranged from 20° to 80° with a step size of < 0.02°. In order to obtain accurate results, the samples (either bulk or wire) were thoroughly grounded into fine powders. The finely grounded powders were then filled inside a standard sample holder, and the XRD data were recorded at ambient conditions. In case of the small amount of powder, a zero background holder was used. In order to avoid excessive exposure to x-ray beam on the sample and control the exposure area, programmable slits were used in the incident beam side.

From the XRD data obtained, the phase identification was performed using X' Pert Highscore software with support of the ICDD PDF II database. This technique has been also used for a semi-quantitative phase analysis. The volume percentages of different phases in the samples were assessed semi-quantitatively, from the integrated x-ray peak intensities, using the relation:

$$\text{Vol.\% of phase X} = \frac{\sum \text{Integrated peak intensities of phase X}}{\sum \text{Integrated peak intensities of all phases}}$$

The *d*-values of selected peaks of the sample were used for its lattice parameter calculations using the relation $\frac{1}{d^2} = \frac{h^2+k^2}{a^2} + \frac{l^2}{c^2}$, since the sample has tetragonal symmetry. Here, *a* & *c* are lattice parameters of the sample and (*hkl*) are the Miller indices of lattice plane. The full widths at half maxima (FWHM) of selected peaks of the samples were also used for assessing the lattice strain and grain size. FWHM of an XRD peak depends on factors like crystallite size, lattice strain, instrumental parameters, etc. The lattice strain and crystallite size can be calculated from the Williamson-Hall plot (FWHM × $\cos\theta$ versus $\sin\theta$). The slope of the plot gives lattice strain, and the intercept gives crystallite size (Williamson *et al.* 1953).

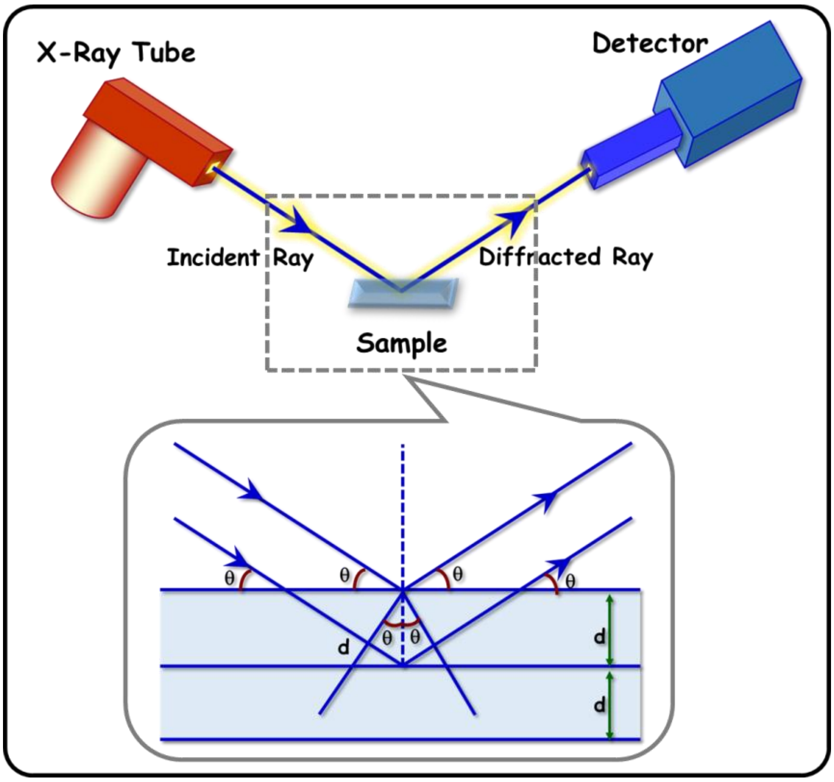

Figure 3.3: Schematic representation of the x-ray diffractometer

3.3.1.2 Scanning electron microscopy (SEM)

Scanning electron microscopy is used to have a direct observation of the sample microstructure and morphology. It is a non-destructive method to examine a large area of the sample and obtain information on the structure at the sub-micron level. The essential requirement is that the samples must be electrically conductive, at least at the surface, and electrically grounded to prevent the accumulation of electrostatic charge at the surface. If the samples are nonconductive, they must be coated with an ultrathin coating of electrically conducting material like gold. Besides the surface topographic studies, the SEM can also be used for determining the chemical composition of a material, its fluorescent properties, and the formation of magnetic domains and so on.

In order to take a SEM image, the specimen is bombarded by a convergent electron beam, which is scanned across the surface. The SEM image is formed after step by step sequential scanning of the sample with an electron probe. The working principle of the SEM is shown in Figure 3.4. The primary electrons produced from the electron gun are focused into a small-diameter called electron probe that is scanned across the specimen, making use of the fact that electrostatic or magnetic fields, applied at right angles to the beam, can be used to change its direction of travel. The electrons interact with electrons in the sample producing various signals including secondary electrons, backscattered electrons, characteristic x-rays, auger electrons, etc. These signals contain information about the sample's surface topography and composition. By scanning simultaneously in two perpendicular directions, a square or rectangular area of specimen (known as a raster) can be covered and an image of this area can be formed by collecting secondary electrons from each point on the specimen. i.e. The intensity of one of the detected signals (at a time) is amplified and used to the intensity of a pixel on the image in the computer screen. The electron beam then moves to next position on the sample, and the detected intensity gives the intensity in the second pixel and so on. The SEM can be operated in many different modes like secondary electron mode, back scattered electron mode, electron backscattered diffraction mode, x-ray mode, etc. The secondary electrons excited by the incident beam originate from a small volume and give information about the fine details of the specimen. The resolution in this mode is about 1-10 nm.

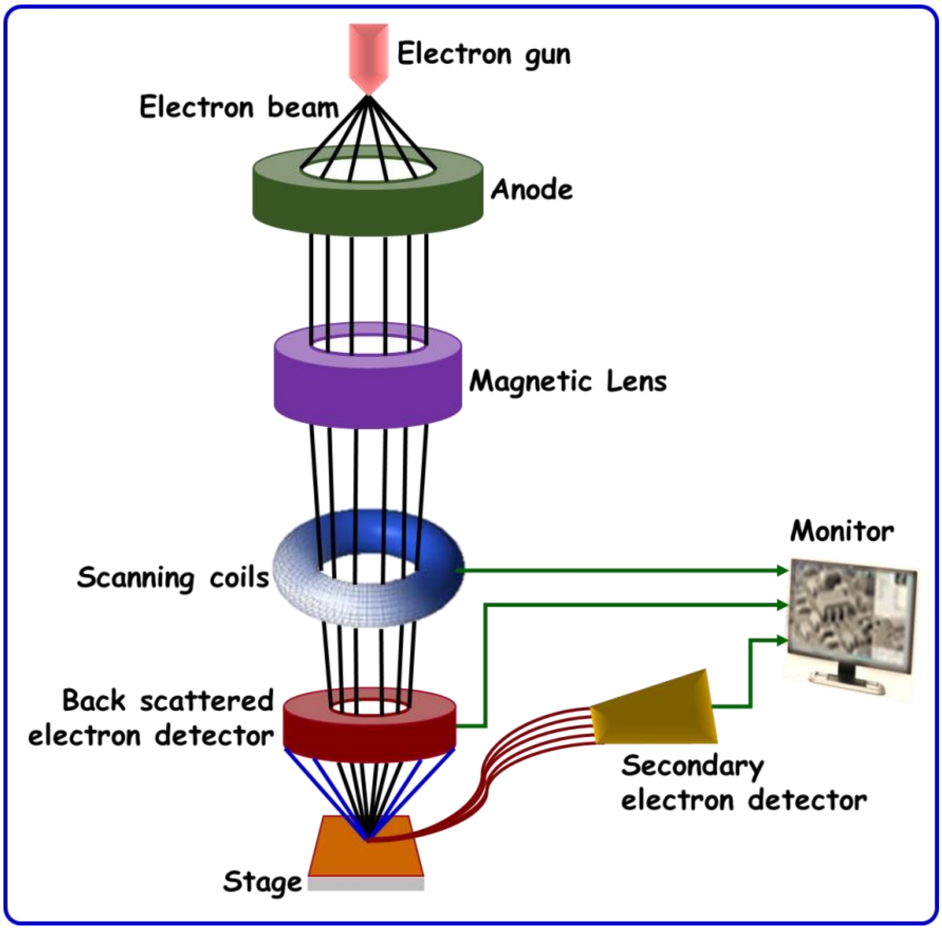

Figure 3.4: Schematic representation of SEM

In the present study, the microstructural analysis of the bulk samples was done using a JEOL JSM 5600 LV scanning electron microscope equipped with an energy dispersive x-ray spectrometer (Phoenix) used in secondary electron imaging (SEI) mode.

Freshly fractured surfaces of the samples were mounted on brass studs using adhesive carbon tapes. No gold coating is needed since the samples are electrically conducting. Then, the brass studs with the mounted samples were loaded on the sample holder of the microscope. The typical magnifications value chosen for the SEM images in the present study were 5000X and 3000X. The maximum resolution of the instrument is about 3.5 nm. For wire samples, the microstructural analysis was done using a CryoSEM, and polished surfaces of the samples with no conductive coating were also used.

3.3.1.3 Energy dispersive spectroscopy (EDS)

Energy dispersive spectroscopy (EDS) can provide information regarding elemental distribution in the samples. In EDS, x-rays emitted by the sample in response to being hit with charged particles (beam of electrons) are analyzed. An electron from an inner shell (K-shell) of an atom is ejected due to the collision with a primary electron, and it creates a hole (vacancy). An electron of higher energy (L-shell) within the atom will be attracted and moves into the vacant position. This electron transition results in the release of energy (falls in the x-ray spectrum region) exactly equal to the difference in energy between the lower energy hole orbit and the higher energy electron orbit. The number and energy of this x-ray are characteristic of the atom and orbit of origin thus yielding analytical data. Generally, the higher the atomic number of the atom, the higher the energy of the characteristic x-rays it will emit (per shell) and the higher number of low energy lines it will emit. In short, each element has a unique atomic structure allowing x-rays that are characteristic of an element's atomic structure to be identified uniquely from each other. This qualitative EDS spectrum can be either photographed or plotted. This data can then be further analyzed to produce either an area elemental analysis (displayed as a dot map) or a linear elemental analysis (displayed as a line scan) showing the distribution of a particular element on the surface of the sample.

EDS employs pulse height analysis in which a detector is giving output pulses proportional in height to the x-ray photon energy is used in conjunction with a pulse height analyzer (in this case a multichannel type). A solid state detector is used because of its better energy resolution. Incident x-ray photons cause ionization in the detector, producing an electrical charge, which is amplified by a sensitive preamplifier located close to the detector. Both detector and preamplifier are generally cooled with liquid nitrogen to minimize electronic noise. The limitation of EDS is that it cannot detect elements having atomic weight lesser than carbon. In the present study, EDS analysis was done using automated EDS system integrated to SEM.

3.3.1.4 Optical microscopy

Optical microscopy is mainly used for analyzing the cross-sectional features of the wires samples. It is also used for the investigation of sample microstructure and morphology. It gives information on the geometry, size, orientation, and the interfaces between core/sheaths for the wires samples. The principle behind the optical microscopes is similar to the function of lenses, and their magnification is a function of the number of lenses and resolution is a function of the ability of a lens to gather light. Main features of the optical microscope are lenses, eyepieces, light source and camera. Leica EZ4 HD model microscope was used for the present study. It has high-quality 4.4:1 zoom (magnification from 8X-35X) and seven LEDs for illumination. The LEDs provide transmitted, incident and oblique light for high quality illumination and contrast of any application. The integrated high definition digital camera (maximum resolution of 2048 × 1536) offers a fast live image on a computer screen or HD display transforming a stereomicroscope into a USB microscope. It captures 3 M pixel color images directly onto SD card or computer. The intuitive imaging software allows for easy fine tuning, capture, and archiving of images and also allows for basic annotation and measurements. For taking optical images, samples of small size 1-2 cm were cut from long conductors, polished mechanically and then placed under the microscope in suitable holders. The exact estimation of core and sheath cross-sectional areas of wires were calculated from the optical microscopy with the help of software associated with the microscope.

3.3.2 Superconducting characterization techniques

Superconducting properties of the material can be investigated by using both transport and magnetic measurements. Each method has its own merits and demerits. The superconducting parameters T_C, J_C and $J_C(H)$ were measured using both transport and magnetic measurements for assessing the quality of samples. Superconducting transport measurements such as resistivity versus temperature (ρ-T) and current versus voltage (I-V) were carried out using a closed cycle cryocooler integrated cryostat (Sumititomo Heavy Industries Ltd (SRDK-408)) by *dc* four-probe technique. The temperature of the sample was precisely monitored using two temperature controllers (Lakeshore-340 & 332, Westerville, OH). Magnetic measurements of the sample include both *ac* and *dc* magnetic studies. The temperature dependence of *ac* susceptibility (χ-T) was measured using a closed-cycle *ac* susceptometer (Advanced Research Systems, ARS-CS202S-DMX-19 SCC, Macungie, PA). All the measurements were fully automated with a computer using

GPIB interfaced Labview software. The *dc* magnetic measurements were carried out using PPMS (Physical Property Measurement System), in collaboration with Cambridge University, UK and JNCASR (Jawaharlal Nehru Centre for Advanced Science and Research, Bangalore). An in-house PPMS (Quantum Design DynaCool) equipped with 9 T conduction cooled superconducting switch-less magnet system installed in May 2014 was also used for *dc* magnetic measurements. Magneto transport measurement were also carried out in order to determine the critical fields (H_{C2} and H_{irr}) of the samples and also to find the majority charge carriers in the samples. Details of the different experimental techniques used for studying superconducting properties are described in this section.

3.3.2.1 Transport measurements

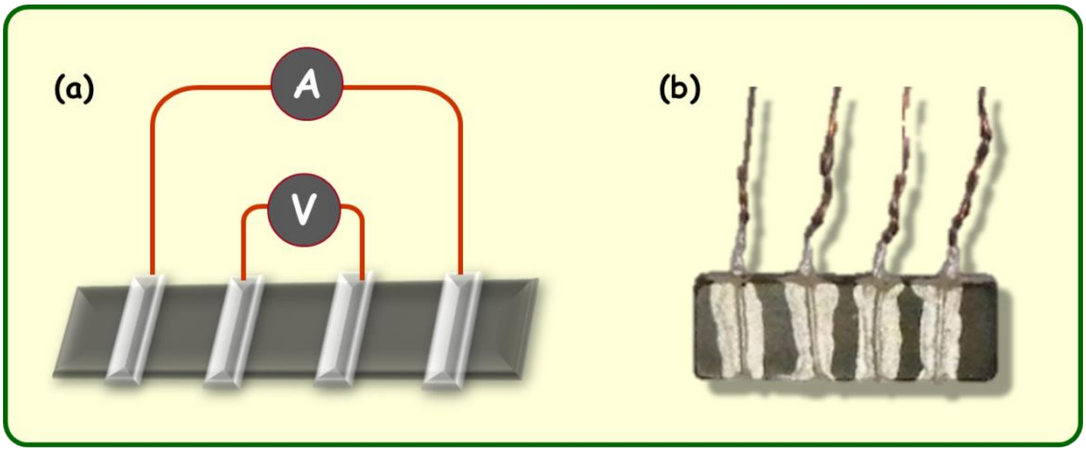

Figure 3.5: (a) Schematic diagram of *dc* four probe method for transport measurement and (b) the photograph of a typical sample used for four probe measurement

Transport measurements in respect of both resistance versus temperature (*R-T*) and current versus voltage (*I-V*) characteristics of the samples were used to determine the T_C and I_C of the samples, respectively. The *dc* four probe method is used for transport measurement of the samples. This method uses separate pairs for current carrying and voltage sensing electrodes. i.e. current is passed through a pair of current leads and the voltage drop across the sample is measured by a separate pair of leads. Thus, the voltage drop in the current carrying wires and the contacts are prevented from being added to the actual value of voltage, and a more accurate measurement is obtained than two terminal sensing. A schematic diagram of the four probe resistivity measurement and a typical photograph of this arrangement used in the present study of bulk samples are given in Figure 3.5. In the case of bulk samples, for fixing leads to the sample high-quality copper wires were wound into the grooves made on the samples. Then, silver paint was pasted above the Cu wire as shown in Figure 3.5. The sample was placed inside the sample holder, and the leads from the sample were soldered to the terminal leads of the cryostat. For wire samples, they were cut into 2-3 cm length and then put into the sample holder. The terminal leads were then directly soldered to the sample using orthophosphoric acid as a flux, after thoroughly cleaning the sheath surface.

a) Resistivity - temperature (ρ-T) measurements

Resistivity - temperature (ρ-T) measurements were mainly used to determine the critical temperature (T_C) and transition width (ΔT_C) of the samples. The temperature at which resistivity falls sharply is taken as the T_C and the difference between the temperatures corresponding to the 90% and 10% of normal state resistivity (T_{Conset} - $T_{Coffset}$) is defined as ΔT_C for the samples. Residual resistivity ratio (RRR) of the samples was also calculated from the ρ-T characteristics using the formula RRR = ρ_{300K}/ρ_{55K}, which gives an insight into the sample quality. In the present study, a programmable milliampere source (Keithley 220/6220) and nano voltmeter (Keithley 181/2182A) were used for the ρ-T measurements. A current of 0.1 A was generally used for the ρ-T measurements.

b) Current - voltage (I-V) measurements

The current carrying capacity of the samples were determined by current - voltage (I-V) measurements. For I-V measurements, a computer controlled pulsed current method was employed using a *dc* power supply (Aplab 9711P) having a maximum current rating of 100 A. After each current pulse, sufficient time was given to cool the sample before next measurement to reduce the Joule heating effect due to the current leads and their contacts. The self-field transport I_C of the samples was estimated using a criterion of 1 μV/cm from I-V characteristics. Then, the corresponding critical current densities (J_C) of the samples were calculated as $J_C = I_C/A$, where A is the cross-sectional area of the sample. All the transport J_C values of the samples were measured at a temperature of 12 K.

3.3.2.2 Magnetic measurements

The superconducting properties T_C and J_C were also determined from magnetic measurements. Characterization of superconductors by magnetic measurements has several advantages over the resistivity measurements. They are:

(i) Samples do not require electrical contacts but can be small or even in the powder form.

(ii) A magnetic signal is enough to characterize the material at low temperatures.

(iii) We can probe the entire sample volume and, therefore, get a volume average of the sample's magnetic response. This can be contrasted with the resistivity measurements where the measuring current flows through a single, least resistance percolative path.

(iv) The superconducting volume fraction can be estimated.

(v) The signal is obtained even if the superconducting path is not continuous.

(vi) The critical current densities can be measured independent of contacts and of intergranular weak links.

Both *ac* and *dc* magnetization methods have been used in the present study. They are two entirely different tools that provide different ways of examining magnetic properties. Both these techniques relay on sensing coils used to measure the variation in the magnetic flux due to magnetized sample. Details of these magnetic measurements used in the present study are described in this section.

a) *AC* susceptibility versus temperature (χ-T) measurements

The *ac* Susceptibility technique is extensively used to study superconducting transition, vortex dynamics, and critical current density, grain connectivity, relaxation process and to map magnetic phase diagram. It is a simple technique in which susceptibility is measured directly. Moreover, the applied field is very small, and thus it can be easily established. This method uses the mutual inductance principle, hence gives a rapid means of measuring samples without the need for current or voltage terminals. In this method, the sample is centered within a primary coil while driven with an external *ac* field. This produces a time-varying magnetization that is detected by a secondary coil. Usually, a lock-in amplifier is used to analyze this signal that is related to the materials ac magnetic properties. Alternatively, superconducting quantum interface device magnetometers (SQUID), and vibrating sample magnetometers (VSM) are also used to measure the magnetic moment of the sample. The schematic representation of working principle of an *ac* susceptometer is given in Figure 3.6. The magnetic susceptibility, χ is a measure of how "magnetic" a material is and that represents the response of the material to an applied field H. i.e., $\chi = M/H$, M - sample's magnetization. However, an *ac* susceptibility measurement involves the application of a varying magnetic field, H_{ac} and recording the samples response by a sensing coil. Therefore $\chi = dM/dH_{ac}$. In this measurement, the moment of the sample is actually changing in response to an applied *ac* field, allowing the dynamics of the magnetic system to be studied. Since the actual response of the sample to an applied *ac* field is measured, the magneto dynamics can be studied through the complex susceptibility ($\chi' + i\chi''$). The real component χ' represents the component of the susceptibility that is in phase with the applied *ac* field, while χ'' represents the component that is out of phase. The imaginary component χ'' is related to the energy losses, or in other words, the energy absorbed by the sample from the *ac* field. Both χ' and χ'' are very sensitive to thermodynamic phase changes and used to measure transition temperatures. A sharp decrease in the real part χ' represents the diamagnetic response of the superconductor by the external magnetic field, whereas the imaginary part indicates dissipative processes in the sample. The χ-T measurements of the samples also provide an insight into the granular behavior of the samples (Zhang(a) *et al.* 2008; Polichetti *et al.* 2008). A typical feature of granular samples in *ac* susceptibility is two drops in χ' accompanied by two peaks in χ''. The step at high temperatures corresponds to the response of individual grains of the material, whereas that at lower temperatures is due to the intergrain connectivity. This method also offers an opportunity to determine the frequency dependence of the complex susceptibility that leads to information about relaxation processes and the relaxation times of the magnetic systems studied. An advantage of the *ac* susceptibility measurement is that it is very sensitive to small changes in moment, *M(H)*. Since the *ac* measurement is sensitive to the slope of *M(H)* and not to the absolute value, small magnetic shifts can be detected even when the absolute moment is large.

In the present work, the critical temperature, T_C of the superconducting samples was verified by *ac* susceptibility versus temperature (χ-T) measurements. The block diagram of the *ac* magnetic susceptibility measurement unit (Advanced Research Systems, Model: CS202*F-DMX-19 SCC) used in the present study is given in Figure 3.6. Both bulk and wire samples are fixed in the sample holder tube and then inserted into a system containing both primary and secondary coils (ARS). An excitation field is applied to the primary coil and the secondary coils pick up the change of induction voltage across the coils due to the superconducting shielding current using a lock-in-amplifier (Stanford Researh Systems (SRS 850), USA). The temperature of the sample was precisely monitored using Lakeshore-340 temperature controller. The measurements were programmed with a computer using GPIB interfaced Labview software. The onset of diamagnetism in χ', the value χ' having a negative value, was taken as T_C of the superconducting sample. In the present study, χ-T for all the samples were measured at a frequency of f = 208 Hz and *ac* field, $H_{ac} = 4.94 \times 10^{-4}$ T. Moreover, the *ac* susceptibility at different frequencies for varying temperatures at a fixed *ac* field was recorded to study the flux creep dynamics in the samples. The different frequencies chosen are $f = 208$, 333, 533, 733, and 999 Hz for $H_{ac} = 0.49$ mT.

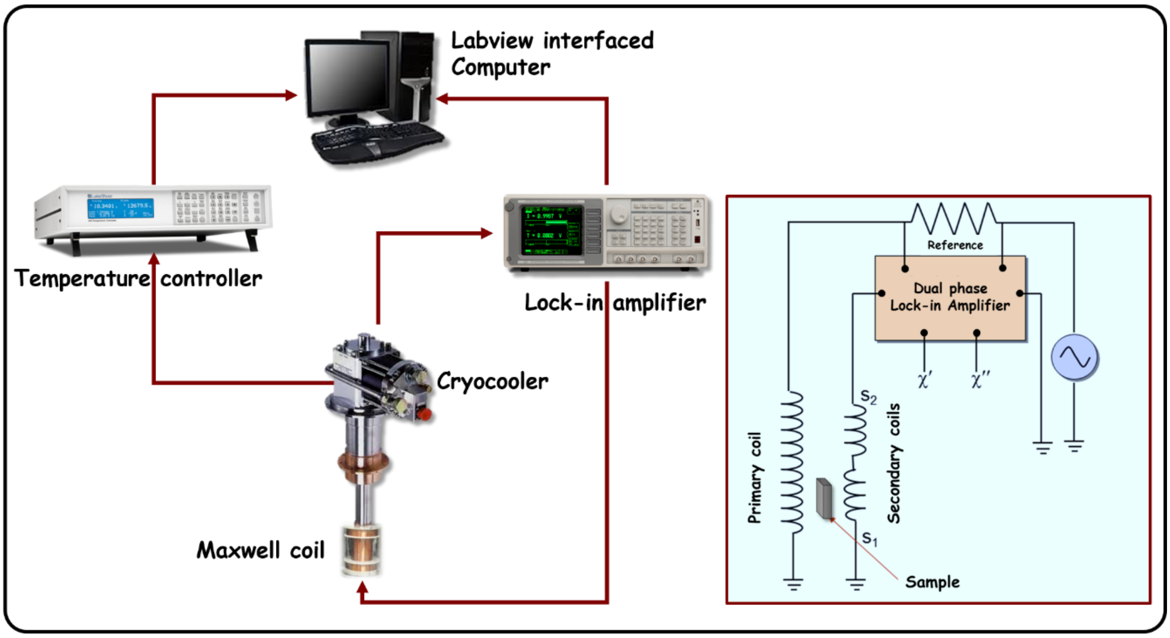

Figure 3.6: Block diagram of the *ac* magnetic susceptibility measurement unit and its schematic representation

b) *DC* magnetic moment versus field (*M-H*) measurements

In a *dc* magnetization measurement, a sample is subjected to and magnetized by a static *dc* field usually arising from an iron core, or superconducting magnet. Unlike *ac* susceptibility method, in this method the moment of the sample does not change with time. Here also an *ac* output signal is detected but that signal arises from the periodic movement of the sample. In *dc* magnetization method, the sample is moved relative to a detection coil that is used to measure variations in flux due to the magnetized sample. The output signal from the detection coil can be measured and related to the materials magnetic properties. In short, the sample is magnetized by a constant magnetic field and then the magnetic moment of the sample is measured thereby producing a *dc* magnetization curve, *M(H)*. In the present study *dc* magnetic measurements (magnetic moment versus applied *dc* field) of the samples were carried out using VSM and SQUID based PPMS in collaboration with JNCASR, Bangalore and Cambridge University, UK; also using VSM based Quantum Design DynaCool PPMS (at NIIST (CSIR), Trivandrum). In both VSM and SQUID based systems, the sample is made to vibrate and the electrical signal thus produced is detected by the stationary coils around the sample. This induced voltage or signal is proportional to the magnetic moment of the sample, the amplitude and frequency of vibration. If the amplitude and frequency of oscillation are kept constant, the induced signal is proportional to the magnetic moment alone. The PPMS system mainly consists of a cryostat control system, chamber temperature control system, magnetic field control system, chamber atmosphere control system, and vacuum system. The cryostat control system and chamber temperature control system together maintain appropriate temperatures of the system for normal operation. The magnetic field control system controls the magnetic field at the sample location by means of the superconducting magnet and leads, the magnet controller, software, and the magnet shield. The configuration of the PPMS DynaCool System are shown in Figure 3.7.

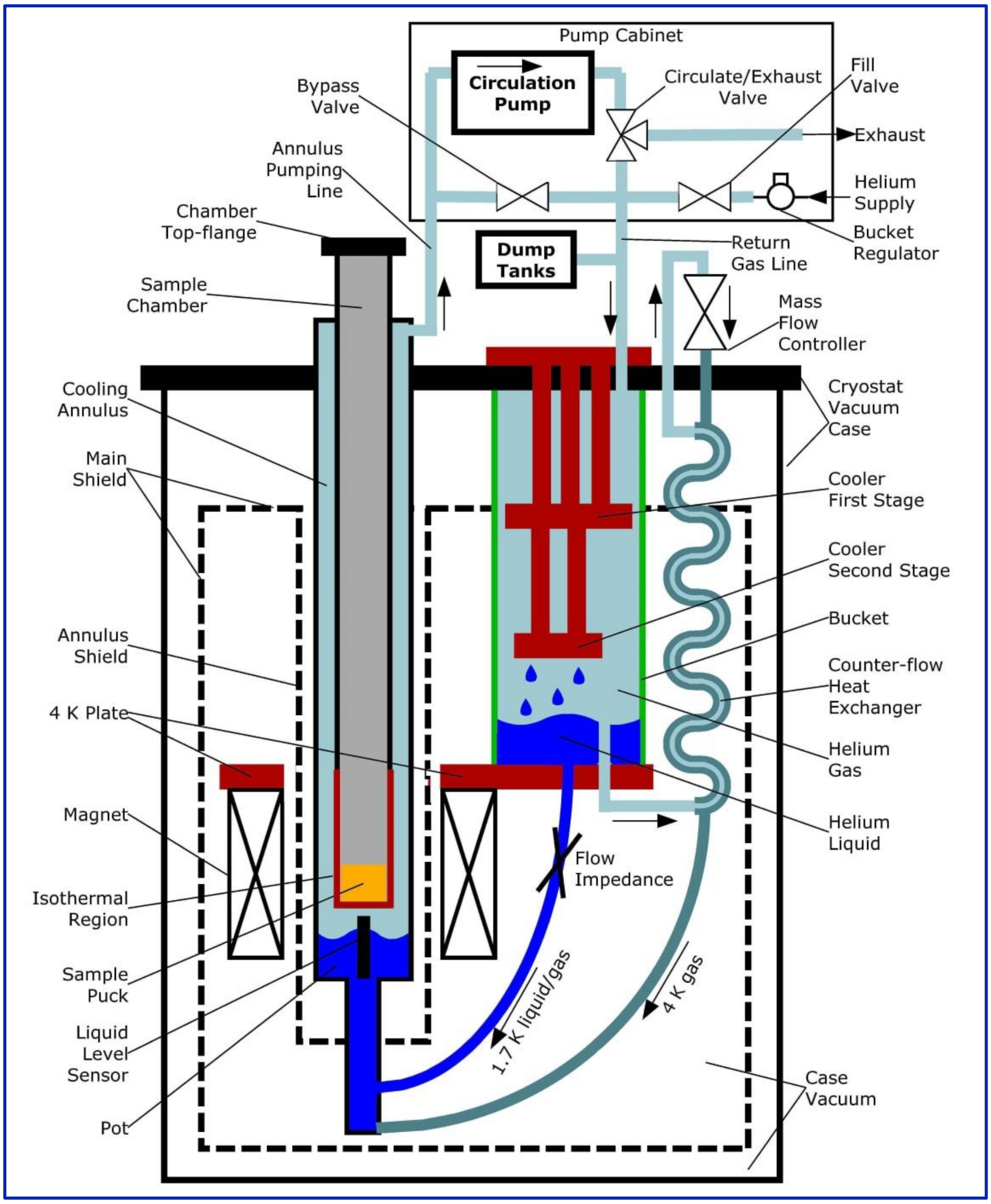

Figure 3.7: The configuration of the PPMS DynaCool System

The critical current density, J_C of the superconducting sample can be calculated from the *dc* magnetic moment versus field (*M*-*H*) measurements. Magnetic field dependence of the critical current density, $J_C(H)$ of the sample can be estimated from the width of the M-H loop based on Bean critical state model (Bean, C.P. 1962) using the formula: $J_{Clocal} = 20\Delta M/a(1\text{-}a/3b)$, where a and b are sample dimensions perpendicular to the applied field and ΔM is the width of the hysteresis loop, and $J_{Cglobal} = 30\Delta M/\langle r\rangle$, where $\langle r\rangle$ is the average grain size. ΔM can be calculated using the formula $\Delta M = M^{+} - M^{-}$. In the present study, the magnetization measurements were carried out at different temperatures 5, 10, 20, 30 and 35 K. Bulk samples of typical dimensions were used for the measurements. The measurements were done with a magnetic field applied along the longest dimension of the sample. The flux pinning force density, F_P ($F_P = J_C(H) \times H$) and the dependence of the pinning force on applied magnetic field was also analyzed from the magnetic J_C data.

3.3.2.3 Magneto-transport measurements

In this thesis work, magneto-transport measurements like ρ-T at varying magnetic fields and Hall Effect measurements were done to determine the critical fields and charge carrier concentration of the samples, respectively. In the present study the above measurements were done in an in-house PPMS. Rectangular pellets of uniform size was used for the measurements. The ρ-T measurements were taken at different magnetic fields from 0-9 T and the transition width of the superconductor increases with applied magnetic field. The upper critical field, H_{C2} of the superconductors can be calculated by taking the 90% of normal state resistivity (ρ_n) just above the T_C. Temperature corresponding to 90% ρ_n was noted for each magnetic field ρ-T measurement and then field versus temperature graph (H-T diagram) was plotted. From the slope of the H-T diagram we can estimate the $H_{C2}(0)$ using the formula $H_{C2}(0) = -0.693T_C\ [dH_{C2}/dT\ ]_{TC}$, where $[dH_{C2}/dT]_{TC}$ is the slope of the H-T plot at T_C. Similarly, H_{irr} of the samples were also evaluated by taking 10% of ρ_n and then plot corresponding H-T diagram.

Hall Effect measurement is used to determine the charge carrier density and the type of dominant carriers (electrons or holes). A transverse voltage is developed if we place a current carrying sample with in the magnetic field in such a way that the direction of both current and field are perpendicular. This is the principle of Hall Effect and the transverse voltage induced is called the Hall voltage. Hall voltage was measured by connecting voltage leads at the middle of the pellets, exactly perpendicular to the line of the current leads and to the direction of applied magnetic field. The magnetic field was applied in such a way that its direction is perpendicular to the plane of the rectangular pellet. Even though the voltage leads were exactly opposite to each other, the hall voltage will certainly contain a component of longitudinal resistance. This longitudinal contribution can be avoided by measuring the magneto resistance at both magnetic field directions, since the longitudinal resistance is symmetric to the field whereas the hall resistance is asymmetric. Hence, the magnetic field was swept from 9 to -9 T and then the Hall voltage was estimated by subtracting out the longitudinal part. From that, the Hall coefficient R_H was calculated as $R_H = \rho_{xy}/B$; $\rho_{xy} = [\rho_{(+H)} - \rho_{(-H)}]/2$ is the transverse resistivity (Hall resistivity). The sign of R_H gives an indication of majority charge carriers within the sample. If it is negative, electrons are the majority charge carriers and if it is positive, the majority carriers are holes. Carrier density (n) of the sample was also calculated from the measured hall coefficient using $R_H = -1/ne$.

CHAPTER 4

SYNTHESIS AND CHARACTERIZATION OF $SmFeAsO_{1-x}F_x$ BULK SAMPLES WITH THE INTRODUCTION OF A NOVEL PRE-PROCESSING ROUTE

As discussed in the preceding chapters the main interest on rare earth based iron oxypnictides stems from their relatively high critical temperatures (T_C) up to 55 K (Kamihara *et al.* 2008; Chen(c) *et al.* 2008; Aswathy *et al.* 2010) and very high upper critical fields (H_{C2}) up to ~ 300 T (Jaroszynski(b) *et al.* 2008). The parental material REFeAsO (RE - rare earth) is an antiferromagnetic semimetal with spin density wave (SDW) instability and does not show superconductivity. This compound has a tetragonal crystal structure with *P4/nmm* space group at room temperature. However, this material undergoes a tetragonal to orthorhombic structural phase transition on cooling which is partly believed to be driven by the magnetic instability that occurs in the iron plane. Superconductivity is introduced in iron pnictide systems by chemical doping as a result of the consequent suppression of SDW instability observed in the parental compounds. They are the first non-cuprate materials exhibiting superconductivity at relatively high temperatures upon electron or hole doping. The rare earth element substitution alone causes an enhancement of T_C more than double to that of the first reported La-based oxypnictide (Ren(a) *et al.* 2008b). Another versatility of this comprehensive class of superconductors lies in the possibility for any site substitution. However, it is very difficult to precisely control the composition of the compound according to the nominal stoichiometry. Besides this, the compounds contain arsenic whose chemical characteristics are hard to manipulate under laboratory conditions, sometime hazardous breakage is likely to occur due to over pressure developed inside the evacuated quartz tubes. Because of the complex synthesis route only a limited number of research groups are engaged in the preparation of the new family of iron-based superconductors (Kamihara *et al.* 2008; Aswathy *et al.* 2010; Ren(a) *et al.* 2008b). The superconducting properties such as T_C, H_{C2}, and J_C directly or indirectly depend on the synthesis method. The transition temperature, T_C, seems to be mainly determined by chemical composition and structure, whereas H_{C2} and J_C are influenced by microstructures that can be optimized by varying processing conditions. In order to accomplish a specific, exact and profound understanding of physical and superconducting properties; good quality crystalline materials are highly desirable.

Among the different rare earth iron oxypnictides, $SmFeAsO_{1-x}F_x$ (Sm1111) system is considered to be much promising due to its high T_C (Ren(a) *et al.* 2008b), relatively high H_{C2} (Senatore *et al.* 2008) and significant intergrain current density (Yamamoto *et al.* 2008b). In this chapter, we present the development of a simple route to synthesize Sm1111 superconductor in bulk form which mitigates the above problems and provides good quality samples at a relatively low temperature. One of the main features of the method is the introduction of a pre-processing step by which good quality Sm1111 samples with relatively high transport J_C could be synthesized at a lower heat treatment temperature of 850 °C (Anooja *et al.* 2012) compared to the existing methods.

4.1 Preparation of Sm1111 bulk samples by a novel pre-processing route

4.1.1 Introduction

Considering the methods of synthesis followed for polycrystalline $REFeAsO_{1-x}F_x$ superconductor, both ambient pressure and high pressure techniques have been widely used (Aswathy *et al.* 2010). Enormous investigations have intensively focused on the preparation and properties of the fluorine doped REFeAsO superconductor even from the first report by Kaminhara *et al.* (Kaminhara *et al.* 2008). In the first report, the superconducting $LaFeAsO_{1-x}F_x$ compounds were synthesized by following a solid state reaction method using LaAs, FeAs, dehydrated La_2O_3, La and LaF_3 powders at a higher temperature of 1250 °C for 40 h. For heat treatment, a mixture of powders was placed inside evacuated quartz tubes with Ar partial pressure. Binary compounds of FeAs and REAs were separately prepared as a precursor for the synthesis of final compound. In some reports (Shekhar *et al.* 2008; Takabayashi *et al.* 2008), a precursor of LaAs, Fe_2As and FeAs was made together by mixing RE, Fe and As powders in the atomic ratio of 1:3:3 and was heated at 900 °C for 12 h. The use of these binary compounds of arsenic would reduce the chances of explosion of the sealed quartz tube during the final reactions. Soon after, A. S. Sefat *et al.* (Sefat *et al.* 2008c) reported a different set of reactants REAs, Fe_2As, RE_2O_3, REF_3 and As in order to avoid the use of highly reactive RE powder. Nevertheless, an impurity phase of $RE_{4.67}(SiO_4)_3O$ phase was present in the product due to surface reaction of the pellet with the quartz tube because of the high processing temperatures (1250 °C). Researchers from Chinese group (G. F. Chen *et al.* (Chen(a) *et al.* 2008)) prepared $REFeAsO_{1-x}F_x$ using Fe_2O_3 as an oxygen source instead of the highly stable La_2O_3. Using

Fe_2O_3, they could reduce the processing temperature to 1150 °C. RE1111 was also prepared by the so-called two-step solid state reaction method with the starting materials REAs, Fe, Fe_2O_3, and FeF_2/FeF_3 powders as F source instead of REF_3 (Martinelli *et al.* 2008; Zhang *et al.* 2009). Both F doped and oxygen deficient REFeAsO superconductor having higher T_C values was also prepared using the high pressure sintering method with pressures as high as 6 GPa at 1250 °C for 2 h (Kametani *et al.* 2009b).

In the above reports, fluorine doped rare earth (RE) iron oxypnictides (RE1111) in bulk form are prepared by the two step method wherein FeAs and REAs are prepared in the first step and are added to the remaining ingredients in the second step in order to reduce volatile loss of As (Martinelli *et al.* 2008; Zhang(c) *et al.* 2009; Chen(a) *et al.* 2008; Chen(d) *et al.* 2010a; Kametani *et al.* 2009b). However, the method demands high temperature (> 1150 °C) or high pressure (~ 6 GPa) to obtain good quality samples. At higher temperatures, the probability for the breakage of quartz tube is high and that would lead to the failure of the experiment. Moreover, this synthesis process is non ideal due to the volatility of some components such as F and As. Moreover, the processing at elevated temperatures quite often leads to reaction of the sample with the container (mainly quartz). This demands the usage of expensive materials like Nb, Ta and Ti foil to wrap the bare samples in order to prevent the reaction between sample and quartz tube. Even if starting materials are mixed at the correct composition, the prepared substance contains a spurious phase whose composition differs from the nominal one. Furthermore, it is difficult to avoid the presence of the secondary phase REOF which is very stable and its concentration increase as the dopant concentration increases.

Great efforts are being continued by researchers to prepare the iron-based superconductors under both ambient pressures and lower temperatures. A reliable method should be developed to obtain F doped REFeAsO superconductors with high quality. Here, we could successfully reduce the processing temperature by introducing a pre-processing stage. The synthesis method is essentially a single step process, i.e. all the ingredients are processed together. However, the heat treatment was done in two stages. In the first stage, all the ingredients were processed at an optimized pre-processing temperature in vacuum/inert atmosphere and then the pre-processed sample was again ground, repelletized and sealed in an evacuated quartz tube for the final heat treatment.

4.1.2 Optimization of the pre-processing temperature

The pre-processing temperature was chosen after analysing the samples heat treated at temperatures ranging from 300 to 400 °C with an interval of 10 °C. $SmFeAsO_{1-x}F_x$ with x = 0.3 composition was choosen for this study. The samples were prepared by stoichiometric mixing and grinding of Sm, Fe, As, Fe_2O_3 and FeF_2 powders (M/s Alfa Aesar, purity 99.9%) inside a glove box filled with high purity argon. After homogenous mixing, these samples were compacted into rectangular pellets with dimensions of 15 × 5 × 2 mm^3, under a pressure of 500 MPa. The pellets were sealed inside evacuated quartz tubes. The sealed tubes were subjected to heat treatment at different temperatures in a programmable muffle furnace having stability and accuracy better than ±1 °C controlled using Eurotherm-2404 temperature controller.

Analysis of the samples processed in the first stage, at temperatures in the range 300-400 °C, shows that they can be categorized into three types depending on their color, shape and phase assemblage. Typical XRD pattern of the samples from each category is shown in Figure 4.1 and the corresponding photographs of this pre-processed sample with quartz tube is shown in Figure 4.2. The samples processed at 300-350 °C remain intact without much change in the original reddish color and shape (Figure 4.2(a)). XRD analysis of a typical sample from this batch processed at 320 °C shows that the sample does not undergo any reaction (Figure 4.1 Sm320). Whereas, the samples processed in the range 360-380 °C deform into brown powders (Figure 4.2(b)) with *in situ* formation of SmAs and minor quantities of FeAs. While, the ingredients Fe_2O_3 and FeF_2 remain unreacted (Figure 4.1 Sm370, sample processed at 370 °C). At temperatures above 380 °C, the major part of the sample fuses into metallic globules which stick to the surface of the quartz tube and some part remains as powder along with an arsenic coating on the inner surface of the tube. A photograph of the sample pre-processed at 400 °C (Sm400) is shown in Figure 4.2(c). Neither the fused mass nor the As coating could be fully retrieved for further processing. The XRD pattern of the fused mass contains additional peaks of SmOF and Sm_2O_3 along with SmAs and FeAs. However, peaks corresponding to Fe, FeF_2 and Fe_2O_3 were not observed (Figure 4.1 Sm400).

The choice of the phase assemblage of a precursor and the reactivity of its individual phases have major roles in the preparation of any complex compound through solid state route. The final phase purity, processing temperature and duration mainly depend on the above factors. From the above results, we observed that the pre-processing of the reaction mixture at an optimized temperature range of 360-380 °C has probably yielded a precursor having the right phase assemblage and good reactivity. The precursor has not been allowed to undergo fusion, but the temperature is tuned such that reacted binary phases such as SmAs and FeAs are formed *in situ*. These phases will have higher reactivity compared to those used for two step process in which these are usually prepared separately at a higher temperature of 500-900 °C (Zhang(c) *et al.* 2009; Chen(d) *et al.* 2010a; Kametani *et al.* 2009b). Therefore, the second category of powder (powder pre-processed at 360-380 °C) was chosen as a precursor for second stage processing and further investigation has shown that it is an appropriate precursor.

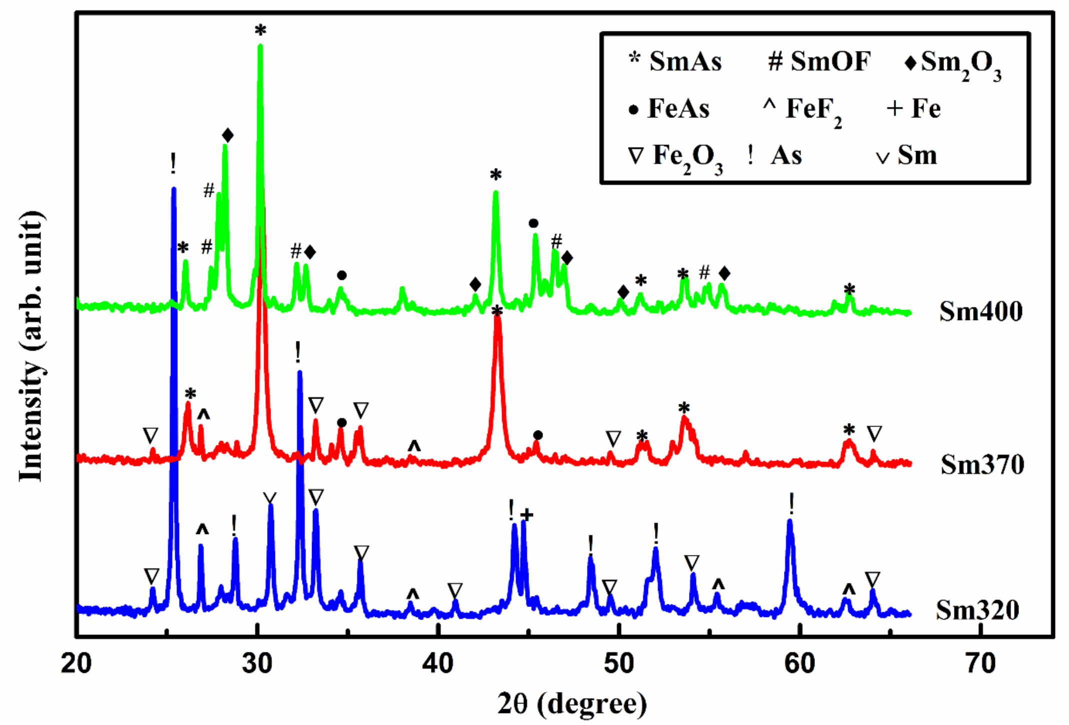

Figure 4.1: XRD patterns of pre-processed Sm1111 at 320, 370 and 400 °C

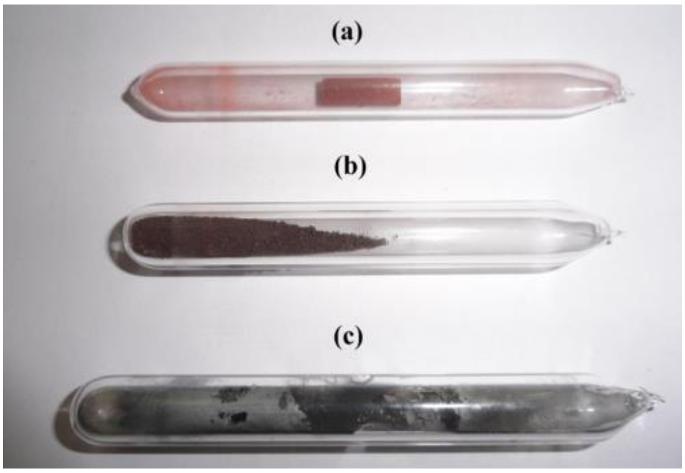

Figure 4.2: Photographs of pre-processed Sm1111 at (a) 320 °C, (b) 370 °C and (c) 400 °C

4.1.3 Final preparation of Sm1111 bulk samples

The powder pre-processed at 370 °C was used for the preparation of Sm1111 bulk samples. Various steps involved in the preparation process are shown schematically in Figure 4.3. All the ingredients were stoichiometrically weighed and mixed using an agate mortar and pestle inside a glove box with high purity argon atmosphere. The ingredients chosen were Sm, Fe, As, Fe_2O_3 and FeF_2. The homogeneously mixed powder was then compacted into rectangular pellet and sealed inside an evacuated quartz tube. The sealed quartz tube was then heat treated at 370 °C for 5 h. The powder sintered at 370 °C was used as a precursor for the synthesis of Sm1111 bulk samples. The precursor powder was again ground using an agate mortar and pestle in order to make a fine and homogeneous mixture. This homogeneous mixture was again pelletized under a pressure of 500 MPa with dimensions of 15 × 5 × 2 mm^3. The intermediate grinding and pressing helps to enhance the reactivity between the *in situ* formed binaries and also to obtain dense pellets. Moreover, since the pre-processed precursor is given an intermediate grinding before the final heat treatment, the metallic particles fully disperse in the matrix and hence do not agglomerate or fuse together; but only increases the reactivity. The pellets were placed in evacuated sealed quartz tubes. The sealed tubes were then subjected to final heat treatment at 850 °C for 50 h in a programmable muffle furnace. No partial melting or globule formation is found during the processing. The second stage processing at 850 °C for 50 h using the second category of precursor yielded clean, black and dense rectangular pellets.

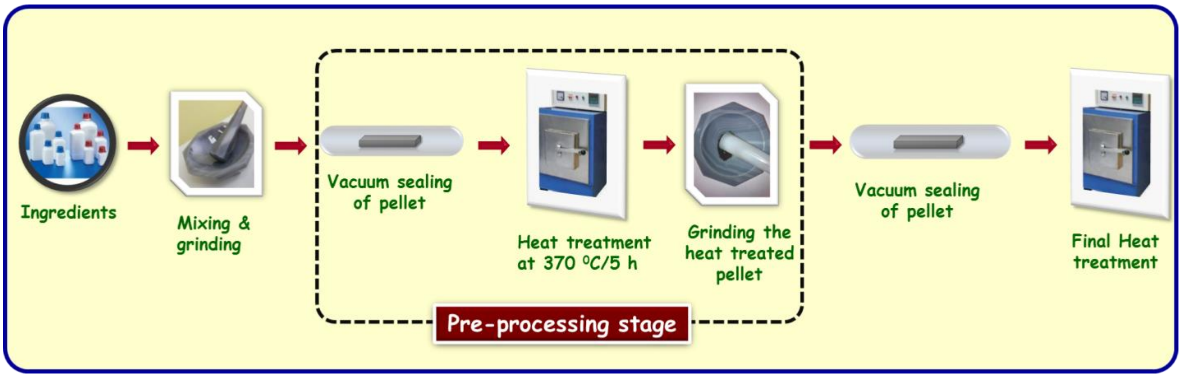

Figure 4.3: Process for preparation of Sm1111 bulk samples used in the present study

In short, the pre-processing of the reaction mixture at an optimized temperature range of 360-380 °C has probably yielded a precursor having the right phase assemblage and good reactivity and that may be the main reason for achieving good quality Sm1111 samples at a relatively low temperature as low as 850 °C. It is to be also noted that the samples subjected to the second stage heat treatment are not wrapped with any expensive metallic foil as has been usually done for the two step process, yet clean pellets devoid of any reaction with quartz tube have been obtained. Apart from the bulk sample preparation, this synthesis route can also be a solution for the major obstacle, i.e. reaction of the sheath metal with the reaction mixture especially with the RE and As, in the development of iron pnictide wires (Zhang *et al.* 2010). Since the pre-processed precursor does not have any free RE or As, their reactivity with the sheath material will be drastically reduced and hence there is a great scope for using inexpensive metals in the fabrication of iron pnictide wires.

4.2 Studies on the effect of F variation on Sm1111 synthesized by the pre-processing route

4.2.1 Introduction

Superconductivity of 1111 type iron pnictides can be enhanced by either fluorine doping at oxygen site or by the creation of oxygen deficiency. In the case of Sm1111 system the transition temperature (T_C) reaches up to 55 K in high pressure synthesized oxygen deficient samples ($SmFeAsO_{0.85}$) and $SmFeAsO_{1-x}F_x$ prepared by the high temperature high pressure method (Ren(a) *et al.* 2008b; Yang(b) *et al.* 2009). The undoped material SmFeAsO shows an anomaly in both resistivity and magnetic transition as a result of origin of SDW and structural phase change. The spin density wave and the phase transition are suppressed, and superconductivity emerges with increasing F doping. Systematic characterizations for evolution of the superconductivity and SDW and/or structural transition with F doping are important for understanding the underlying physics. In this section, the effect of F variation on the structural and superconducting properties of Sm1111 system, synthesized through the pre-processing route, is presented.

4.2.2 Experimental details

Samples with nominal compositions of $SmFeAsO_{1-x}F_x$ (x = 0, 0.1, 0.2, 0.3, and 0.4) were synthesized by the pre-processing route as described in the preceding section. The samples with fluorine content x = 0, 0.1, 0.2, 0.3 and 0.4 are labeled as Sm0, Sm1, Sm2, Sm3 and Sm4 respectively. The phase identification of the samples was performed using an x-ray diffractometer (Philips X'Pert Pro) with CuKα radiation employing a proprietary high speed detector and a monochromator at the diffracted beam side. Microstructural examination was done using a scanning electron microscope (JEOL JSM 5600LV). Superconducting transport measurements such as resistivity versus temperature (ρ-T) and current versus voltage (I-V) were carried out using a closed-cycle cryocooler integrated-cryostat by *dc* four-probe technique. The temperature dependence of *ac* susceptibility (χ-T) was measured using a closed-cycle *ac* susceptometer. The temperature of the sample was precisely controlled and monitored using two temperature controllers (Lakeshore-340&332) employing DT-670B-CU sensor. The *dc* magnetic measurements were carried out by physical property measurement system on parallelepiped shaped samples having a size of about 4 × 2 × 2 mm^3.

4.2.3 Results and discussion

Figure 4.4 shows the XRD patterns of Sm1111 samples with fluorine content x = 0, 0.1, 0.2, 0.3 and 0.4 (Sm0, Sm1, Sm2, Sm3 and Sm4). Analysis of the patterns reveals that all samples contain $SmFeAsO_{1-x}F_x$ as the major phase confirming the formation of iron pnictides at temperatures as low as 850 °C. All the major peaks can be well indexed based on the tetragonal ZrCuSiAs type structure with the space group *P4/nmm*. The parental compound (Sm0) contains small quantities of FeAs along with the major phase. In addition to the main phase and FeAs, the fluorine doped samples also contain SmOF which increases with increase in the nominal composition of fluorine, while FeAs remains almost unchanged. Semi-quantitative phase analysis of the samples was also done from the XRD data using the formula; vol.% of phase X = (ΣIntegrated peak intensities of phase X)/(ΣIntegrated peak intensities of all phases), and the results are given in Table 4.1. It is seen that the sample Sm0 contains Sm1111 phase as high as 92.9 vol.% while presence of secondary phases such as SmOF and FeAs reduces the volume fraction of Sm1111 phase in the fluorine doped samples. These secondary phases are normally observed even in samples processed at temperatures above 1150 °C (Ren(a) *et al.* 2008b; Martinelli *et al.* 2008; Yang(b) *et al.* 2009) and in the present case the volume fraction of these phases are comparable to those synthesized at higher temperatures.

Lattice parameters of the samples (*a* and *c*) can be calculated from the XRD pattern using the formula $\frac{1}{d^2} = \frac{h^2+k^2}{a^2} + \frac{l^2}{c^2}$, since all the samples have tetragonal symmetry at room temperature. The variation of lattice parameters with respect to nominal F content is plotted in Figure 4.5(a). It is noticed that both the *a* axis and *c* axis parameters decrease systematically with increase in concentration of F. Replacing O^{2-} with F^- brings extra electron carriers and disorder into the Fe-As layer. This reduces the coulomb repulsion between the FeAs layer and SmO layer. Moreover, the ionic size of F^- is smaller than that of O^{2-}. The reduction of lattice values is reflected in the XRD pattern as a right shift of the main peak (*102*) as shown in Figure 4.5(b). The peak position shifts gradually to right from Sm0 to Sm4.

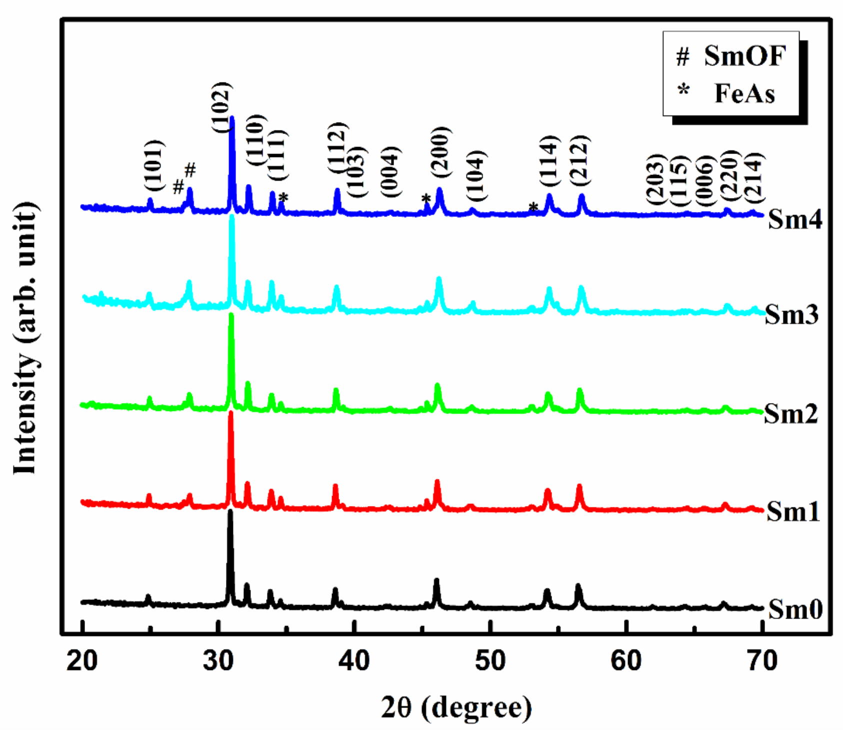

Figure 4.4: XRD patterns of the Sm1111 samples with different doping levels of fluorine. The peaks of Sm1111 are indexed

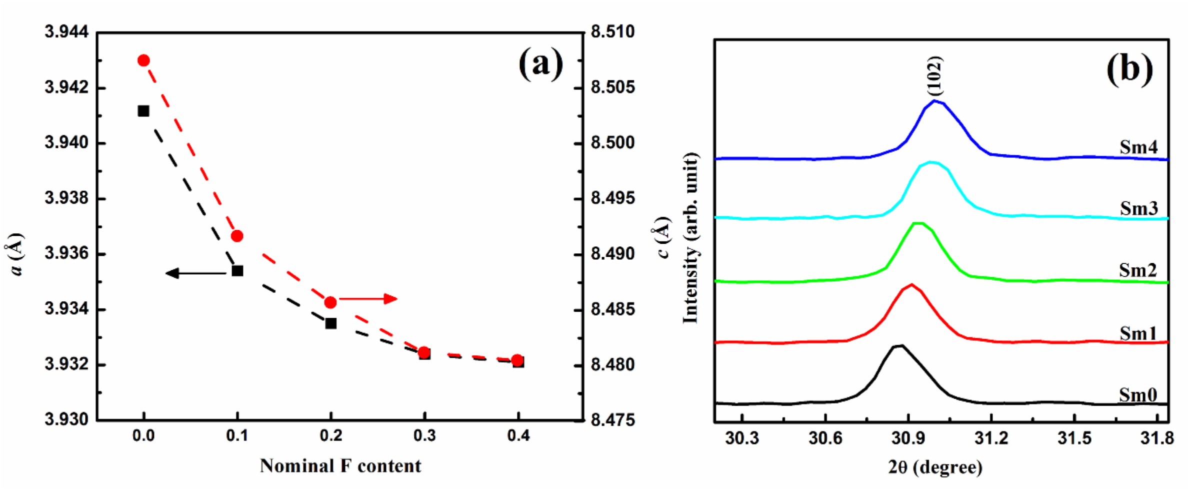

Figure 4.5: (a) The variation of lattice parameters with respect to F content (b) an enlarged view of the main peak (*102*) of XRD pattern

Table 4.1: Phase analysis of F doped Sm1111 samples

Sample name	**Vol.%. of phases**		
	Pure	**SmOF**	**FeAs**
Sm0	92.9	0	7.1
Sm1	84.6	6.5	8.9
Sm2	83.3	8.1	8.6
Sm3	80.7	10.4	8.9
Sm4	80.6	10.3	9.1

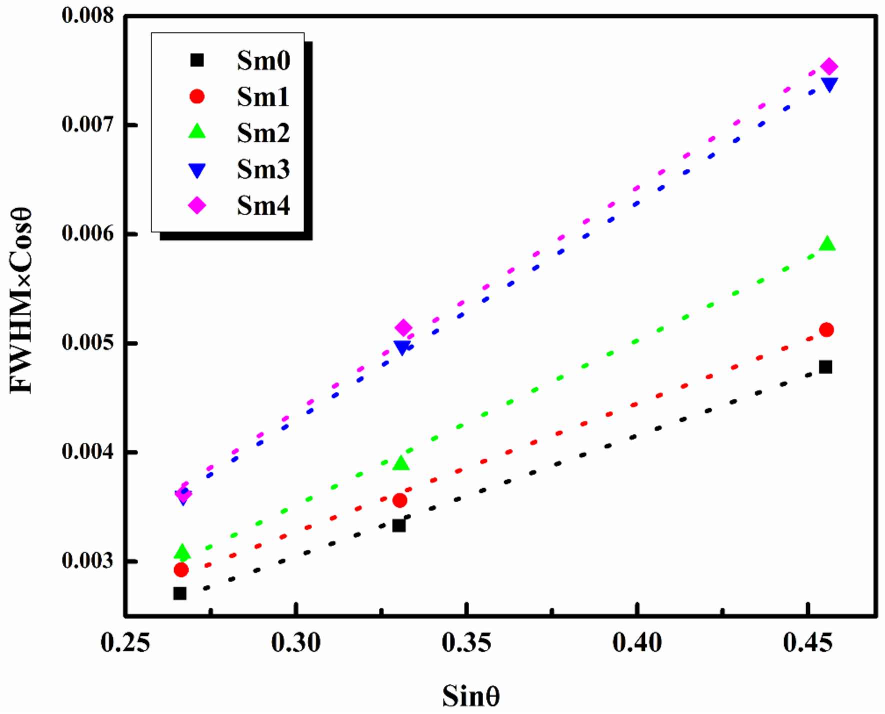

Figure 4.6: Williamson-Hall plots of the (*102*), (*112*) and (*114*) planes for the Sm1111 samples with different F doping levels and the dashed lines represent the linear fits to the data points

Figure 4.6 shows the Williamson-Hall plots of the (*102*), (*112*) and (*114*) planes for the Sm1111 samples with different F doping levels and the dashed lines represent the linear fits to the data points. The slope of FWHM × *cosθ* versus *sinθ* gives the lattice strain within the system and it was observed that the slope of the plot increases with increase in the F doping level. This is due to the strain developed within the system by the substitution of fluorine at oxygen site.

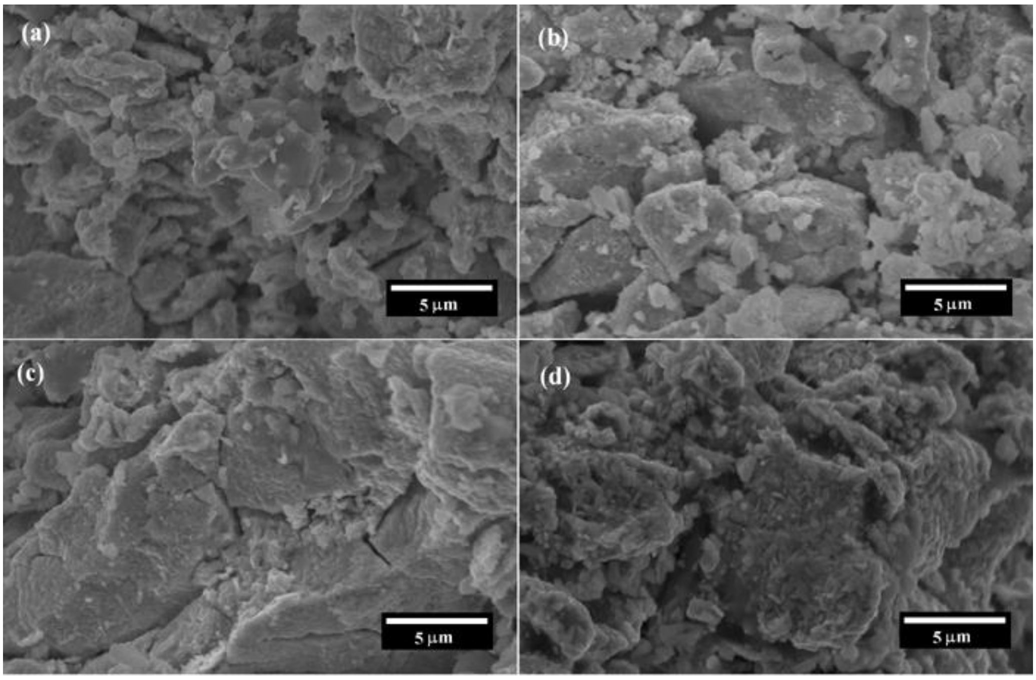

Figure 4.7: SEM images of the fractured surfaces of (a) Sm1, (b) Sm2, (c) Sm3 and (d) Sm4

The microstructural analysis of all the fluorine doped samples was performed using SEM. Figure 4.7 shows the SEM images of freshly fractured surfaces of Sm1, Sm2, Sm3 and Sm4 pellets respectively. The images show that the microstructure is almost homogeneous with some voids. An improvement in grain size and a decrease in porosity can be observed as the fluorine content increases from Sm1 to Sm3. However, the sample Sm4 which has maximum fluorine content exhibits slightly higher porosity and lesser grain size compared to Sm3. Thus, it can be inferred that the microstructure of the samples improved with F doping up to an optimum doping concentration of x = 0.3. Further, the elemental analysis of the samples was done by the energy dispersive x-ray (EDS) analysis equipped with the SEM. A typical EDS of the sample Sm3 is given in Figure 4.8. It shows the presence of only Sm, Fe, As, O, and F, without any other foreign elements. The peaks corresponding to Cu and C are due to the carbon coated Cu sample grid.

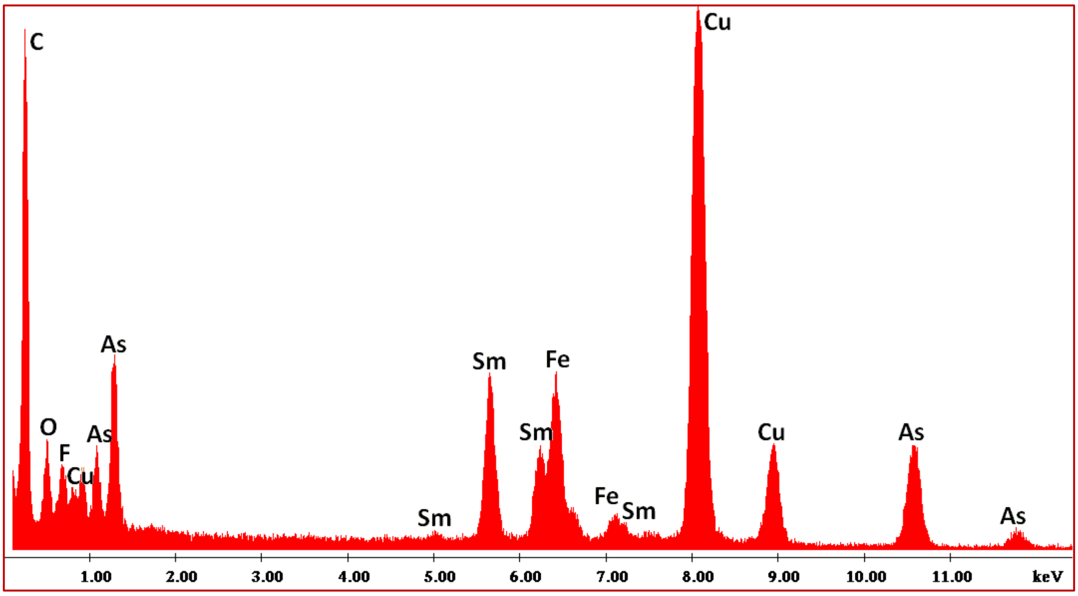

Figure 4.8: EDS analysis of the sample Sm3

Figure 4.9 shows ρ-T plots for the pure and fluorine doped samples. The temperature dependence of resistivity shows exactly similar characteristics as the previous reports (Yang(b) *et al.* 2009; Liu(b) *et al.* 2008). An anomalous peak associated with structural transition and spin density wave instability is observed around 150 K in Sm0 (Yang(b) *et al.* 2009; Liu(b) *et al.* 2008; Margadonna *et al.* 2009). But fluorine doping leads to a gradual suppression of the anomalous peak and its shifting to lower temperatures. The resistivity in the anomalous region drops for Sm1, but still there exists a trace of the anomaly. The substitution of fluorine for oxygen introduces charge carriers into the Fe-As layers and suppresses the phase transition. The anomalous behavior of the ρ-T plot is completely suppressed in the samples with $x \geq 0.2$ and the normal state resistivity of samples decreases with decrease in temperature up to the emergence of superconductivity. A T_{Conset} of 55.3 K is obtained for Sm4. Such high transition temperatures have already been reported for this system processed above 1160 °C, but we could achieve the same at 850 °C. The T_{Conset} of samples Sm0, Sm1, Sm2 and Sm3 are found to be 20.1, 38.1 and 53.4 K respectively. An enlarged view of the ρ-T plot around T_C is given in the inset of Figure 4.9. The $T_{Coffset}$ of Sm1 seems to be below 12 K which is beyond the limit of the measurement system. Therefore, the ΔT_C has been measured only for Sm2, Sm3 and Sm4 which is given in Table 4.2. The residual resistivity ratio (RRR = ρ_{300}/ρ_{60}) estimated for all the superconducting samples is included in Table 4.2. These RRR values are lesser than La1111 system indicating stronger impurity scattering similar to previous reports (Sefat *et al.* 2008c).

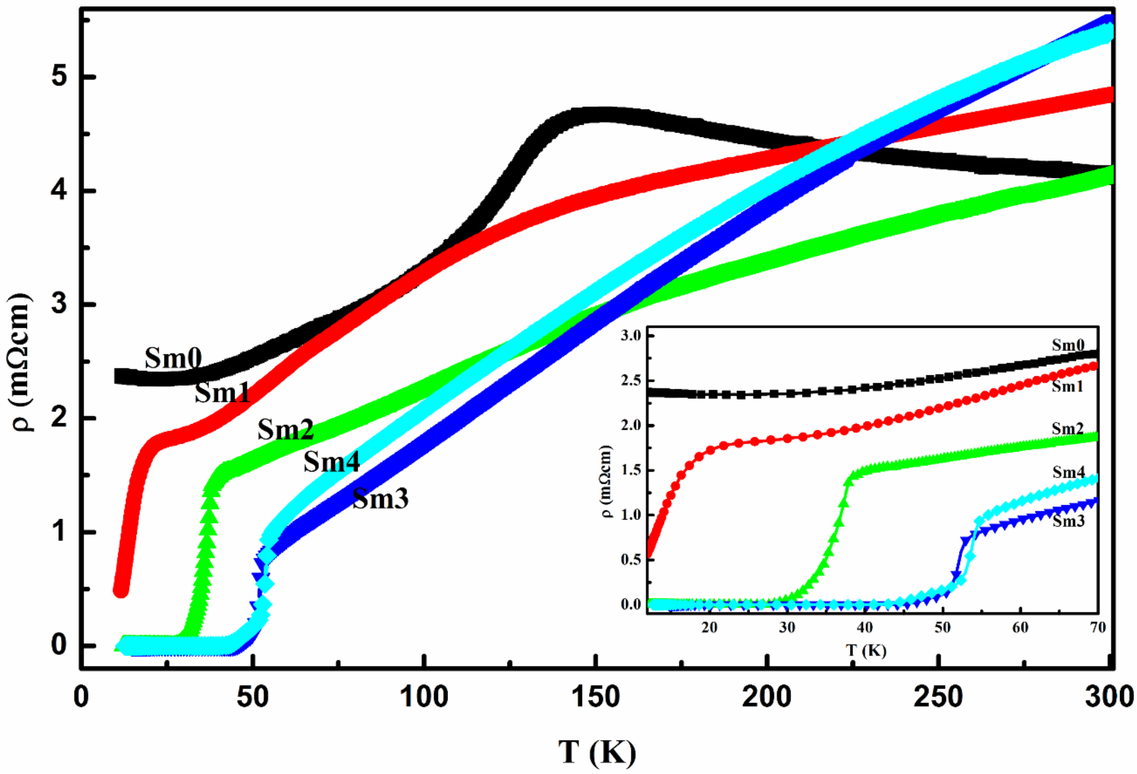

Figure 4.9: ρ-T plots for various fluorine doped samples. Inset shows an enlarged view around T_C

Table 4.2: Different parameters observed for Sm1111 with different fluorine contents

Sample name	T_C (K) from		ΔT_C (K)	RRR	I_C (A)	J_C (A/cm^2)
	ρ-T	χ-T				
Sm0	-	-	-	-	-	-
Sm1	20.1	18	-	1.98	-	-
Sm2	38.1	35	5.7	2.34	7.3	182
Sm3	53.4	51.3	4.3	5.51	30.1	752
Sm4	55.3	52	7.2	4.66	19.8	495

In order to determine the current carrying capacity of the samples, we measured the self-field transport I_C using a criterion of 1 µV/cm from *I-V* characteristics. The transport J_C values at 12 K for all the samples are listed in the Table 4.2 which shows that J_C is maximum for Sm3 having a doping concentration of x = 0.3. A J_C value of 752 A/cm^2 is obtained for that sample. The J_C of Sm4 sample which exhibited the highest T_C is found to be lower (495 A/cm^2) than Sm3. The *I-V* plot for the F doped samples is shown in Figure 4.10. The increased grain size and reduced porosity as observed from SEM are presumed to be the reason for the higher J_C value in Sm3 compared to Sm4, though the latter exhibits higher T_C.

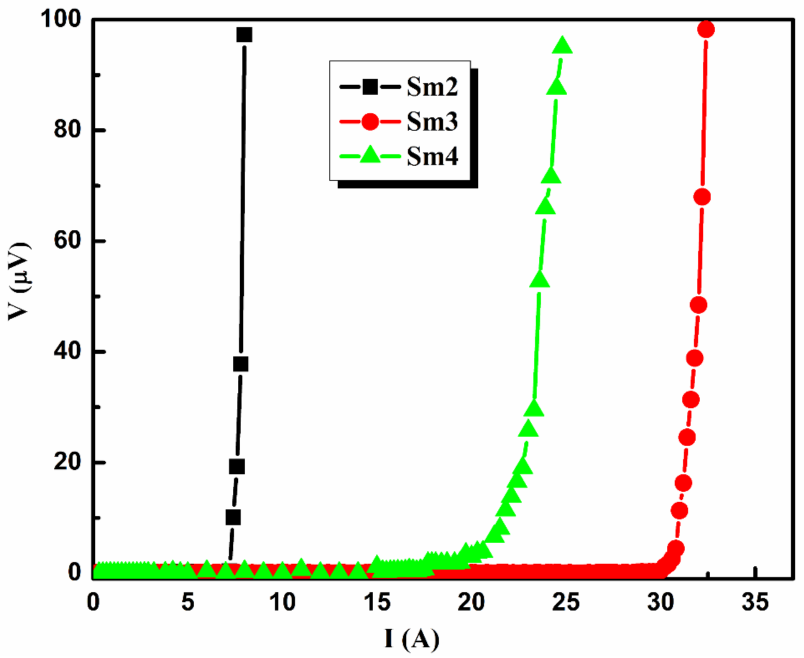

Figure 4.10: *I-V* plots of samples Sm2, Sm3 and Sm4

The *ac* susceptibility versus temperature (χ-T) plots of the F doped samples measured at an *ac* frequency, $f = 208$ Hz and *ac* field, $H_{ac} = 0.49$ mT are shown in Figure 4.11 (in figure both χ' and χ'' have been normalized with χ'_{max} and χ''_{peak}). The transition temperatures were also determined from *ac* susceptibility measurement (χ-T). In addition to this, the χ-T measurement gives information about the granular nature of the samples. For a granular superconductor, the contribution of magnetic response at high temperatures is mainly from the individual grains which are electrically disconnected from each other. But at lower temperatures, the connections between the neighboring grains become superconducting and thus the bulk superconductivity becomes relevant. The real and imaginary parts of the *ac* susceptibility ($\chi = \chi' + i\chi''$) represent two complementary aspects of flux dynamics of a superconductor. A sharp decrease in the real part χ', just below the critical temperature T_C, is a consequence of diamagnetic shielding and a peak in the imaginary part χ'' represents energy losses due to the dissipative phenomena associated with the vortex motion inside the sample. The T_C values obtained from the χ-T plots are given in Table 4.2, which is in agreement with those obtained from ρ-T plot. In the χ-T plot of Sm3, one can easily distinguish a double step in the real part of χ-T. A double step in χ' accompanied by two peaks in χ'' is a known feature of a granular magnetic response of high temperature superconductors. This is also consistent with the previous reports on iron oxypnictides (Polichetti *et al.* 2008). The step near T_C is due to the superconducting grain shielding, while that at lower temperature is due to the intergrain shielding. In this case, one expects a near T_C peak in χ'', which occurs when the *ac* field penetrates just to the center of grains, and a lower temperature peak corresponding to complete penetration of the *ac* field in the weak-link matrix. In the present study, corresponding to the low temperature step, there is a well-defined peak in the imaginary part of χ-T at a characteristic temperature T_P, while the expected near-T_C peak is not well resolved. It is well accepted that inhomogeneous superconductors also exhibit such features and this has been discussed for Sm1111 as well (Zhang(a) *et al.* 2010; Yamamoto *et al.* 2011). Hence, the observed extended diamagnetic transition along with the double step feature can be considered as a combined effect of the presence of secondary phases and the electromagnetic granularity of the sample.

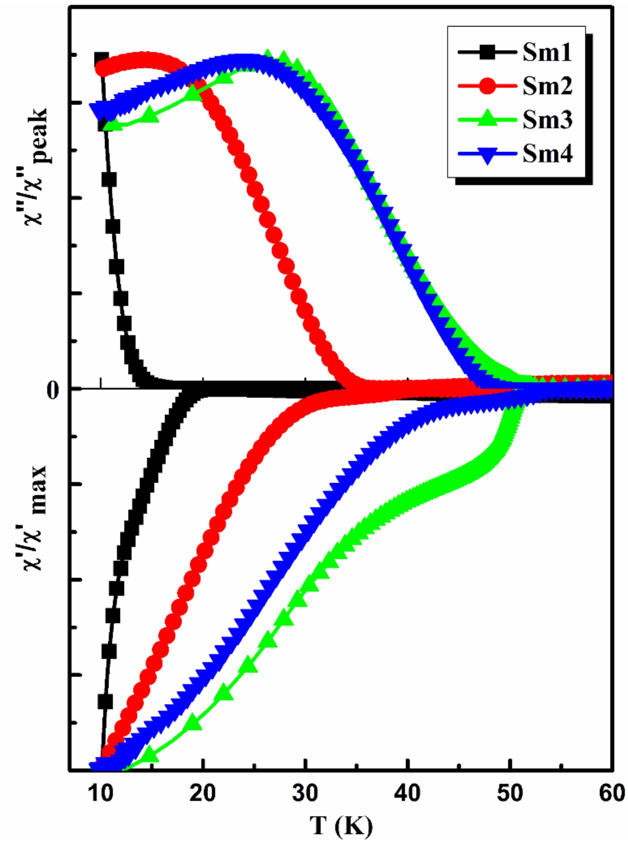

Figure 4.11: Normalized χ-T plots of F doped Sm1111 samples

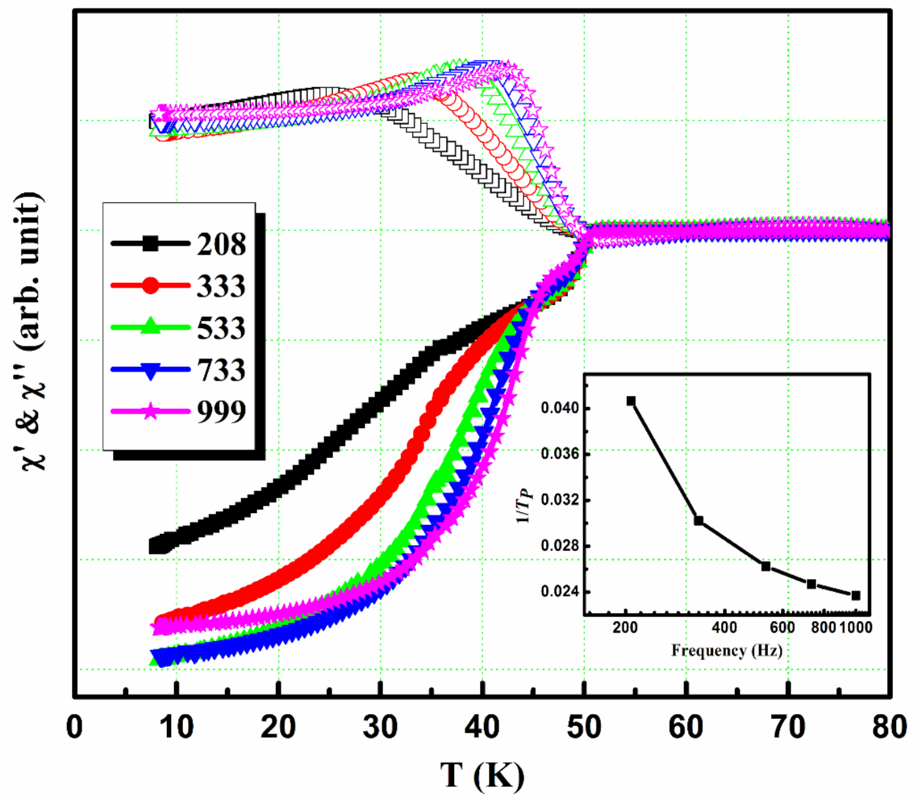

Figure 4.12: χ-*T* plots of the sample Sm3 at different frequencies of *ac* signals. Inset shows the dependence of 1/T_P with frequency

Figure 4.12 shows the χ-T plots of the sample Sm3 at various *ac* frequencies and at a fixed *ac* field. The frequencies chosen are 208, 333, 533, 733, and 999 Hz at a fixed H_{ac} = 0.49 mT. Both the real and imaginary parts of the sample show frequency dependence. In the real part the step height decreases with increasing frequency, still the diamagnetic onset transition temperature remains the same irrespective of the frequency. The peak position of the imaginary part (T_P) shifts to the right and the peak height increases with increasing the frequency of *ac* signal. The right shift of T_P is an indication of decrease in the amount of magnetic flux penetrating the superconductor with increasing frequency. The strong frequency dependence of both the height and the position of the χ'' peak has been interpreted in the framework of different models. In the framework of Muller's model (Müller, K. H. 1990), the frequency dependence is ascribed to effects of magnetic relaxation during the *ac* cycle and it is taken into account by considering flux creep effects with in the sample. The shift in peaks with the increase in frequency is due to the insufficient time for intergranular vortices to relax and penetrate into the superconductor during each cycle. For complete penetration of flux lines, the pinning force density between the grains is to be weakened. This is possible only when the temperature increases and hence the peak temperature, T_P, increases with increase in frequency. In the present case the observed peak is much higher which cannot be explained using flux creep alone. The strong frequency dependence of T_P is also observed in YBCO samples at H_{ac} > .075 mT that can be explained by thermally activated flux creep model (Nikolo *et al.* 1989). This behavior can be interpreted by an Arrhenius rate equation $f = f_0\exp(-U/k_BT)$, where f_0 is an attempt frequency and U is the activation energy for flux creep. The exponential dependence of $1/T_P$ with frequency is given in the inset of Figure 4.12.

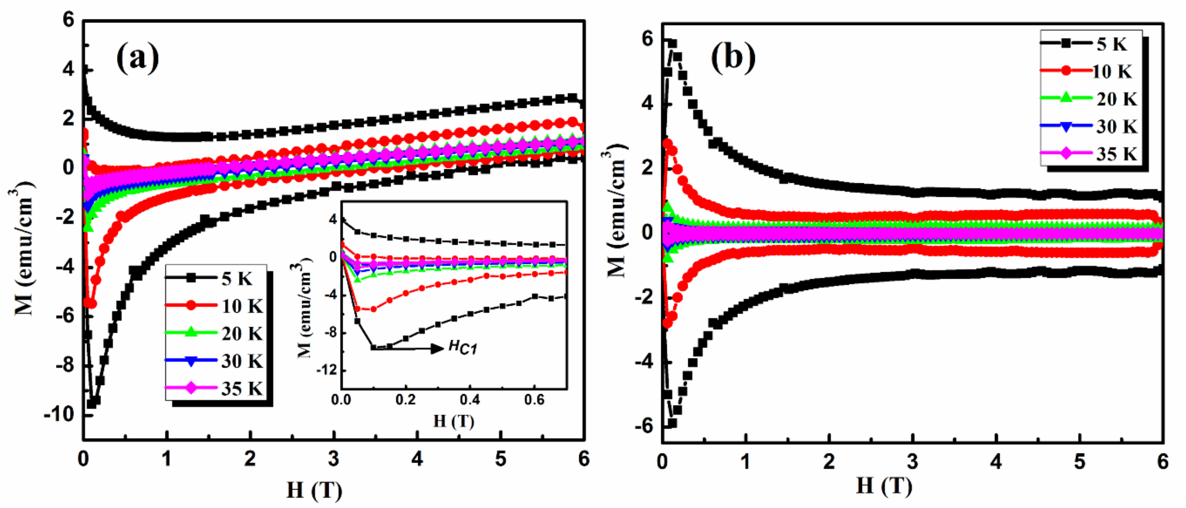

Figure 4.13: (a) *M-H* loop of the sample Sm3 at different temperatures *T* = 5, 10, 20, 30 and 35 K and (b) paramagnetic background subtracted *M-H* loop for the sample Sm3 at *T* = 5, 10, 20, 30 and 35 K. Inset of figure (a) shows an enlarged view of *M-H* loop in the low field region

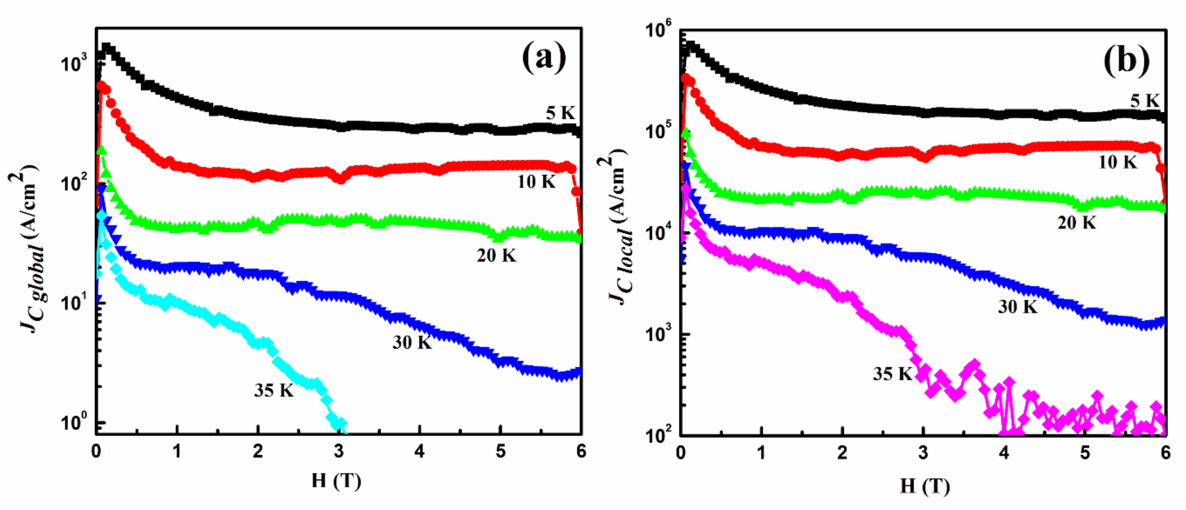

Figure 4.14: Magnetic field dependence of (a) global J_C and (b) local J_C of the sample Sm3 at different temperatures *T* = 5, 10, 20, 30 and 35 K derived from *M-H* loop using extended Bean critical state model

The magnetization hysteresis loops (*M-H* loops) of the sample Sm3 measured at different temperatures T = 5, 10, 20, 30 and 35 K are shown in Figure 4.13(a). The magnetization M of the sample is calculated as $M = m/\mathrm{V}$ (emu/cm^3), where m is the measured magnetic moment of the sample having sample dimensions of ~ 4 × 2 × 2 mm^3 and V is the volume of the sample. Initially, with the applied magnetic field the magnetic moment of the sample decreases due to the diamagnetic shielding and then a positive magnetization was produced inside the sample after a particular low field. This positive magnetization results from the magnetic flux penetration through the sample and the field at which the magnetization starts increasing can be taken as the lower critical field (H_{C1}) of the sample. Inset of Figure 4.13(a) shows an enlarged view of *M-H* loop in the low field region. An H_{C1} of around 0.1 T was obtained for the sample Sm3 at 4.2 K. The sample also showed asymmetric *M-H* loop with respect to the field axis. It is to be noted that all the *M-H* curves have a slight positive slope with increasing field. Such a slope is often related to the presence of combined effect of paramagnetic moment of Sm^{3+} ion and magnetic impurity phases present in the sample. This paramagnetic background observed in all curves can be well fit by a Langevin expression (Tarantini *et al.* 2008). According to this, the mean value of the two branches of *M-H* loop represents the paramagnetic magnetization, $M_P = (M^+ + M^-)/2$ plus the small reversible magnetization of the vortex lattice. This paramagnetic magnetization was deducted from the experimentally obtained *M-H* loops and the paramagnetic background subtracted *M-H* loops for the sample Sm3 at T = 5, 10, 20, 30 and 35 K are shown in Figure 4.13(b).

The sample Sm3 shows quite large hysteresis loop width ($\Delta M = M^+ - M^-$) compared to existing reports which implies either strong flux pinning and/or good intergranular coupling (Senatore *et al.* 2008; Yamamoto *et al.* 2008a). With applied magnetic field, the *M-H* loop width decreases up to around 2 T at 5 K, after that the width remains constant even up to the field of 6 T without any indication of decreasing the width of the hysteresis loop. This indicates that the Sm1111 based superconductors are capable of maintaining the J_C even at very high fields. The rapid decrease in the wide hysteresis loop width with external magnetic field in the low field region is a typical behavior for granular superconductors. The granularity of the samples was also studied by *ac* magnetic susceptibility measurements and has been discussed in this section. The granular behavior is related to the weak link of the grain boundaries which is extremely sensitive to the magnetic field. The width of superconducting loop decreases as temperature increases; consistent with the usual behavior of critical current density of a granular superconductor. At 30 K, the width of the superconducting gap is much smaller than that at 5 K in the same field. In addition, the rate of decrease of loop width with applied magnetic field increases with increasing temperature. Hence, the magnetic properties of the samples are more sensitive to the magnetic field at higher temperatures.

The magnetization loop width (ΔM) is related to the critical current density (J_C) of a superconductor and J_C can be calculated from the M-H loops using the extended Bean critical state model (Bean, C.P. 1962). For granular superconductors, the magnetization hysteresis convolutes contributions from both intergranular and intragranular current flow. The sample contains a large array of grains and grain boundaries through which the current can flow. Application of a magnetic field to these polycrystalline samples sets up screening currents both within grains and on a macroscopic scale. Consequently, the irreversible magnetic moment ΔM is a direct measure of these screening currents. Assuming if current flows uniformly over the whole sample, then the global critical current density can be calculated as $J_{Cglobal} = 20\Delta M/\mathrm{a}(1 - \mathrm{a}/3\mathrm{b})$, where a and b are the dimensions of the sample in cm perpendicular to the magnetic field with a < b. Figure 4.14(a) shows the global J_C of the sample Sm3 at different temperatures derived from the M-H data. A J_C value of 1.4×10^3 A/cm^2 was obtained for Sm3 in the low field region at 5 K. But, the J_C drops drastically with the increase of the applied field (from 0 to 2 T), which illustrates that the grain boundaries have weak-link behavior for the granular Sm3 sample. However, it becomes stable over a wide range of applied magnetic field from 2 to 6 T and temperature < 20 K. For weakly coupled polycrystalline samples flux penetration occurs preferentially at grain boundaries, pores or non-superconducting second phases at lower fields. At higher field, the grain boundary pinning becomes weak and magnetic flux starts to penetrate into the grains. Almost constant J_C value in the high magnetic field range is an indication of strong flux pinning within the grains of the sample. This superior $J_C(H)$ behavior is a high lighting feature of iron-based superconductors. At high temperature range (30 and 35 K) J_C decreases with applied magnetic field. However, the global J_C evaluated from M-H data are much higher than the transport J_C values measured. This is apparently because the magnetization is dominated by the large contribution of the intragranular currents flowing within the grains which in turn overestimate the J_C value.

The intragrain J_C (critical current density within the grain) was also evaluated on the basis of $J_{Clocal} = 30\Delta M/\langle r\rangle$, $\langle r\rangle$ is the average grain size in cm, after grinding the sample into powder. The average grain size of the sample was determined from SEM image which is about 5 μm. An intragrain J_C of the order of 7×10^5 A/cm^2 was obtained for the Sm3 sample at 5 K in the low field region. J_{Clocal} also reduces with applied field. However, its value is more than 1.5×10^5 A/cm^2 at 5 K and 6 T, and has a very weak dependence on the field. This shows that the sample has a fairly large pinning force within the grain. The defects induced due to fluorine doping enhances the inherent vortex pinning and thereby the intragrain J_C. Both intragrain J_C and intergrain J_C considerably decreases with temperature. At a temperature of 35 K, J_C drops drastically with the increase of the applied field. This shows that the magnetic flux pinning ability has been reduced in the sample at the high temperature. The intragrain J_C obtained is about two orders of magnitude higher than the intergrain J_C. The large difference between intergrain J_C and intragrain J_C is due to the weak link between the grains with in the sample. This weak link behavior is an inherent property of iron-based superconductors.

In short, Sm1111 bulk superconducting samples with $T_C > 50$ K and significant transport J_C of 752 A/cm^2 can be obtained at an optimum fluorine concentration of $x = 0.3$, synthesized at a relatively low temperature of 850 °C under ambient pressure condition by the pre-processing route. An intragrain J_C of the order of 7×10^5 A/cm^2 was also obtained for the optimum doped sample and that exhibits large pinning force within the grain. In order to reduce the wide difference between magnetic J_C and transport J_C, the process needs further refinement in order to enhance phase purity, microstructure and hence the transport J_C.

4.3 Conclusions

$SmFeAsO_{1-x}F_x$ superconducting bulk samples were synthesized at a significantly low temperature of 850 °C by introducing a novel pre-processing step. The samples prepared at such low temperatures and ambient pressure show a T_C of 55.3 K, which has been observed earlier only for samples processed at high temperatures or pressures. Further a transport J_C 750 A/cm^2 at 12 K and magnetic intragrain J_C of 7×10^5 A/cm^2 at 5 K has been measured for the fluorine doped Sm1111 bulk sample. The main advantage is that it is not necessary to afford high temperatures and pressures or expensive sheath materials for the synthesis of iron oxypnictide polycrystalline bulk samples. The synthesis route detailed herein can also help in surpassing the hurdles for the development of other iron pnictide conductors.

CHAPTER 5

EFFECT OF RARE EARTH (RE: Gd, Ce & Y) DOPING AT Sm^{3+} SITE IN $SmFeAsO_{1-x}F_x$ BULK SAMPLES

5.1 Introduction

$SmFeAsO_{1-x}F_x$, a superconductor belonging to the 1111 family of iron pnictides has received considerable attention in the field of superconductivity because of its very high upper critical field of the order of 100 T and a relatively high T_C (Kamihara *et al.* 2008; Chen(c) *et al.* 2008; Senatore *et al.* 2008; Aswathy *et al.* 2008). Experiments were done rapidly to characterize the physical properties of this material and to explore different possibilities for further raising their superconducting properties like T_C, J_C and H_{C2} (Ren(a) *et al.* 2008a; Ren(a) *et al.* 2008b; Wei *et al.* 2008). New insights into underlying physics of high T_C superconductivity are also anticipated since the iron oxypnictides have some similarities to the cuprates with simultaneous existence of a few significant dissimilarities too. La1111 system behaves like MgB_2 in which thermal fluctuations of vortices do not significantly affect their behavior in the presence of strong magnetic fields to a large extent as it happens in the layered cuprates (Fuchs *et al.* 2008). However, the situation is different for Sm1111 system having greater mass anisotropy and enhanced thermal fluctuations (Jaroszynski *et al.* 2008a). Generally, the electronic band structure of the parent iron-based superconductors (REFeAsO, RE - rare earths) is semi-metallic, consisting of hole and electron Fermi surface pockets, separated by a (π, π) wave vector in momentum space (Mazin, I. I. 2010). They have a layered crystal structure belonging to the tetragonal *P4/nmm* space group with alternating FeAs and REO layers in which conductivity occurs mainly in the FeAs layers while the REO layers act as charge reservoirs. Here, the FeAs layer is negatively charged, and REO layer is positively charged. The parent material shows a structural transition with temperature from tetragonal to orthorhombic phase and exhibits spin density wave (SDW) order. Chemical doping in REFeAsO can suppress the structural transition and thereby SDW, leading to superconductivity. The carrier concentration in the FeAs layer increases by the substitution of F^- at O^{2-} site or Th^{4+} at Re^{3+} site and an increase in T_C is achieved by the creation of more carriers in the FeAs layer (Chen(c) *et al.* 2008; Zhigadlo *et al.* 2010). On doping the density of states of the system at the Fermi level was found to increase as the cell volume gets reduced, favoring the T_C enhancement. Both F^- for O^{2-} and Th^{4+} for RE^{3+} substitutions induce electrons as the charge carriers in the FeAs layer. Oxygen deficiency also induces superconductivity; the crystal structure could be significantly modified compared with that of the parent compound, and T_C becomes maximum when the $FeAs_4$-lattices form a regular tetrahedron (Lee(a) *et al.* 2008). Usually, in cuprate based superconductors any change made into the conducting layer (CuO layer) destroys superconductivity; however superconductivity is induced by doping in the FeAs layer of iron pnictides (Awana *et al.* 2010). In short, this system can sustain deliberately done changes in the conducting layer like doping at the Fe site and the creation of As vacancies.

Another key attraction of 1111 family is the versatility of doping at different sites at the same time and thereby regulating the electronic properties of this system. Partial replacement of elements in the reservoir layer with those having different valency or ionic radius causes lattice distortion and modification of crystalline as well as electronic structures. There are reports on doping at rare earth site along with fluorine doping that improves or modifies the superconducting properties of iron pnictides (Yi *et al.* 2008b; Ganguli *et al.* 2010). Majority of the reports show that rare earth site doping was done with an element having smaller ionic radius in order to obtain T_C enhancement. The higher T_C value is attributed to the increased internal chemical pressure from local lattice distortion induced by smaller size dopants.

In this chapter, we have studied the impact of rare earth doping at Sm site in $SmFeAsO_{0.7}F_{0.3}$ superconductor on both its structural and superconducting properties. Elements having both smaller and larger ionic radii compared to Sm^{3+} were chosen for doping. The 4f rare earth element Ce (101 pm), Gd (93.5 pm) on either side of Sm (95.8 pm) and a well-established non-4f element Y (90 pm) were selected as dopants for the study. This chapter is mainly divided into two sections - the first section comprises the doping effect of 4f elements such as Gd^{3+} and Ce^{3+} in Sm1111 system and their impact on both structural and superconducting properties. The effect of Y^{3+}, a non-4f element, doping in Sm1111 is given in the next section of this chapter.

5.2 Experimental details

Conventional solid state method was adopted for the preparation of the samples throughout this work. The materials and method used for each set of samples are described under the corresponding sections. The phase identification of the samples was performed using an x-ray diffractometer (Philips X'Pert Pro) with CuKα radiation employing a proprietary high speed detector and a monochromator at the diffracted beam side. Microstructural analysis of the samples was done using a scanning electron microscope (JEOL JSM 5600 LV). Superconducting transport measurements such as resistivity versus temperature (ρ-T) and voltage versus current (I-V) were carried out using standard *dc* four probe method in a closed cycle cryocooler integrated cryostat. The temperature dependence of *ac* susceptibility (χ-T) was measured using a closed cycle *ac* susceptometer. The *dc* magnetization measurements were carried out by Physical Property Measurement System (PPMS, Quantum Design). The ρ-T variation with applied magnetic fields and Hall Effect measurements were also done in a PPMS (Quantum Design DynaCool) using the four-probe method. The details of characterization techniques used for the samples have been given in Chapter 3.

5.3 Effect of Gd^{3+} and Ce^{3+} doping at rare earth site of $SmFeAsO_{0.7}F_{0.3}$ bulk superconductor

Polycrystalline samples of $Sm_{1-y}RE_yFeAsO_{0.7}F_{0.3}$ (RE = Gd, Ce) were prepared using conventional solid state reaction method under ambient pressure. Powders of Sm, Fe, Fe_2O_3, and As were used as the starting materials (M/s Alfa Aesar, purity 99.9%). For rare earth site doping, pure metal powders of Gd and Ce were used. A nominal stoichiometric composition of $SmFeAsO_{0.7}F_{0.3}$ (Sm3), $Sm_{1-y}Gd_yFeAsO_{0.7}F_{0.3}$ (y = 0.05, 0.1, 0.15, 0.2; named SmGd05, SmGd1, SmGd15, SmGd2 respectively), $Sm_{1-y}Ce_yFeAsO_{0.7}F_{0.3}$ (y = 0.05, 0.1, 0.15, 0.2; named SmCe05, SmCe1, SmCe15 and SmCe2 respectively) were chosen. The ingredients were stoichiometrically weighed and mixed thoroughly to form a homogeneous mixture. All chemical handlings were performed in an argon-filled glove box. The homogeneous mixture was compacted into rectangular pellets having dimensions of $15 \times 5 \times 2$ mm^3, under a pressure of 500 MPa. The pellets were sealed inside evacuated quartz tubes and subjected to the following heat treatment procedure. The samples were pre-processed at a temperature of 360 ºC for 5 h. The pre-processed samples were again ground, pelletized, and sealed in evacuated quartz tubes and sintered at 850 °C for 30 h. In order to obtain dense pellets, the samples were again heat treated at a higher temperature of 1000 °C for 20 h. All the heating procedures were done in a programmable muffle furnace.

5.3.1 Structural properties of the samples

The powder x-ray diffraction pattern of all the samples after heat treatment are shown in Figure 5.1. All the main peaks of the samples can be indexed on the basis of tetragonal ZrCuSiAs type structure with the space group *P4/nmm*. In addition to the main phase, impurity phases of SmOF and FeAs are also present in all the samples. However, no secondary phases corresponding to Gd or Ce or their derivatives could be detected. The volume percentage of SmFeAsO, SmOF, and FeAs was estimated from the XRD data using the formula; vol.% of phase X = (ΣIntegrated peak intensities of phase X)/(ΣIntegrated peak intensities of all phases), and the data is given in Table 5.1. The superconducting volume fraction is found to be about 90% or above for all the samples.

Figure 5.2(a) and Figure 5.2(b) are enlarged representations of XRD pattern around the main peak (*102*). The peak shows a shift in 2θ with doping. The (*102*) peak of Gd doped samples shifts towards the right, whereas that of Ce doped ones displays a left shift with increasing doping content, y. This is of course due to the RE^{3+} (Gd & Ce) doping at Sm^{3+} site. The ionic radius of Gd^{3+} is smaller than that of Sm^{3+}, but the ionic radius of Ce^{3+} is larger with respect to Sm^{3+}. Doping with an element having smaller ionic radius usually gives a lattice parameter contraction, while doping with an element of larger ionic radius displays lattice expansion. Hence, the shift in position of the peaks in XRD pattern depicts the change of lattice parameters with Gd^{3+} and Ce^{3+} dopings at Sm^{3+} site. The lattice parameters were calculated from Rietveld refined x-ray diffraction patterns. The substitution range of the dopants at the Sm^{3+} site in $SmFeAsO_{0.7}F_{0.3}$ system was determined by measuring the change of lattice parameters with nominal content, y. This is an accepted method of determining the extent of substitution due to which the lattice parameters increase or decrease linearly with increasing doping concentration and finally remains constant despite the increment in dopant concentration (Vegard, L. 1921).

Figure 5.3(a) and Figure 5.3(b) show the variation of lattice parameters *a* and *c* with y in $Sm_{1-y}RE_yFeAsO_{0.7}F_{0.3}$ (RE = Gd, Ce). The lattice parameters obtained for the sample Sm3 (y = 0) are *a* = 3.934 Å and *c* = 8.484 Å. In the case of Gd doped samples, both *a* and *c* lattice parameters decrease systematically with nominal increase in dopant concentration by substitution of Gd^{3+} for Sm^{3+}. For y = 0.15, both the lattice parameters reduce to *a* = 3.925 Å and *b* = 8.468 Å, but remain almost constant beyond y = 0.15. This suggests that the solubility limit of the Gd^{3+} ions is reached at y = 0.15 in the $SmFeAsO_{0.7}F_{0.3}$ system. Since the ionic size of Gd^{3+} is smaller than that of Sm^{3+}, the above result confirms the successful substitution of Gd^{3+} at Sm^{3+} site. However, Ce^{3+} doping at Sm^{3+} site results in an elongation of both *a* and *c* lattice parameters. The lattice values increase systematically with nominal increase in dopant concentration (y) and reach *a* = 3.941 Å and *b* = 8.499 Å for y = 0.15 of Ce^{3+} at Sm^{3+} site and remain almost stagnant for y > 0.15. This is reasonable since the ionic size of Ce^{3+} is larger than that of Sm^{3+}.

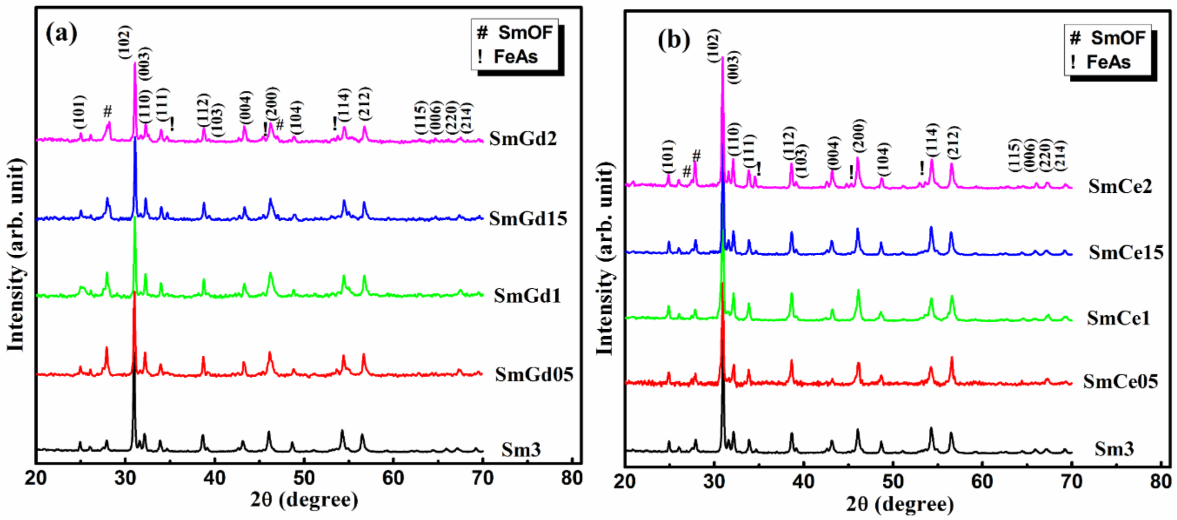

Figure 5.1: XRD patterns of (a) Gd^{3+} doped and (b) Ce^{3+} doped samples

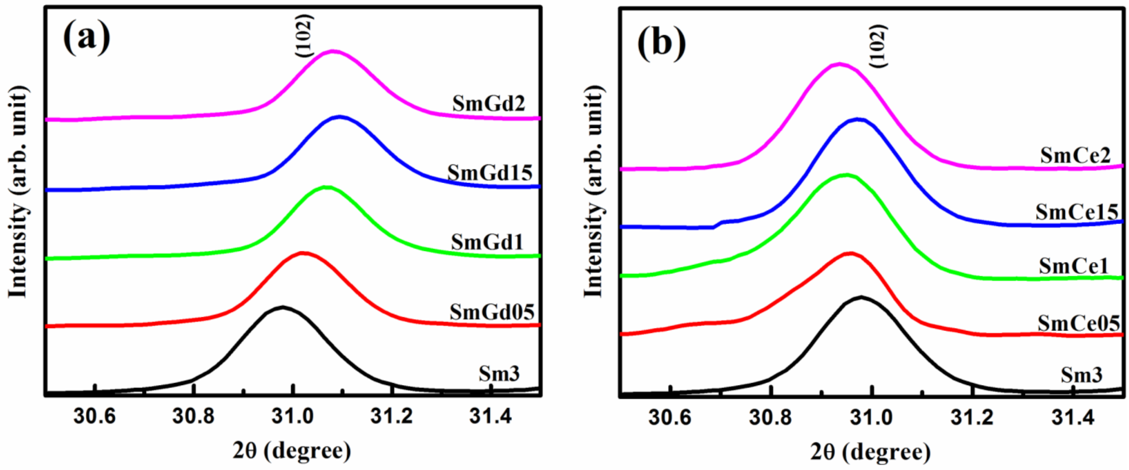

Figure 5.2: Enlarged view of the main peak (*102*) of (a) Gd^{3+} doped and (b) Ce^{3+} doped samples with respect to Sm3

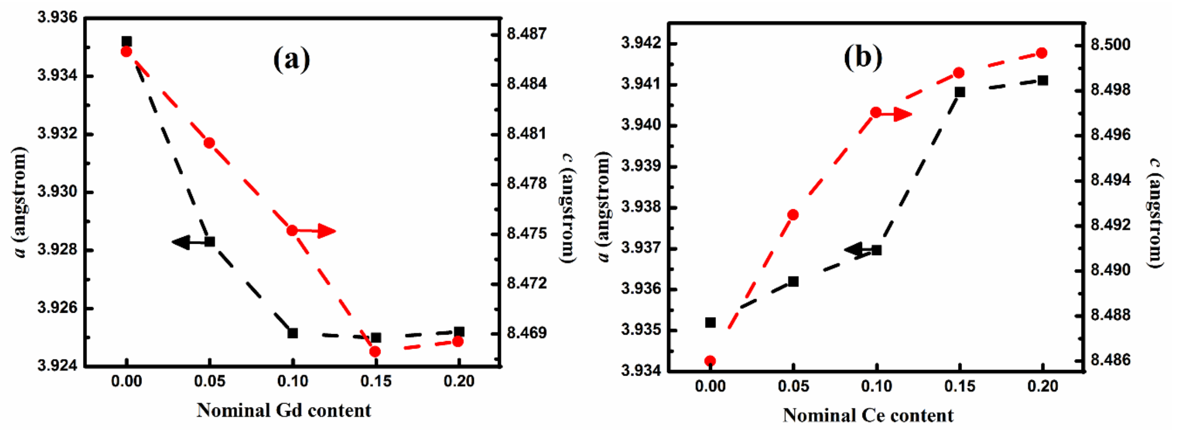

Figure 5.3: Variation of lattice parameters *a* and *c* of the samples $Sm_{1-y}RE_yFeAsO_{0.7}F_{0.3}$ (RE = Gd, Ce) with variation in (a) nominal Gd content and (b) nominal Ce content

Table 5.1: Phase analyses from XRD spectra

Sample Name	**Vol.% of phases**		
	Main Phase	**SmOF**	**FeAs**
Sm3	94.4	4.2	1.4
SmGd05	90.9	7.4	1.7
SmGd1	91.8	6.4	1.8
SmGd15	91.5	6.4	2.1
SmGd2	90.6	7.1	2.3
SmCe05	94.6	4.3	1.1
SmCe1	94.9	4.1	1.0
SmCe15	93.8	4.9	1.3
SmCe2	89.6	7.4	3.0

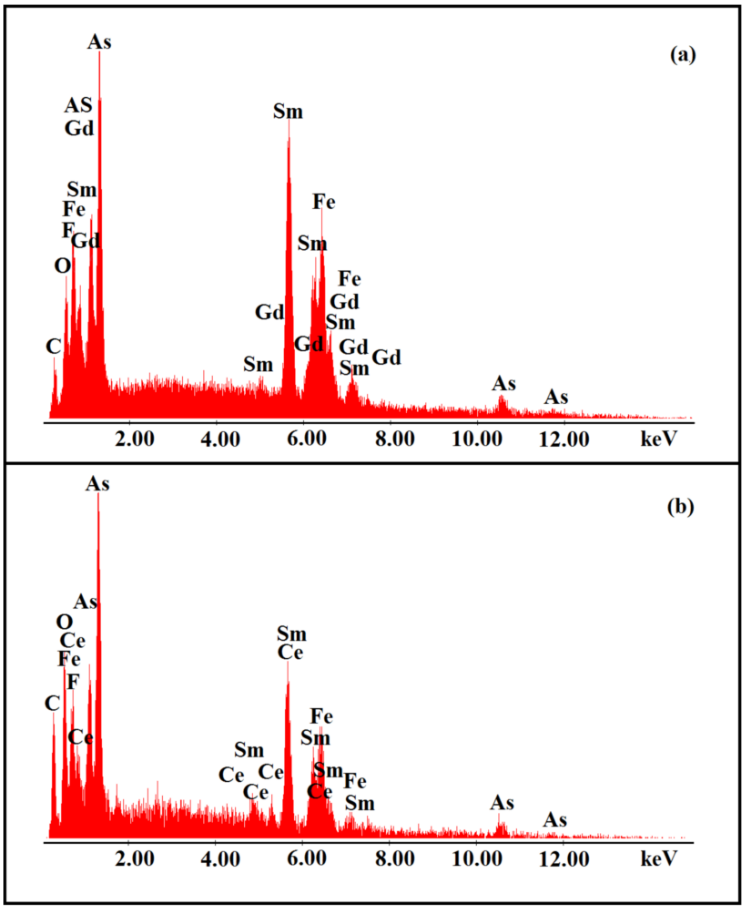

Figure 5.4: EDS spectra of the samples (a) SmGd1 ($Sm_{0.9}Gd_{0.1}FeAsO_{0.7}F_{0.3}$) and (b) SmCe1 ($Sm_{0.9}Ce_{0.1}FeAsO_{0.7}F_{0.3}$)

In order to determine the composition of the samples, we have performed EDS (energy dispersive x-ray analysis) spot analysis on all the samples and typical EDS patterns of Gd^{3+} and Ce^{3+} doped ones (SmGd1 and SmCe1) are shown in Figure 5.4. The C peak observed in the spectra is due to the carbon tape used for sample fixing on the SEM stub. The compositional analysis shows that Fe, As, O and F amounts to a stoichiometry of around 1, 0.9, 0.7 and 0.2, respectively for all the samples. Though the quantification of light weight elements using EDS is not fully reliable, the observations clearly indicate fluorine loss in all the samples. The doped samples contain the presence of Ce and Gd peaks in SmCe1 and SmGd1, respectively. In the EDS spectrum of SmGd1 an overlap of Sm and Gd exists since their energy levels are close enough. Nevertheless, the quantitative Sm and Gd/Ce composition of all the samples evaluated from EDS is given in the Table 5.2. Sm/RE ratio in all the samples is almost equal to the corresponding nominal value. The phase formation and effective doping of Gd/Ce in Sm1111 observed in XRD is thus confirmed using EDS.

Table 5.2: Compositional analyses using EDS spectra

Sample Name	**Sm & Gd\Ce composition from EDS**				**Density (g/cm^3)**
	Sm		**Gd\Ce**		
	Initial	**Final**	**Initial**	**Final**	
Sm3	1.000	0.986	0.000	0.000	4.85
SmGd05	0.950	0.935	0.050	0.044	4.87
SmGd1	0.900	0.869	0.100	0.090	5.32
SmGd15	0.850	0.827	0.150	0.146	5.28
SmGd2	0.800	0.772	0.200	0.194	5.39
SmCe05	0.950	0.927	0.050	0.042	5.33
SmCe1	0.900	0.865	0.100	0.084	5.38
SmCe15	0.850	0.826	0.150	0.118	5.30
SmCe2	0.800	0.793	0.200	0.166	5.28

Significant microstructural variation resulting from both Gd^{3+} and Ce^{3+} doping at Sm site is observed from the SEM images of the samples. Figure 5.5 shows the SEM images of the freshly fractured surfaces of samples Sm3 and selected samples of Gd^{3+} (SmGd1 & SmGd2) and Ce^{3+} (SmCe1 & SmCe2) doped ones. All the samples exhibit a layered flaky morphology, a typical feature of iron pnictides. The pure sample, Sm3 exhibits a mix of layered flaky structure with well-defined edges and occasional granularity present near the voids. With rare earth site doping, these voids get reduced and the sample density increases. The densities of the samples were also calculated using Archimedes' principle and the obtained values are included in Table 5.2. We can see that the co-doping in Sm1111 system increases the density of the samples and their values are getting closer to the theoretical density of iron pnictides (Ding(c) *et al.* 2011). The layered grains are stacked randomly and hence the weak links present at the grain boundaries limit the transport current flow. With Ce^{3+} doping, the microstructure changes from layered flaky nature of pure Sm3 to more granular (Figure 5.5 SmCe1 and SmCe2). It is also observed that higher doping of Ce^{3+} degrades the microstructure (SmCe2 in Figure 5.5). The average grain sizes of the samples were also estimated statistically using software. The grain size of the samples Sm3, SmGd1 and SmGd2 is found to be almost same and is around 3.5 μm. However, smaller grains having size of about 1.8 μm and 1.6 μm are obtained for SmCe1 and SmCe2, respectively.

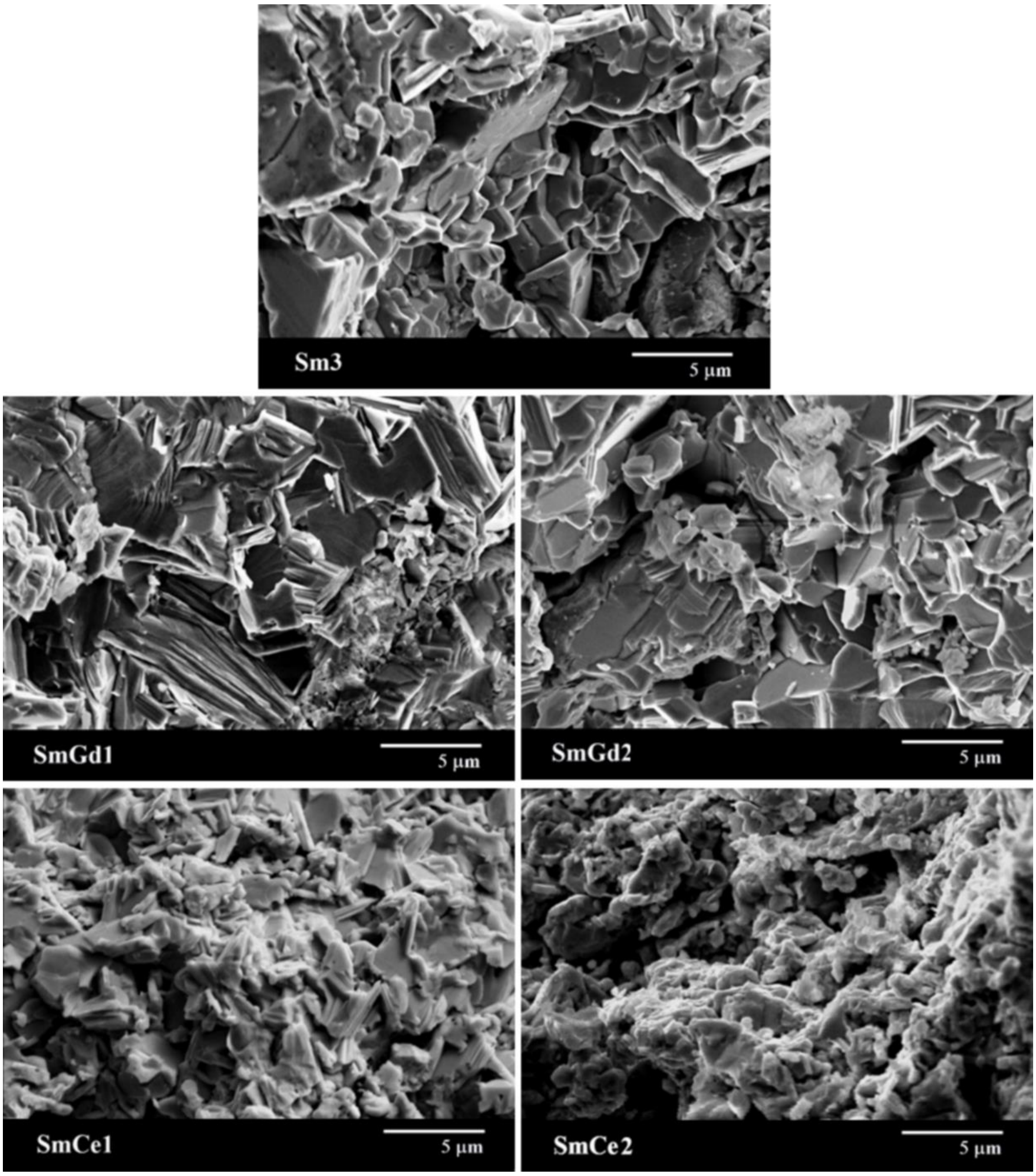

Figure 5.5: SEM images of Sm3 ($SmFeAsO_{0.7}F_{0.3}$) and selected samples from both Gd and Ce doped ones

5.3.2 Superconducting properties of the samples

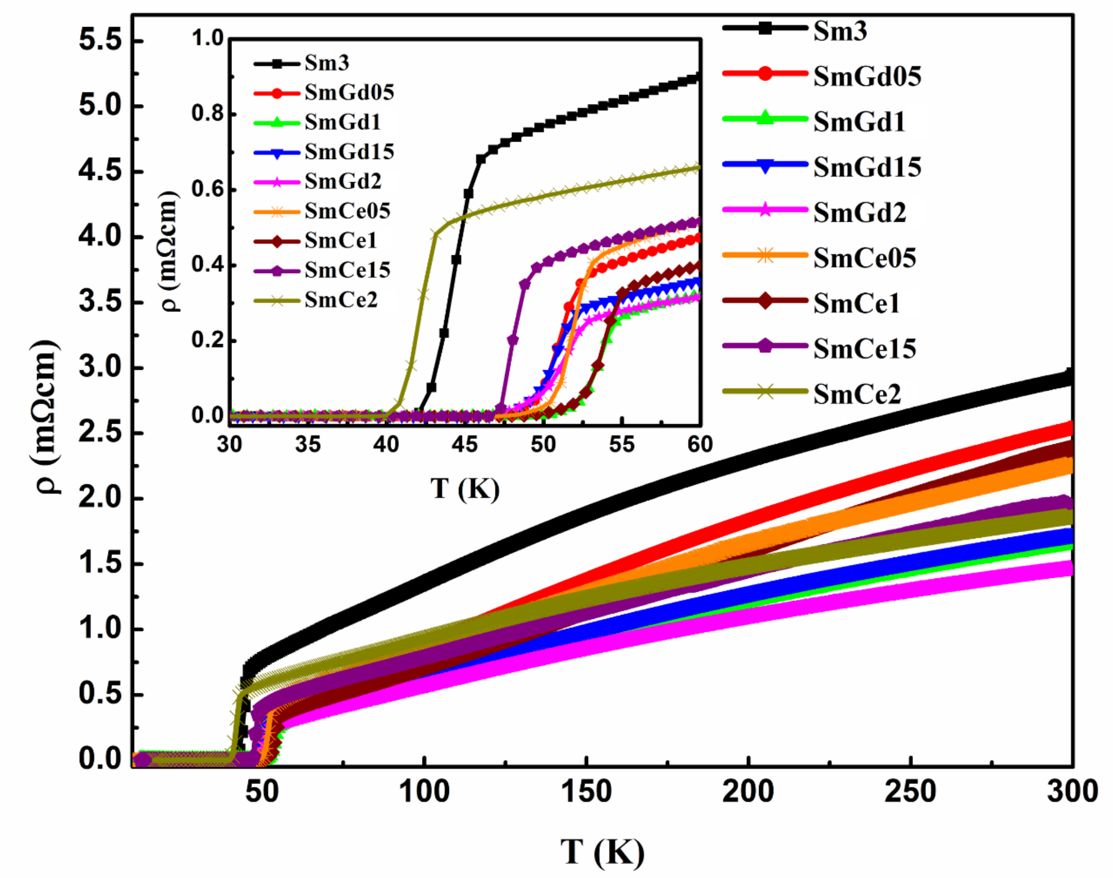

Figure 5.6: ρ-*T* plots of Sm3 ($SmFeAsO_{0.7}F_{0.3}$) as well as Gd^{3+} and Ce^{3+} doped samples; inset is an enlarged view around T_C

Figure 5.6 shows the resistivity versus temperature (ρ-T) plots of $Sm_{1-y}RE_yFeAsO_{0.7}F_{0.3}$ (RE = Gd, Ce) samples at zero magnetic field. The temperature at which resistivity falls sharply is taken as the T_C and the observed T_C values of all the samples are given in Table 5.3. All the samples show rather narrow transitions into the superconducting state at their respective transition temperatures and the sample Sm3 has a T_C at 46 K. But this value is lower than the highest T_C value (~ 55 K) reported for Sm1111 system elsewhere (Ren(a) *et al.* 2008b; Anooja *et al.* 2012). The difficulty in preventing or controlling the volatile loss of fluorine at higher processing temperature could be the main reason behind the reduction in T_C. However, in the present work all the samples i.e. fluorine only doped sample and Ce and Gd co-doped samples were prepared using the same fluorine stoichiometry and all these were synthesized under identical conditions. Therefore, we used $SmFeAsO_{0.7}F_{0.3}$ as the reference sample. It is to be noted that due to the volatile loss of fluorine, the value of F content in all the samples is almost identical and below the optimum level as observed from EDS.

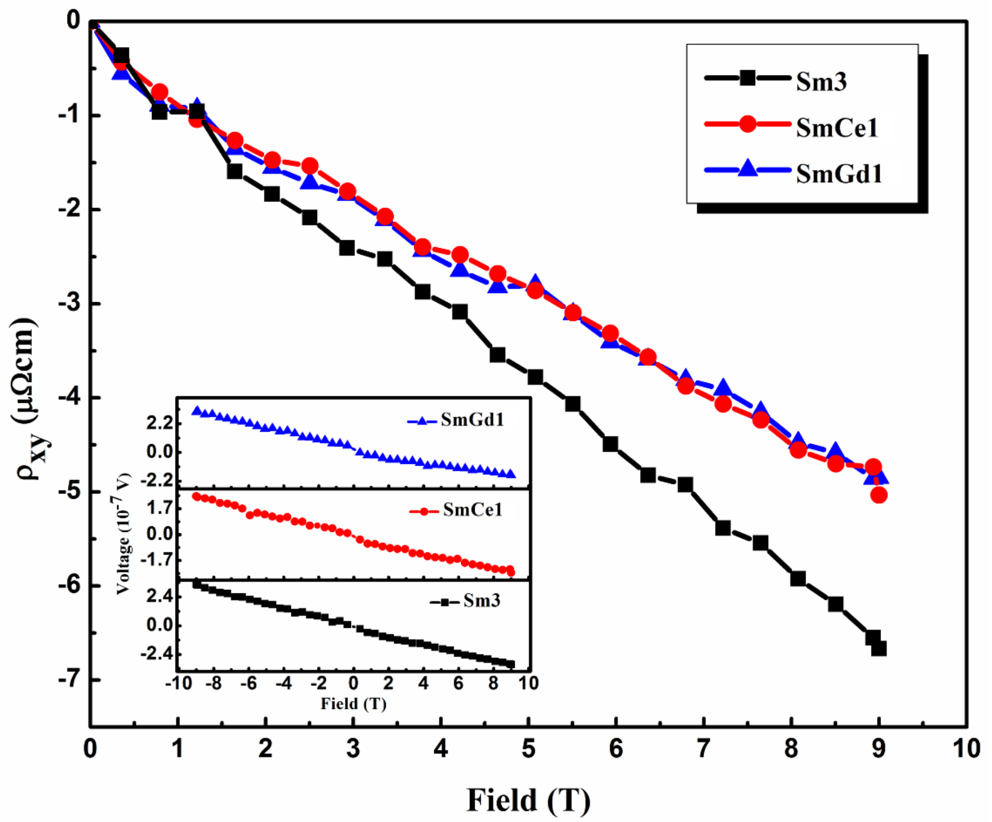

Figure 5.7: Magnetic field dependence of Hall resistivity, ρ_{xy} of the samples Sm3, SmCe1 and SmGd1 measured at 100 K. Inset shows the measured voltage at 100 K by varying the magnetic field from 9 to -9 T

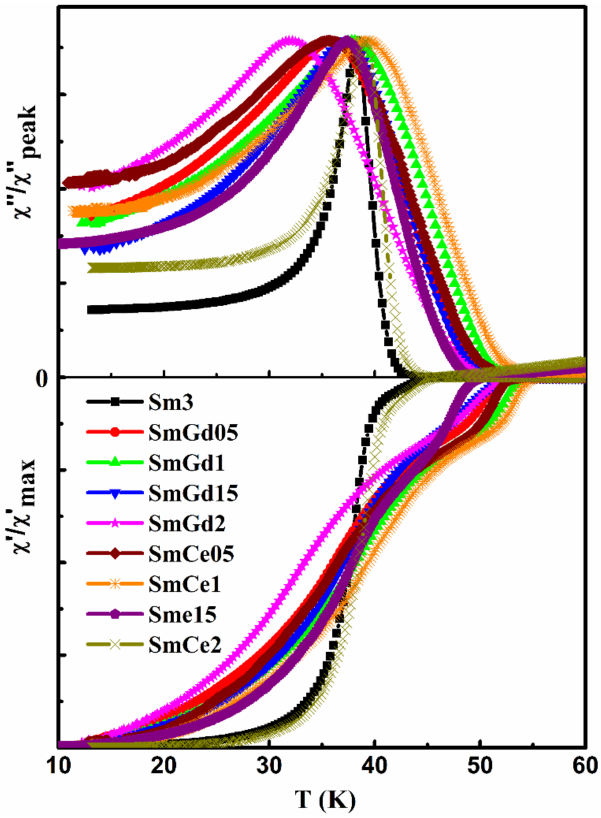

Figure 5.8: Normalized χ-T plots of Sm3 ($SmFeAsO_{0.7}F_{0.3}$) as well as Gd^{3+} and Ce^{3+} doped samples with frequency, f = 208 Hz and ac field, $H_{ac} = 4.94 \times 10^{-4}$ T

Interestingly, it is also observed that both Gd^{3+} and Ce^{3+} doping with y = 0.1 increases the T_C from 46 to around 55 K. An enlarged view of ρ-T plot near T_C is given in the inset of Figure 5.6. A T_C of 54.6 K is obtained by Gd^{3+} substitution at Sm^{3+} site (y = 0.1) and a T_C of 55.0 K for Ce^{3+} (y = 0.1) substituted sample. The T_C value of the Gd^{3+} doped sample improves from 46 to 52.4 K for a stoichiometry of y = 0.05 and reaches a maximum at y = 0.1. Further doping of Gd^{3+} slightly reduces the T_C value and then remains almost constant irrespective of further increasing the dopant concentration. In the case of Ce^{3+} doping, maximum T_C is obtained for y = 0.1 and further doping reduces the T_C. It was observed that the over doping of Ce^{3+} considerably reduces the T_C. In the present case the optimum doping concentration obtained for both Gd^{3+} and Ce^{3+} doping is found to be around y = 0.1.

Moreover, the normal state resistivity (ρ_{300}) of the sample Sm3 decreases with rare earth site doping and the resistivity of all samples show nearly linear behavior with temperatures down to a characteristic temperature and thereafter the resistivity drops more quickly down to T_C. The abrupt deviation from linearity in the ρ-T plot is due to the presence of pseudogap, already reported in Sm-based iron pnictides (Solov'ev *et al.* 2009; Arushanov *et al.* 2011). Another observation is the suppression of this pseudo gap at optimum doping of both Ce and Gd. The residual resistivity ratio RRR (ρ_{300}/ρ_{55}) of the doped samples increased significantly up to the optimum doping level of y = 0.1 with respect to that of Sm3 (up to 6.2 from 3.4), indicating stronger impurity scattering in the rare earth doped ones. The ρ_{300} and RRR values of all samples are given in Table 5.3.

Table 5.3: Different parameters observed for Sm3 and Gd^{3+} and Ce^{3+} doped samples

Parameters		**Samples**							
		Sm3	**SmGd05**	**SmGd1**	**SmGd15**	**SmGd2**	**SmCe1**	**SmCe15**	**SmCe2**
T_C (K)	**ρ-T**	45.6	52.4	54.6	52.7	52.6	55.0	49.6	43.9
	χ-T	45.1	52.0	54.0	52.1	52.1	54.7	49.4	44.1
ΔT_C (K)		4.8	4.4	4.1	4.8	5	5.5	3.1	4
ρ_{300} (mΩcm)		3.1	2.5	1.7	1.7	1.5	2.4	1.9	1.8
RRR		3.5	6.2	6.2	5.4	5.3	6.1	3.9	2.8

In the case of Gd^{3+} doping, Sm^{3+} is replaced with a smaller ion which would create an internal chemical pressure in the system. Here, the substitution of a smaller Gd^{3+} ion in place of Sm^{3+} reduces both *a* and *c* values of the system and creates an isotropic lattice shrinkage. This triggers charge transfer from the charge reservoir layer (Sm_2O_2) into the conducting FeAs layer of Sm1111 system (Tropeano *et al.*

2009; Shi *et al.* 2011). Consequently, the T_C of the system increases with Gd doping, but only up to y = 0.1, beyond which T_C shows a decreasing tendency. This type of behavior was already reported in Y doped RE1111 systems (Ganguli *et al.* 2010; Tropeano *et al.* 2009; Yang(a) *et al.* 2011; Shirage *et al.* 2008). Application of an external pressure into the system also exhibits similar tendency if the sample is in the under doped region (Yi *et al.* 2008c; Sefat, A. S. 2011). While the effect of pressure for over doped iron pnictide compounds is different or even opposite, i.e. in over doped samples, monotonic decrease of T_C with pressure is expected (Takahashi *et al.* 2008; Takabayashi *et al.* 2008; Yi *et al.* 2008a). However, in the present case, the F doped sample is in under doped region and hence Gd^{3+} doping induces a positive chemical pressure on T_C, up to its optimum doping level.

Even though creation of an internal chemical pressure is regarded as an essentiality for the suppression of SDW instability and T_C enhancement, it is interesting to observe that Ce^{3+} doping in the multiband superconductor Sm1111 exhibits a lattice parameter increase and a substantial enhancement in T_C up to y = 0.1. It is to be noted that, unlike other rare earth elements, elemental Ce can attain multiple valency of 3 and 4 or mixed valency depending on the surrounding environment at lower temperatures (Alam *et al.* 2014). The delocalized 4f electrons in cerium can fluctuate between two extreme valence states dependent upon their local atomic configurations within the system. In the present case, the structural modification created by the larger Ce^{3+} ion does not favor an increase in T_C but it is probably due to a change in valency from 3^+ to 4^+ at low temperatures that increases the charge density in the conducting layer. The possibility of variation of valency at lower temperatures could be the reason for the observed T_C enhancement. The observations conclude that, despite the difference in lattice parameter variation and origin of T_C enhancement, both Ce^{3+} and Gd^{3+} doped systems show a critical doping level of y = 0.1 and the maximum T_C achieved is around 55 K. Thus, the variation of T_C with doping content i.e. dT_C/dy shows a sign reversal above y = 0.1. Doping of Ce^{3+} and Gd^{3+} ions can modify the Sm1111 system both structurally and in terms of density of states only up to a critical point above which the system gets distorted.

Although, Ce and Gd doping in Sm1111 system have different impact on the system, both of them eventually enhance the T_C through effective increase in carrier concentration. Hence, an assessment of the charge density of the optimally doped samples is highly essential. For this, we conducted Hall Effect measurements on selected samples (RE-free sample, Sm3 and optimally doped samples from RE doped sets, SmGd1 and SmCe1). The measurements were done on rectangular pellets of uniform thickness and the details of measurements were given in Chapter 3. In order to avoid the contribution from longitudinal resistance, the magnetic field was swept from 9 to -9 T and then the Hall voltage was estimated by subtracting out the longitudinal part. The variation of transverse resistivity (ρ_{xy}) with magnetic field at a fixed temperature of 100 K for the samples Sm3, SmCe1, and SmGd1 are shown in Figure 5.7. Inset of Figure 5.7 shows the measured voltage at 100 K by varying the magnetic field from 9 to -9 T.

Both Sm3 and RE doped samples show negative Hall resistivity and also exhibit linear field dependence. From these linear ρ_{xy}-B plots, the Hall coefficient of the samples were calculated as $R_H = \rho_{xy}/B$. The R_H values for the samples are -7×10^{-9} m^3/C, -5.1×10^{-9} m^3/C, and -5.0×10^{-9} m^3/C for Sm3, SmCe1, and SmGd1, respectively. The negative R_H values indicate that electrons are the majority charge carriers in the samples (Riggs *et al.* 2009). We can also see that this negative value of R_H decreases with RE doping, indicating the increase in charge carrier density of the samples with both Gd and Ce doping at Sm site. Moreover, the obtained R_H values for optimally doped samples are almost equal which shows that the charge carrier densities within the optimally doped samples are more or less same and also higher than Sm3. The charge carrier densities for the samples Sm3, SmCe1, and SmGd1 (calculated from the equation $n_e = 1/R_He$) are 0.89×10^{27}/m^3, 1.23×10^{27}/m^3, and 1.25×10^{27}/m^3, respectively. Thus, substitution of both smaller and larger ions at Sm site relatively improves the charge carrier density of the system and hence favors the T_C enhancement. The lattice shrinkage due to smaller iso-valent Gd ions in Gd doped samples and mixed valency nature of Ce in Ce doped ones assist the increase in charge density.

The real (χ') and imaginary (χ'') components of the *ac* susceptibility (at frequency, f = 208 Hz and *ac* field, $H_{ac} = 4.94 \times 10^{-4}$ T) as a function of the temperature have been investigated. Both χ' and χ'' have been normalized with χ'_{max} and χ''_{peak}, respectively. Figure 5.8 shows the temperature versus χ'/χ'_{max} and χ''/χ''_{peak} of all the samples. All the samples exhibit diamagnetic transition in χ' and corresponding T_C values obtained are given in Table 5.3. Moreover, the χ' of *ac* magnetic susceptibility is a measure of the energy stored in the sample due to the diamagnetic response of the screening current induced in the superconductor by the external magnetic field, whereas χ'' is proportional to the energy loss due to the vortex motion. In the present study, the real part χ' shows double step transition in all the samples. However, the double-stepping nature is not pronounced in the undoped sample and the sample SmCe2. A double step transition in the real part and corresponding double peak in the imaginary part of *ac* susceptibility is a property of granular superconductors (Salamati *et al.* 2004). Corresponding to the lower temperature transition, the χ'' plot shows a peak; although the peak corresponding to the higher temperature transition is not well resolved in Figure 5.8. The observed double step nature of χ', an indication of granular behavior of our samples, confirms the inherent property of iron pnictides (Polichetti *et al.* 2008; Bonsignore *et al.* 2011). In granular superconductors, screening current flows concurrently among the grains (intergrain current) and within the grains (intragrain current). Therefore, the output signal of *ac* measurement is a contribution of these two types of screening currents within the superconductor. Hence, the double step in χ' of our samples can be also attributed to the existence of both intergrain and intragrain currents flow happening in the samples. It is also observed that the diamagnetic transition width gets broadened, and the depth of the first drop increases with an increase in doping up to the optimum doping level as shown in Figure 5.8. The lowering of T_C due to Ce doping at y = 0.2 makes the nature and position of *ac* susceptibility curve for SmCe2 closer to that of the undoped sample, resembling the reduction in T_C and revival of pseudo gap in the resistivity data of SmCe2.

The *dc* magnetization of the sample was measured as a function of applied magnetic field at different temperatures 5, 10, 20, 30, and 35 K. Figure 5.9(a) shows the magnetization (*M-H*) loops of the samples Sm3 and the optimally doped samples (SmCe1 and SmGd1) at 5 and 20 K, with applied magnetic fields up to 6 T. The obtained *M-H* curve is asymmetrical in nature, as already reported in RE1111 superconductors (Yamamoto *et al.* 2008b). Application of an external magnetic field produces a negative magnetization inside the sample up to a particular field, and then the magnetization starts to increase and takes a positive value. The effect is evidently more pronounced for the Gd doped sample. The field at which magnetization starts to increase is taken as the lower critical field (H_{C1}) of the samples. An enlarged view of the *M-H* curve at 5 K around H_{C1} is shown in Figure 5.9(b). For the sample Sm3, H_{C1} of 0.12 T is found at 5 K. Doping increases the H_{C1} values, i.e., H_{C1} ~ 0.2 T for SmCe1 and H_{C1} ~ 0.18 T for SmGd1. Here, the *M-H* curves can be treated as a superposition of both the superconducting contribution and a paramagnetic background. The paramagnetic contribution comes from the presence of RE^{3+} magnetic ions and magnetic impurity phases. It is also interesting to note that the paramagnetic background detected is very high in Gd^{3+} doped samples. This can be attributed to relatively high paramagnetic moment of the Gd^{3+} ions (7.94 μB for Gd^{3+}, 2.4 μB Ce^{3+} and 0.84 μB for Sm^{3+}). Reports on GdFeAsO$_{1-x}$F$_x$ samples also reveal that strong paramagnetic background in these samples arises due to the presence of Gd^{3+} (Cui *et al.* 2010). This paramagnetic background can be evaluated as a mean of the upper and lower hysteresis branch, $M_P = (M^+ + M^-)/2$, for each loop and this has been deducted from the experimentally obtained *M-H* curves.

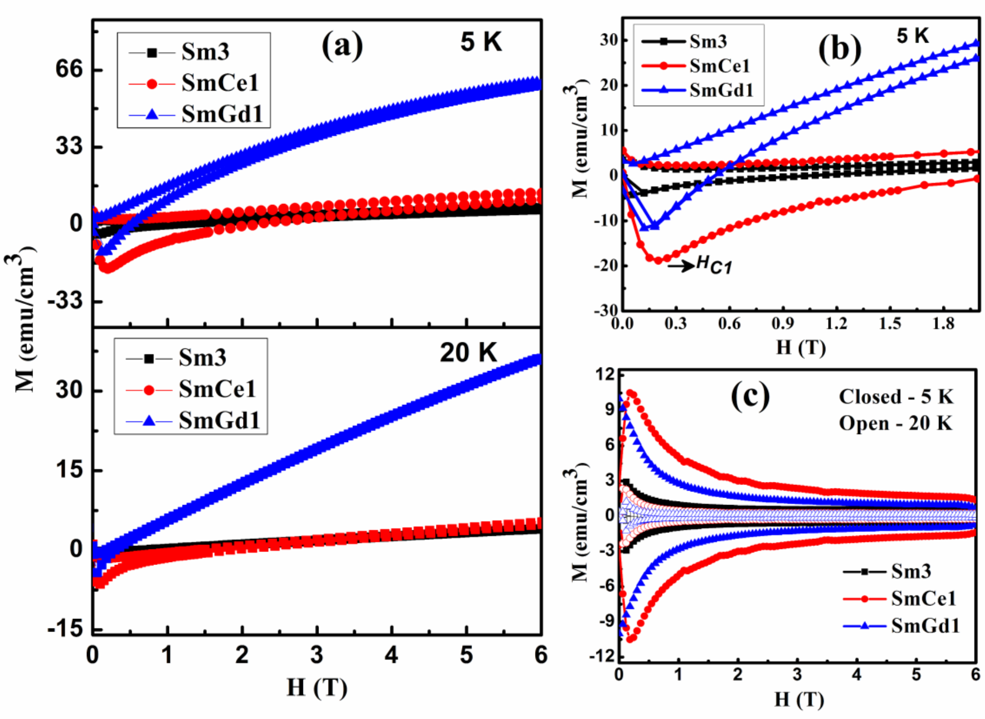

Figure 5.9: (a) *M-H* plots of the samples Sm3, SmCe1 and SmGd1 at temperatures 5 and 20 K (b) an enlarged view of the plots around H_{C1} and (c) the paramagnetic background subtracted hysteresis curves for the respective samples

Figure 5.9(c) shows the paramagnetic background subtracted hysteresis curves of the respective samples. At 5 K, the *M-H* curves of all three samples show a clear hysteresis loop. With increasing temperature, the width of the loop is found to decrease for all the samples. Rare earth site doping with both Ce^{3+} and Gd^{3+} considerably enhances the *M-H* loop width at 5 and 20 K. The maximum loop width is obtained for the sample SmCe1. Also, the maximum width of the background subtracted curve is found to be at a low magnetic field (around H_{C1}) and then the width reduces rapidly with increasing field and then demonstrates a field independent property. This typical behavior of granular superconductors is due to the weak link nature of the grain boundaries, and its extreme sensitivity towards the magnetic field. However, at higher fields the width of the hysteresis curve remains almost constant up to the highest measured magnetic field of 6 T.

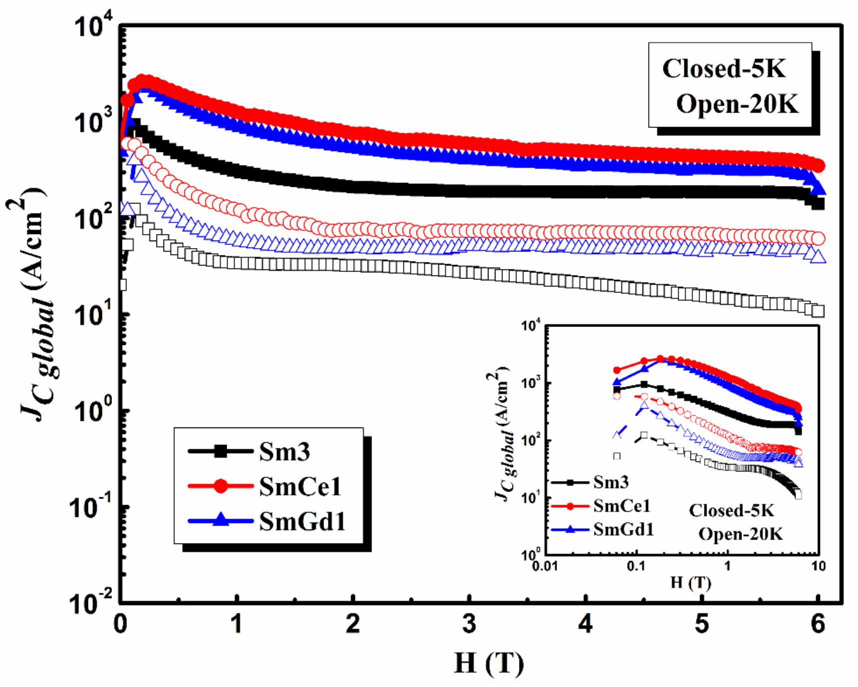

Figure 5.10: Magnetic J_C derived from the *M-H* plots for the samples Sm3, SmCe1 and SmGd1 at 5 and 20 K. Inset shows the double logarithmic J_C-*H* plots with second peak effect at 20 K

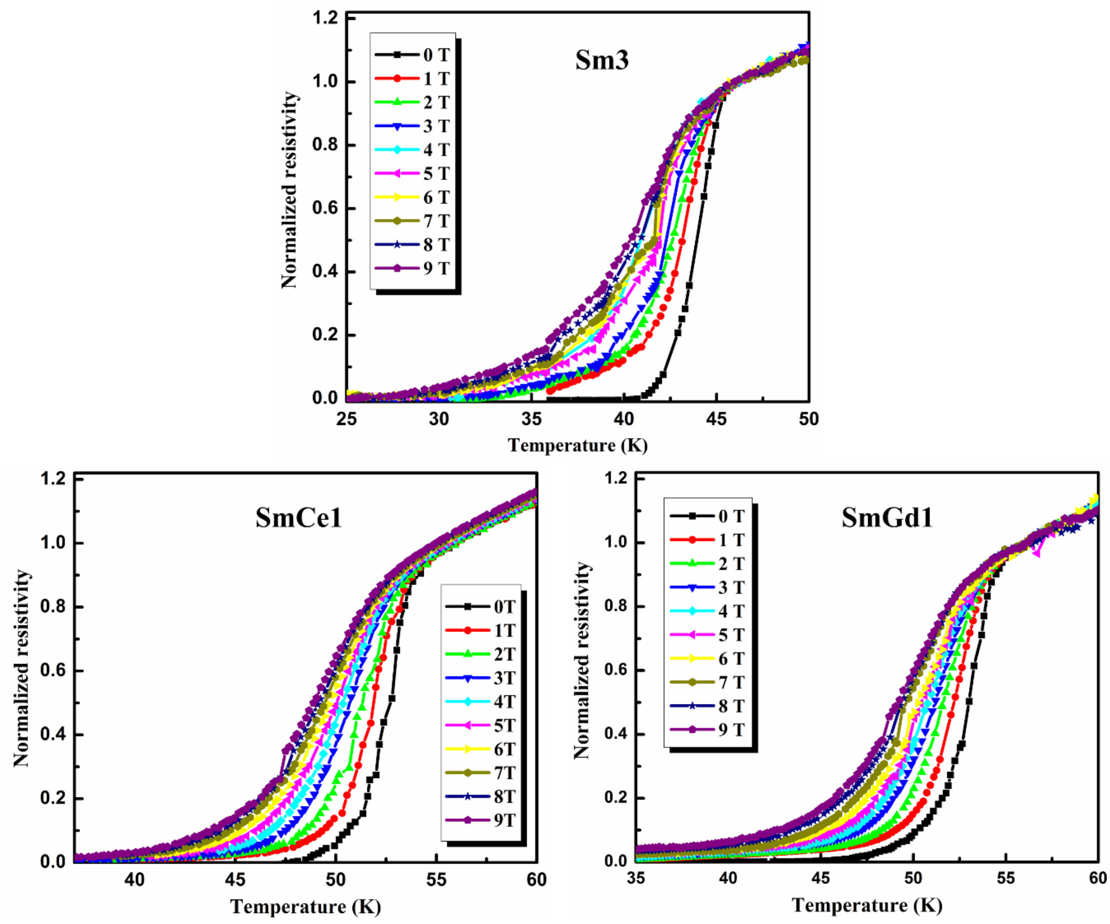

Figure 5.11: ρ-*T* plots for the samples Sm3, SmCe1 and SmGd1 under varying magnetic fields from 0 - 9 T

The critical current density (J_C) values estimated from the *M-H* loops at 5 and 20 K of the samples Sm3, SmCe1 and SmGd1 are displayed in Figure 5.10. The width of the *M-H* loop (ΔM) is due to the irreversible magnetization retained in the sample due to the flux pinning property of the superconductors. ΔM was calculated as $M^+ - M^-$; M^+ and M^- are the magnetization produced in the increasing and decreasing branches. The numerical value of ΔM is proportional to critical current density of the superconductor and the length scale of the current flow. Using Bean critical state model (Bean, C.P. 1962), we can calculate intergrain/global J_C ($J_{Cglobal}$ - current flowing through the entire sample) and intragrain/local J_C (J_{Clocal} - current flowing within the grains). $J_{Cglobal}$ of the samples has been evaluated from the width of the *M-H* loop as $J_{Cglobal} = 20\Delta M/a(1-a/3b)$; where a and b are the dimensions of the sample perpendicular to the applied magnetic field, a < b. Here; ΔM is in emu/cm^3, sample dimensions are in cm, and the obtained J_C is in A/cm^2. The sample Sm3 shows a $J_{Cglobal} \sim 0.9 \times 10^3$ A/cm^2 in the low field region. However, $J_{Cglobal}$ values of $\sim 2.5 \times 10^3$ A/cm^2 are obtained for both the doped samples at around 0.18 T at 5 K. Though, these J_C values show a decreasing tendency with field up to around 2 T, J_C remains constant ($\sim 0.8 \times 10^3$ A/cm^2 for SmCe1, $\sim 0.5 \times 10^3$ A/cm^2 for SmGd1, and $\sim 0.2 \times 10^3$ A/cm^2 for Sm3) with further increase in magnetic field. These J_C values are distinctly better than those observed in randomly oriented polycrystalline cuprates, which are typically ~ 100 A/cm^2 (Seuntjens *et al.* 1990). Thus, the rare earth site doping in $SmFeAsO_{0.7}F_{0.3}$ considerably improves the J_C of the samples, in addition to the enhancement of T_C and H_{C2} values. It is also found that J_C of Ce^{3+} doped sample is higher than the Gd^{3+} doped one in the high field region; and its value is four times higher than the F only doped sample (Sm3). No obvious second peak in $J_{Cglobal}$-H is observed for the samples at 5 and 20 K. But, there exists reports revealing the second peaking in Sm1111 samples at temperature close to T_C. Therefore, for the close observation, a double logarithmic representation of $J_{Cglobal}$-H was plotted and is shown in the inset of Figure 5.10. At 20 K, the F only doped sample, Sm3, depicted the second peak in the high field region. However, this is not clearly visible in the rare earth site doped samples even up to the highest magnetic field applied. This can be attributed to the very high H_{C2} values of the rare earth doped samples as discussed in the succeeding section.

The intragrain J_C (J_{Clocal}) was also calculated using the equation $J_{Clocal} = 30\Delta M/\langle r \rangle$, where $\langle r \rangle$ is the grain size in cm. An average grain size of 3.5 μm for Sm3 and SmGd1 and 1.8 μm for SmCe1 was estimated from the SEM images. At 5 K, J_{Clocal} of 3.5×10^6 A/cm^2

was obtained for the Ce doped sample which is almost one order higher than the intragrain J_C of Sm3 i.e. around 5.0×10^5 A/cm^2. Ce^{3+} doping at Sm site in Sm3 remarkably enhances the J_C value within the grain over the entire magnetic field. Gd^{3+} doping in Sm3 also improves the J_{Clocal} values, but lesser compared to Ce^{3+} doped ones. A J_{Clocal} of ~ 1.3×10^6 A/cm^2 was obtained for SmGd1. The microstructural analysis has already revealed that optimum doping of Ce^{3+} gives well-connected grains of smaller size. In addition, the lattice mismatch between Ce^{3+} and Sm^{3+} is higher than that between Gd^{3+} and Sm^{3+}. This in turn results in comparatively higher flux pinning in SmCe1 sample than in SmGd1 at higher fields. The above reasons seem to be responsible for the better J_C-H behavior of SmCe1 over the entire field region studied.

The H_{C2} values of the samples Sm3, SmCe1 and SmGd1, have been also evaluated from the temperature dependence of their resistivity under varying magnetic fields. Figure 5.11 shows the field dependent ρ-T plots for the samples Sm3, SmCe1 and SmGd1 with the magnetic fields varying from 0 to 9 T. The transition width broadens with the applied magnetic field in which there is a considerable reduction in $T_{Coffset}$ value with a slight decrease in T_{Conset}. This broadening was already reported in RE1111 pnictides and cuprate based superconductors and could be interpreted in terms of weak links or flux flow existing in the sample (Gao(b) *et al.* 2008; Sun *et al.* 2011). Weak link behavior of our samples has been revealed from their *ac* magnetic susceptibility measurements and discussed earlier. The magnetic field and temperature dependence of resistivity give information about the upper critical field, H_{C2} and irreversibility field, H_{irr}. The resistivity data was normalized with respect to the normal state resistivity at 65 K and then using the criteria of 90% and 10% of the normal state resistivity (ρ_n - resistivity value just above transition), both H_{C2} and H_{irr} was estimated. H_{C2} at zero temperatures for the samples is given by the Werthamer-Helfand-Hohenberg (WHH) formula $H_{C2}(0) = -0.693T_C\ [dH_{C2}/dT]_{TC}$. The slope $[dH_{C2}/dT]_{TC}$ was calculated from the temperature dependence plot of H_{C2}.

Figure 5.12 shows the H-T phase diagram i.e. the temperature dependence of both H_{C2} (closed symbol) and H_{irr} (open symbol) of the samples Sm3, SmCe1 and SmGd1, derived from the ρ-T plots at different magnetic fields. The dH_{C2}/dT ~ -5.4 T/K for Sm3, dH_{C2}/dT ~ -10.1 T/K for SmCe1 and dH_{C2}/dT ~ -9 T/K for SmGd1 are obtained from the H-T phase diagram and the corresponding $H_{C2}(0)$ values are 170, 385 and 340 T, respectively. Thus, very high value of H_{C2} is achieved by rare earth site doping in $SmFeAsO_{0.7}F_{0.3}$ system. The H_{irr} values were also estimated following the same WHH formula, from the slope of the H-T curves corresponding to 10% ρ_n. The H_{irr} values obtained for the samples Sm3, SmCe1, and SmGd1 are 34.7, 51.1, and 46.5 T, respectively. We can see that the irreversibility field of the samples SmCe1 and SmGd1 are rather high compared to that of Sm3. Therefore, it is evident that simultaneous doping at oxygen and rare earth site increases the number of effective pinning centres in the form of lattice defects and substantially increases the critical fields of Sm1111 system. The enhanced $J_C(H)$ performance and very high upper critical fields in addition to the relatively high T_C around 55 K confirm the significant enhancement of superconducting properties by rare earth site doping in $SmFeAsO_{0.7}F_{0.3}$ system.

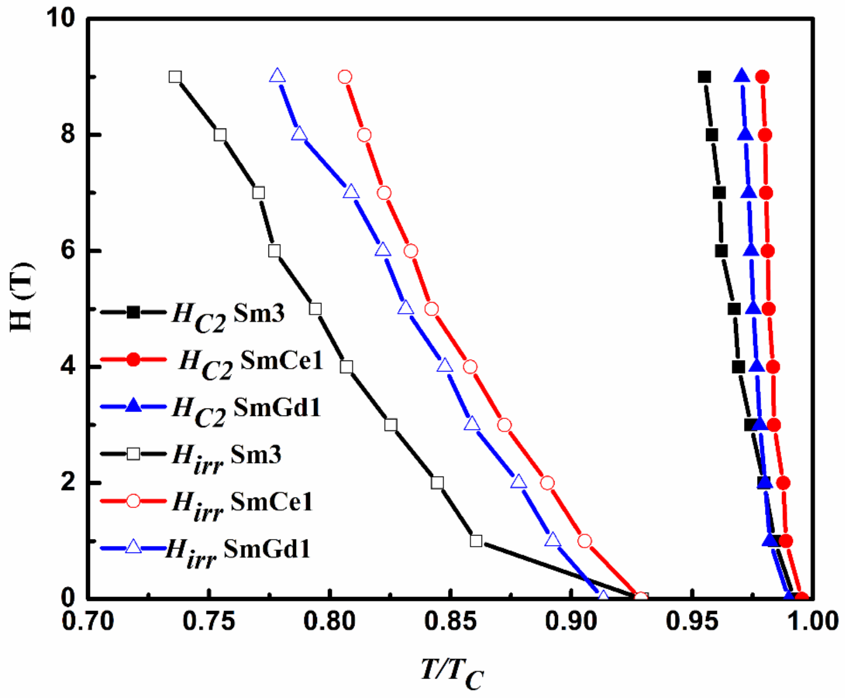

Figure 5.12: ***H-T* phase diagram of the samples Sm3, SmCe1 and SmGd1; H_{C2} and H_{irr} were determined from 90% and 10% points on the ρ-*T* plot at different magnetic fields**

5.3.3 Conclusions

In summary, rare earth site doping in addition to F^- doping at O^{2-} site has a significant impact on both structural and superconducting properties of $SmFeAsO_{1-x}F_x$. We observed that higher T_C can be obtained even upon doping with a larger ion, Ce^{3+}, at the rare earth site Sm^{3+}. T_C increased from 45 to around 55 K for both Gd^{3+} and Ce^{3+} doped samples. Even though Ce and Gd doping have their own signature in T_C enhancement; both are found to increase the charge carrier concentration. Very high upper critical fields have also been obtained by rare earth site doping in $SmFeAsO_{0.7}F_{0.3}$. In addition, rare earth site doping improves the critical current density of the samples throughout the entire range of magnetic field studied. Enhanced flux pinning due to additional doping at Sm^{3+} site is found to be responsible for the improved $J_C(H)$ performance. Ce^{3+} doped samples give much better properties in the high field region than the Gd^{3+} doped ones.

5.4 The role of Y^{3+} doping on the structural and superconducting properties of Sm1111 and its comparison with other (RE, Y)1111 (RE - La, Ce, and Nd) iron oxypnictides

Yttrium is a smaller non-4f element that has been tried as a dopant in different RE1111 systems and the properties of the Y doped RE1111 samples changed according to the rare earth chosen (Ganguli *et al.* 2010; Tropeano *et al.* 2009; Shirage *et al.* 2008; Prakash *et al.* 2009). Yttrium doping was found to be fruitful in terms of T_C enhancement in La1111, Ce1111 and Nd1111 systems (Ganguli *et al.* 2010; Tropeano *et al.* 2009; Anooja *et al.* 2012). Nevertheless, the existing reports on yttrium doping in Sm1111 claim contradictory results (Lai *et al.* 2012; Chen(d) *et al.* 2010b). An analysis of the impact of yttrium doping on the next lanthanide system in the periodic table, Sm1111, is endeavored here. Accordingly, a comprehensive analysis of the influence of yttrium doping especially on Sm1111 system and a comparison with that of other Y doped RE1111 systems such as La1111, Ce1111 and Nd1111 has been presented in this section. Polycrystalline samples with nominal stoichiometry of $Sm_{1-y}Y_yFeAsO_{0.7}F_{0.3}$ (y = 0.0, 0.1, 0.2 and 0.3) labelled as SmY0, SmY1, SmY2 and SmY3, respectively were synthesized by solid state reaction method through the pre-processing step. High purity Sm, Y, Fe, As, Fe_2O_3, and FeF_2 (Aldrich > 99.9%) were used as starting materials. Stoichiometric amounts of all the starting materials were weighed, mixed and ground in a glove box having high purity Argon atmosphere. The homogenous mixture was pelletized and sealed in evacuated quartz tubes. The samples were processed by following the heat treatment procedure, 360 °C/5 h + 900 °C/50 h with intermediate grinding, pelletizing and vacuum sealing.

5.4.1 Structural properties of $Sm_{1-y}Y_yFeAsO_{0.7}F_{0.3}$ samples

Figure 5.13 shows the XRD patterns of the Y doped samples of Sm1111 synthesized in the present work. The main peaks of the XRD pattern are indexed with the major phase of SmFeAsO that has ZrCuSiAs type structure. All the samples contain minor amounts of secondary phases such as SmAs, FeAs, and SmOF. The intensity of SmAs and FeAs remains almost invariant irrespective of the Y content. However, the Y doped Sm1111 samples show presence of YOF that increases with increasing Y content. The XRD patterns of the Y doped RE1111 samples reported so far were also indexed on the basis of the tetragonal ZrCuSiAs type structure with REFeAsO as the major phase. Apart from REAs, FeAs and REOF, the impurity phases due to yttrium doping are found to be Y_2O_3 and/or YOF. The inset of Figure 5.13 shows an enlarged view of the main peak (*102*) of the Y doped Sm1111 samples. Here, we observe a left-shift in the pattern of the Y doped samples compared to the undoped sample SmY0 indicating a possibility for the increase in lattice parameters *a* and/or *c* with increasing Y content. Usually, it is observed that the lattice parameter *c* decreases on electron doping and the lattice parameter *a* increases on hole doping along with corresponding shifts in the XRD pattern. On doping fluorine at oxygen site in RE1111 system, the XRD patterns of the fluorine doped (F doped) samples show a right shift with respect to that of parental compound. This is a reflection of the *c* axis contraction resulting from F doping. Hence, the lattice parameters of these samples were calculated and have been included in Table 5.4.

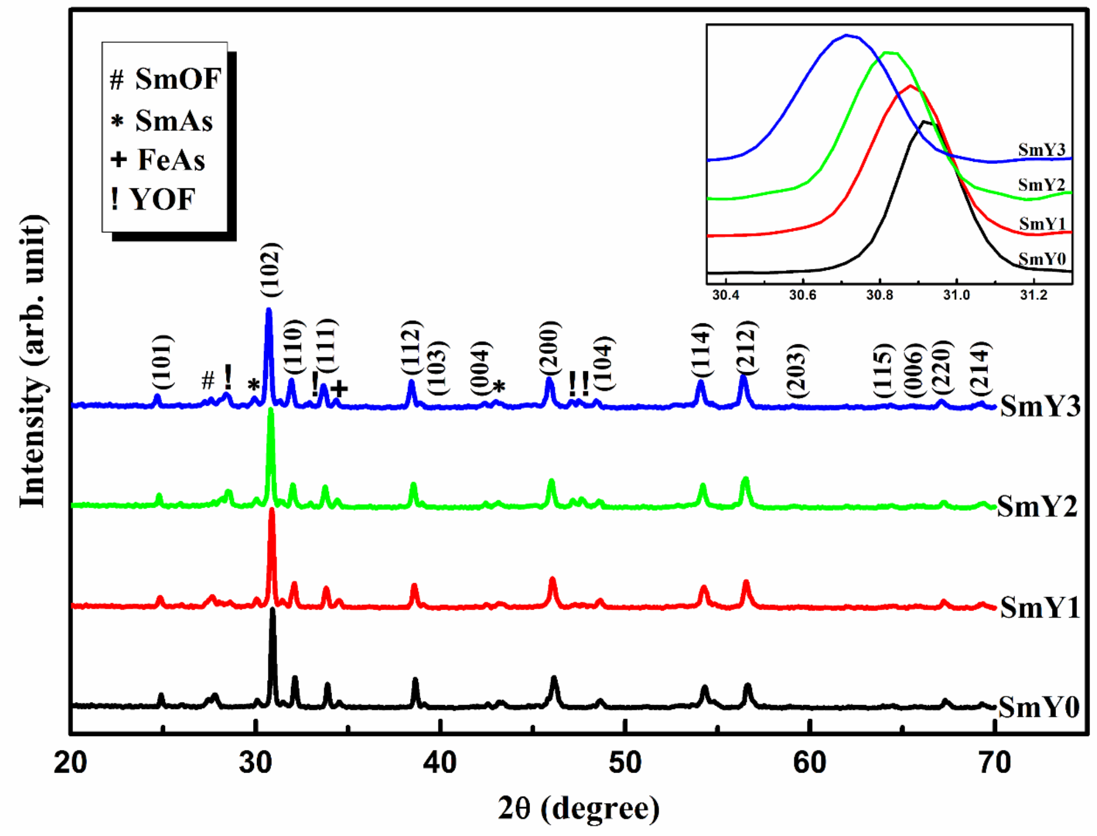

Figure 5.13: XRD patterns of undoped and Y doped samples

Table 5.4: Lattice parameters observed for undoped and Y doped Sm1111 samples

Samples	Lattice Parameters	
	***a* (Å)**	***c* (Å)**
SmY0	3.9324	8.5126
SmY1	3.9399	8.5342
SmY2	3.9454	8.5421
SmY3	3.9490	8.5542

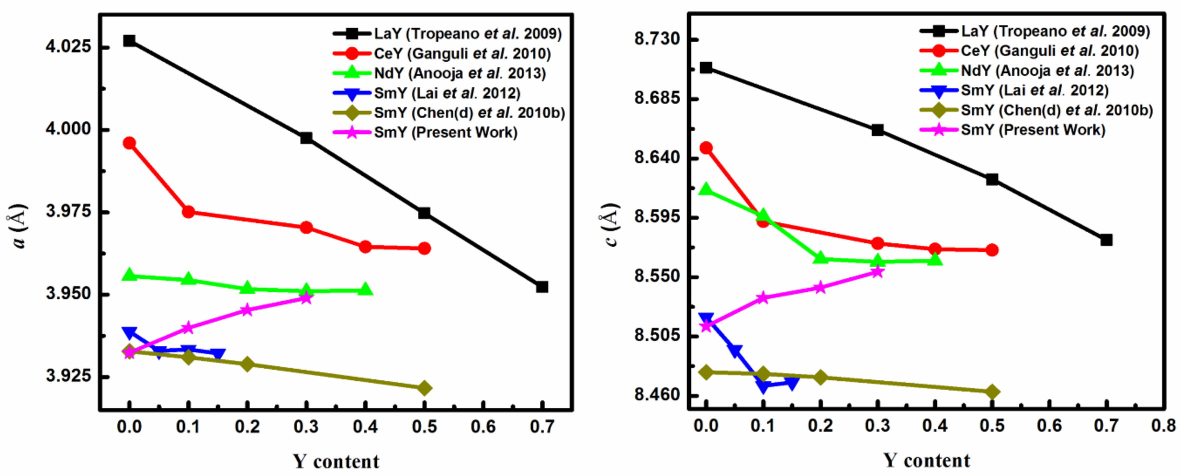

Figure 5.14: The variation of lattice parameters *a* and *c* for undoped and Y doped samples of Sm1111 and its comparison with existing (RE, Y)1111 systems

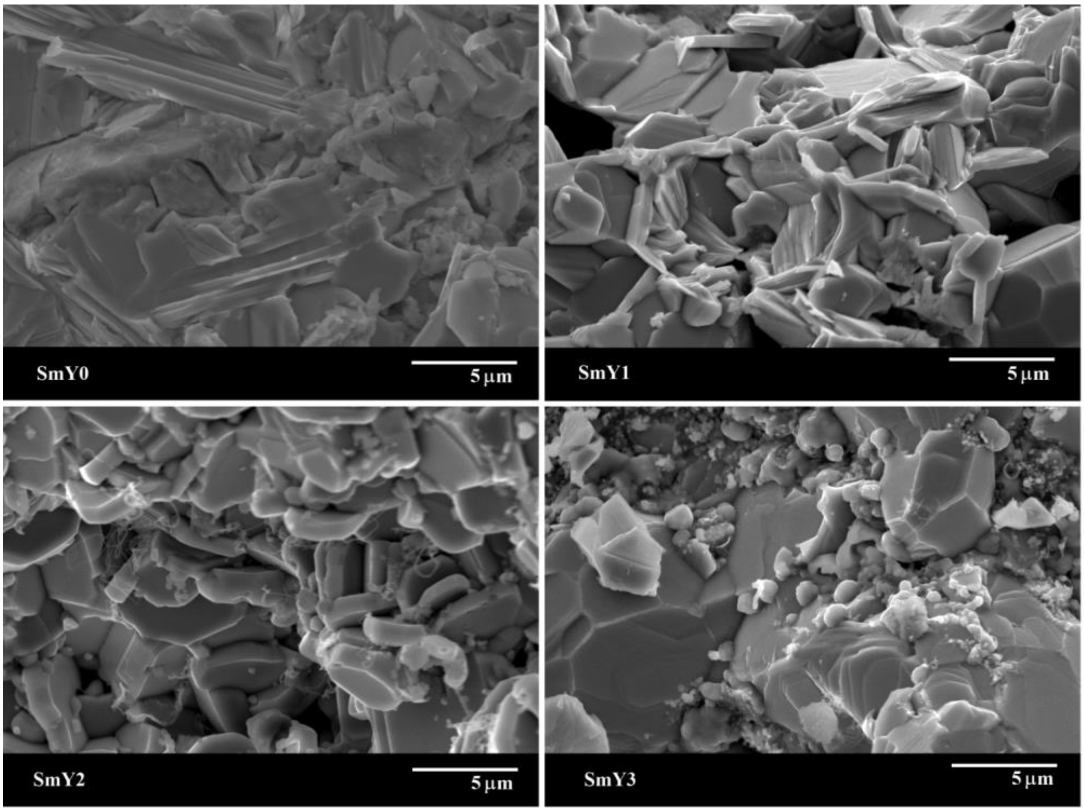

Figure 5.15: SEM images of the undoped and Y doped Sm1111 samples

The lattice parameter variations observed in as prepared samples of Y doped Sm1111 and existing results on other (RE, Y)1111 systems (Ganguli *et al.* 2010; Tropeano *et al.* 2009; Anooja *et al.* 2012; Lai *et al.* 2012; Chen(d) *et al.* 2010b) are displayed in Figure 5.14. It is found that both *a* and *c* values, of the Y doped samples in the present study, increase thereby causing an enhancement in cell volume. This is evident from the left-shift observed in the peak corresponding to (*102*) plane. However, the observation is at odds with the results obtained for the other Y doped RE1111 systems including the Y doped Sm1111 system reported elsewhere. Figure 5.14 shows that generally there is a decreasing trend in lattice parameters. It is also seen that the extent of decrease or percentage of lattice reduction is strongly dependent on the rare earth of the 1111 system chosen. The crystal ionic radius of yttrium is 90 pm and that of La, Ce, Nd and Sm are 103.2, 101, 98.3 and 95.8 pm respectively. The ionic radius decreases from La to Sm. On comparing the ionic radius of yttrium with that of the above lanthanides, the ionic radii difference with yttrium is maximum for La and minimum for Sm. Thus, the gradation in crystal ionic radii difference between yttrium and the lanthanides is in the order La > Ce > Nd > Sm. The larger the difference in ionic radii of a dopant with that of the doping site element, the higher is the inner chemical pressure induced. The more the inner chemical pressure, the more is the lattice contraction. This can be the reason for the maximum lattice parameter reduction observed in the Y doped La1111 system (Figure 5.14). The increase in lattice contraction favors charge transfer between conducting layer and charge reservoir layer thereby enhancing the T_C. Hence, it is obvious that the extent of T_C enhancement for the Y doped RE1111 system with respect to the undoped system decreases on moving from La to Sm. This has been observed in La and Ce based systems reported elsewhere (Tropeano *et al.* 2009; Shirage *et al.* 2008; Prakash *et al.* 2009; Kadowaki *et al.* 2009). In Nd1111 system, our experimental results show a T_C hike of about 4 K (Anooja *et al.* 2013) which is still lower than that shown in Ce1111 system, as expected. But, the influence of the so called lanthanide contraction is found to be different for Sm1111 system. In Y doped Sm1111 systems reported elsewhere, both enhancement and reduction in T_C have been observed (Lai *et al.* 2012; Chen(d) *et al.* 2010b) even though the system shows a reduction of *a* and *c* value in both cases.

The ionic radius, valence state and electron affinity of the ions in a crystal are the different factors that decide bond length within its structure. If site selective substitution in a compound increases the electron affinity of the system, then bond length of that system reduces and hence the lattice parameter. Since yttrium is iso-valent, contraction in lattice due to variation in charge density can be discarded. Regarding ionic radii, the relatively smaller difference in ionic radii between Y^{3+} and Sm^{3+} also has little impact on lanthanide contraction. However, our samples differ from the other Y doped Sm1111 systems mainly in the preparation conditions and nominal F content chosen which is F = 0.3 in the present case and F = 0.2 elsewhere (Lai *et al.* 2012; Chen(d) *et al.* 2010b). Thus, the secondary phases such as YOF and SmOF will be comparatively higher due to higher F content and they presumably affect the crystal lattice also. Though the F content is nominal for the Y-free Sm1111 system, the oxyfluoride derivatives due to yttrium doping seems to influence the lattice parameters which finally results in a noticeable reduction (~ 10 K) of T_C.

The microstructure of the fractured surfaces of the present samples ($Sm_{1-y}Y_yFeAsO_{0.7}F_{0.3}$) is shown in Figure 5.15. The microstructure of undoped Sm1111 sample appears homogeneous with long flaky grains. On yttrium doping, a distinct change in the grain morphology appears. In the Y doped samples, the grains have irregular shapes with distinct grain boundaries. However, the grains seem to be tilted in all the doped samples and these tilted grains certainly play a vital role in the degradation of intergranular super-current flow. Moreover, with the increase in Y content, a systematic deterioration in the microstructure concerning the homogeneity and grain morphology is observed. Among all the doped samples, the microstructure of SmY3 exhibits poor homogeneity and grain connectivity. Polycrystalline samples of La/Sm/Nd1111 pnictides examined to date show severe problems related to grain-to-grain connectivity, raising the concern of depression of superconducting order parameter and thereby the current flow at grain boundaries as observed in cuprates. The microstructural analysis reported so far confirms that layered structure with large grains is a common feature of Sm1111 superconductors (Kametani *et al.* 2009a; Yamamoto *et al.* 2011).

5.4.2 Superconducting properties of $Sm_{1-y}Y_yFeAsO_{0.7}F_{0.3}$ samples

The resistivity versus temperature (ρ-T) plots of all Y doped RE1111 systems exhibit metallic behavior from room temperature to the superconducting transition temperature with a hump around 200 K, characteristic of iron pnictides especially Sm1111 (Solovjov *et al.* 2011). The ρ-T plots of our samples ($Sm_{1-y}YyFeAsO_{0.7}F_{0.3}$) are shown in Figure 5.16. It is observed that T_C gradually decreases from 53.9 to 43.7 K with increasing Y content from x = 0 to 0.3. It is also seen that the samples with higher Y content are found to have higher room temperature resistivity than the samples with lower Y content, which can be due to the presence of the YOF phase which increases with increase in Y content. Here, the residual resistivity ratio (RRR = ρ_{300}/ρ_{55}) for the Y doped samples decreases as the Y content increases and is generally lower than the undoped sample (Table 5.5). The RRR values are found to follow the same trend in other Y doped RE1111 systems also (Ganguli *et al.* 2011; Tropeano *et al.* 2009; Anooja *et al.* 2013; Lai *et al.* 2012; Chen(d) *et al.* 2010b). The RRR value of a material is a measure of the sample quality and homogeneity. An increase in the amount of defects or impurity increases the residual resistivity at T_C due to impurity scattering and leads to the lowering of RRR value. Similarly, ΔT_C (T_{Conset} - $T_{Coffset}$) is also an indicator of sample crystallinity and homogeneity. The ΔT_C measured for all the Y doped samples is higher than the undoped sample SmY0 (Table 5.3).

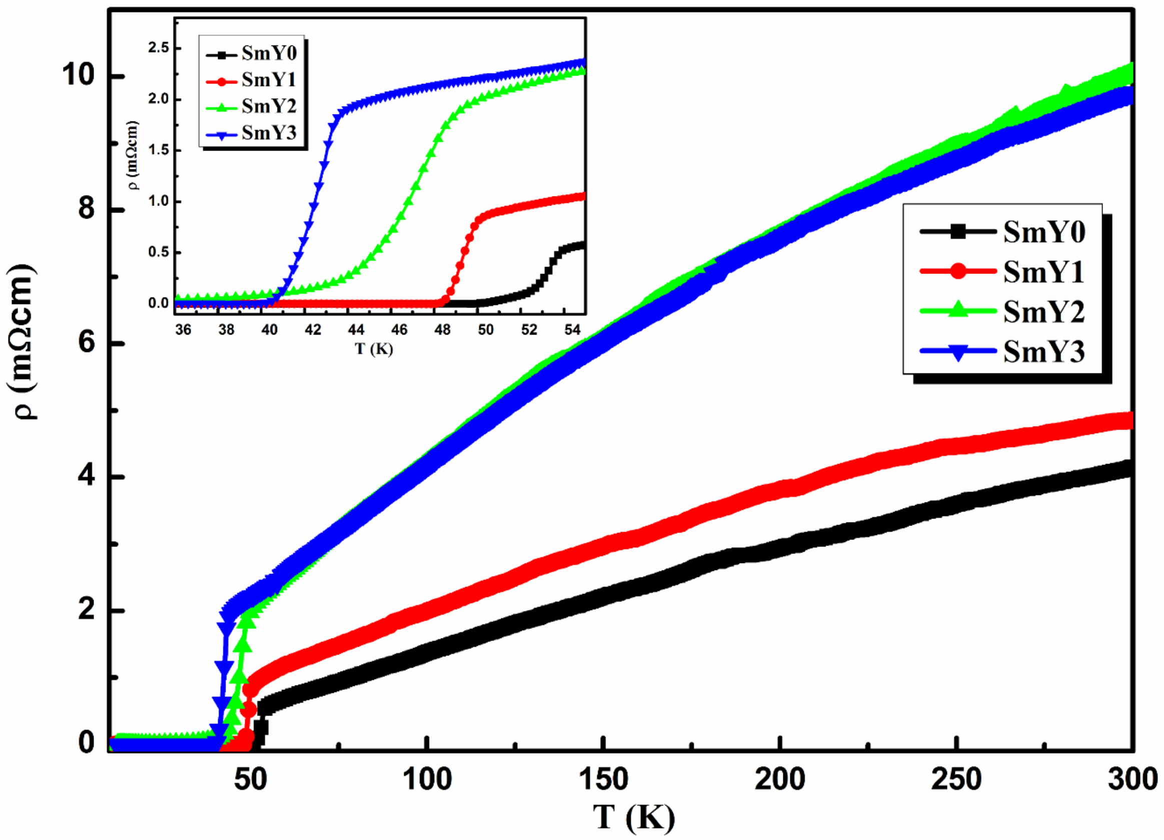

Figure 5.16: ρ-T plots for undoped and Y doped Sm1111 samples

Table 5.5: Different parameters observed for undoped and Y doped Sm1111 samples

Samples	**T_C (K)**		**ΔT_C (K)**	**RRR**	**I_C (A)**	**J_C (A/cm^2)**
	ρ-T	**χ-T**				
SmY0	53.9	53.4	1.8	7.14	18	450
SmY1	50.5	50.3	3.5	4.57	14.5	362
SmY2	49.5	49.1	5.1	4.40	11.5	287
SmY3	43.7	43.3	4.1	4.12	1.6	40

The variation of T_C with varying Y content for the as prepared samples of Y doped Sm1111 and the existing results on other (RE, Y)1111 systems (Ganguli *et al.* 2010; Tropeano *et al.* 2009; Anooja *et al.* 2012; Lai *et al.* 2012; Chen(d) *et al.* 2010b) are shown in Figure 5.17. It shows that in La/Ce/Nd1111 systems, T_C enhances with Y doping; while for the Sm1111 system T_C decreases. Even though Lai et. al. (Lai *et al.* 2012) claim that T_C of Sm1111 can be increased from 37 to 39.5 K with slight doping of yttrium (x = 0.05), both the undoped and Y doped samples are found to have much lower T_C values than those reported for Sm1111 (> 40 K) by many other groups (Chen(c) *et al.* 2008; Yang(a) *et al.* 2011; Zhao(b) *et al.* 2010; Liu(b) *et al.* 2008). In brief, the results show that the benefits of yttrium doping at lanthanide site can be achieved only up to Nd.

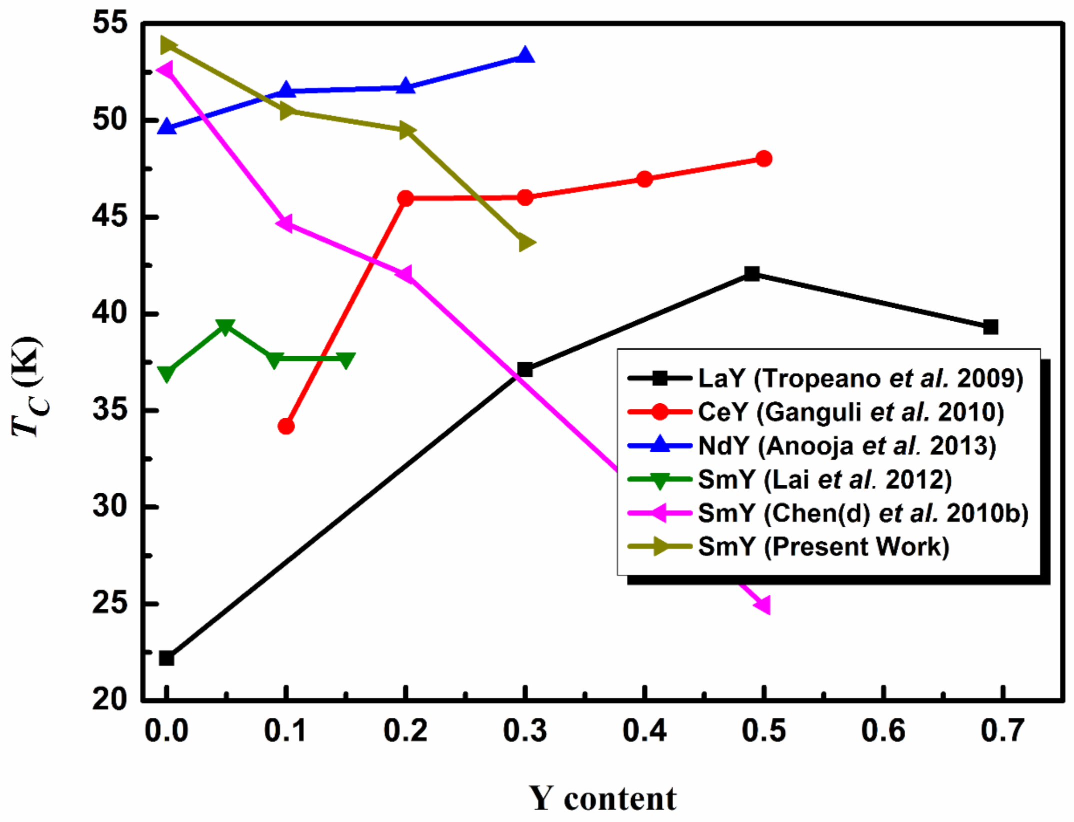

Figure 5.17: Plots comparing the variation of T_C for undoped and Y doped samples of Sm1111 with existing (RE, Y)1111 systems

Though intriguing results on T_C enhancement have been reported for various Y doped RE1111 systems, reports on the transport I_C of these systems are limited due to the grain connectivity issues prevailing in these materials. In the present study, we have determined the influence of Y doping on the transport current of bulk Sm1111. Figure 5.18 shows the *I-V* plots of the samples measured at 12 K and the transport I_C values along with their corresponding J_C are listed in Table 5.3. It is observed that the transport current of all samples decreases with Y doping. The current carrying capability is severely degraded in SmY3 due to the increased amounts of secondary phases and reduced grain connectivity as observed in XRD and SEM, respectively. Thus, it can be inferred that yttrium doping in Sm1111 system makes considerable change in its electronic structure, phase assemblage and grain morphology which deteriorate the transport properties of the system, unlike the other RE1111 systems.

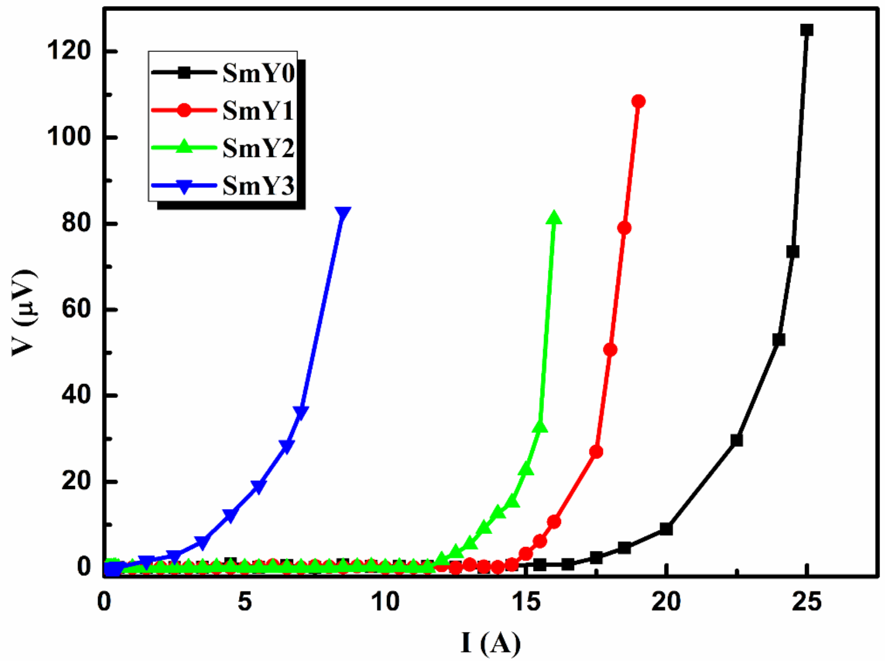

Figure 5.18: *I-V* plots of undoped and Y doped Sm1111 samples at 12 K

The temperature dependence of *ac* susceptibility (χ-T) for the undoped and Y doped samples (measured at an *ac* field, H_{ac} of 0.49 mT and frequency of 208 Hz) is given in Figure 5.19. The χ-T measurement is another simple and expedient tool to confirm superconductivity and to gain information on the granularity of polycrystalline samples. The T_C obtained from the diamagnetic transitions of the undoped and Y doped samples is in good agreement with the observations from ρ-T measurements. In the *ac* susceptibility measurement, the moment of the sample changes in response to an applied *ac* field, which provides an understanding of the magneto dynamics prevailing in the system. The complex susceptibility ($\chi' + i\chi''$) measured comprises of a real part and an imaginary part. The real component χ' represents the component of the susceptibility that is in phase with the applied *ac* field, while χ'' represents the component that is out of phase. The imaginary component χ'' is related to the energy losses or the energy absorbed by the sample from the *ac* field. The double step transition in χ', characteristic of iron based superconductors, is exhibited in all samples except SmY3. It is implied that the two steps: near T_C and below T_C, correspond to the contributions from intragranular and intergranular currents, respectively (Polichetti *et al.* 2008; Salamati *et al.* 2004). The upper step or near T_C step is a sign of bulk superconductivity established in a superconductor by individual grains unlike the lower temperature step, which is due to the phase locking of the superconductor order parameter of adjacent grains. Thus, it can be presumed that the absence of lower temperature step in SmY3 is due to the poor intergranular current flow across adjacent grains.

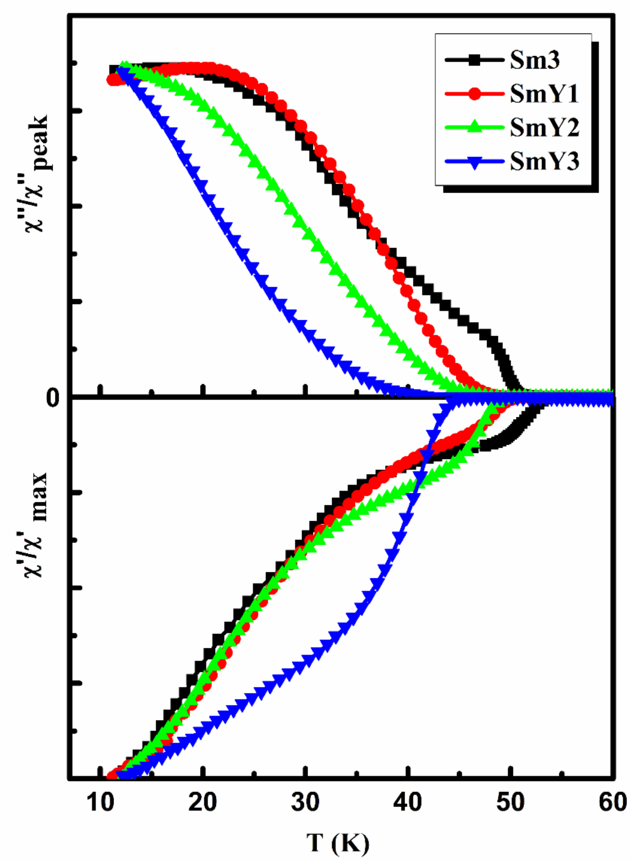

Figure 5.19: Normalized χ-T plots for undoped and Y doped Sm1111 samples

The comprehensive analysis of all the structural and superconducting parameters of yttrium doped Sm1111 system suggests that the comparable ionic size and iso-valent nature of samarium and yttrium ions cause considerable decrease in T_C and the microstructural deterioration degrades the J_C of pristine Sm1111.

5.4.3 Conclusions

This section has discussed the influence of Y doping on the structural, superconducting and magnetic properties of $SmFeAsO_{0.7}F_{0.3}$ (Sm1111) and a comparison of the results with Y doped La1111, Ce1111 and Nd1111 systems. It is found that unlike the La, Ce and Nd based systems which all exhibit enhancement of T_C on Y doping, the T_C of Sm based system reduces upon Y doping. The iso-valent substitution of lanthanides such as La, Ce and Nd in F doped RE1111 with Y is found to reduce the lattice parameters and correspondingly exert a chemical pressure that enhances the T_C of these compounds. In the case of Sm, a relatively smaller lanthanide, substitution of Y results in a lattice expansion leading to a depression of T_C. However, yttrium doping in RE1111 systems with still smaller RE ions need to be explored to confirm the relationship between ionic size and T_C.

5.5 Summary of rare earth site doping study

Iso-valent rare earth site doping using 4f elements such as Gd^{3+} and Ce^{3+} and using a non-4f element Y^{3+} gives different impacts on both structural and superconducting properties of $SmFeAsO_{0.7}F_{0.3}$ superconductor. Doping of 4f elements i.e. Gd^{3+} and Ce^{3+} at the rare earth site of $SmFeAsO_{0.7}F_{0.3}$ significantly enhances the superconducting properties such as critical temperature (T_C), critical fields and critical current densities. Both Gd^{3+} and Ce^{3+} doping increases the T_C from 45 to 55 K irrespective of their difference in ionic size compared to Sm^{3+}. Besides, very high upper critical field and better J_C-H performance are obtained for the rare earth site doped samples for the entire field of study. However, the doping of the non-4f element, Y^{3+} at Sm^{3+} gives a negative impact on the superconducting properties of $SmFeAsO_{0.7}F_{0.3}$ system. Comparing the results obtained for yttrium doped Sm1111 superconductor with other yttrium doped RE1111, it is inferred that the partial substitution of lanthanides such as La, Ce, and Nd with yttrium systematically enhances T_C of the system to different levels depending on their crystal ionic radii difference with yttrium whereas yttrium doping does not seem to be beneficial for Sm1111 because of its comparable ionic size with Sm^{3+}.

CHAPTER 6

EFFECT OF ALKALINE EARTH METAL FLUORIDE (CaF_2 AND BaF_2) DOPING IN Sm1111 BULK SUPERCONDUCTOR

6.1 Introduction

Superconductivity is induced in iron pnictides by chemical doping as a result of the consequent suppression of SDW instability that occurs in the parental compound (Nomura *et al.* 2008). Doping of fluorine at oxygen site introduces extra charge carriers in the conduction layer and thereby induces superconductivity. In this case, superconductivity results from the combined effect of both the charge density increment and the *c* axis contraction resulting from the coulomb's attractive force. The substitution at RE site with tetravalent cationic species in addition to the fluorine doping is also found to enhance superconducting properties such as T_C, J_C and H_{C2} (Martinelli *et al.* 2008; Wang(a) *et al.* 2008; Wen *et al.* 2008). Here also the main motive is to enable *c* axis contraction. In iron pnictides, superconductivity can also be categorized on the basis of the type of dominant charge carriers i.e. electrons or holes. In the initial reports on iron pnictide superconductors, the role of electron doping with fluorine seemed to be the only way to overcome SDW thereby achieving superconductivity. Later, a T_C of 25 K was reported in $La_{1-x}Sr_xFeAsO$ by substituting La with Sr, assuring that hole doping can also turn these materials into superconductors (Wen *et al.* 2008) i.e. iron pnictides are symmetric in terms of both hole and electron doping. Superconductivity at about 38 K was also found in $Ba_{1-x}K_xFe_2As_2$, belonging to the hole doped superconductors (Rotter *et al.* 2008). Fluorine doping at O site induces electrons as charge carriers into the FeAs layer, whereas doping at RE^{3+} site with a bivalent ion (alkaline earth metal ions) induces holes as charge carriers in the FeAs layer. However, doping of both electrons and holes in a single system is a different scenario and can give rise to modified electronic, magnetic, and superconducting properties. $SmFeAsO_{1-x}F_x$ has been proved to be a promising candidate among RE1111 system both in terms of its superconducting properties and practical applications. Hence, in this chapter, the combined effect of both electron and hole doping (binary doping) in SmFeAsO is investigated by simultaneous doping F^- at O^{2-} site (electron doping) and Ca^{2+}/Ba^{2+} at Sm^{3+} site (hole doping). For that, a single source of alkaline earth metal fluorides such as CaF_2 and BaF_2 were chosen.

6.2 Experimental details

Polycrystalline bulk samples were prepared by using single step method with three stages of heat treatment process including the pre-processing stage. Samples with nominal compositions of $Sm_{1-x}A_xFeAsO_{1-2x}F_{2x}$ (A - alkaline earth metals of Ca and Ba) with x = 0.15, 0.2 were synthesized by stoichiometric mixing of the ingredients. The details of preparation have been already included in Chapter 4. Here, CaF_2 and BaF_2 were used as fluorine source, instead of FeF_2, for $Sm_{1-x}Ca_xFeAsO_{1-2x}F_{2x}$ and $Sm_{1-x}Ba_xFeAsO_{1-2x}F_{2x}$, respectively. Weighing and mixing were done inside a glove box filled with high purity argon. The samples were compacted into rectangular pellets with dimensions of 15 × 5 × 2 mm^3, under a pressure of 500 MPa and the pellets were barely placed in an evacuated sealed quartz tube. Then they were subjected to the following heat treatment procedure of 360 °C/5 h + 850 °C/30 h + 1150 °C/20 h with intermediate grinding and pressing. The parental compound, SmFeAsO and an F doped sample, ($SmFeAsO_{0.7}F_{0.3}$) and ($SmFeAsO_{0.6}F_{0.4}$) were also prepared under identical conditions using FeF_2 as fluorine source.

The phase identification of the samples was performed using an x-ray diffractometer (Philips X' Pert Pro) with CuKα radiation employing a proprietary high speed detector and a monochromator at the diffracted beam side. Microstructural examination of the samples was done using a scanning electron microscope (JEOL JSM 5600 LV). Superconducting transport measurements such as resistivity versus temperature (ρ-T) and current versus voltage (I-V) were carried out using a closed cycle cryocooler integrated cryostat by *dc* four probe technique. The temperature dependence of *ac* susceptibility (χ-T) was measured using a closed cycle *ac* susceptometer. All the *dc* magnetization measurements, Hall Effect measurements, and ρ-T variation with applied magnetic fields were done in an in-house PPMS system (Quantum Design).

6.3 Structural and superconducting properties of CaF_2 doped Sm1111

$Sm_{1-x}Ca_xFeAsO_{1-2x}F_{2x}$ bulk samples and the reference fluorine only doped samples were prepared as described in Section 6.2. The samples are labeled as Sm0 (SmFeAsO), Sm3 ($SmFeAsO_{0.7}F_{0.3}$), SmCa15 ($Sm_{0.85}Ca_{0.15}FeAsO_{0.7}F_{0.3}$) and SmCa2 ($Sm_{0.8}Ca_{0.2}FeAsO_{0.6}F_{0.4}$). The impact of simultaneous Ca^{2+} doping at Sm^{3+} (hole doping) and F^- doping at O^{2-} (electron doping) on the structural and superconducting properties of Sm1111 system is described in detail in the following sections.

6.3.1 Structural properties of CaF_2 doped Sm1111

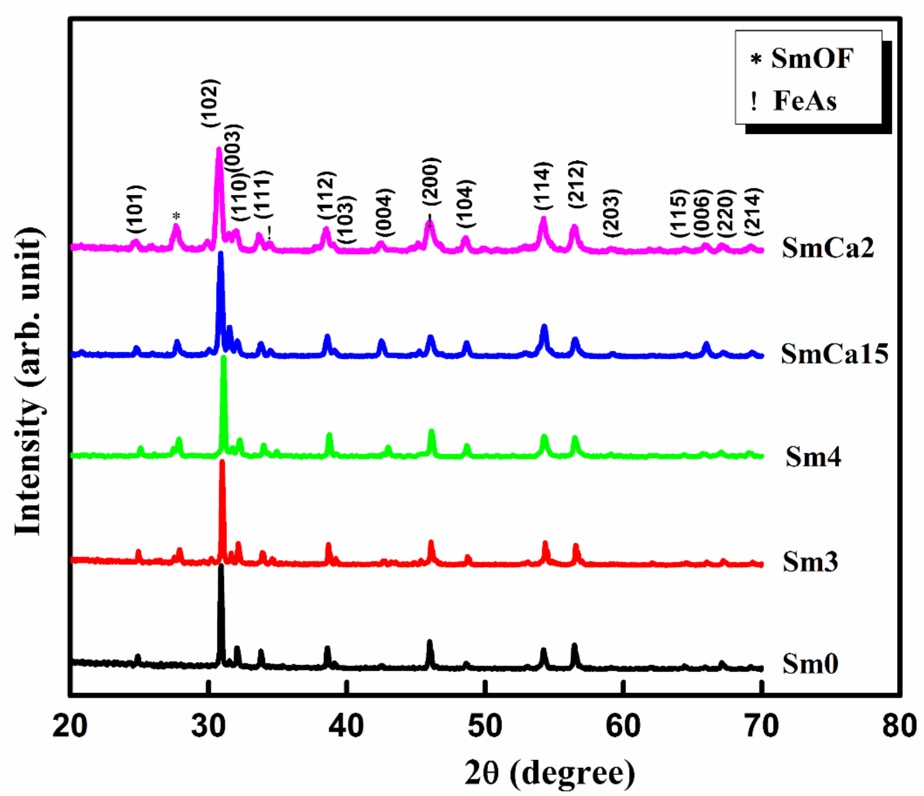

Figure 6.1: XRD patterns of the pure (Sm0), F doped (Sm3 and Sm4) and co-doped samples (SmCa15 and SmCa2)

Figure 6.1 shows the XRD patterns of all the samples and the main peaks have been indexed based on the tetragonal ZrCuSiAs-type structure (Nomura *et al.* 2008). The major phase SmFeAsO is formed with small amounts of SmAs and FeAs in all the samples. SmOF is present in all the samples except the parental compound. In the co-doped samples, there are no peaks corresponding to CaF_2 or any other Ca containing compounds. This indicates that Ca is completely incorporated into the crystal structure of the SmFeAsO superconductor. Considering the main peak (*102*) of the parental compound SmFeAsO, the peak of F doped sample, $SmFeAsO_{0.7}F_{0.3}$ shifts towards right and that of the co-doped samples, $Sm_{1-x}Ca_xFeAsO_{1-2x}F_{2x}$ shifts towards left systematically, as shown in Figure 6.2(a). The peak shift is reasonable since the ionic radius of this bivalent Ca^{2+} ion (1.00 Å) is larger than that of Sm^{3+} (0.95 Å). The left shift of the peak is well distinct and it increases with Ca concentration. The systematic shifting with Ca^{2+} doping strongly suggest that Ca^{2+} ions do get into the lattice structure of SmFeAsO. The initial reports on iron pnictides indicate a left shift of XRD peaks for hole doping and a right shift in the case of electron doping (Wen *et al.* 2008; Yang(b) *et al.* 2009), which attributes a lanthanide expansion in the former case and a lanthanide contraction in the latter one.

Table 6.1: Lattice parameters observed for the undoped, F-only doped and CaF_2 doped samples

Samples	Lattice Parameters	
	***a* (Å)**	***c* (Å)**
Sm0	3.9448	8.5080
Sm3	3.9369	8.4854
Sm4	3.9349	8.4789
SmCa15	3.9430	8.5027
SmCa2	3.9494	8.5140

The lattice constants *a* and *c* of all the samples were obtained from Rietveld refinements on the XRD data employing the Fullprof program and the values obtained are given in the Table 6.1. Both *a* and *c* values decreased in the F doped samples compared to the parent compound. On binary doping, both *a* and c values decrease with respect to the parent compound and then start to increase with increase in concentrations of Ca. The *a* value obtained for SmCa2 is higher than both the parent compound and the F doped one and this increment is reflected in the left shift of the (*102*) peak as seen in Figure 6.2(a). Usually, electron doping (F doping) reduces the *c* value as a result of the combined effect of the smaller ionic size of F^- than O^{2-} and the reduced coulomb repulsion between the conductive layer (FeAs) and charge reservoir layer (SmO). However, in the case of hole doping, the substitution of a larger bivalent element in the place of a smaller trivalent rare earth ion RE^{3+} enhances *c* value (Wen *et al.* 2008). Here, a combined effect of electron and hole doping can be seen. Up to an optimum Ca concentration the *c* value decreases i.e. electron doping effect is prominent and this probably arises from the decrease in inter layer distance between FeAs and SmO. Further doping of Ca increases the *c* value which indicates a dominance of hole doping effect.

The full width at half maximum (FWHM) was also estimated for three significant peaks of the XRD patterns of all the samples (Figure 6.2(b)). It is observed that the FWHM values for the co-doped samples are much higher than the pure and F doped samples and SmCa2 shows the highest value. All the samples are highly crystalline and the average grain size of the co-doped samples is found to be increasing (discussed in the succeeding section). Even though there is considerable increase in grain size, the FWHM values of the co-doped samples are also increasing. Hence, the increase in FWHM for co-doped samples can be attributed to the strain from substitutional defects created in the crystal lattice due to the combined addition of Ca^{2+} at Sm^{3+} site and F^- at O^{2-} site.

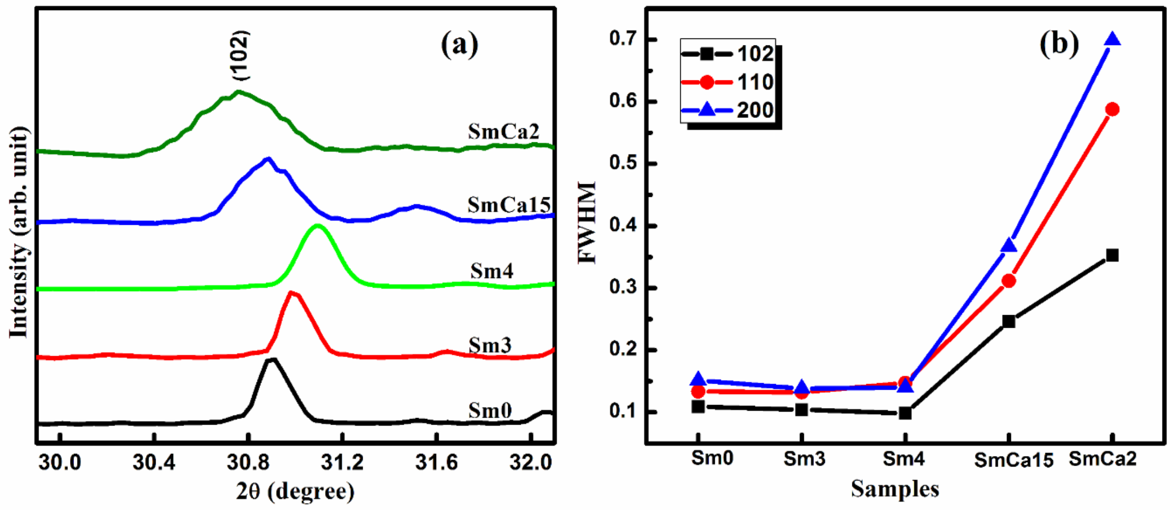

Figure 6.2: (a) Enlarged view of the (*102*) peaks of the XRD patterns of all the samples (b) FWHM of the (*102*), (*110*) and (*200*) peaks of the corresponding samples

An important observation from the powder XRD patterns (Figure 6.1) is the prominence of (*00l*) peaks in the co-doped samples (SmCa15 and SmCa2), which has never been observed in any iron pnictide compound so far. In the present case, all the (*00l*) planes are prominent in the co-doped samples. The peak height of SmCa2 is found to be lesser than that of SmCa15, yet remains higher than the pure and F doped sample. In BSSCO based superconductors (Vinu *et al.* 2009; Cecchetti *et al.* 2000), the orientation of such (*00l*) planes is always connected with the texturing of the samples and *c* axis alignment which in turn helps in increasing the J_C of the samples. In order to observe the impact of the (*00l*) plane alignment on the grain morphology, SEM images of freshly fractured surfaces of all the samples were taken and are shown in Figure 6.3.

A drastic change in the microstructure is observed for co-doped samples with respect to the pure and the F doped samples. In general, all the samples show flaky nature characteristic of iron oxypnictide superconductors. Regarding RE1111 systems, we have observed considerable change in the grain morphology on substituting RE site with other dopants (Anooja *et al.* 2013). In the present case, the flaky nature of the grains and the extent of layering and the grain size have enhanced dramatically with co-doping. Moreover, the microstructure of the co-doped samples is denser as compared to the parent and F doped samples. Among the co-doped samples, SmCa15 displays the best microstructure. Further doping of Ca, increases the misorientations in the microstructure compared to SmCa15, but maintains the morphology. The microstructural changes observed in the co-doped samples is attributed to the addition of CaF_2. It is known that calcium compounds can modify and control the microstructure of certain oxide ceramics and in some cases they promote abnormal grain growth with preferred orientation of grains

(Altay *et al.* 2003; Shuba *et al.* 2002; Tani *et al.* 2007). A close observation of the co-doped samples reveals that though the individual grains are layered extensively, the grains are oriented randomly. The grain orientation can be improved by mechanical working while translating these bulk samples into practical conductors.

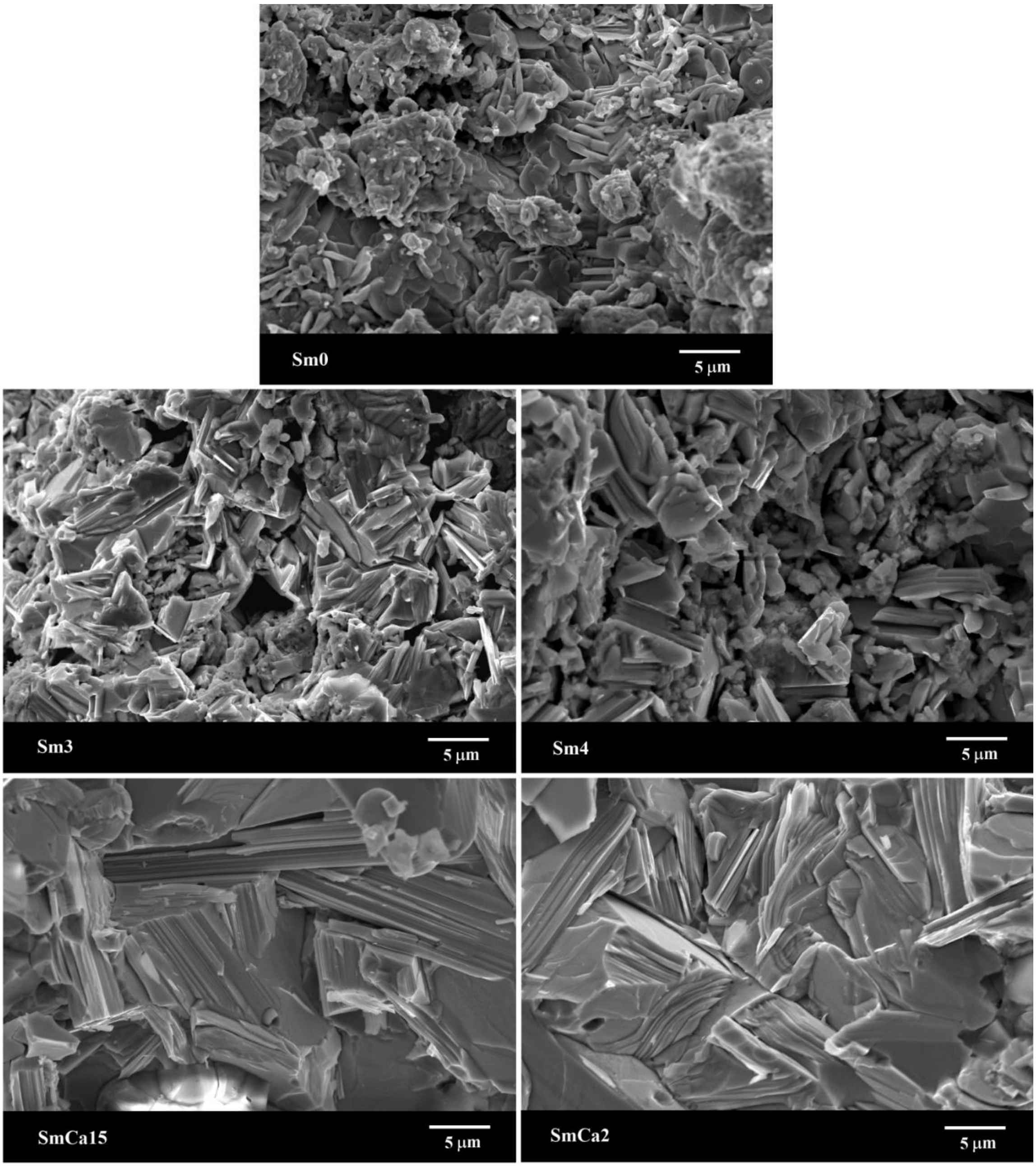

Figure 6.3: SEM images of the pure (Sm0), F doped (Sm3 and Sm4) and co-doped samples (SmCa15 and SmCa2)

6.3.2 Superconducting properties of CaF_2 doped Sm1111

The critical temperature (T_C) and critical current (I_C) of the all the samples have been determined using the standard four probe method. Figure 6.4 shows the resistivity versus temperature (ρ-T) plots of the CaF_2 doped Sm1111 samples with various doping concentrations and the inset of the Figure 6.4 shows their enlarged view around T_C. The T_C values obtained from the ρ-T plots are given in the Table 6.2.

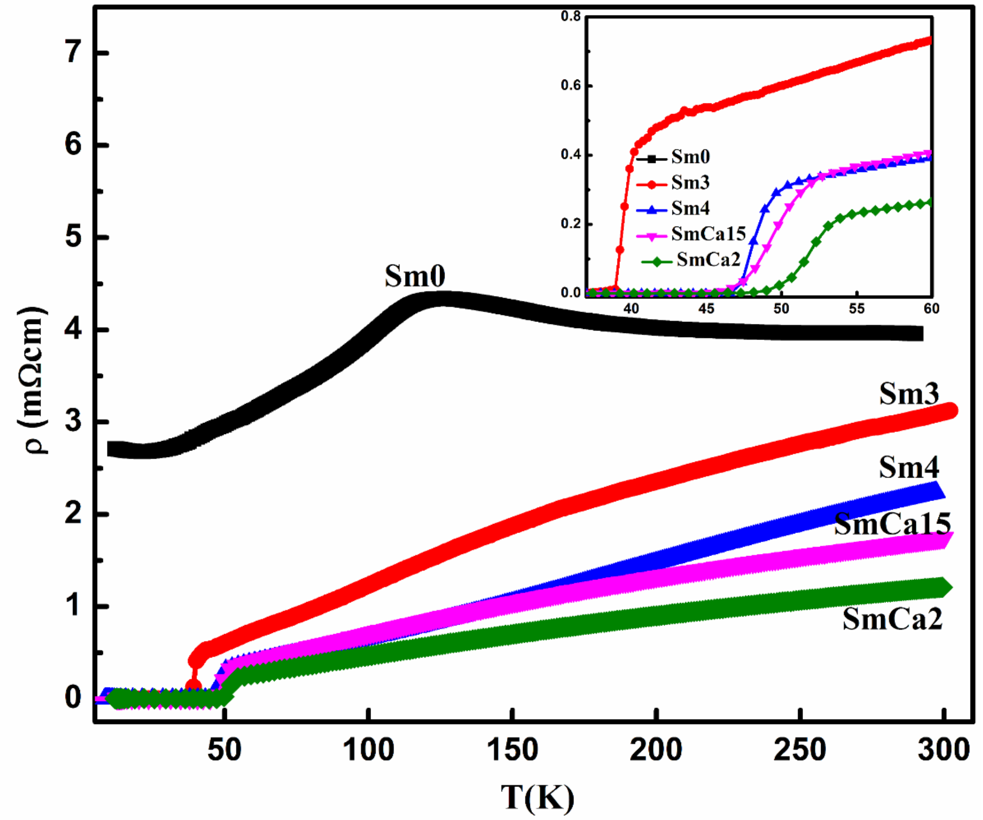

Figure 6.4: ρ-T plots of all the samples. The inset shows an enlarged view of the resistivity change close to T_C

Table 6.2: Electrical and superconducting parameters observed for the F-only doped and CaF_2 doped samples

Samples	T_C (K)		ρ_{300} (mΩcm)	RRR	I_C (A)	J_C (A/cm^2)
	ρ-T	χ-T				
Sm3	40.5	40.3	3.11	4.7	8.7	435
Sm4	49.6	49.5	2.21	6	10	500
SmCa15	52.0	51.7	1.74	4.7	17.6	880
SmCa2	53.8	53.5	1.21	5.2	15.1	755

In Sm0, the resistivity curve is almost linear at higher temperatures, from 150 K onwards it starts to increase gradually and forms a broadened peak around 130 K and decreases thereafter. This anomalous behavior in resistivity arises due to the structural and magnetic transitions occurring in this system (Margadonna *et al.* 2009; Ding(b) *et al.* 2008). In the F doped sample Sm3, the temperature dependence of resistivity above T_C deviates from its linearity and again decreases rapidly leading to superconducting transitions. These features are the indication of a pseudo gap regime existing in the samples resulting from the spin density wave instability (Solov'ev *et al.* 2009; Arushanov *et al.* 2011). But, the sample Sm3 shows a T_C of 40.5 K which is lower than the T_C reported for Sm1111 system elsewhere (Rotter *et al.* 2008; Anooja *et al.* 2012). The lowering of T_C, observed in the present case, is due to the volatile loss of fluorine at higher processing temperature (1150 °C). For co-doped samples, the ρ-T plots are almost linear down to T_C. However, by incorporating more Ca^{2+}, the charge concentration of the system is tuned appropriately. Fluorine doping increases the electron density in the conducting FeAs layer, meanwhile hole density increases by the replacement of Sm^{3+} ion with Ca^{2+}. On doping 15% of Ca at Sm site, the T_C reaches up to 52 K from 40.5 K and a maximum T_C of 53.8 K is achieved in SmCa2. Thus, it is inferred that higher T_C values reported for F doped Sm1111 samples can be easily achieved by co-doping of holes and electrons using CaF_2 as a single source. Apart from achievement of higher T_C the co-doping refines the microstructure also.

From the ρ-T plot, ρ_{300K} and RRR (residual resistivity ratio, RRR = ρ_{300K}/ρ_{55K}) were also calculated which give an insight into the sample quality; the values obtained are given in Table 6.2. The normal state resistivity of the co-doped samples reduces significantly and it again decreases with the increase in the doping concentration of Ca. As the amount of Ca^{2+} ions being incorporated at Sm^{3+} site increases, the T_C also increases. So the decrease in normal state resistivity and increase in T_C suggest the improvement in charge carrier concentration of the system by attaining a charge balance of holes and electrons. The higher RRR value and lower normal state resistivity indicate the lower impurity scattering and enhanced carrier density in the co-doped samples.

Since, we deliberately added both electrons and holes into the system, the electronic structure of the system would be possibly different from the solo electron doping and hole doping. In order to get an information about the majority charge carriers present in the system, Hall Effect measurements were conducted in the co-doped sample having maximum T_C, i.e. SmCa2. Figure 6.5 shows the measured transverse resistivity (ρ_{xy}) with respect to applied magnetic field at a fixed temperature of 100 K. As discussed in Chapter 3 the ρ_{xy} was evaluated from Hall voltage data measured by sweeping the magnetic field from -9 to 9 T and the observed data has been given in the inset of Figure 6.5. Hall coefficient (R_H) value of -5.9×10^{-9} m^3/C is obtained for SmCa2 and the negative value of R_H indicates that electrons are the majority charge carriers in the present binary doped system. This is obvious, since the doping concentration of F^- is double to that of Ca^{2+}. The carrier concentration within the sample, SmCa2 derived using the above R_H value is $1.1 \times 10^{27}/m^3$.

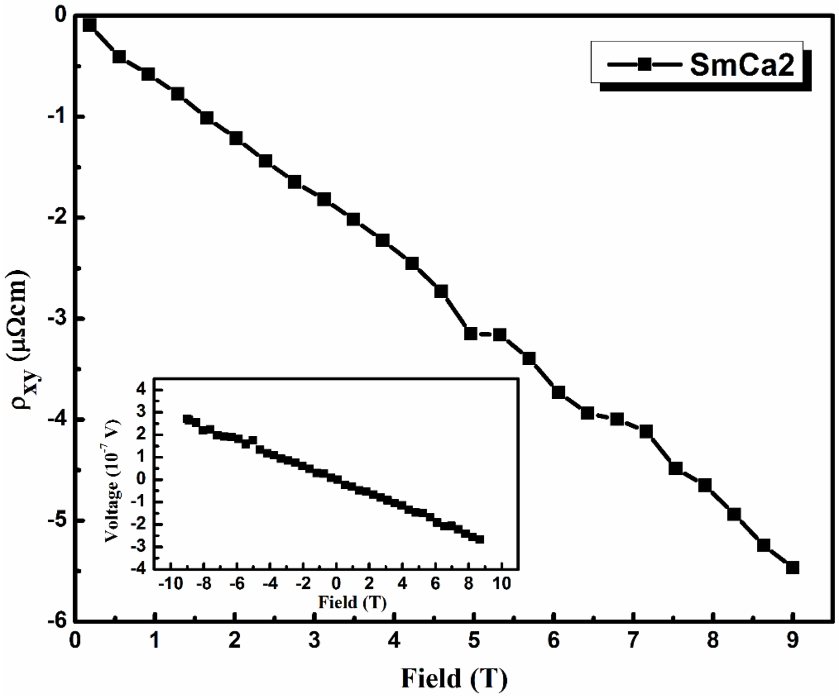

Figure 6.5: Hall resistivity, ρ_{xy} versus magnetic field of the sample SmCa2 at 100 K. Inset shows the measured Hall voltage at 100 K by varying the magnetic field from 9 to -9 T

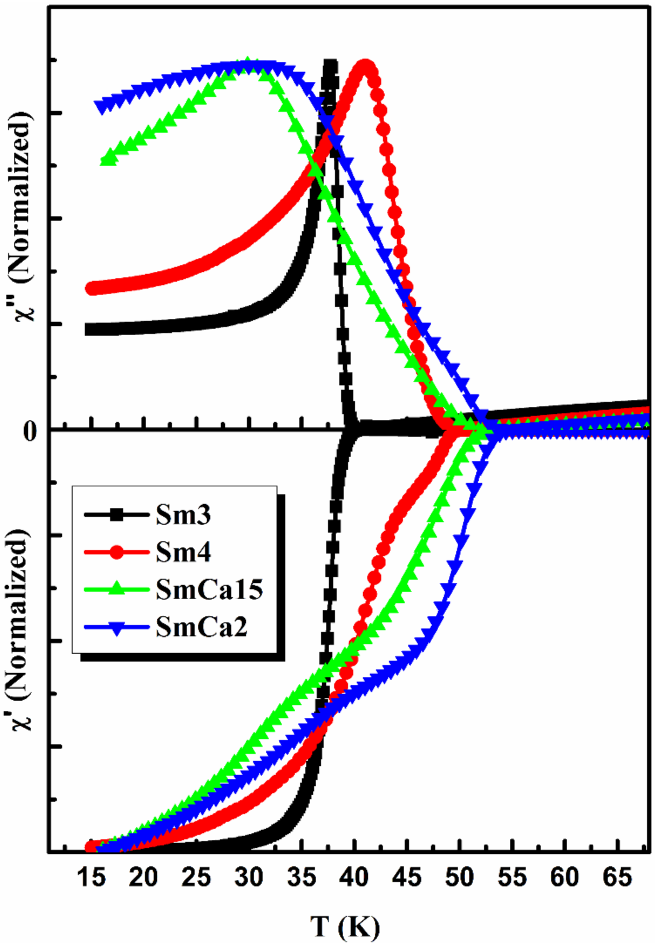

Figure 6.6: χ-T plots of F doped and CaF_2 doped samples at frequency, f = 208 Hz and *ac* field, H_{ac} = 4.94 × 10^{-4} T

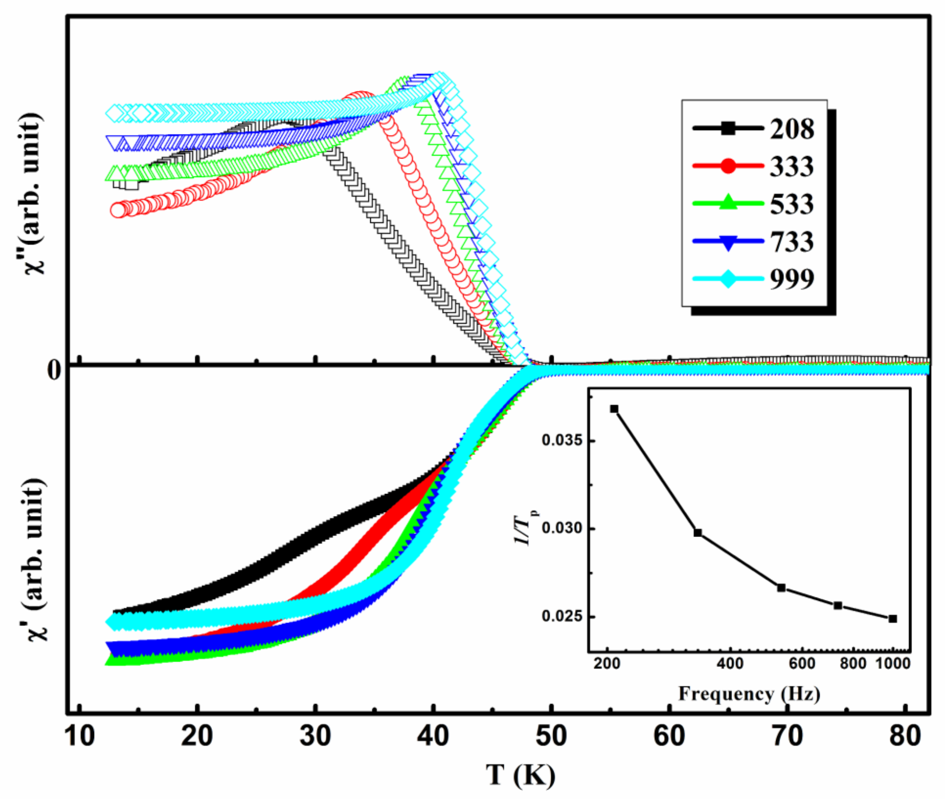

Figure 6.7: χ-T **plots of the co-doped sample SmCa15 at different frequencies. Inset shows the dependence of 1/T_P with frequency**

The T_C values of the samples were also verified using *ac* susceptibility studies and the values obtained are in good agreement with those from transport studies. Figure 6.6 shows the normalized *ac* magnetic susceptibility (χ' and χ'' have been normalized with χ'_{max} and χ''_{peak} respectively) of all the samples as a function of temperature (at frequency, f = 208 Hz and *ac* field, H_{ac} = 4.94 × 10^{-4} T). The temperature at which the real part (χ') undergoes a diamagnetic transition is taken as T_C and is given in Table 6.2. The *ac* magnetic susceptibility can be also used to study properties such as granularity, flux pinning and vortex dynamics of all type-II superconductors. The real part of *ac* magnetic susceptibility (χ') is a measure of the energy stored by the sample due to the diamagnetic response of the screening current induced in the superconductor by the external magnetic field, whereas the imaginary part (χ'') is proportional the energy converted into heat due to the vortex motion.

The real part χ' of both co-doped samples show double step transitions. The step like behavior of the real part of the χ-T plot is an indication of granularity present in our samples in which screening current may flow among the grains (intergrain current), and at the same time screening current flows inside the single grains (intragrain current). This feature is usually explained by the model of a ‘better’ phase embedded in a ‘worse’ matrix, such as intragrains embedded in intergrains or grains embedded in weak links (Gomory, F.

1997; Bonsignore *et al.* 2011). Hence, the contributions at high temperatures correspond to the response from individual grains of the material, while that at lower temperatures is due to the intergrain connectivity. In correspondence to each step in χ', there exists a peak in the imaginary part χ''. However, the peak near T_C is not clearly visible in the case of SmCa15. But for SmCa2, both the peaks are well resolved. The χ'' peak at a characteristic temperature (T_P) shifts prominently towards high temperature region and also broadens with increase in CaF_2 concentration. Moreover, for the co-doped samples, the depth of the first step related to intragrain diamagnetic response in χ' increased with increase in doping concentration. The χ-T measurements reported for doped variants of iron pnictides and also YBCO samples exhibit analogous features such as the decrease in peak height and peak broadening (Gomory, F. 1997).

Figure 6.7 shows the χ-T plots at different signal frequencies from 208 to 999 Hz for a typical sample SmCa15. The characteristic peak position T_P moves towards right and its height increases monotonically with increasing frequency. The frequency variation from 208 to 999 Hz leads to a T_P shift of about 12 K. The frequency dependence of χ is much higher than that reported for high T_C cuprates (Nikolo *et al.* 1989). The onset temperature of χ' is not modified by frequency; however, the double step nature of transition in χ' is suppressed above 533 Hz. This provides a clear indication that the amount of magnetic flux penetrating the superconductor decreases with increasing frequency. The thermally activated flux creep phenomenon proposed for conventional type-II superconductors can explain this type of behavior i.e. at higher frequencies; a higher temperature is required for flux creep to take place. The thermally activated flux flow and flux creep have a vital role in the $J_C(H)$ performance of high temperature superconductors and χ-T measurements at higher harmonics can help in analyzing this vortex dynamics. The strong frequency dependence of T_P obey the Arrhenius rate equation $f = f_0\exp(-U/k_BT)$, where f_0 is an attempt frequency and U is the activation energy for flux creep. Inset of Figure 6.7 is the $1/T_p$ versus frequency plot for the sample SmCa15. We can see that the characteristic temperature T_p exponentially depends on the *ac* field frequency.

Figure 6.8 shows the results of transport *I-V* measurements done on all the doped samples at 12 K (sample size ≈ 15 × 2 × 1 mm^3). The critical currents (I_C) of the samples were determined from the *I-V* plots using the standard criterion of 1μV/cm and the corresponding critical current densities (J_C) of the samples were calculated ($J_C = I_C /A$ where A, cross-sectional area) and given in Table 6.2. The I_C values of the co-doped samples are found to increase significantly and this is attributed to the combined effect of the modified microstructure and the considerable enhancement of T_C of the co-doped samples. A maximum transport I_C of 17.6 A at 12 K (J_C = 880 A/cm^2) was obtained for SmCa15 which exhibited the best microstructure. This shows that I_C is significantly enhanced at an optimum doping concentration of around x = 0.15, which is double to that of the solo F doped sample. Upon increasing the Ca concentration further, (i.e. x = 0.2), a slight decrease in I_C value occurs and this is because of its inferior microstructure in spite of its marginally higher T_C compared to the sample with x = 0.15.

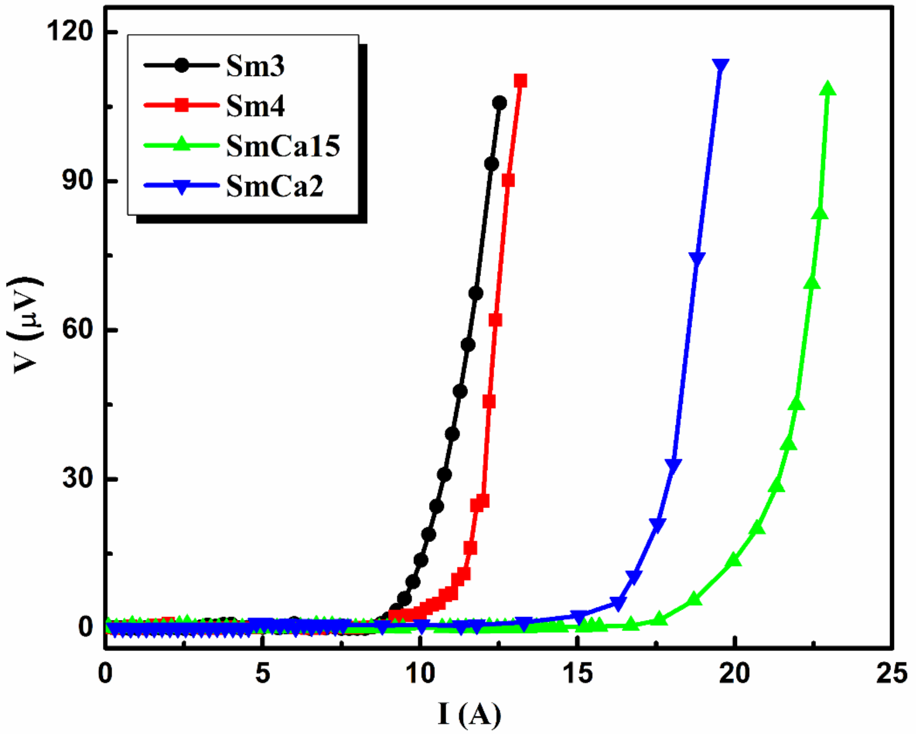

Figure 6.8: *I-V* plots of the F doped (Sm3 and Sm4) and co-doped samples (SmCa15 and SmCa2) measured at 12 K

Even though there are several reports on transport J_C in iron pnictides especially in Sm1111 and 122 systems, majority of those reports are on wires and tapes and only a few reports are available on bulk polycrystalline samples (Wang(a) *et al.* 2013; Fujioka *et al.* 2013; Kametani *et al.* 2009a). The only report on transport J_C in bulk samples is that observed in oxygen deficient - high pressure synthesized Sm1111 system (J_C = 463 A/cm^2 at 39 K) by the Kametani's group (Wang(a) *et al.* 2013). In the present work, a transport J_C as high as 880 A/cm^2 has been obtained by simultaneous doping of Ca^{2+} and F^- into Sm1111 system at ambient pressures. The transport J_C observed in the present sample, synthesized at ambient pressures, is a result of the refined microstructure with highly enhanced grain size and preferred orientation along (*00l*) plane achieved by CaF_2 doping. The influence of CaF_2 doping on the microstructure and preferential orientation along (*00l*) plane can be well exploited for the achievement of improved transport J_C in Sm1111 tapes. Majority of the *ac* susceptibility and *I-V* measurements conducted on RE1111 samples recurrently emphasize the inherent granularity and intergrain connectivity problems. Though several reports exist on doping studies, pressure effects and spectroscopic measurements in iron pnictides; only a few of them seem to be worthy in proposing a fruitful solution for conductor fabrication.

6.3.3 Conclusions

The overall analysis of CaF_2 doping in SmFeAsO system shows that along with a relatively high T_C, we could achieve a significantly high transport J_C. Microstructures of the doped samples are improved tremendously with a preferred orientation of the grains along (*00l*) planes particularly for the sample with x = 0.15 stoichiometry. The T_C is found to increase remarkably by binary doping with a maximum of 53.8 K. A transport J_C of 880 A/cm^2 is also achieved in the above bulk sample. On recalling the history of BSCCO based superconductors, it can be understood that the *c*-axis alignment and characteristic anisotropy of these compounds helped in attaining very high J_Cs in tape forms. Hence, it is expected that iron pnictide conductors with highly improved current carrying capacity can be realized if the misoriented grains are suitably aligned using thermo-mechanical processing as in the case of BSCCO based conductors.

6.4 Structural and superconducting properties of BaF_2 doped Sm1111

BaF_2 doped bulk samples of $Sm_{1-x}Ba_xFeAsO_{1-2x}F_{2x}$ were also prepared following the procedure as described in Section 6.2. The samples are labeled as SmBa15 ($Sm_{085.}Ba_{0.15}FeAsO_{0.7}F_{0.3}$) and SmBa2 ($Sm_{0.8}Ba_{0.2}FeAsO_{0.6}F_{0.4}$). The impact of simultaneous Ba^{2+} doping at Sm^{3+} (hole doping) and F^- doping at O^{2-} (electron doping) on the structural and superconducting properties of Sm1111 system is described in detail in the succeeding sections.

6.4.1 Structural properties of BaF_2 doped Sm1111

The XRD patterns of the BaF_2 doped samples along with that of F-only doped samples and undoped sample are shown in Figure 6.9. SmFeAsO is found to be the major phase formed in all the samples and the patterns are indexed in Figure 6.9. X-ray analysis also revealed that there are no peaks corresponding to BaF_2 or its derivatives in the co-doped samples, supporting the effective doping of BaF_2 in SmFeAsO system. In addition to the main phase, all the samples contain minor amounts of impurity phases such as FeAs and SmOF. An enlarged view of the main peak of the XRD pattern is given in Figure

6.10(a). It is seen that all the BaF_2 doped samples show a left shift compared to F-only doped and undoped samples. This left shift is due to the larger ionic size of Ba^{2+} ions with respect to Sm^{3+} ions.

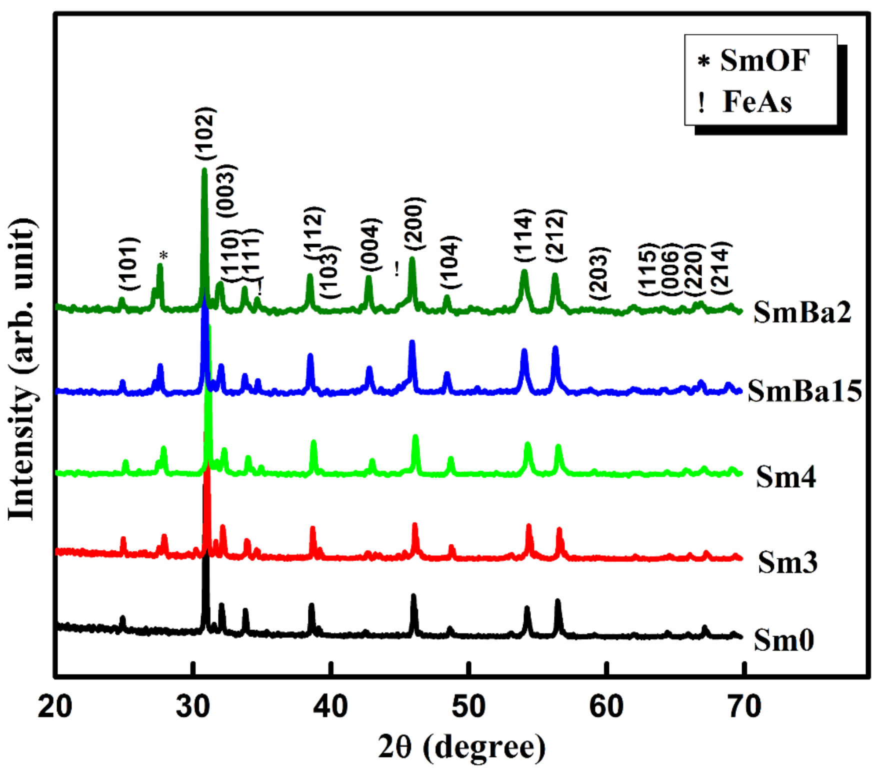

Figure 6.9: XRD patterns of the pure (Sm0), F doped (Sm3 and Sm4) and co-doped samples (SmBa15 and SmBa2)

Table 6.3: Lattice parameters calculated for the undoped, F-only doped and BaF_2 doped samples

Samples	**Lattice Parameters**	
	***a* (Å)**	***c* (Å)**
Sm0	3.9448	8.5080
Sm3	3.9369	8.4854
Sm4	3.9349	8.4789
SmBa15	3.9490	8.5107
SmBa2	3.9514	8.5210

This is also reflected in their lattice constant (*a* and *c*) values, calculated from the XRD pattern using Rietveld refinements. The lattice parameters calculated for all the samples are tabulated in Table 6.3. Higher *a* and *c* values were obtained for the BaF_2 doped samples. In short, doping with a larger ion led to elongation of the system. The higher lattice values and the corresponding left shift of the main peak in the XRD pattern again confirmed the effective incorporation of Ba^{2+} ions into the system. FWHM values of selected peaks were also calculated for each sample and the variation of FWHM with sample was plotted and is shown in Figure 6.10(b). Here, higher FWHM values are observed for BaF_2 doped samples. This result is similar to CaF_2 doped ones. Higher FWHM values are expected to occur either due to decreased grain size or increased lattice strain.

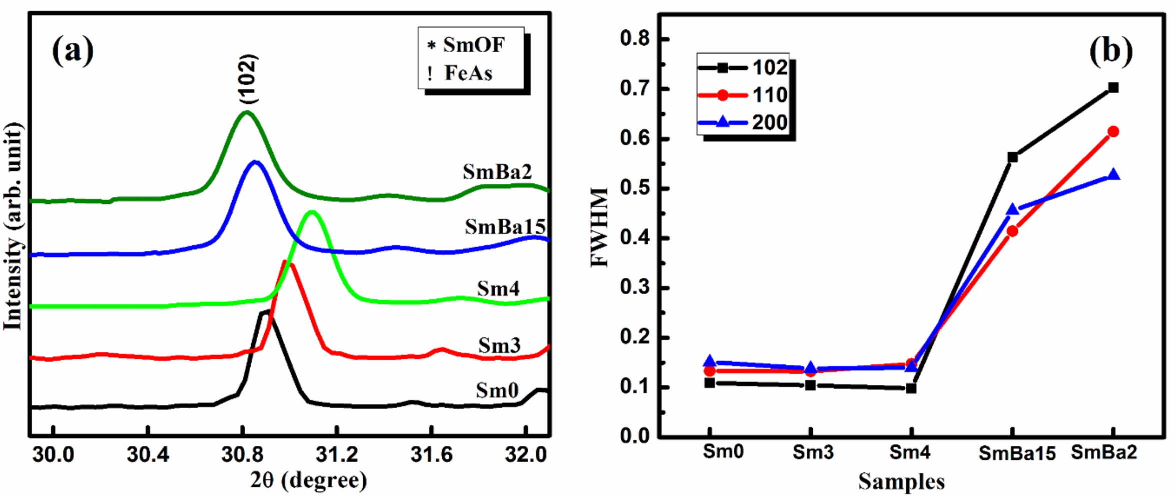

Figure 6.10: (a) Enlarged view of the (*102*) peaks of the XRD pattern of all the samples (b) FWHM of the (*102*), (*110*) and (*200*) peaks of the corresponding samples

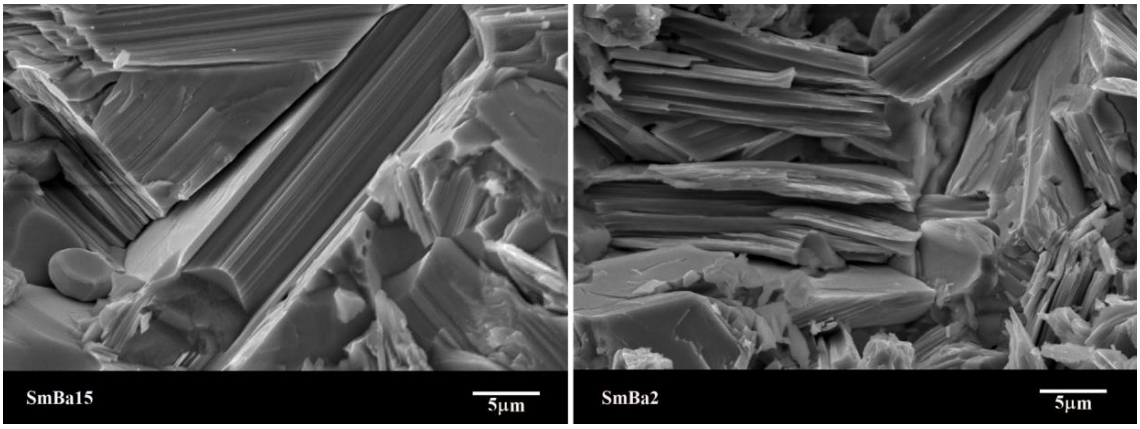

Figure 6.11: SEM images of the co-doped samples (SmBa15 and SmBa2)

Figure 6.11 shows the SEM images of the co-doped samples, SmBa15 and SmBa2. A drastic change in microstructure is also observed with BaF_2 doping in Sm1111 system with respect to the pure **(**Sm0) and F doped (Sm3 and Sm4) samples as shown in Figure 6.3 and 6.11. The extent of layering and the grain size have been improved considerably. Moreover, the density of the samples increases by co-doping. Similar to CaF_2 doping, BaF_2 is also found to assist the abnormal grain growth. However, the layered grains are oriented randomly. The increased grain size observed in the microstructure of the co-doped samples rules out the possible influence of grain size in FWHM. Thus, it is inferred that lattice strain due to substitution is the solo reason of increase in FWHM. Larger size difference between Ba^{2+} and Sm^{3+} ions has produced higher strain into the system, thereby increase the FWHM values in spite of the larger grains.

6.4.2 Superconducting properties of BaF_2 doped Sm1111

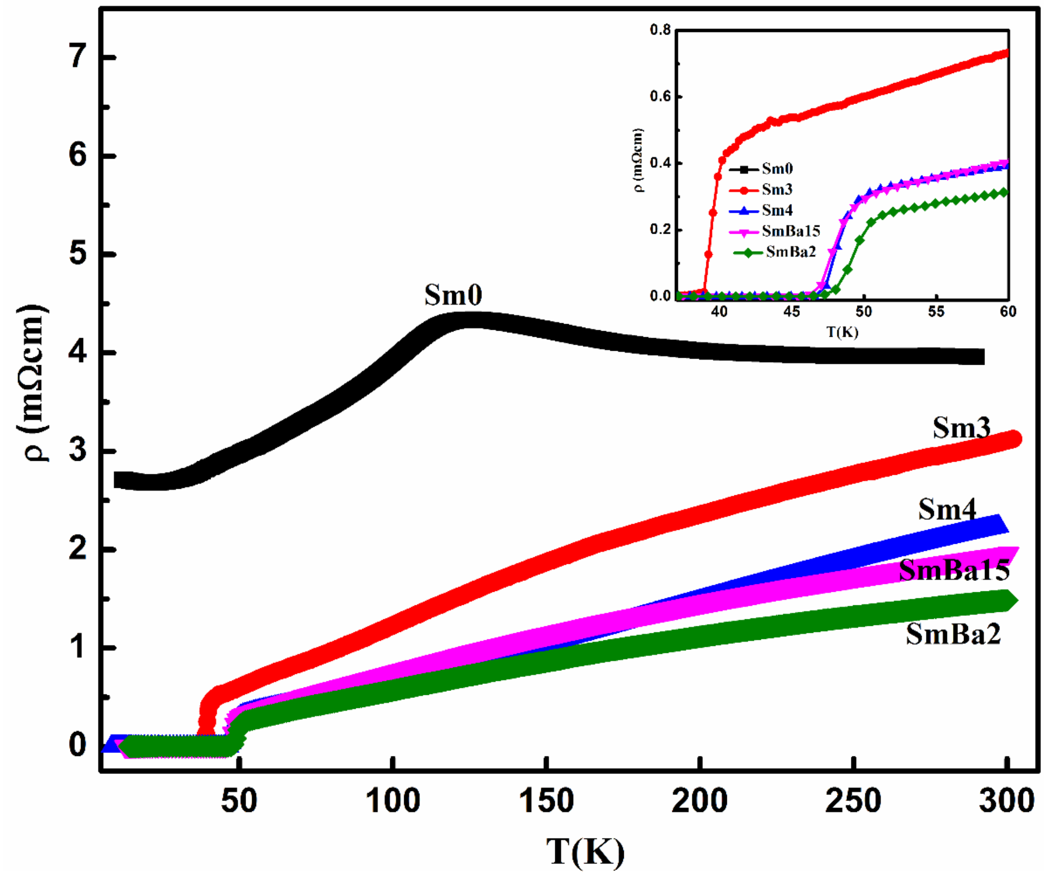

Figure 6.12: ρ-T plots of undoped, F doped and BaF_2 doped samples. The inset shows an enlarged view of the resistivity change close to T_C

Resistivity versus temperature measurements were done in BaF_2 doped samples and compared with that of F-only doped samples and undoped sample. Figure 6.12 shows the resistivity versus temperature plots of all the BaF_2 doped samples. The inset shows an enlarged view of the resistivity change in the vicinity of T_C. The obtained T_C values are given in Table 6.4. The T_C values increase with BaF_2 doping and a maximum T_C of 51 K is obtained for the sample SmBa2. Comparing with F-only doped samples, we can see that the sample SmBa15 shows higher T_C (T_C = 49.4 K) than the corresponding F alone doped sample, Sm3 (T_C = 40.5 K). However at higher concentration of Ba, the T_C enhancement is marginal with respect to the corresponding F-only doped, Sm4. Upon BaF_2 doping, the charge concentration of the system increases considerably by simultaneous doping of both Ba^{2+} at Sm^{3+} site and F^- at O^{2-} site which favors the T_C enhancement. However, the very large ionic radius of Ba^{2+} ion results in lattice elongation and the increased separation between layers reduces the charge transfer between the charge reservoir and conduction layers in the system. Hence, on increasing the doping concentration of BaF_2 (x = 0.2), these two effects limit the T_C enhancement. Consequently, the T_C of SmBa2 (T_C = 51K) is not as high as compared to that of F-only doped sample Sm4 (T_C = 49.6 K). The normal state resistivity at room temperature and residual resistivity ratio were also calculated from the ρ-T plots of the samples and are given in Table 6.4. Lower ρ_{300K} values and higher RRR values were also found for BaF_2 doped samples indicating the better quality of the samples.

Table 6.4: Electrical and superconducting parameters observed the F-only doped and BaF_2 doped samples

Samples	T_C (K)		ρ_{300} (mΩcm)	RRR	I_C (A)	J_C (A/cm^2)
	ρ-T	χ-T				
Sm3	40.5	40.3	3.11	4.7	8.7	435.0
Sm4	49.6	49.5	2.3	6	10	500.0
SmBa15	49.4	49.2	1.96	5.4	17.5	875.0
SmBa2	51.0	50.7	1.49	5.3	16.6	830.0

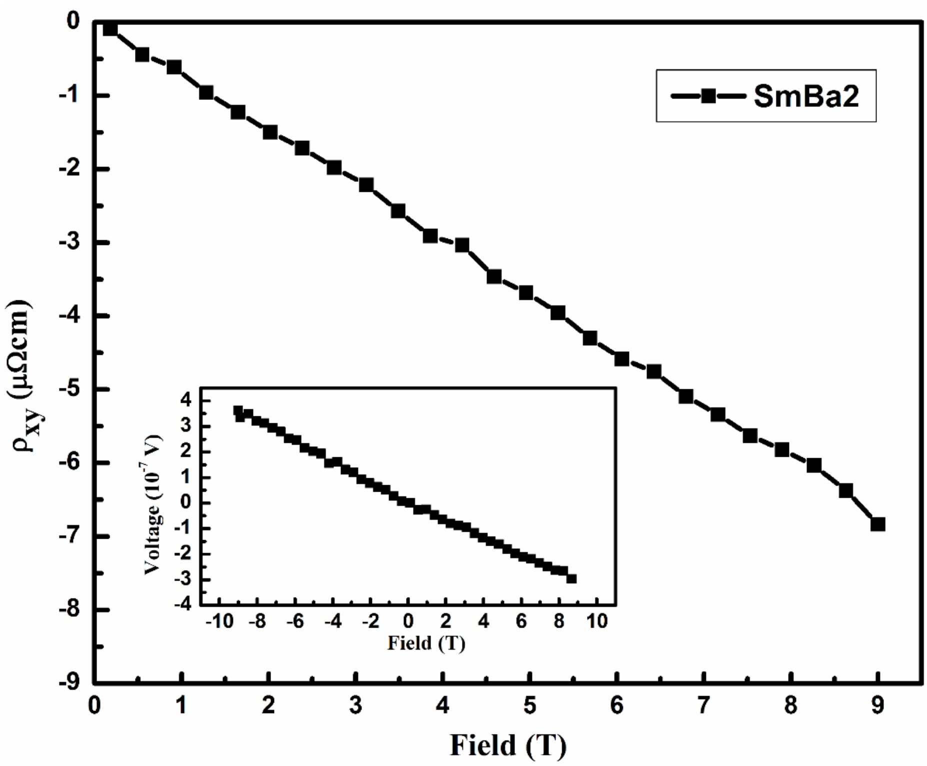

Figure 6.13: Hall resistivity, ρ_{xy} versus magnetic field of the sample SmBa2 at 100 K. Inset shows the measured Hall voltage at 100 K by varying the magnetic field from 9 to -9 T

The majority charge carriers within the BaF_2 doped sample with maximum T_C was also determined from the Hall Effect measurement. The ρ_{xy} with applied magnetic field at a fixed temperature of 100 K and the corresponding Hall voltage data from -9 to 9 T are given in Figure 6.13. The sample SmBa2 has an R_H value of -7.5×10^{-9} m^3/C which implies that the majority charge carriers in the system are electrons. However, the higher R_H value compared to that of smCa2 indicates that the BaF_2 doped system has a lower charge carrier density than the CaF_2 doped ones. The estimated carrier density for SmBa2 is $0.8 \times 10^{27}/m^3$. This is because of the relatively lower lattice shrinkage in the BaF_2 doped sample (as observed from XRD) which limits the charge transfer from the reservoir layer to the conductive FeAs block.

The *ac* susceptibility data of the BaF_2 doped samples along with that of F-only doped samples are given in the Figure 6.14. All the measurements were done at a frequency, f = 208 Hz and an *ac* field, $H_{ac} = 4.94 \times 10^{-4}$ T. The T_C values found from χ-T plots are given in Table 6.4 and the values are almost same as those obtained from the ρ-T measurement. The real part, χ' of the BaF_2 doped samples exhibits double step transitions which is an indication of the flow of both the intergrain and intragrain currents through the samples. With respect to each transition in the real part, well resolved peaks are also observed in their corresponding imaginary part, χ''. The near T_C peak results from *ac* field penetration into the center of the grains or occurs from the intragrain pinning existing in the samples. The presence of near T_C peak in the BaF_2 doped samples indicates the improved intragrain pinning within the samples as a result of combined substitution of Ba^{2+} and F^- at Sm^{3+} and O^{2-} sites, respectively. The lower temperature peak in χ'' occurs due to the penetration of *ac* field through the weak links prevailing between the grains.

The frequency dependence of χ with temperature for the co-doped sample SmBa15 is shown in Figure 6.15. The selected frequencies are 208, 333, 533, 733 and 999 Hz. The susceptibility, χ shows a strong dependence on the frequency of the applied *ac* field. It is also seen that this frequency dependence is much more enhanced than that of the sample SmCa15 (Figure 6.7). The characteristic temperature T_p shifts to higher temperature and the height of the χ'' peak at T_p increases with increasing the frequency. This type of behavior of χ'' peak at T_p on increasing the frequency is usually observed if the intergrain vortex lattice is in the vortex glass phase (Bonsignore *et al.* 2011). The depth of diamagnetic response from the intragrain part (near T_C step) decreases upon increasing the frequency. One can also observe that the corresponding χ'' peak is not well resolved above 533 Hz and disappears at f = 999 Hz. At the lower temperature region both χ' and χ'' show strong frequency dependence. The exponential dependence of T_p on frequency ($f = f_0\exp(-U/k_BT)$) is given in the inset of Figure 6.15.

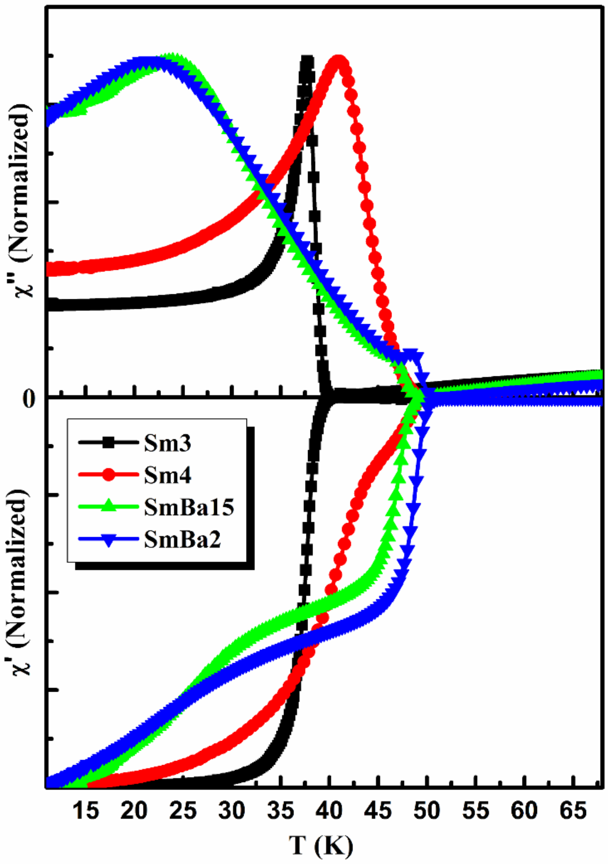

Figure 6.14: Normalized χ-T plots of the F doped and BaF$_2$ doped samples at frequency, f = 208 Hz and *ac* field, $H_{ac} = 4.94 \times 10^{-4}$ T

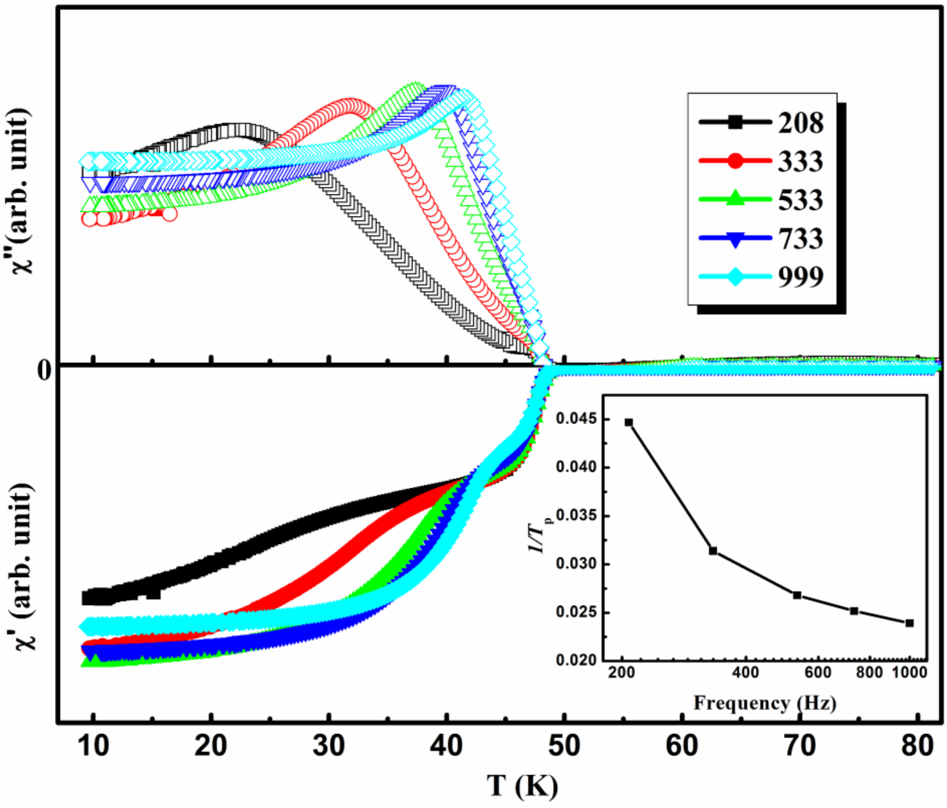

Figure 6.15: χ-T plots of the co-doped sample SmBa15 at different frequencies. Inset shows the dependence of 1/T_P with frequency

The Transport critical current (I_C) of the BaF_2 doped samples were calculated from the *I-V* measurements carried out using the standard 1 μV/cm criteria. The obtained *I-V* data (at T = 12 K) along with the data of F-only doped samples are shown in the Figure 6.16. The I_C values and the corresponding J_C values are given in Table 6.4. As observed in CaF_2 doped samples, the BaF_2 doped samples also yield high transport critical current density. This is mainly due to the refined microstructure and the enhanced grain size achieved as a result of BaF_2 doping. The sample SmBa15 has shown the maximum J_C. The J_C values obtained for the co-doped samples SmBa15 and SmBa2 are 875 A/cm^2 and 830 A/cm^2 respectively.

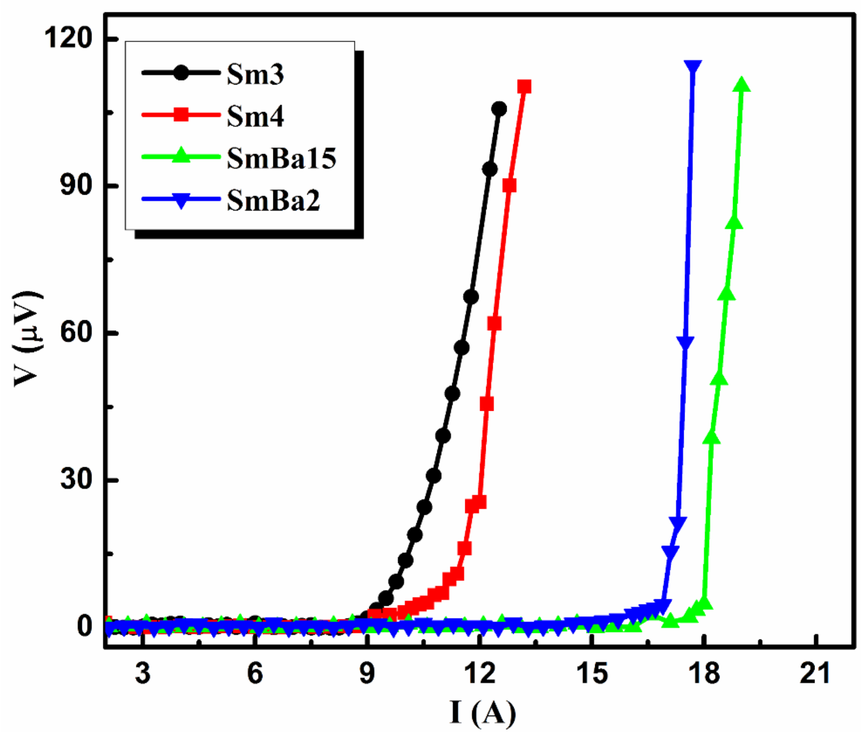

Figure 6.16: *I-V* plots of the F doped (Sm3 and Sm4) and co-doped samples (SmBa15 and SmBa2) measured at 12 K

6.4.3 Conclusions

In conclusion, BaF_2 doping in Sm1111 system improved both structural and superconducting properties as observed for the CaF_2 doped samples. Regarding the structural properties, substantial refinement in microstructure is obtained for the co-doped samples SmBa15 and SmBa2. BaF_2 doping also enhances the T_C value, but the increment is only marginal as compared to the CaF_2 sample. This is due to the relatively large ionic size of Ba^{2+}. *AC* susceptibility analysis reveals the presence of both intragrain and intergrain currents; however the intergrain contribution shows stronger frequency dependence than the CaF_2 doped samples suggesting the possibility of vortex glass phase at lower temperatures. Transport *I-V* measurements also confirm that the BaF_2 doped samples also can sustain higher J_C values as in the case of CaF_2 doped samples.

6.5 Magnetic properties of binary doped Sm1111 bulk superconductors

Studies on *dc* magnetic properties conducted on selected samples have been discussed in this section. The behavior of the samples in presence of a magnetic field gives an insight into their J_C-H performance and lower and upper critical field values (H_{C1} and H_{C2}). The magnetic characterizations done on the samples include magnetic moment versus field (*M-H*) measurements at different temperatures below the critical temperature of the samples and ρ-T measurement under varying magnetic field from 0 to 9 T. The samples chosen for magnetic field characterizations are SmCa15, SmBa15 (binary doped samples having maximum transport J_C) and the corresponding F-only doped sample Sm3.

The *dc* magnetic hysteresis curves (*M-H* plots) obtained for the samples at two temperatures (5 and 20 K) are given in the Figure 6.17. The applied magnetic fields varied between 0 to 9 T. Samples in the form of powder were used for this measurement and the obtained moments have been normalized with respect to their corresponding weight (i.e. moment in emu/g). The width of the hysteresis loop is the contributions of flux pinning prevailing inside the samples (irreversible magnetization) and from the paramagnetic moments present in the samples. The *M-H* loops shown in Figure 6.17 are not symmetric about the x-axis. The paramagnetic background present in the samples give rise to an upturn of the *M-H* loops towards a positive moment value, that is more pronounced for the sample SmBa15 due to the extra paramagnetic contribution from of Ba^{2+} ions in addition to Sm^{3+}. The paramagnetic contribution (M_P) has been calculated using the equation $Mp = (M^+ + M^-)/2$, here M^+ and M^- are moments in the field-increasing branch and field-decreasing branch, respectively. From Figure 6.17, it is clearly observed that the loop widths of co-doped samples (SmCa15 and SmBa15) are significantly larger than the F-only doped sample (Sm3) at both temperatures.

The *M-H* measurement of the samples in the low field region gives an indication about their lower critical field, H_{C1}. Figure 6.18 is an enlarged view of the *M-H* curves in the low field region at 5 K. The samples display a negative moment with increasing applied magnetic field up to a particular field and there after the values start increasing. The negative moment results from the diamagnetic response of the samples and after that particular field the moment shows a deviation from the decreasing nature due to the field penetration within the samples. The field corresponding to this deviation can be taken as the H_{C1} of the samples. The H_{C1} values obtained are 0.12 T for Sm3 and 0.14 T for both the co-doped samples.

In order to evaluate the irreversible magnetic contribution alone, we have to subtract the paramagnetic component from the data. The Mp subtracted curves for the samples are shown in Figure 6.19. At 5 and 20 K the co-doped samples have significantly larger loop widths (ΔM) than the sample Sm3. The larger hysteresis loop widths of the co-doped samples indicate their strong pinning properties than the F-only doped sample. The samples display maximum ΔM value in low field region, more specifically around their lower critical field. At 5 K, the co-doped samples (SmCa15 and SmBa15) show almost similar behavior throughout the entire magnetic field studied and their values are competing. Beyond H_{C1}, ΔM values of all the samples decrease exponentially and then remain constant for further increase in field. But at 20 K, the width of the sample SmCa15 displays a decreasing tendency in the high field region. However, in the low field region both the co-doped samples have higher loop width than Sm3. The sample SmBa15 more or less maintains the same loop width throughout the entire magnetic field at both temperatures. We can also see that the loop widths of all the samples decrease largely with increase in temperature.

From the M-H data of powdered samples, the critical current density within the grains, (J_{Clocal}) has been derived using the equation $J_{Clocal} = 30\ \Delta M/\langle r\rangle$, where $\langle r\rangle$ is the grain size estimated from the SEM images of the samples. Average grain sizes of 5 μm for sm3 and 8 μm for co-doped samples respectively were taken for calculating J_{Clocal}. Figure 6.20 shows the magnetic field dependence of J_{Clocal} at temperatures 5 and 20 K. At 5 K, both SmCa15 and SmBa15 have higher J_C values than that of Sm3, especially in the high field region. A maximum intragrain J_C (J_{Clocal}) of around 9×10^5 A/cm^2 is obtained for both the co-doped samples in the low field region at 5 K. With the application of magnetic field, the J_C of the samples first decreases and then remains almost constant above 4 T. That is, the samples show field independent behavior in the range 4-9 T. Hence, the co-doped samples also exhibit better J_C-H performance than that of the F-only doped sample at temperatures far below T_C. At 20 K, the self-field J_C value of SmCa15 is as high as that of SmBa15 and higher than Sm3. But, we can see that the J_C of SmCa15 does not show the field independent behavior, it gradually decreases with increasing field up to the maximum applied field and the values are still higher than that of Sm3. However, the BaF_2 doped sample shows better J_C-H performance over the entire magnetic field and temperature studied. At 20 K the samples Sm3 and SmBa15 also exhibit peak effect in the high field region. Additional lattice defects created by Ba^{2+}/Ca^{2+} doping apart from fluorine doping act as pinning centers and thereby improve their flux pinning properties both in self-field and in the presence of applied fields up to 9 T. However, at higher temperatures and fields the pinning property of BaF_2 doped sample is superior to that of CaF_2 doped sample.

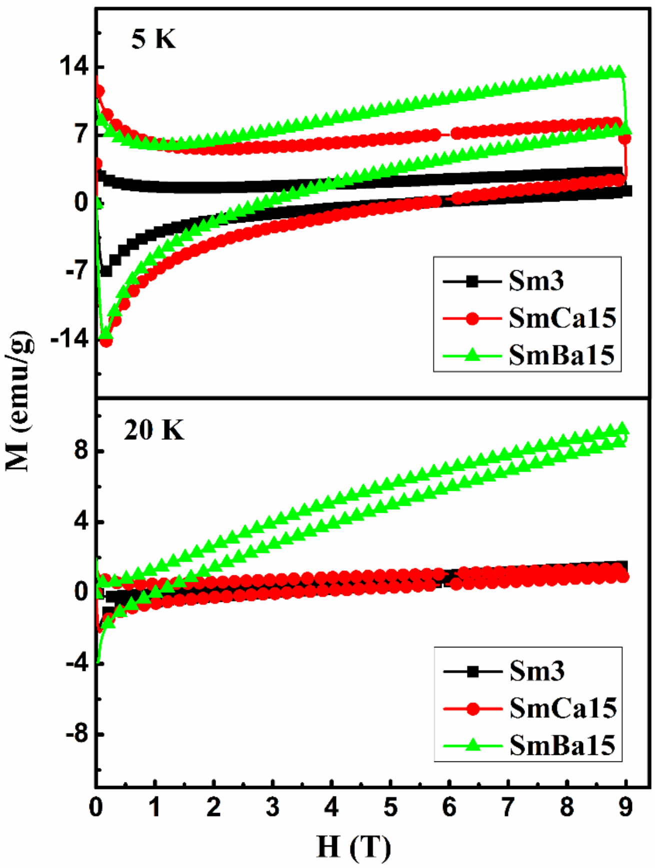

Figure 6.17: *M-H* plots of the samples Sm3, SmCa15 and SmBa15 at temperatures 5 and 20 K

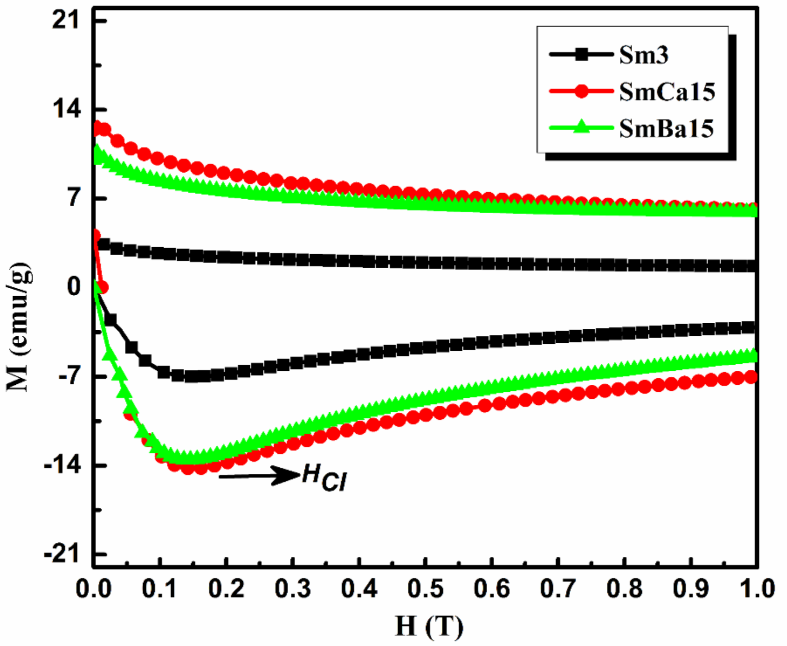

Figure 6.18: An enlarged view of the *M-H* curves in the low field region at 5 K

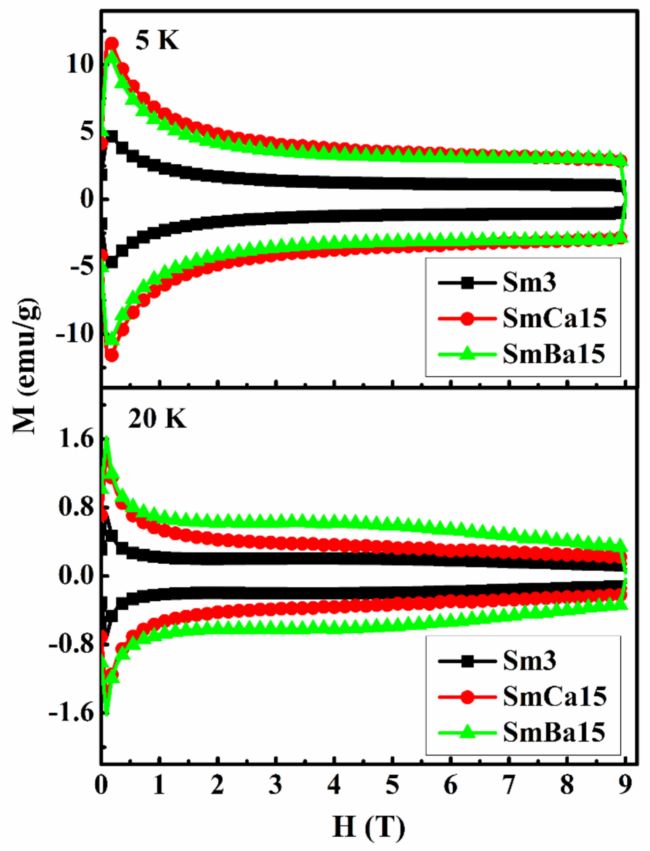

Figure 6.19: The paramagnetic background subtracted hysteresis curves for the samples Sm3, SmCa15 and SmBa15 at temperatures 5 and 20 K

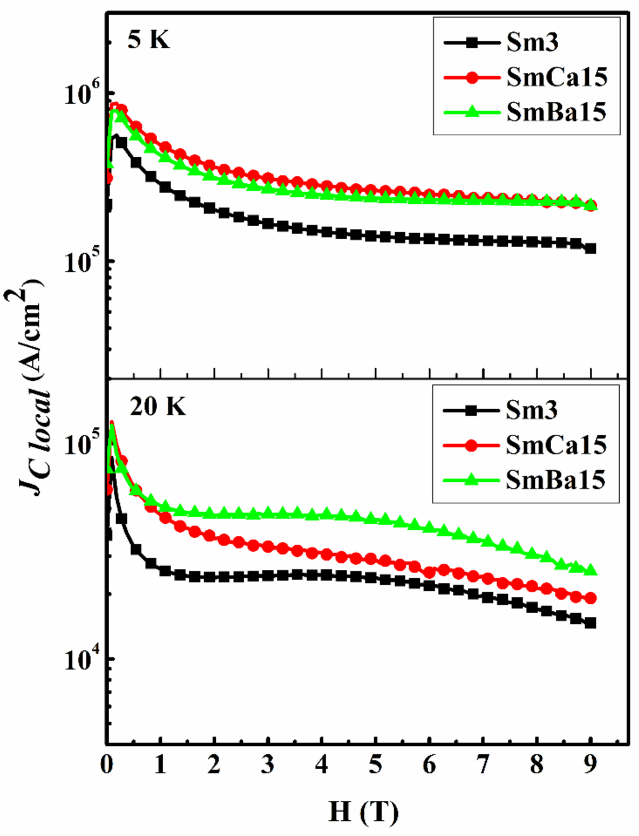

Figure 6.20: Magnetic J_C derived from the *M-H* plots for the samples Sm3, SmCa15 and SmBa15 at temperatures 5 and 20 K

The variations in resistivity versus temperature plots of the selected samples under different magnetic fields up to 9 T is shown in Figure 6.21. All the graphs are normalized with respect to the resistivity value at temperatures just above their T_C. The transition width broadened with the application of field for all the samples. The upper critical fields (H_{C2}) and irreversibility fields (H_{irr}) of the samples have been calculated from this data using the criteria of 90% and 10% of ρ_n, where ρ_n is the resistivity value just above transition.

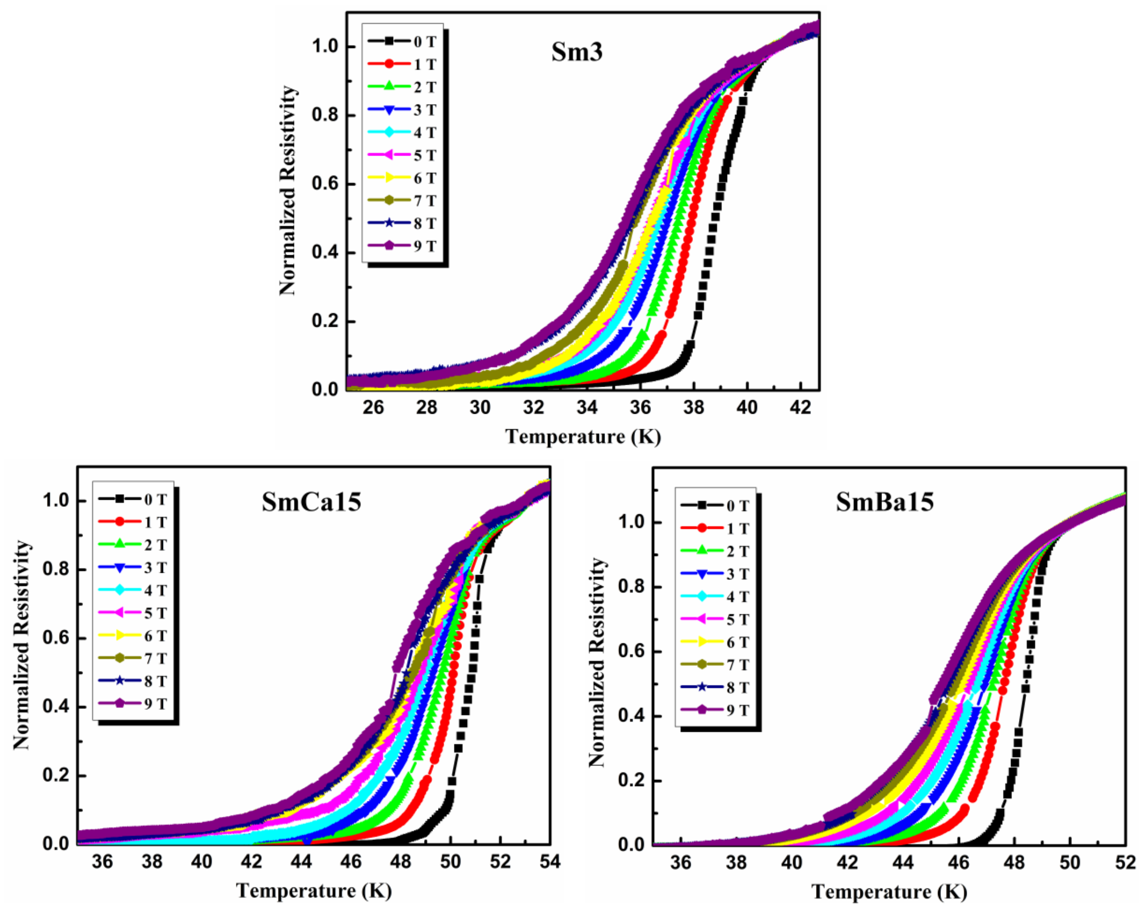

Figure 6.21: ρ-T plots under different magnetic fields varying from 0-9 T for the samples Sm3, SmCa15 and SmBa15

Then the H-T phase diagram of the samples was plotted as shown in Figure 6.22, for both H_{C2} and H_{irr}. From the plots $H_{C2}(0)$ and $H_{irr}(0)$ values were estimated for all the samples using the WHH formula: $H_{C2}(0) = -0.693T_C\ [dH_{C2}/dT]_{TC}$. Here, for easy comparison the temperature axis is normalized with their corresponding T_C. The slope $[dH_{C2}/dT]_{TC}$ obtained for the samples Sm3, SmCa15 and SmBa15 are -6.4, -7.6 and -11.4 T/K, respectively. The corresponding $H_{C2}(0)$ values evaluated are 179, 273 and 354 T, respectively. Interestingly, the co-doped samples are found to have larger slope values than the sample Sm3. Among the co-doped samples SmBa15 displays the maximum slope and hence has the maximum H_{C2} value (354 T) which is extremely high. The enhanced flux pinning capability of the co-doped samples results from the simultaneous doping at both Sm^{3+} and F^- sites using alkaline earth metal fluorides and this could be responsible for their high H_{C2} values. The H_{irr} values of the samples have been also estimated and are 36 T for Sm3, 43 T for SmCa15 and 53 T for SmBa15. Here again, reasonably high H_{irr} values are achieved for the co-doped samples.

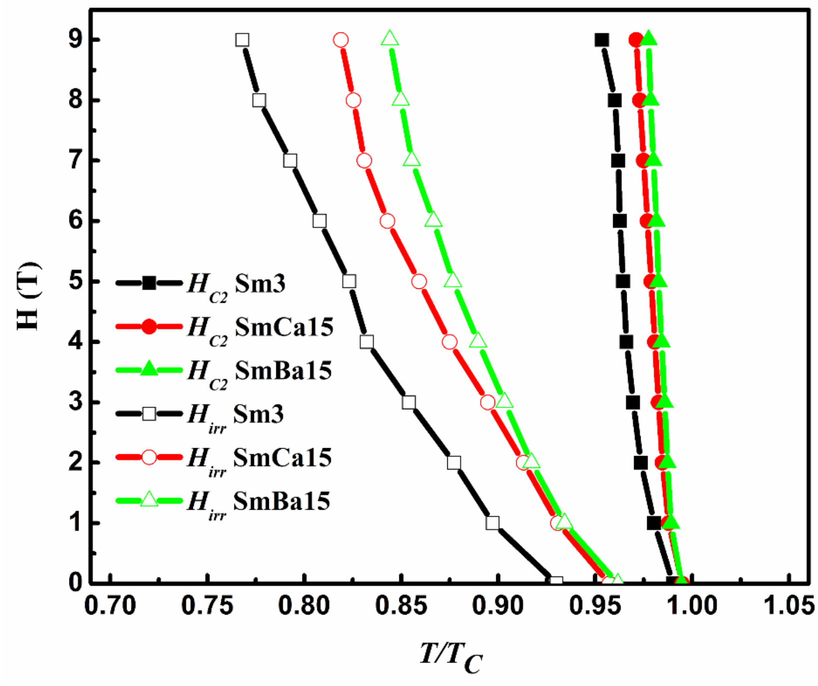

Figure 6.22: *H-T* phase diagram of the samples Sm3, SmCa15 and SmBa15

In short, the co-doped samples (CaF_2 and BaF_2 doped ones) are found to have highly enhanced magnetic properties besides their improved microstructural and superconducting properties compared to the F-only doped samples. Better J_C-H behavior and substantially high values of H_{C2} and H_{irr} are achieved for the alkaline earth metal fluoride doped samples due to the enhanced flux pinning properties. Among the co-doped samples the BaF_2 doped sample has yielded much better properties even better than the CaF_2 doped sample at higher magnetic fields. Relatively larger ionic size of Ba^{2+} definitely creates more lattice mismatch which results in enhanced flux pinning.

6.6 Summary of binary doping study

The combined effect of electron and hole doping in SmFeAsO system was investigated by simultaneous substitution of Ca^{2+}/Ba^{2+} at Sm^{3+} site and F^- at O^{2-} site in the parental system using a single source of alkaline earth metal fluorides namely, CaF_2 and BaF_2. The critical temperature is found to increase remarkably by this binary doping. One of the interesting observations in this study is that alkaline earth metal fluoride doping in Sm1111 system has made tremendous improvement in the microstructure of the co-doped samples as depicted in the SEM images. Consequent to the dramatic change in microstructure and the significant enhancement in T_C, the transport J_C of the co-doped samples increases remarkably. The transport J_C is doubled for the co-doped samples SmCa15 and SmBa15 with respect to the solo F doped sample. Another motivating aspect of CaF_2 doping is the achievement of preferred orientation of the (*00l*) planes as seen in XRD. This result strongly indicates the scope for development of SmFeAsO based conductors with higher current carrying capacity by properly aligning the preferentially oriented planes of the system along a single axis by methods such as PIT, as done in the case of BSCCO based tapes. The in-field properties of Sm1111 system have been also enhanced considerably by the alkaline earth metal fluoride doping. Improved flux pinning gained from additional defects created by Ca^{2+}/Ba^{2+} doping leads to superior J_C-H performance and upper critical field for the co-doped samples than the F-only doped samples. In short, the binary dopants of CaF_2 and BaF_2 seem to be potential candidates for solving the grain connectivity concerns in iron pnictides paving the way towards conductor development.

CHAPTER 7

PREPARATION, PROCESS OPTIMIZATION, AND CHARACTERIZATION OF Sm1111 WIRES

7.1 Introduction

For the technological applications related to electric power and energy, the superconducting materials must be molded into the form of wires/tapes. Research on development of iron-based superconductors with large transport J_C is being pursued in advanced countries (Ma (b) *et al.* 2012). Since iron pnictides are mechanically hard and brittle, to deform them into wires is difficult. So far many techniques such as diffusion method, coating technique, and Powder In Tube (PIT) method have been developed for making LTS and HTS materials into wires and tapes forms. Among these, PIT method is relatively easy and inexpensive to fabricate conductors with uniform properties and is often used for making wires of brittle superconducting materials such as Nb_3Sn (Kunzler *et al.* 1961), MgB_2 (Flukiger *et al.* 2003), and BSCCO superconductors (Hikata *et al.* 1989). So this method is also convenient for the brittle iron-based superconducting wires. In PIT method, precursor powder is filled in metal tubes, mechanically processed into wires and then heat treated. The PIT technique is classified into two types - *in situ* and *ex situ*. A considerable difference exists between *in situ* and *ex situ* methods. In *in situ* method, a mixture of the powders of starting materials is directly used, whereas in *ex situ*, a powder of synthesized superconducting material is used. In both processes, these powders are packed into a metal tube and groove rolled into desired dimensions and finally subjected to heat treatment. Another challenge is that the synthesis of iron-based superconductor requires a relatively high temperature which would result severe fluorine loss. Iron-based superconducting wires were first fabricated by Gao *et al.* (Gao(b) *et al.* 2008) using PIT method. They adopted the *in situ* PIT method for making iron pnictide wires, and later M Fujioka *et al.* followed the *ex situ* method (Fujioka *et al.* 2011). The main disadvantage of *ex situ* fabrication of F doped Sm1111 wire is the loss of fluorine during the heat treatment of the precursor powder. However, by adding a binder along with the ingredients namely, Sm, Fe, As, and F during the second sintering stage, the F loss can be reduced. In the present study, we use an *in situ* method in which the powder pre-processed at 370 °C was used as the precursor for filling the metal tube. However, the superconducting properties of *in situ* PIT processed wires strongly depend on the quality of the precursor powder, chemical compatibility and workability of sheath material, and processing temperature. Therefore, the chemical compatibility/reactivity of sheath materials with precursor powder and effects of processing temperature are studied in detail and discussed in the first part of this chapter.

7.2 Method adopted for Sm1111 wire development in the present study

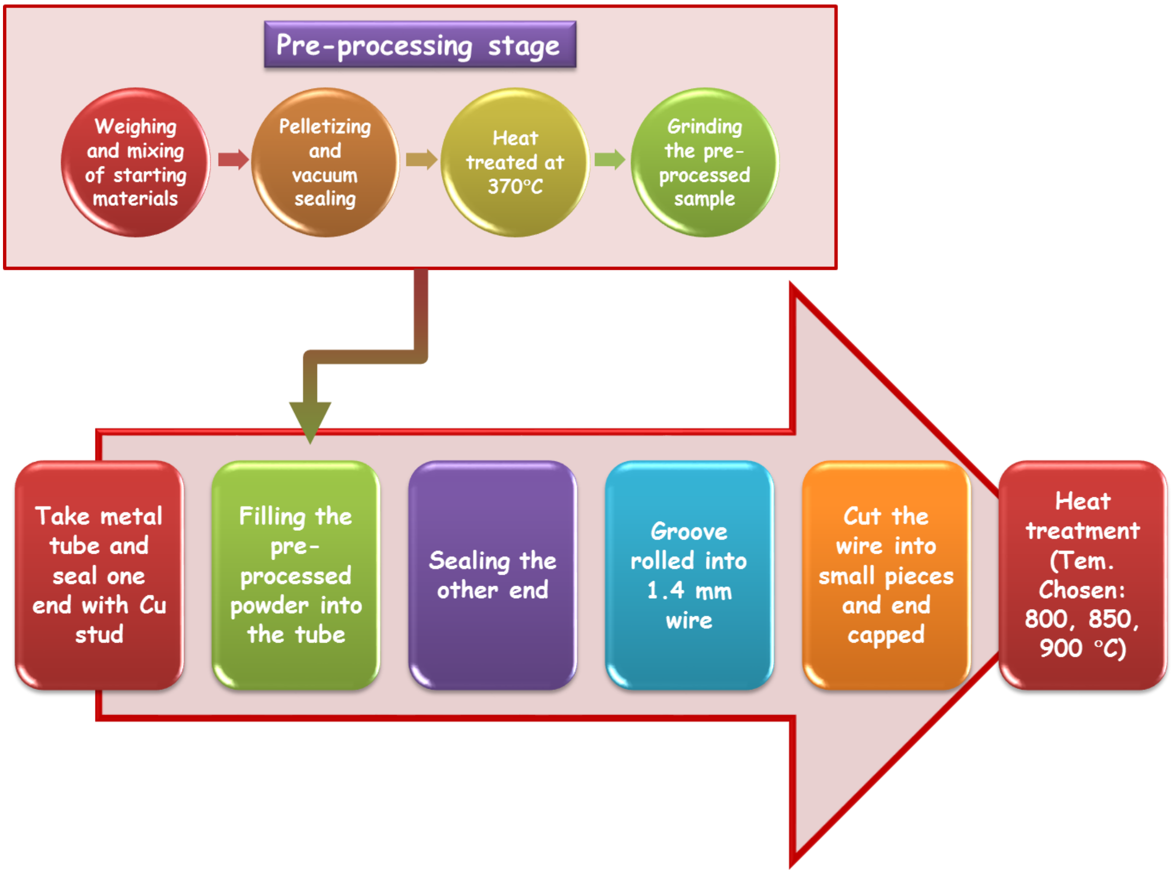

Figure 7.1: Block diagram of the preparation method used for SmFeAsO$_{1-x}$F$_x$ wire samples

SmFeAsO$_{1-x}$F$_x$ wires have been fabricated by the conventional PIT method (Varghese *et al.* 2007). All the ingredients were stoichiometrically weighed and then mixed thoroughly with a mortar and pestle inside a glove box. The homogenous powder was pelletized and vacuum sealed in evacuated quartz tubes. The tubes were subjected to pre-processing at a temperature of 370 °C for 5 h. The pre-processed samples were then ground homogeneously and filled inside the one-end sealed metal tubes having an OD/ID : 6/4 mm and then mechanically compacted. Copper studs were used as plugs for end sealing. After filling, the other end of the tubes were also sealed using Cu studs and crimpled mechanically on both sides. The composite tubes were then groove rolled down to the desired dimensions, typically 1.4 mm diameter. The long wires were then cut into small pieces and the ends of the wires were pressed and capped. They were then heat treated at

800-900 °C for 40 h in high purity argon atmosphere. After heat treatment, short length samples were cut for various structural and superconducting characterizations. A block diagram for the fabrication of $SmFeAsO_{1-x}F_x$ wires is given in Figure 7.1. The photographs of the as rolled $SmFeAsO_{1-x}F_x$ wires and the rolling machine used in the present study are given in Figure 7.2.

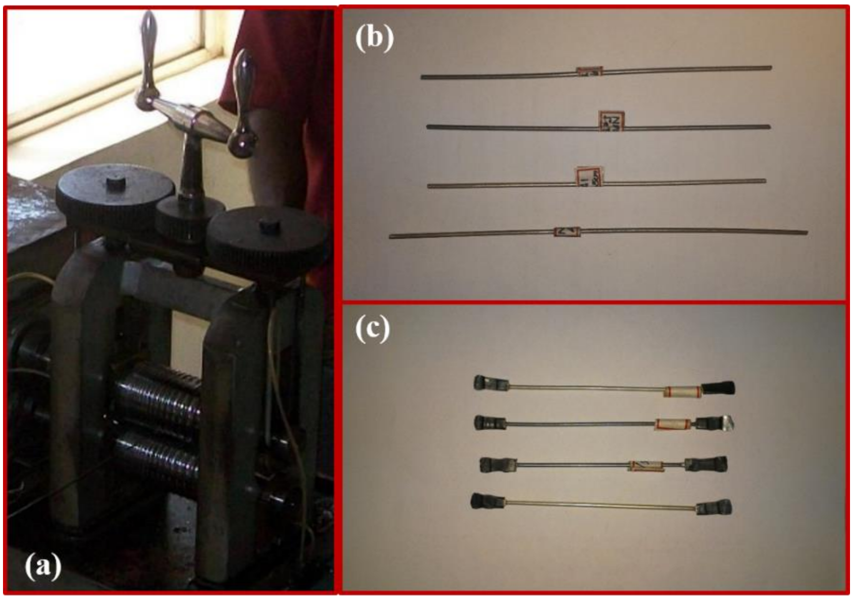

Figure 7.2: The photographs of (a) the rolling machine (b) the as rolled $SmFeAsO_{0.7}F_{0.3}$ wires and (c) the wires after end capping

7.3 Temperature and sheath metal optimization of $SmFeAsO_{0.7}F_{0.3}$ wires

7.3.1 Introduction

One of the main challenges encountered during wire development by the PIT process is to find a suitable sheath metal which is devoid of chemical reaction with the compound at elevated temperatures. In the case of iron pnictides the issue becomes more severe due to the requirement of long processing duration (~ 40 h). Thus, the choice of the metallic sheath has been reduced to those elements or metals showing little or no reaction with pnictides at the heat treatment temperature. At the same time, we must also choose a sheath material that does not degrade the superconducting properties of the superconducting core. Moreover, iron pnictides are brittle in nature and hence it is very difficult to roll down into wires. Therefore, the metal sheath must have adequate strength to give mechanical support to the brittle superconducting core and should be ductile enough to withstand the mechanical working. So, in this chapter, five commonly used sheath metals such as Ag, Cu, Fe, Ni and SS were chosen and their impact on the phase formation and superconducting properties were studied to find a suitable candidate for the preparation of iron pnictide superconducting wires. In order to get good superconducting properties, we have to also optimize the processing temperature, since the method of processing of $SmFeAsO_{0.7}F_{0.3}$ (Sm3) wires are entirely different from that of bulk synthesis. Therefore, the wires prepared from the different sheath metals (Sm3/Ag, Sm3/Cu, Sm3/Fe, Sm3/Ni, and Sm3/SS) were heat treated at three different processing temperatures of 800, 850, and 900 °C, respectively. The Sm3/Ag wire samples heat treated at 800, 850, and 900 °C were labelled as Ag800, Ag850, and Ag900, respectively and all other metal sheathed wires were also named accordingly.

7.3.2 Results and discussion

In order to find the interfacial reaction between the different sheath metals and the superconducting core (Sm3), the optical micrographs of the cross-sectional view of all the metal sheathed wires processed at different temperatures were taken. The optical micrographs of the polished cross-section of different metal sheathed wires heat treated at 800, 850, and 900 °C are shown in Figures 7.3. All the wire samples have a diameter of 1.4 mm. It is observed from the images that none of the metal sheaths undergo any interfacial reaction with the superconducting core. However, from the images it is clearly seen that only in the Ag sheathed wire samples (Ag800, Ag850, and Ag900) the black dense superconducting core region could be retained at all the processing temperatures. In all other metal sheathed wire samples, the sheath metal diffuses into the superconducting core region at the processing temperatures and reduces the superconducting volume fraction significantly. It is also observed that the diffusion is more extensive in Sm3/Ni, and Sm3/SS samples. In the case of Sm3/Ni wire samples, the superconducting core is almost completely replaced by a composite containing the metal sheath and the Sm1111 core. Therefore, the above results indicate that among the five metals studied Ag is the most suitable sheath material for $SmFeAsO_{1-x}F_x$ wire development in terms of chemical compatibility between the superconducting core and the sheath. It is also observed that at a higher temperature of 900 °C (shown in Figure 7.3) the shape of the outer Ag sheath got deformed since the processing temperature is approaching the melting point of silver.

Figure 7.4 shows the SEM images of the cross-sections of different metal sheathed wire samples processed at 850 °C. A distinct and clear separation between the sheath metal and core region is observed for all samples except the Ni sheathed wire (Figure 7.4(d)). However, the core region appears to be metallic in all the samples except Sm3/Ag. A black, dense core devoid of sheath metal is obtained only for Ag sheathed samples. In all other metal sheathed samples, the sheath metal diffuses into the core and this leads to reduction of superconducting volume fraction of the core. The situation is very bad in the case of Sm3/Ni sample wherein it is even difficult to distinguish the boundary between the core and metal sheath and making it to look like a single piece of metal.

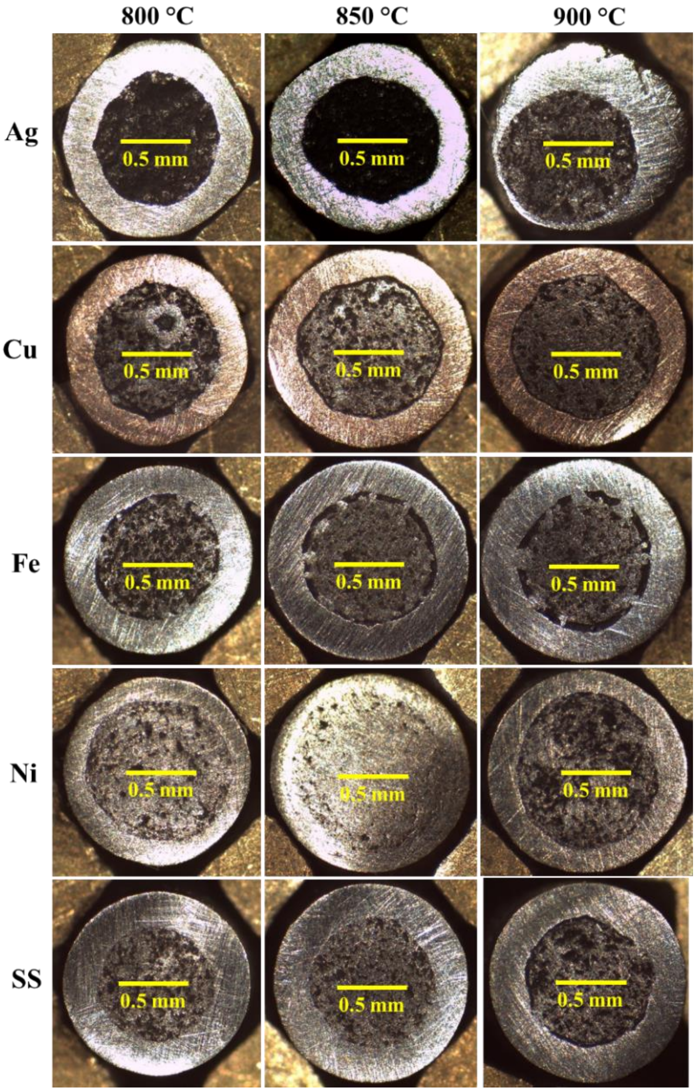

Figure 7.3: Optical images of the cross-sections of five different metal (Ag, Cu, Fe, Ni, and SS) sheathed Sm3 wires heat treated at 800, 850, and 900 °C

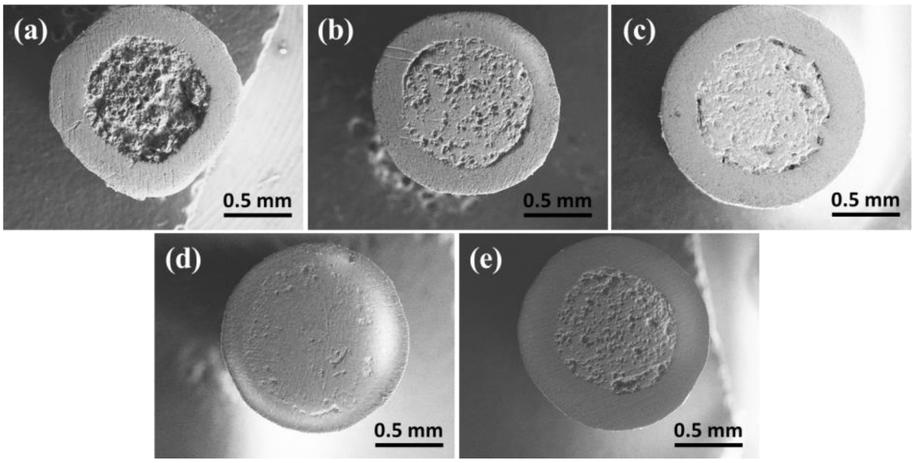

Figure 7.4: SEM images of the cross-sections of (a) Sm3/Ag, (b) Sm3/Cu, (c) Sm3/Fe, (d) Sm3/Ni, and (e) Sm3/SS wire samples heat treated at 850 °C

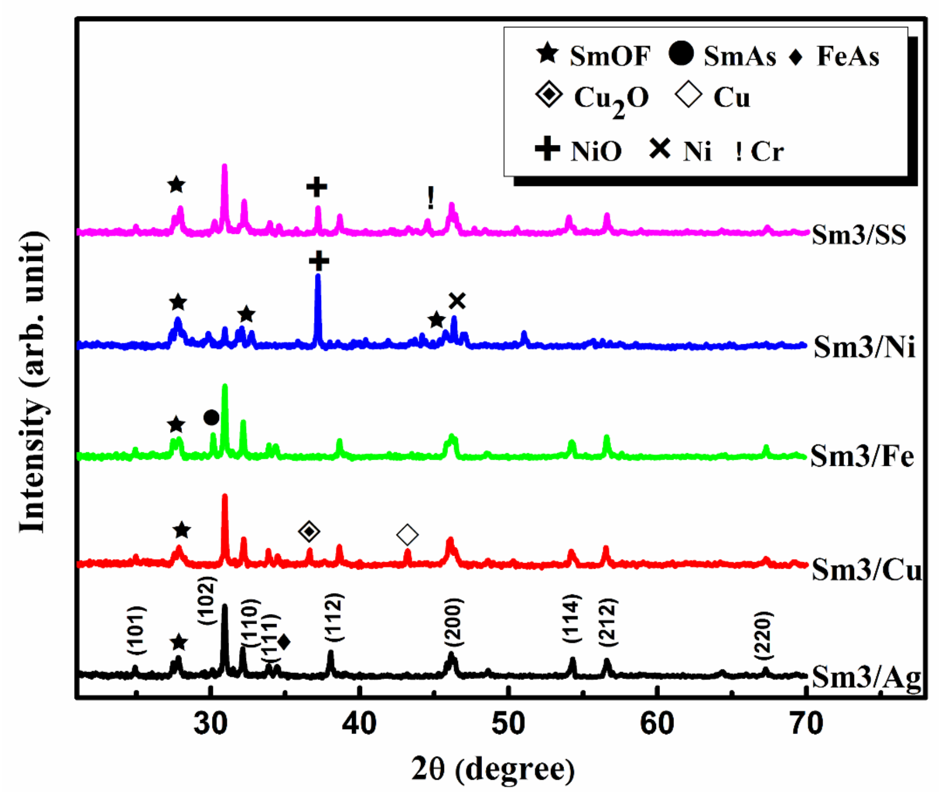

Figure 7.5: XRD patterns of the different metal sheathed wire samples heat treated at 850 °C

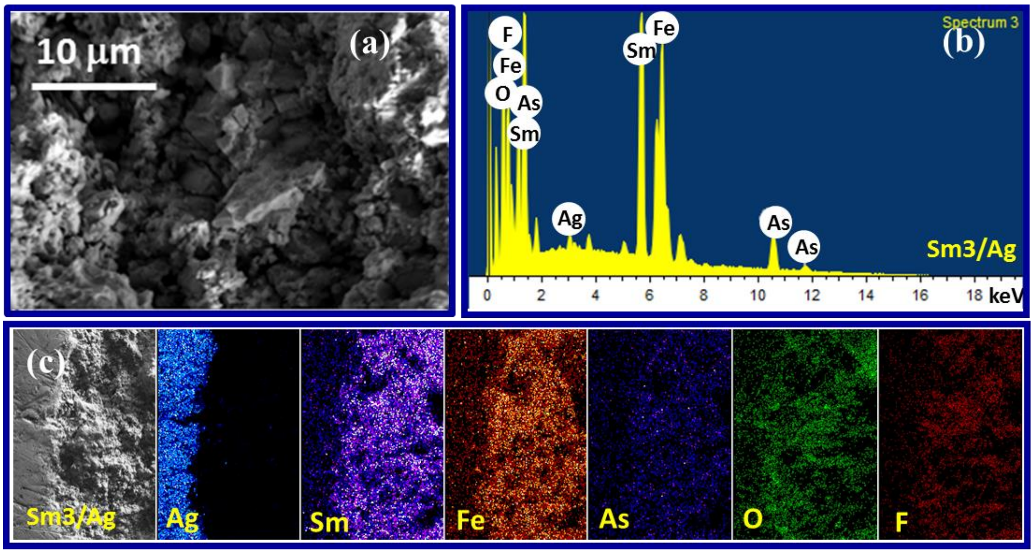

Figure 7.6: (a) SEM image of the superconducting core of Ag sheathed Sm1111 wire sample, (b) EDS spectrum taken on the core area and (c) elemental mapping at the interfacial region

Powder XRD analysis was also done for getting more information about the phases present in the superconducting core. For this, the powder was retrieved from the wire samples by mechanically peeling off the sheath metal and then powdering the core material. Figure 7.5 shows typical XRD patterns of the five different metal sheathed wire samples heat treated at 850 °C. The $SmFeAsO_{0.7}F_{0.3}$ phase present in all the patterns are indexed with their corresponding (*hkl*) planes. In addition to the main phase, the generally observed impurity phases (such as SmAs, and SmOF) and also other foreign phases resulted from the sheath material were also indexed. It can be seen that the additional phases due to the sheath material is formed in the case of Sm3/Cu, Sm3/Ni, and Sm3/SS samples. Additional phases of Cu_2O and Cu are formed in the case of Sm3/Cu, whereas NiO and Ni are found in Sm3/Ni, and Sm3/SS samples. For Sm3/Ni, the major phase obtained is NiO and the contribution from $SmFeAsO_{0.7}F_{0.3}$ phase is negligible. However, for Sm3/Ag and Sm3/Fe no other foreign phases are found. Therefore, Ag and Fe can be considered as chemically compatible to $SmFeAsO_{1-x}F_x$ and these may be acceptable as sheath materials for making wires.

Enlarged SEM and the corresponding EDS spectra of the superconducting core region of different metal sheathed samples were also taken to have more information on the microstructure of the core, sheath-core interface and elemental distribution within the core. The results are given in Figure 7.6 to 7.10. Distinct microstructural changes are obtained for the samples depending on the sheath metals. Well defined $SmFeAsO_{1-x}F_x$ grains are formed only in Sm3/Ag samples. From the enlarged view, we can also see the presence of voids and cracks in the sample, characteristics of iron pnictides. The loss of volatile arsenic and fluorine during the heat treatment would be the reason for the presence of voids. In all other cases, the sheath metal diffuses into the core region and fills the voids present. However, the diffusion of metals into the superconducting core region degrades the formation of $SmFeAsO_{1-x}F_x$ in these samples. The microstructure of Sm3/Ni is entirely different from others due to the fact that practically no $SmFeAsO_{1-x}F_x$ phase is formed in this case.

The elemental analysis of the samples was also conducted from their respective EDS spectra. Intensities of the spectrum corresponding to Sm3/Fe, Sm3/Ni, and Sm3/SS are found to be low since their electrical conductivity is relatively low compared to Ag and Cu. From the EDS spectra, we can see that the elements corresponding to the sheath metal are found in the superconducting core for all the samples. However, the contribution from the metal part is very feeble in Sm3/Ag sample. In Sm3/Fe sample, only a small amount of additional contribution from the Fe sheath metal is found. In addition, the compositional analysis from EDS spectra also revealed that $SmFeAsO_{1-x}F_x$ with the initial stoichiometry is only found in the superconducting core of Sm3/Ag wire sample.

The elemental mapping using EDS at the interfacial region gives an insight into the distribution of sheath metal into the core region. Images labelled as (c) in Figure 7.6 to

7.10 show the elemental mapping for different metal sheathed wire samples. In that, the first column shows the SEM images at the metal-core interface. The second to the seventh columns show the mappings of the corresponding sheath metal and the elements contained in the superconductor core namely Sm, Fe, As, O, and F respectively. In the mapping, the colored dots denote the presence of the elements and the black background shows its absence. From the mapping, it is clear that there is no diffusion of Ag into the core region. Moreover mapping of elements in the core phase such as Sm, Fe, As, O, and F in Sm3/Ag show a dense and uniform distribution even though there was a diffusion of elements from the core to sheath area. However, the sheath metal shows a distribution over the entire area of analysis for Sm3/Cu, Sm3/Fe, Sm3/Ni, and Sm3/SS samples due to the inter diffusion between the sheath metal and elements in the core region. However, in Sm3/Fe the presence of metal element is relatively lower and the composition of Sm1111 phase is better compared to others, except Sm3/Ag. The presence of core elements in the inner region is relatively low in Cu, Ni, and SS sheathed samples and this is the lowest in Sm3/SS sample. From the above results, we can conclude that among the five metals studied Ag is the most suitable sheath material for $SmFeAsO_{1-x}F_x$ compound to fabricate wires.

The resistance verses temperature plots (*R-T*) of all metal sheathed samples processed at different temperatures are separately given in Figure 7.11. Figure 7.11(a) shows the *R-T* plots of Ag sheathed samples heat treated at different temperatures. We can see that all the samples have superconducting transition and the T_C of all the samples is around 57.5 K. This transition temperature for wire samples is slightly higher than that obtained for bulk $SmFeAsO_{0.7}F_{0.3}$. The *R-T* plots of Fe sheathed samples heat treated at different temperatures are given in Figure 7.11(b). Here, the sample processed at 850 °C only exhibits a complete zero resistance transition. The other two samples display only a tendency of superconducting transition, but no zero resistance is attained. The sample Fe850 has a T_C of only 37 K. Presence of a significant fraction of SmAs phase in Sm3/Fe sample as detected from the XRD pattern (Sm3/Fe in Figure 7.5) could be the reason for the observed T_C reduction of the Fe sheathed sample. However, the wire samples heat treated at 850 °C give the maximum T_C for both Sm3/Ag and Sm3/Fe wire samples. There are no superconducting transitions for Sm3/Cu, Sm3/Ni, and Sm3/SS wire samples at all temperatures as shown in Figure 7.11(c), 7.11(d) and 7.11(e), respectively. Hence, the presence of large fractions of impurity phases formed due to the sheath material namely, Cu, Ni and SS completely suppress the superconducting property of the respective wires.

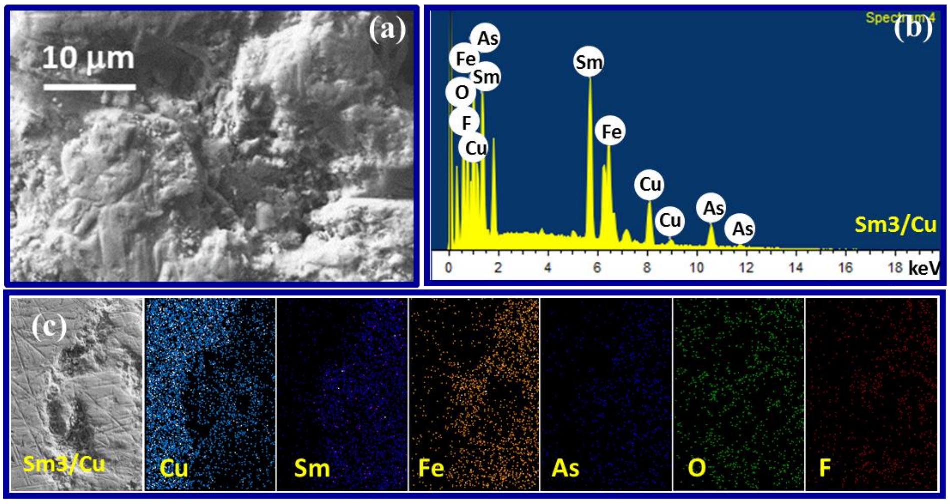

Figure 7.7: (a) SEM image of the superconducting core of Cu sheathed Sm1111 wire sample, (b) EDS spectrum taken on the core area and (c) elemental mapping at the interfacial region

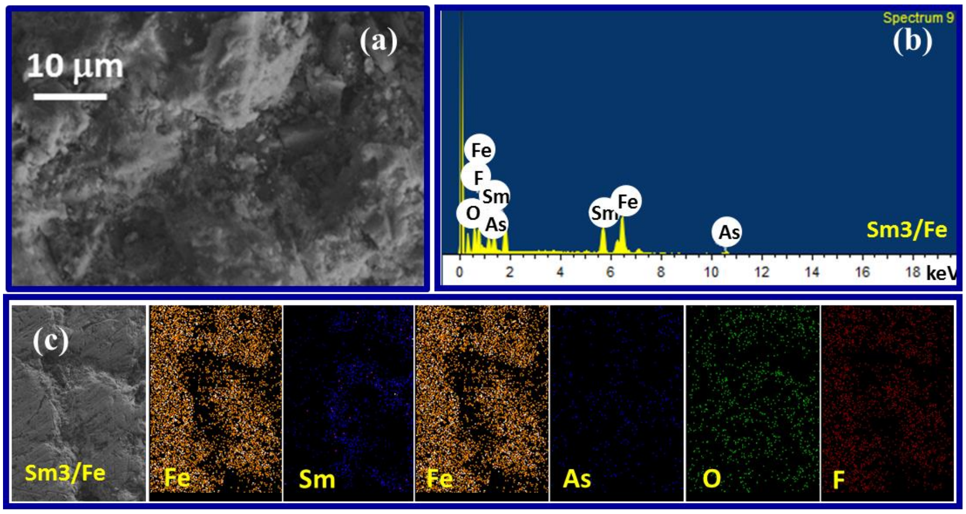

Figure 7.8: (a) SEM image of the superconducting core of Fe sheathed Sm1111 wire sample, (b EDS spectrum taken on the core area and (c) elemental mapping at the interfacial region

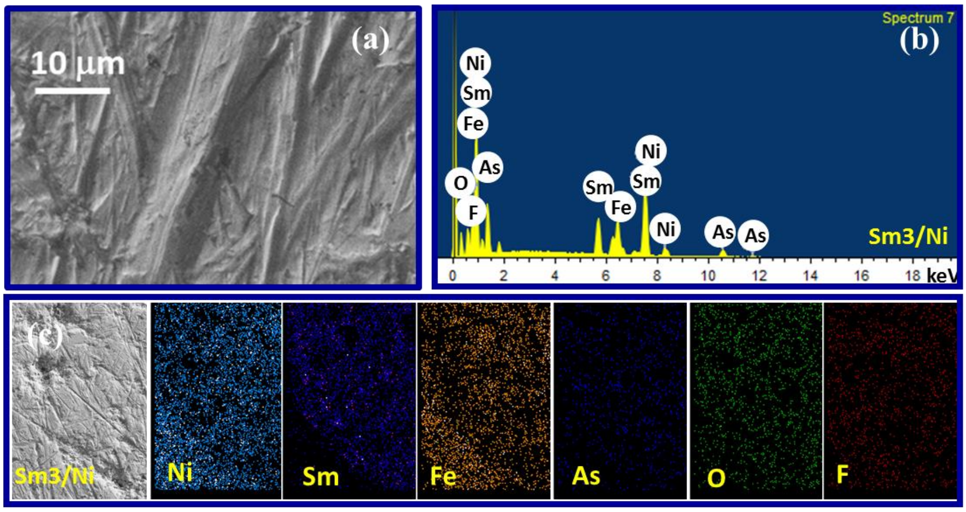

Figure 7.9: (a) SEM image of the superconducting core of Ni sheathed Sm1111 wire sample, (b) EDS spectrum taken on the core area and (c) elemental mapping at the interfacial region

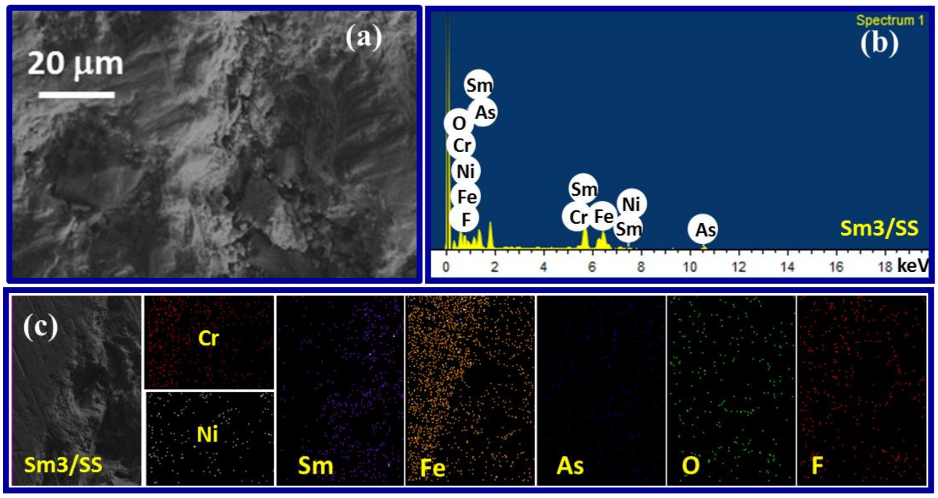

Figure 7.10: (a) SEM image of the superconducting core of SS sheathed Sm1111 wire sample, (b) EDS spectrum taken on the core area and (c) elemental mapping at the interfacial region

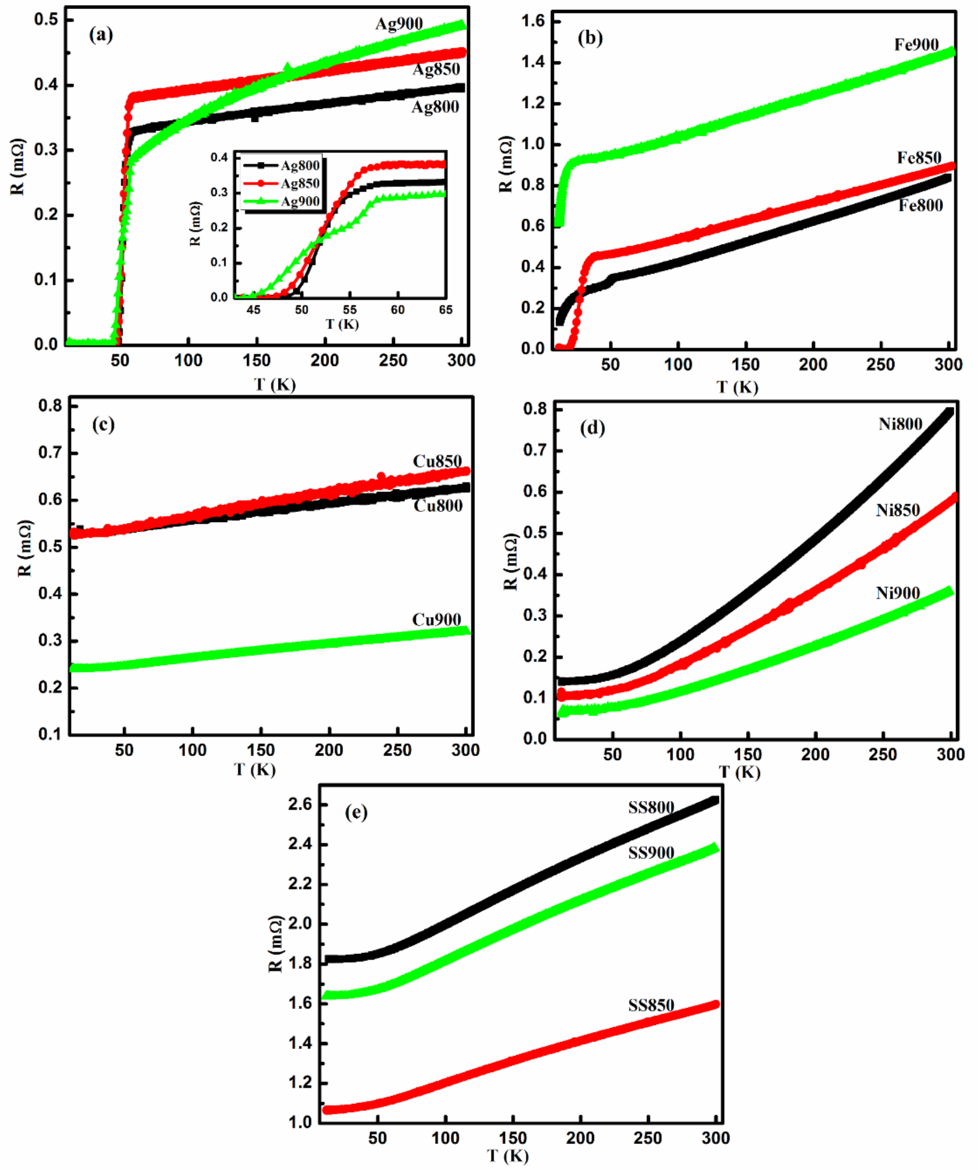

Figure 7.11: *R-T* plots of (a) Sm3/Ag, (b) Sm3/Fe, (c) Sm3/Cu, (d) Sm3/Ni, and (e) Sm3/SS samples processed at different temperatures

7.3.3 Conclusions

The effect of different sheath materials on the phase formation and superconducting properties of $SmFeAsO_{0.7}F_{0.3}$ wire samples are studied using five metals Ag, Cu, Fe, Ni, and SS. In Cu, Ni, and SS sheathed wire samples, significant quantities of secondary phases are formed from the corresponding sheath metals and this considerably reduces the superconducting volume fraction. Resistance versus temperature study shows that the presence of these impurity phases completely degrades their superconducting properties. No superconducting transition is observed for the Sm3/Cu, Sm3/Ni, and Sm3/SS wire samples. We found that Ag and Fe sheath metals are chemically compatible to $SmFeAsO_{1-x}F_x$ superconductors at elevated temperatures and among them Ag gives the best results. Temperature variation studies on these wire samples shows that for both Ag and Fe sheathed wires, the optimum processing temperature is around 850 °C.

7.4 Critical current properties of Sm1111 wires

From the application point of view, one of the preferential requirements is the current carrying capability of our superconducting wire samples. For iron-based superconductors, attaining relatively high transport current density is very significant. However, there exist certain hurdles to achieve this. The main limitations of the development of Sm1111 wires with large transport current density are the difficulty in maintaining the composition of samples since the fluorine is highly volatile during the heat treatment and the presence of unavoidable impurity phases especially the wet phase FeAs which blocks the grain-to-grain connectivity. Studies on bi-crystalline 122 category of iron pnictides also reveals that high-angle grain boundary largely deteriorates critical current density of the samples (Lee(c) *et al.* 2009). Hence, the development of iron pnictide wires with large critical current density is very challenging. In the present work, we have followed the *in situ* method, but instead of using the usual ingredient powders we have used the powder pre-processed at 370 °C for filling the metal tube.

The current-voltage characteristics of our wire samples were studied in order to find the transport critical current density (transport J_C) of the samples. Figure 7.12 shows the *I-V* plots of the superconducting Sm1111 wire samples measured at 12 K. It is seen that the Ag sheathed wires processed at the three temperatures exhibit significant critical current (I_C) values. The I_C values obtained for the Ag sheathed wire samples are 24.5, 31, and 15.5 A for Ag800, Ag850, and Ag900 respectively. The corresponding J_C values are also calculated using the formula $J_C = I_C/A$; where A is the area of cross-section of the core region which is around 50% of the total cross-sectional area of the wire samples. The J_C values are 3185, 4030, 2015 A/cm^2 respectively for Ag800, Ag850, and Ag900 samples. All these values are higher than the J_C of existing *in situ* processed $SmFeAsO_{1-x}F_x$ wires (Wang(b) *et al.* 2010). But for Fe sheathed sample, only a small amount of the transport critical current is found. The maximum transport critical current measured in the sample Fe850 is only 2.5 A at 12 K and the corresponding J_C is 325 A/cm^2. This is mainly due to the largely reduced volume fraction of the superconducting core, the poor grain-to-grain connectivity and the lower transition temperature of the sample. From the above results, we can conclude that the Ag sheathed samples heat treated at 850 °C gives the highest transport critical current density (4030 A/cm^2). Since we followed the *in situ* method, we could restrict the processing temperatures less than 900 °C. Moreover, the use of preprocessed powder as precursor not only helps to reduce the processing temperature but also helps to attain better transport J_C values. In short, the Sm1111 superconducting wire samples with Ag as sheath metal processed at 850 °C gives the best properties in terms of T_C and J_C values.

The critical current density of the Ag sheathed $SmFeAsO_{0.7}F_{0.3}$ wire heat treated at 850 °C was also derived from the magnetic hysteresis (*M-H*) curve. Figure 7.13 shows the *M-H* plots of SmAg850 at different temperatures of 5, 10, 20, 30, and 35 K. The magnetization of the sample is given in terms of emu/cm^3 and the applied magnetic field varies up to 9 T. At 5 K, the sample displays a large hysteresis width in the low field region. However, the *M-H* curve exhibits a tapering behavior in the high field region. This indicates the weak link behavior of the grain boundaries which are extremely sensitive to the applied magnetic field. With increase in temperature also, the width of the *M-H* loop decreases considerably, yet shows a noticeable width even at 35 K in the low field region and a maximum width is observed at a lower magnetic field corresponding to its H_{C1}. This indicates the better flux pinning properties of the sample in the low field region. The derived magnetic J_C ($J_{Cglobal}$) using the extended Bean critical state model of the wire sample at different temperatures is given in Figure 7.14. A magnetic J_C of 7.7 × 10^3 A/cm^2 is obtained for the Ag sheathed Sm1111 wire sample in the low field at 5 K. But, further the $J_{Cglobal}$ shows a decreasing tendency with magnetic field, yet remains almost constant up to around 8 T. Moreover, the $J_{Cglobal}$ decreases with increasing measurement temperatures and the rate of decrease with applied field also increases with temperature. Here, the $J_{Cglobal}$ value of wire sample is higher than that obtained for the bulk sample Sm3 (1.4 × 10^3 A/cm^2) as discussed in Chapter 4. The improved core density of the wires in view of the PIT process would be the reason for this higher J_C value. However, a significant difference exists between the measured transport and magnetically derived J_C values. This is because the transport J_C mainly depends on the grain-to-grain connectivity. The intrinsic granular nature of iron pnictides and poor grain boundary connectivity issues limit the transport J_C of the Sm1111 wire samples. Hence, the main concern is to reduce the gap between the magnetic and transport J_C of Sm1111 wire samples.

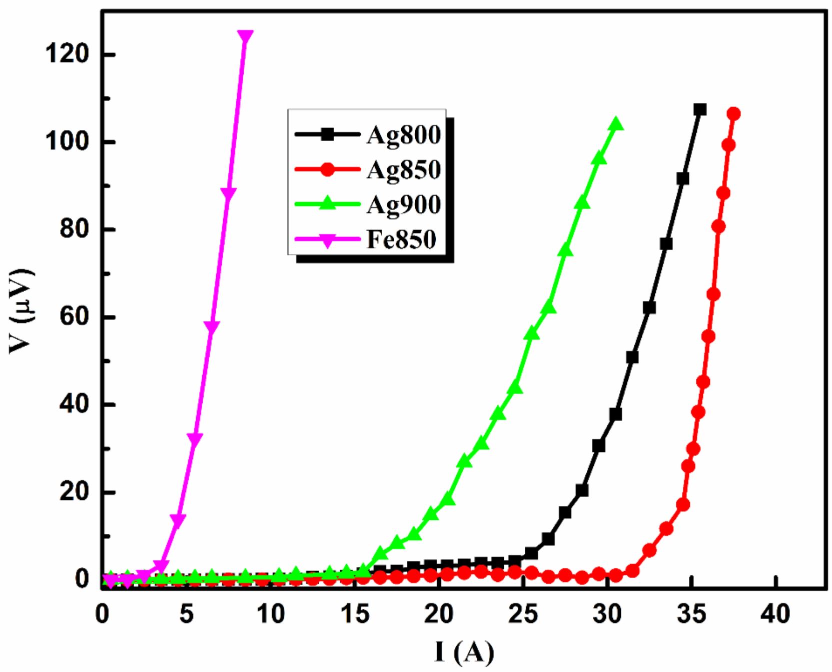

Figure 7.12: ***I-V*** **plots of Sm1111 wire samples measured at 12 K**

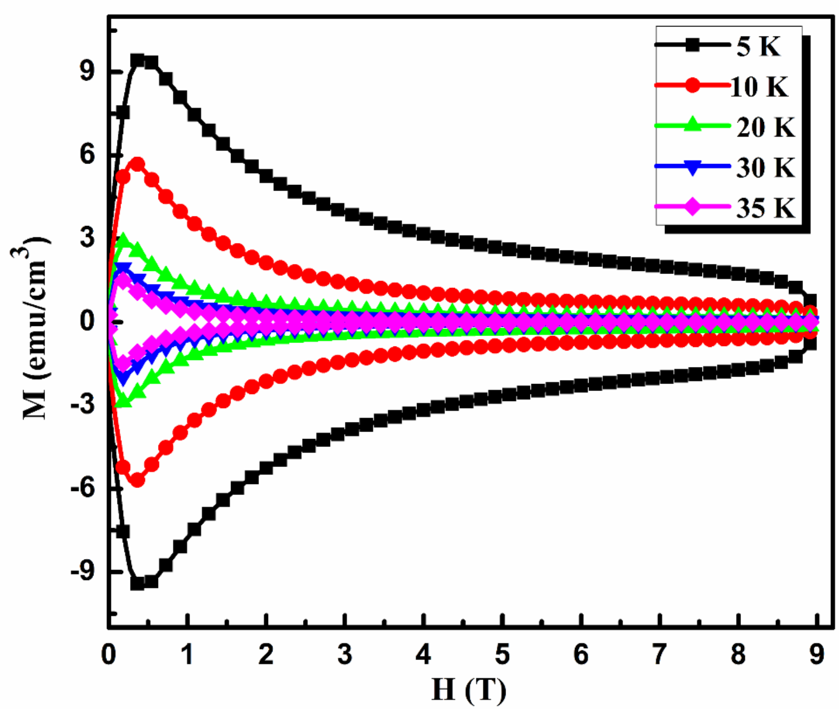

Figure 7.13: ***M-H*** **curves of the wire sample SmAg850 at** ***T*** **= 5, 10, 20, 30 and 35 K**

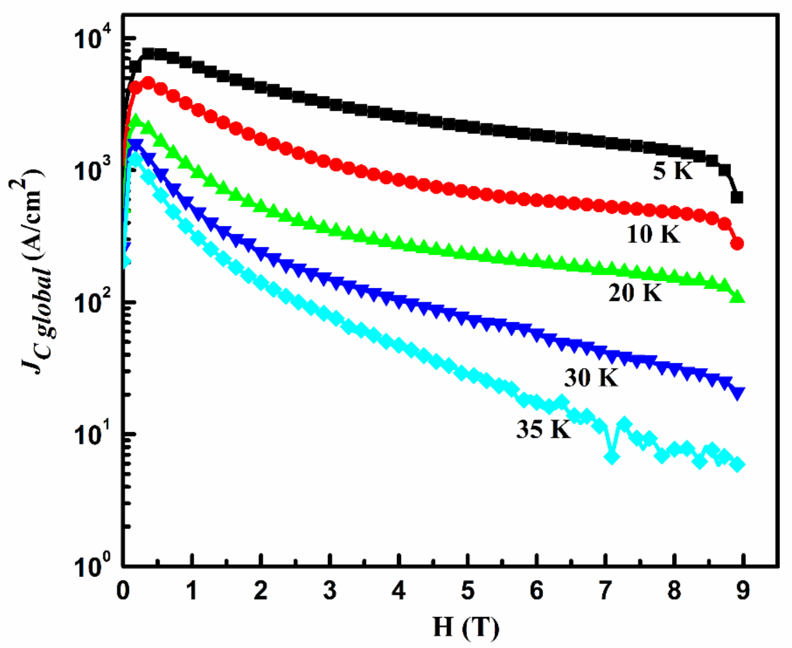

Figure 7.14: Magnetic field dependence of global J_C of the wire sample SmAg850 at different temperatures T = 5, 10, 20, 30 and 35 K

7.5 Selective metal addition in Ag sheathed Sm1111 wires to improve their transport properties

7.5.1 Introduction

The transport J_C achieved for the Sm1111 wires (~ 4 × 10^3 A/cm^2 at 12 K) as discussed above are far below the magnetically derived intragrain J_C (J_{Clocal}) of the iron pnictides. The J_{Clocal} of $SmFeAsO_{1-x}F_x$ wires evaluated from the M-H measurements as discussed in the above section is of the order of 10^5 A/cm^2. The large difference between J_{Clocal} and transport J_C is due to the presence of impurity phases, electromagnetic granularity and the weak link behavior among the superconducting grains. Recently, researchers in this area are making intensive efforts to improve the transport current carrying capability of iron-based superconductors. Various techniques have been introduced to enhance the transport J_C of superconductors. Among them, chemical addition is an effective method to enhance the J_C of the superconductors. Additives to the system may help to promote the superconducting phase formation or act as conductive bridge between the grains and thereby improve the grain-to-grain connectivity or introducing pinning centers. Early studies in cuprate based superconductors such as Ag addition in YBCO and Pb addition in BSCCO commendably improved their superconducting as well as transport properties (Hudakova *et al.* 2007; Biju *et al.* 1995). Therefore, there is a scope for further increasing the transport J_C of Sm1111 superconductor by selective metal addition. This section deals with the effect of selective metal addition on the superconducting and transport properties of Sm1111 wires. Two typical low melting metals such as Sn and Mg were chosen for this purpose. From the preliminary studies, it is seen that the Mg addition completely deteriorates the superconducting properties of the system. Whereas, the Sn addition significantly improved both the superconducting and transport properties of the Sm1111 wire samples. The work on impact of Sn addition in Ag sheathed Sm1111 wire samples is briefly presented below.

7.5.2 Experimental details

Sn added Sm1111 wires were prepared by *in situ* PIT method, using the pre-processed powder. Firstly, a homogeneous mixture of Sm, As, Fe, Fe_2O_3, and FeF_2 was prepared with a nominal stoichiometry of $SmFeAsO_{0.7}F_{0.3}$ and this was subjected to pre-processing at a temperature of 370 °C. The pre-processed sample was again ground and different weight percentage (10, 20, and 30 wt%) of Sn powder was added. The Sn added samples were sealed inside Ag tubes. The composite tubes were then groove rolled into wires of 1.4 mm OD. These were then cut into short length samples and end sealed. The sealed wires were heat treated at 850 °C for 40 h. In order to compare the properties of the Sn added samples, a set of $SmFeAsO_{0.7}F_{0.3}$ (Sm3) wire samples without Sn was also prepared under identical conditions. The Sn added samples are named as SmSn1, SmSn2, and SmSn3 respectively for 10 wt%, 20 wt%, and 30 wt% of Sn addition.

7.5.3 Results and discussion

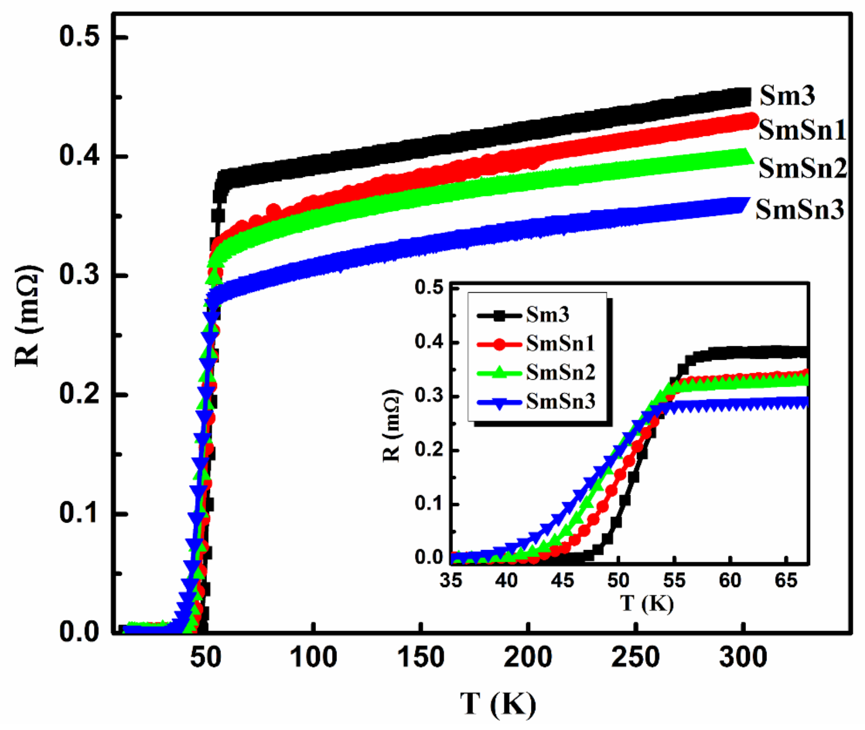

Figure 7.15: ***R*-*T* plots of Sm3 and the Sn added Sm1111 wire samples**

Figure 7.15 shows the *R-T* plots of Sn added samples along with that of the reference sample Sm3. All the Sn added samples show superconducting transition and exhibit zero resistance. The transition temperature of Sn added samples are slightly lower than that of the pure Sm3 sample (57 K). A T_C of 55.8 K is obtained for the sample SmSn1; subsequently with increase in Sn addition the T_C value decreases to 55 K and 54.2 K for SmSn2 and SmSn3 samples respectively. The reason for the slight lowering of T_C may be due to the deformation of the crystal structure of Sm1111 and the formation of impurity phases caused by Sn addition. Also the transition width of the Sn added samples becomes larger compared to the pure sample, Sm3. However, the T_{Conset} of Sn added samples show only a slight change; but the offset T_C drops considerably. This can be interpreted as due to the non-uniform distribution of Sn or Sn containing phase within the wire samples. This means that some regions of the wire sample have almost the same T_C as that of pure Sm3 sample whereas in other areas of the wire have a lower T_C resulting from the Sn addition. It is also observed that the normal state resistance (R_{300K}) of the samples decreases systematically with increase in Sn addition.

Table 7.1: Transport properties of Sn added Sm1111 wire samples

Sample name	**T_C (K)**	**I_C (A) at 12 K**	**J_C at 12 K (A/cm^2)**
Sm3	57	31	4030
SmSn1	55.8	34	4420
SmSn2	55	36	4680
SmSn3	54.2	40	5200

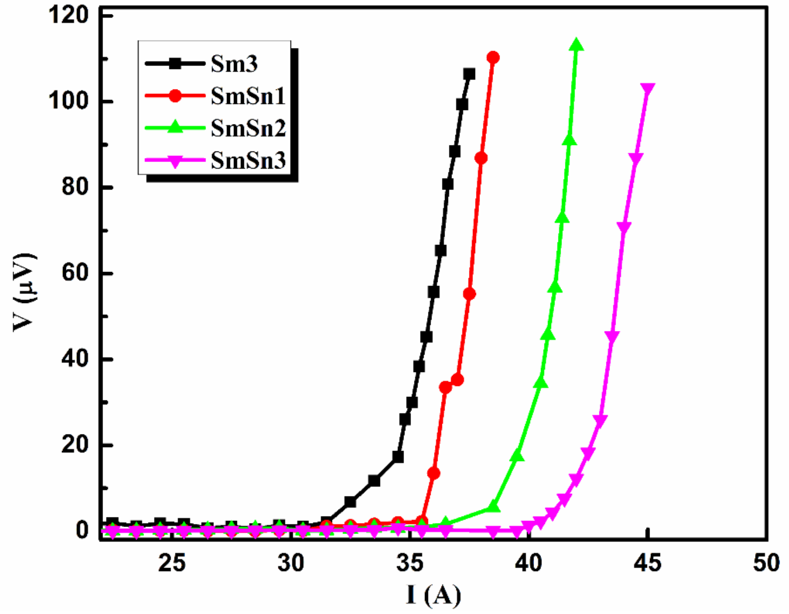

Figure 7.16: *I-V* plots of Sm3 and the Sn added Sm1111 wire samples

Transport properties of Sn added wire samples are studied from their respective *I-V* characteristics. Figure 7.16 shows the obtained *I-V* plots of the Sn added samples along with that of Sm3 sample. We can see that incorporation of Sn into the pure sample promotes the current carrying capability of the samples. For 30 wt% Sn added sample, a transport I_C of 40 A and a corresponding J_C of 5200 A/cm^2 at 12 K are obtained. Table 7.1 summaries the observed T_C and I_C values for pure and Sn added samples. The results show that though there is a slight decrease in T_C, the Sn added samples exhibit improved transport properties compared to the pure sample. In $SmFeAsO_{1-x}F_x$ samples, one of the main reasons for the lower transport current is the presence of FeAs wetting phase which blocks the current flow between the superconducting $SmFeAsO_{1-x}F_x$ grains. However, addition of Sn powder to the pre-processed precursor powder would cause a reaction between the precursor and the added Sn powder when it is subjected to further heat treatment. The precursor obtained after pre-processing at 370 °C mainly contains a mixture of SmAs and FeAs (discussed in Chapter 4). While the addition of Sn powder to the pre-processed precursor powder and further heat treatment would have resulted in a reaction between the FeAs phase and Sn; and thereby reduce the presence of FeAs in the final sample. This may be the main reason for the enhanced transport J_C of the Sn added wire samples.

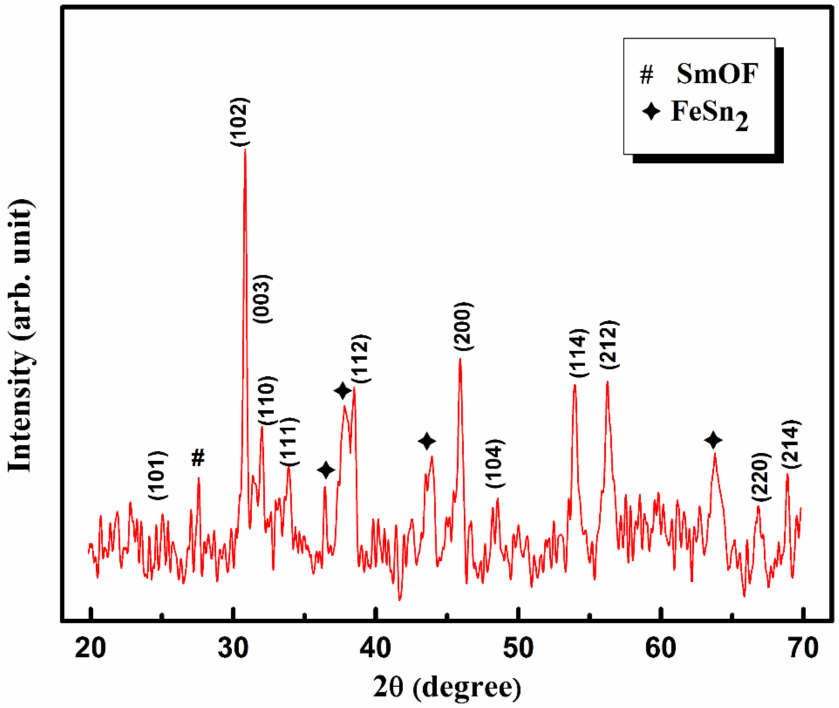

Figure 7.17: XRD pattern of the Sn added wire sample, SmSn3

In order to get an insight into the phase formation and also to confirm the possibility of the reaction between the precursor powder and added Sn powder the XRD pattern of one of the Sn added samples (SmSn3) was taken. The pattern is shown in Figure 7.17. It is seen that the main phase formed is $SmFeAsO_{0.7}F_{0.3}$, the peaks of which are indexed based on the tetragonal ZrCuSiAs type structure with the space group *P4/nmm*. In addition to the main phase the sample also contains impurity phases such as SmOF and $FeSn_2$, a new intermetallic phase. This suggests that a reaction between the added Sn powder and the FeAs phase in the pre-processed precursor powder has taken place. Consequently, the Sn addition reduces the intensity of the impurity phases. It may be noted that the impurity phase FeAs is absent in the Sn added sample as seen from the XRD pattern of SmSn3 (Figure 7.17). Therefore, in effect, the incorporation of Sn into Ag sheathed Sm1111 superconducting wire sample enhances its transport current carrying capacity.

7.5.4 Conclusions

The effect of Sn addition in Sm1111 wire is studied by varying the wt% of Sn and the improvement in transport properties of wire samples are analyzed. It was seen that though Sn addition slightly reduces the transition temperature of the wire samples, their transport J_C is increased. The Sn addition is found to suppress the current blocking wet phase FeAs at the grain boundaries of Sm1111 superconductor and thereby enhances the transport properties of the wires. In general, Sn addition has a positive impact on the transport properties of Sm1111 wire samples.

7.6 Summary

Metal sheathed Sm1111 superconducting wires are prepared by *in situ* PIT method using the pre-processed precursor powder. For this, a suitable sheath metal is initially chosen after studying the effect of five different sheath metals on the structural and superconducting properties of the Sm1111 wire samples. Metals namely, Ag and Fe are found to be chemically compatible to the Sm1111 sample. Among them, Ag is found to be more suitable in terms of superconducting and transport properties. Processing temperature variation studies on wire samples shows that the wires heat treated at 850 °C gives the highest T_C and J_C values. A T_C of 57 K and transport J_C of 4030 A/cm^2 are obtained for *in situ* processed Ag sheathed Sm1111 wires heat treated at 850 °C. Further, the transport J_C of the Ag sheathed Sm1111 wire sample is subsequently enhanced to 5200 A/cm^2 at 12 K by the incorporation of adequate amount of metallic Sn into the wire sample.

CHAPTER 8

SUMMARY AND CONCLUSIONS

8.1 Summary of the work

The main objectives of the thesis work as mentioned in Chapter 2 were to prepare good quality $SmFeAsO_{1-x}F_x$ superconductors at relatively low temperature by developing a simple novel method, and to study the substitution effects at various sites and to improve the superconducting properties like T_C, J_C and H_{C2}, and finally to develop Sm1111 in the form of wires/tapes for technological applications.

The Sm1111 superconductors with better superconducting properties were synthesized by following a novel pre-processing route. In this method all the ingredients weighed stoichiometrically were subjected to a pre-processing at a lower temperature after homogeneous mixing and then the pre-processed powder was used for the final heat treatment. This method could effectively reduce the final processing temperature and yielded Sm1111 superconductors with good superconducting properties. The effect of F variation on the structural and superconducting properties of Sm1111 system, synthesized through the pre-processing route, was also studied. Since $SmFeAsO_{1-x}F_x$ with x = 0.3 gave the best results in terms of both superconducting and transport properties, this composition was chosen for further studies such as rare earth doping at Sm^{3+} site and for wire/tape development. In order to find the influence of rare earth doping on the structural and electro-magnetic properties of Sm1111 iron pnictide, modified compositions such as $Sm_{1-y}RE_yFeAsO_{0.7}F_{0.3}$ (RE - rare earth) were prepared. For that, 4f RE elements having both smaller and larger ionic radii compared to Sm^{3+} were chosen. The elements chosen were $RE^{3+} = Gd^{3+}$, Ce^{3+}. Effect of a non-4f element, Y^{3+} doping at Sm^{3+} site was also studied. Later alkaline earth metal fluoride dopants such as CaF_2 and BaF_2 were chosen to study the combined effect of both electron and hole doping in Sm1111 system. That is, in $Sm_{1-x}A_xFeAsO_{1-2x}F_{2x}$ (A - alkaline earth metals) system, F^- doping at O^{2-} site provides electrons and Ca^{2+}/Ba^{2+} at Sm^{3+} site gives holes to the system.

Finally, $SmFeAsO_{1-x}F_x$ wire samples were developed using *in situ* PIT method. Here, the pre-processed powder as in the case of bulk synthesis, was used for filling the metal tube. Efforts were made to optimize parameters such as sheath metal reactivity and processing temperature. Sheath metals such as Ag, Cu, Fe, Ni and SS were selected to study sheath metal reactivity and their impact on the phase formation, microstructure, superconducting and transport properties of the system. The effect of processing temperature on the structural, superconducting and transport properties of the Sm1111 wire samples were also analyzed. A large difference between the transport J_C and magnetically derived J_C (J_{Clocal}) was found in the wire samples. Hence, an attempt was made to enhance the transport J_C of Sm1111 wires by the incorporation of low melting metals. Addition of Sn considerably advanced the transport current carrying capability of Sm1111 wires.

Both bulk and wire samples were evaluated by structural and microscopic characterization techniques such as XRD, SEM, EDS, and optical microscopy; and superconducting characterization techniques including transport measurements such as ρ-T, I-V; and magnetic measurements such as χ-T, M-H, J_C-H; and magneto transport measurements like ρ-T at different magnetic fields and Hall Effect measurements.

8.2 Conclusions

✓ $SmFeAsO_{1-x}F_x$ (Sm1111) based bulk superconductors with properties competing with international status were synthesized at a considerably low temperature of 850 °C and at ambient pressure by introducing a novel pre-processing route. The pre-processing of the reaction mixture at 360-380 °C yielded a precursor having the right phase assemblage and good reactivity and thereby resulted in good quality Sm1111 samples at a relatively low temperature. The method could overcome the need of high processing temperature and pressure; the need of wrapping the pellets with expensive metal foil; and also reduced the possibility of sheath reactivity in wire development. Studies on optimization of F content in $SmFeAsO_{1-x}F_x$ synthesized by the pre- processing route showed that a maximum T_C of 55.3 K was attained for x = 0.4 and a transport J_C of 752 A/cm^2 for x = 0.3 composition. The sample with x = 0.3, also showed a magnetic J_{Clocal} of 7×10^5 A/cm^2 at 5 K and better $J_C(H)$ performance in the high field region since the defects induced due to fluorine doping enhanced the inherent vortex pinning in the system.

✓ Rare earth doping at Sm^{3+} site in $SmFeAsO_{1-x}F_x$ using 4f elements namely RE^{3+} = Gd^{3+}, Ce^{3+} and a non-4f element Y^{3+} had different impacts on both structural and superconducting properties of the superconductor. 4f-RE^{3+} element doping at Sm^{3+} site increased the T_C of Sm1111 irrespective of their ionic size compared to Sm^{3+} ion. Doping with the smaller Gd^{3+} resulted in lattice contraction and thereby enhanced the T_C; whereas Ce^{3+} doping in Sm1111 exhibited an increase in lattice parameters and yet substantial enhancement of T_C occurred. In both cases the main reason for T_C hike was the increase in charge carrier concentration. Apart from T_C enhancement, the simultaneous doping at oxygen and rare earth sites prominently increased the superconducting properties such as J_C, H_{C1}, H_{C2}, and H_{irr}. Increased number of effective pinning centers in the form of lattice defects created by additional doping at Sm^{3+} would be reason behind it. Among the co-doped samples, Ce^{3+} doped ones exhibited the highest H_{C2} value (385 T) and the best magnetic field dependence of J_C over the entire field of study. This is because the lattice defects created by the larger ion Ce^{3+} acted as very effective pinning centers. Non-4f element, Y^{3+} doping degraded the structural as well as superconducting properties of Sm1111system. Compared to other yttrium doped RE1111 systems, it is inferred that the partial substitution of lanthanides such as La, Ce, and Nd with yttrium systematically enhances T_C of the system to different levels depending on their crystal ionic radii difference with that of yttrium whereas yttrium doping does not seem to be beneficial for Sm1111 because of its comparable ionic size with Sm^{3+}.

✓ Investigations on binary doping in Sm1111 system using alkaline earth metal fluorides such as CaF_2 and BaF_2 enhanced both structural and superconducting properties of Sm1111 superconductor. Microstructures of the samples improved tremendously with binary doping using both CaF_2 and BaF_2 and hence the transport J_C of the binary doped samples increased remarkably. In addition to the enhancement of grain size, CaF_2 doped samples displayed a preferred orientation of (*00l*) planes which was quite interesting. The findings had opened up a scope for the development of Sm1111 based conductors with higher current carrying capacity. A maximum transport J_C of 880 A/cm^2 at 12 K with a T_C of 53.8 K were achieved in the CaF_2 doped sample. BaF_2 doping also enhanced the T_C value, but the increment is only marginal as compared to the CaF_2 doped sample because of the relatively large ionic size of Ba^{2+}. A transport J_C of 875 A/cm^2 at 12 K and a T_C of 49.4 K were obtained by BaF_2 doping in bulk Sm1111 superconductor. Studies on magnetic properties of binary doped Sm1111 bulk superconductors revealed that H_{C2} and $Hirr$ values significantly improved and J_C-H performance also enhanced especially in BaF_2 doped sample due to the enhanced flux pinning resulting from the lattice mismatch created by larger ion doping at Sm^{3+} site.

✓ In order to develop Sm1111 based wires the sheath metal reactivity with Sm1111 compound and its impact on the phase formation and superconducting properties was studied using five different metal sheaths such as Ag, Cu, Fe, Ni, and SS. Among them only Ag and Fe sheathed wires showed superconductivity. Secondary phases corresponding to the sheath metals were formed in the case of Sm1111/Cu, Sm1111/Ni, and Sm1111/SS wire samples whereas no such phases were observed for Sm1111/Fe and

Sm1111/Ag. Hence, Ag and Fe sheath metals were found to be chemically compatible to $SmFeAsO_{1-x}F_x$ samples and among them Ag showed the best transport properties. The effect of processing temperature on the phase formation and superconducting properties of metal sheathed wire samples showed that both Ag and Fe sheathed Sm1111 processed at 850 °C gave the best properties. Sm1111/Ag wire heat treated at 850 °C temperature gave the highest transport critical current density of 4030 A/cm^2 with a T_C around 57 K. Subsequently, the transport J_C of Ag sheathed Sm1111 was further enhanced to 5200 A/cm^2 at 12 K by the incorporation metallic Sn (30 wt%) in to the superconductor core.

8.3 Future directions

- The new synthesis route followed in this work needs fine tuning with respect to the initial starting materials, the nominal stoichiometry and processing conditions at different stages for further enhancement of the superconducting and transport properties.
- Novel preparative methods are to be explored to synthesize phase pure Sm1111 superconductor devoid of the impurity phases namely, SmOF, FeAs, and SmAs which hamper the transport properties of Sm1111 superconductor.
- Impact of doping at Fe and As sites in $SmFeAsO_{1-x}F_x$ superconductor also needs to be studied.
- The role of CaF_2 on the microstructure and preferential orientation along (*00l*) plane is already investigated here in bulk Sm1111samples. There is a great scope for translating the features of CaF_2 doping in to metal sheathed tapes.
- Identifying novel inexpensive sheath metals and exploration for more appropriate metal additives are necessary for the development of low cost metal sheathed Sm1111 wires and tapes with high transport critical current density for technological applications.

References

Abrikosov, A. A. Nobel Lecture: Type-II superconductors and the vortex lattice, *Rev. Mod. Phys.* **2004**, *76*, 975-979.

Abrikosov, A. A.; On the magnetic properties of the superconductors of the second group, *Sov. Phys. JETP* **1957**, *5*, 1174-1182.

Aichhorn, M.; Pourovskii, L.; Vildosola, V.; Ferrero, M.; Parcollet, O.; Miyake, T.; Georges, A.; Biermann, S. Dynamical mean-field theory within an augmented plane-wave framework: Assessing electronic correlations in the iron pnictide LaFeAsO, *Phys. Rev. B* **2009**, *80*, 085101 (15 pp).

Alam, A.; Johnson, D. D. Mixed valency and site-preference chemistry for cerium and its compounds: A predictive density-functional theory study, *Phys. Rev. B* **2014**, *89*, 235126 (4 pp).

Altay A.; Gulgun, M. A. Microstructural evolution of calcium-doped α-alumina, *J. Am. Ceram. Soc.* **2003**, *86*, 623-629.

Anooja, J. B.; Aswathy, P. M.; Sarun, P. M.; Syamaprasad, U. A novel low temperature synthesis route for $SmFeAsO_{1-x}F_x$ bulk superconductor with improved transport properties, *J. Alloy. Compds.* **2012**, *514*, 1-5.

Anooja, J. B.; Aswathy, P. M.; Varghese, N.; Vinod, K.; Bharathi, A.; Syamaprasad, U. Transport and magnetic properties of yttrium doped NdFeAs(O,F) superconductor, *J. Alloy. Compds*. **2013**, *566*, 43-49.

Arushanov, E.; Fuchs, G.; Levcenko, S.; Drechsler, S. L.; Holzapfel, B.; Schultz, L. Scaling of the temperature-dependent resistivity in 122 iron-pnictide superconductors, *Supercond. Sci. Technol.* **2011**, *24*, 105004 (6pp).

Aswathy, P. M.; Anooja, J. B.; Sarun, P. M.; Syamaprasad U. An overview on iron based superconductors, *Supercond. Sci. Technol.* **2010**, *23*, 073001 (20pp).

Awana, V. P. S.; Anand, P.; Vajpayee, A.; Meena, R. S.; Kishan, H.; Husain, M.; Zeng, R.; Yu, S.; Yamaura, K.; Takayama-Muromachi, E. Superconductivity in $SmFe_{1-x}Co_xAsO$ (x=0.0-0.30), *J. Appl. Phys*. **2010**, *107*, 09E146 (3 pp).

Bang, Y. Isotope effect and the role of phonons in the iron-based superconductors, *Phys. Rev. B* **2009**, *79*, 092503 (4 pp).

Bardeen, J.; Cooper, L. N.; Schreiffer, J. R. Microscopic theory of superconductivity, *Phys. Rev.* **1957a**,*106*,162-164.

Bardeen, J.; Cooper, L. N.; Schreiffer, J. R. Theory of superconductivity, *Phys. Rev.* **1957b**, *108*, 1175-1204.

Bardeen, J.; Stephen, M. J. Theory of the motion of vortices in superconductors, *Phys. Rev.* **1965**, *140*, A1197-A1207.

Bean, C.P. Magnetization of hard superconductors, *Phys. Rev. Lett.* **1962**, *8*, 250-253.

Bednorz, J. G.; Muller, K. A. Possible high T_C superconductivity in the Ba−La−Cu−O system, *Phys. B* **1986**, *64*, 189-193.

Biju, A.; Vinod, K.; Sarun, P. M.; Syamaprasad, U. Highly enhanced flux pinning in Pb and rare earth co-doped Bi-2212, *Appl. Phys. Lett.* **2007**, *90*, 072505 (3 pp).

Blatter, G.; Feigel’man, M. V.; Geshkenbein, V. B.; Larkin, A. I.; Vinokur, V. M. Vortices in high-temperature superconductors, *Rev. Mod. Phys.* **1994**, *66*, 1125-1388.

Boeri, L.; Dolgov, O. V.; Golubov, A. A.; Is $LaFeAsO_{1-x}F_x$ an electron-phonon superconductor, *Phys. Rev. Lett.* **2008**, *101*, 026403 (4 pp).

Bonsignore, G.; Gallitto, A. A.; Vigni, M. L.; Luo, J. L.; Chen, G. F.; Wang, N. L.; Shovkun, D. V. Intergrain effects in the AC susceptibility of polycrystalline $LaFeAsO_{0.94}F_{0.06}$, *J. Low Temp. Phys.* **2011**, *162*, 40-51.

Buckel, W.; Kleiner R. Superconductivity fundamentals and applications; Wiley-VCH: Weinheim, **2004**.

Calderón, M. J.; Valenzuela, B.; Bascones, E. Effect of tetrahedral distortion on the electronic properties of iron pnictides, *New J. Phys.* **2009**, *11*, 013051 (9 pp).

Campbell, A.M.; Evetts, J.E. Flux vortices and transport currents in type II superconductors, *Adv. Phys.* **1972**, *21*, 199-428

Canfield, P. C.; Gammel, P. L.; Bishop, D. J. New magnetic superconductors: A toy box for solid-state physicists, Phys. Today, 1998, 51, 40-45.

Canright, G. S.; Vignale, G. Superconductivity and acoustic plasmons in the two-dimensional electron gas, *Phys. Rev. B* **1989**, *39*, 2740-2743.

Cecchetti, E.; Ferreira, P. J.; Vander Sande, J. B. A model for texture development in BSCCO high-Tc superconductors, *Supercond. Sci. Technol.* **2000**, *13*, 1270-1278.

Che, R. C.; Wang, L.; Chen, Z.; Ma, C.; Liang, C. Y.; Lu, J. B.; Shi, H. L.; Yang, H. X.; Li, J. Q. Superconductivity in $(La_{1-x}Ce_x)(O_{0.9}F_{0.1})FeAs$ and $(La_{1-x}Pb_x)OFeAs$, *Europhys. Lett.* **2008**, *83*, 66005 (6 pp).

Chen(a), G. F.; Li, Z.; Li, G.; Zhou, J.; Wu, D.; Dong, J.; Hu, W. Z.; Zheng, P.; Chen, Z. J.; Yuan, H. Q.; Singleton, J.; Luo, J. L.; Wang, N. L. Superconducting properties of the Fe-based layered superconductor $LaFeAsO_{0.9}F_{0.1-\delta}$, *Phys. Rev. Lett.* **2008**, *101*, 057007 (4 pp).

Chen(b), T. Y.; Tesanovic, Z.; Liu, R. H.; Chen, X. H.; Chien, C. L. A BCS-like gap in the superconductor $SmFeAsO_{0.85}F_{0.15}$, *Nature* **2008**, *453*, 1224-1227.

Chen(c), X. H.; Wu, T.; Wu, G.; Liu, R. H.; Chen, H.; Fang, D. F. Superconductivity at 43 K in $SmFeAsO_{1-x}F_x$, *Nature* **2008**, *453*, 761-762.

Chen(d), Y. L.; Cui, Y. J.; Cheng, C. H.; Yang, Y.; Wang, L.; Li, Y. C.; Zhang, Y.; Zhao, Y. Low temperature preparation and superconductivity of F-doped SmFeAsO, *Physica C* **2010a**, *470*, 989-992.

Chen(d), Y. L.; Cui, Y. J.; Cheng, C. H.; Yang, Y.; Zhang, Y.; Zhao, Y. Effect of Y doping on superconductivity and spin-density-wave states in $Sm_{1-x}Y_xFeAsO_{0.8}F_{0.2}$ and $Sm_{1-x}Y_xFeAsO$, *J. Supercond. Nov. Magn.* **2010b**, *23*, 621-624.

Conectus-consortium of European companies to use superconductivity http://www.conectus.org/technology.html

Cui, Y. J.; Chen, Y. L.; Cheng, C. H.; Yang, Y.; Zhang Y.; Zhao, Y. Magnetic properties and superconductivity in $GdFeAsO_{1-x}F_x$, *J. Supercond. Nov. Magn*. **2010**, *23*, 625-628.

Daibo, M.; Fujita, S.; Haraguchi, M.; Iijima, Y.; Itoh, M.; Saitoh, T. Evaluation of a 5T 2nd generation high temperature superconducting magnet with a 200-mm-diameter room temperature bore, *Phys. Procedia* **2013**, *45*, 229-232.

de la Cruz C.; Huang, Q.; Lynn, J. W.; Li, J.; Ratcliff W.; Zarestky, J. L.; Mook, H. A.; Chen, G. F.; Luo, J. L.; Wang, N. L.; Dai, P. Magnetic order close to superconductivity in the iron-based layered $LaO_{1-x}F_xFeAs$ systems, *Nature* **2008**, *453*, 899-902.

deHaas Lorentz, G. L. *Physica* 5:384, 1925.

Ding(a), H.; Richard, P.; Nakayama, K.; Sugawara, K.; Arakane, T.; Sekiba, Y.; Takayama, A.; Souma, S.; Sato, T.; Takahash, T.; Wang, Z.; Dai, X.; Fang, Z.; Chen, G. F.; Luo, J. L.; Wang, N. L. Observation of Fermi-surface–dependent nodeless superconducting gaps in $Ba_{0.6}K_{0.4}Fe_2As_2$, *Europhys. Lett.* **2008**, 83, 47001 (4 pp).

Ding(b), L.; He, C.; Dong, J. K.; Wu, T.; Liu, R. H.; Chen, X. H.; Li, S. Y. Specific heat of the iron-based high-T_C superconductor $SmO_{1-x}F_xFeAs$, *Phys. Rev. B* **2008**, *77*, 180510(R) (4pp).

Ding(c), Y.; Sun, Y.; Zhuang, J. C.; Cui, L. J.; Shi, Z. X.; Sumption, M. D.; Majoros, M.; Susner, M. A.; Kovacs, C. J.; Li, G. Z.; Collings, E. W.; Ren, Z. A. Density effect on critical current density and flux pinning properties of polycrystalline $SmFeAsO_{1-x}F_x$ superconductor, *Supercond. Sci. Technol.* **2011**, *24*, 125012 (7pp).

Fang, M.; Yang, J.; Balakirev, F. F.; Kohama, Y.; Singleton, J.; Qian, B.; Mao, Z. Q.; Wang, H.; Yuan, H. Q. Weak anisotropy of the superconducting upper critical field in $Fe_{1.11}Te_{0.6}Se_{0.4}$ single crystals, *Phys. Rev. B* **2010**, *81*, 020509 (4 pp).

Flukiger, R.; Suo, H. L.; Musolino, N.; Beneduce, C.;Toulemonde, P.; Lezza, P. Superconducting properties of MgB_2 tapes and wires, *Physica C* **2003**, *385*, 286-305.

Fossheim, K.; Sudbø, A. Superconductivity Physics and Applications; John Wiley & Sons Ltd: England, **2004**

Frohlich, H. Theory of the superconducting state. I. the ground state at the absolute zero of temperature, *Phy. Rev.* **1950**, *79*, 845-856.

Fuchs, G.; Drechsler, S. L.; Kozlova, N.; Bartkowiak, M.; Hamann-Borrero, J. E.; Behr, G.; Nenkov, K.; Klauss, H. H.; Maeter, H.; Amato, A.; Luetkens, H.; Kwadrin, A.; Khasanov, R.; Freudenberger, J.; Köhler, A.; Knupfer, M.; Arushanov, E.; Rosner, H.; Büchner, B.; Schultz, L. Orbital and spin effects for the upper critical field in As-deficient disordered Fe pnictide superconductors, *New J. Phys*. **2009**, *11*, 075007 (26 pp).

Fuchs, G.; Drechsler, S. L.; Kozlova, N.; Behr, G.; Köhler, A.; Werner, J.; Nenkov, K.; Klingeler, R.; Hamann-Borrero, J.; Hess, C.; Kondrat, A.; Grobosch, M.; Narduzzo, A.; Knupfer, M.; Freudenberger, J.; Büchner, B.; Schultz, L. High-field pauli-limiting behavior and strongly enhanced upper critical magnetic fields near the transition temperature of an arsenic-deficient $LaO_{0.9}F_{0.1}FeAs_{1-\delta}$ superconductor, *Phys. Rev. Lett*. **2008**, *101*, 237003 (4 pp).

Fujinami, K.; Suematsu, H.; Karppinen, M.; Yamauchi, H. Effect of overdoing on the irreversibility field and critical current density of the $HgBa_2Ca_2Cu_3O_{8+\delta}$ superconductor, *Physica C,* **1998**,*307*, 202-208.

Fujioka, M.; Kota, T.; Matoba, M.; Ozaki, T.; Takano, Y.; Kumakura, H.; Kamihara, Y. Effective ex-situ fabrication of F-doped SmFeAsO wire for high transport critical current density, *Appl. Phys. Express* **2011,** *4*, 063102 (3pp).

Fujitsu, S.; Matsuishi S.; Hosono, H. Iron based superconductors processing and properties, *Int. Mater. Rev.* **2012**, *57*, 311-327.

Ganguli, A. K.; Prakash, J.; Singh, S. J.; Patnaik, S. Role of chemical pressure in enhancing the transition temperature (T_C) and upper critical field (H_{C2}) in the Y-doped Ce-oxyfluoride superconductor, *Eur. Phys. J. B* **2010**, *73*, 177-184.

Gao(a), L.; Xue, Y. Y.; Chen, F.; Xiong, Q.; Meng, R. L.; Ramirez, D.; Chu, C. W.; Eggert, J. H.; Mao, H. K. Superconductivity up to 164 K in $HgBa_2Ca_{m-1}Cu_mO_{2m+2+\delta}$ (m=1, 2, and 3) under quasi hydrostatic pressures, *Phys. Rev. B* **1994**, *50*, 4260-4263.

Gao(b), Z.; Ma, Y. W.; Yao, C.; Zhang, X. P.; Wang, C. L.; Wang, D. L.; Awaji, S.; Watanabe, K. High critical current density and low anisotropy in textured $Sr_{1-x}K_xFe_2As_2$ tapes for high field applications, *Sci. Rep.* **2012**, *2*, 998 (4 pp).

Gao(b), Z.; Wang, L.; Qi, Y.; Wang, D.; Zhang, X.; Ma, Y.; Yang, H.; Wen, H. Superconducting properties of granular $SmFeAsO_{1-x}F_x$ wires with T_C=52 K prepared by the powder-in-tube method, *Supercond. Sci. Technol*. **2008**, *21*, 112001 (4 pp).

Ginzburg, V. L. Nobel Lecture: On superconductivity and superfluidity (what I have and have not managed to do) as well as on the “physical minimum” at the beginning of the XXI century, *Rev. Mod. Phys.* **2004**, *76*, 981-998.

Ginzburg, V. L.; Landau, L. D. On the theory of superconductivity, *Sov. Phys. JETP* **1950**, *20*, 1064-1082.

Gomory, F. Characterization of high-temperature superconductors by AC susceptibility measurements, *Supercond. Sci. Technol.* **1997**, *10*, 523-542.

Goodstein, D.; Goodstein, J. Richard Feynman and the history of Superconductivity, *Phys. perspect.* **2000**, *2*, 30-47.

Gurevich, A. Enhancement of the upper critical field by nonmagnetic impurities in dirty two-gap superconductors, *Phys. Rev. B* **2003**, *67*, 184515 (13 pp).

Gurevich, A. Iron-based superconductors at high magnetic fields, *Rep. Prog. Phys.* **2011**, *74*, 124501 (19pp).

Gurevich, A. Upper critical field and the Fulde-Ferrel-Larkin-Ovchinnikov transition in multiband superconductors, *Phys. Rev. B* **2010**, *82* , 184504 (14 pp).

Hao, J.; Sun, Y.; Xu, Z.; Cao, G. Crystal chemistry and structural design of iron-based superconductors, *Chin. Phys. B* **2013**, *22*, 087410 (11 pp).

Hikata, T.; Sato, K.; Hitotsuyanagi, H. Ag-sheathed Bi-Pb-Sr-Ca-Cu-O ssuperconducting wires with high critical current density, *Japan. J. Appl. Phys.* **1989**, *28*, L82-L84.

Hosono, H.; Matsuishi, S. Superconductivity induced by hydrogen anion substitution in 1111-type iron arsenides, *Curr. Opin. Solid State Mater. Sci.* **2013**, *17*, 49–58.

Hott, R.; Kleiner, R.; Wolf, T.; Zwicknagl, G. Frontiers in superconducting materials: superconducting material – A topical overview; A. V. Narlikar (Ed.), Springer: Berlin, **2005**, 1-50.

Hsu, F. C.; Luo, J. Y.; Yeh, K. W.; Chen, T. K.; Huang, T. W.; Wu, P. M.; Lee, Y. C.; Huang, Y. L.; Chu, Y. Y.; Yan D. C.; Wu M. K. Superconductivity in the PbO-type structure α-FeSe, *Proc. Natl. Acad. Sci.* **2008**, *105*, 14262-14264.

Huang, Q.; Qiu, Y.; Bao, W.; Green, M. A.; Lynn, J. W.; Gasparovic, Y. C.; Wu, T.; Wu, G.; Chen, X. H. Neutron-diffraction measurements of magnetic order and a structural transition in the parent $BaFe_2As_2$ compound of FeAs-based high-temperature superconductors, *Phys. Rev. Lett.* **2008**, *101*, 257003 (4 pp).

Hudakova, N.; Plechacek, V.; Dordor, P.; Flachbart, K.; Knizek, K.; Kovac, J.; Reiffers, M. Influence of Pb concentration on microstructural and superconducting properties of BSCCO superconductors, *Supercond. Sci. Technol.* **1995**, *8*, 324

Hunte, F. J.; Jaroszynski, A.; Gurevich, D. C.; Larbalestier, R.; Jin, A.; Sefat, S.; McGuire, M. A.; Sales, B. C.; Christen, D. K.; Mandrus, D. Two-band superconductivity in $LaFeAsO_{0.89}F_{0.11}$ at very high magnetic fields, *Nature* **2008**, *453*, 903-905.

Ishida, K.; Nakai, Y.; Hosono, H. *J. Phys. Soc. Jpn*. **2009**, *78*, 062001 (20 pp).

Jaroszynski, J., Riggs, S. C.; Hunte, F.; Gurevich, A., Larbalestier, D. C.; Boebinger, G. S.; Balakirev, F. F.; Migliori, A.; Ren, Z. A.; Lu, W.; Yang, J.; Shen, X. L.; Dong, X. L.; Zhao, Z. X.; Jin, R.; Sefat, A. S.; McGuire, M. A.; Sales, B. C.; Christen, D. K.; Mandrus, D. Comparative high-field magnetotransport of the oxypnictide superconductors $RFeAsO_{1-x}F_x$ (R=La, Nd) and $SmFeAsO_{1-\delta}$, *Phys. Rev. B* **2008a**, *78*, 064511 (5 pp).

Jaroszynski, J.; Hunte, F.; Balicas, L.; Y. Jo.; Raičević, I.; Gurevich, A.; Larbalestier, D. C.; Balakirev, F. F.; Fang, L.; Cheng, P.; Jia, Y.; Wen H. H. Upper critical fields and thermally-activated transport of $NdFeAsO_{0.7}F_{0.3}$ single crystal, *Phys. Rev. B* **2008b**, *78*, 174523 (9pp).

Jérome, D.; Mazaud, A.; Ribault, M.; Bechgaard, K. Superconductivity in a synthetic organic conductor (TMTSF)2PF6, *J. Phys. (Paris) Lett.* **1980**, *41*, L95-L98.

Jia, Y.; Cheng, P.; Fang, L.; Luo, H. Q.; Yang, H.; Ren, C.; Shan, L.; Gu, C. Z.; Wen, H. H. Critical fields and anisotropy of $NdFeAsO_{0.82}F_{0.18}$ single crystals, *Appl. Phys. Lett.* **2008**, *93*, 032503 (3 pp).

Jishi, R. A.; Alyahyaei, H. M. Effect of hybridization on structural and magnetic properties of iron-based superconductors, *New J. Phys*. **2009**, *11*, 083030 (8 pp).

Joa, Y. J.; Jaroszynskia, J.; Yamamotoa, A.; Gurevicha, A.; Riggsa, S. C.; Boebingera, G. S.; Larbalestiera, D.; Wenb, H. H.; Zhigadloc, N. D.; Katrychc, S.; Bukowskic, Z.; Karpinskic, J.; Liud, R. H.; Chend, H.; Chend, X. H.; Balicasa, L. High-field phase-diagram of Fe arsenide superconductors, *Physica C* **2009**, *469*, 566-574.

Johnston, D. C. The puzzle of high temperature superconductivity in layered iron pnictides and chalcogenides, *Adv. Phys.* **2010**, *59*, 803-1061.

Johrendt D. Structure–property relationships of iron arsenide superconductors, *J. Mater. Chem.* **2011**, *21*, 13726-13736.

Josephson, B. D. Possible new effects in superconductive tunneling, *Phys. Lett*. **1962,** *1*, 251-253.

Kadowaki, K.; Goya, T.; Mochiji, T.; Chong, S. V. Superconductivity and magnetism in $REFeAsO_{1-x}F_x$ (RE=Rare earth elements), *J. Phys. Conf. Ser.* **2009**, *150*, 052088.

Kametani, F.; Li, P.; Abraimov, D.; Polyanskii, A. A.; Yamamoto, A.; Jiang, J.; Hellstrom, E. E.; Gurevich, A.; Larbalestier, D. C.; Ren, Z. A.; Yang, J.; Dong, X. L.; Lu, W.;

Zhao, Z. X. Intergrain current flow in a randomly oriented polycrystalline $SmFeAsO_{0.85}$ oxypnictide, *Appl. Phys. Lett.* **2009a**, *95*, 142502 (3pp).

Kametani, F.; Polyanskii, A. A.; Yamamoto, A.; Jiang, J.; Hellstrom, E. E.; Gurevich, A.; Larbalestier, D. C.; Ren, Z. A.; Yang, J.; Dong, X. L.; Lu, W.; Zhao, Z. X. Combined microstructural and magneto-optical study of current flow in polycrystalline forms of Nd and Sm Fe-oxypnictides, *Supercond. Sci. Technol.* **2009b**, *22*, 015010 (6pp).

Kamihara, Y.; Hiramatsu, H.; Hirano, M.; Kawamura, R.; Yanagi, H.; Kamiya, T.; Hosono, H. Iron-Based Layered Superconductor: LaOFeP, *J. Am. Chem.Soc.* **2006**, *128*, 10012-10013.

Kamihara, Y.; Watanabe, T.; Hirano, M.; Hosono, H. Iron-Based Layered Superconductor $La[O_{1-x}F_x]FeAs$ (x = 0.05-0.12) with T_C = 26 K, *J. Am. Chem. Soc*. **2008**,*130*, 3296-3297.

Katase, T.; Hiramatsu, H.; Matias, V.; Sheehan, C.; Ishimaru, Y.; Kamiya, T.; Tanabe, K.; Hosono, H. Biaxially textured cobalt-doped $BaFe_2As_2$ films with high critical current density over 1 MA/cm^2 on MgO-buffered metal-tape flexible substrates, *Appl. Phys. Lett.* **2011**, *98*, 242510 (3 pp).

Kitazawa, K. V. Superconductivity: 100th anniversary of its discovery and its future, *Jpn. J. Appl. Phys.* **2012**, *51*, 010001 (14 pp).

Koblischka, M. R.; Murakami, M. Pinning mechanisms in bulk high-T_C superconductors, *Supercond. Sci. Technol.* **2000**, *13*, 738–744.

Koizumi, N. Progress of ITER superconducting magnet procurement, *Phys. Procedia* **2013**, *45*, 225-228.

Kontani, H.; Onari, S. Orbital-fluctuation-mediated superconductivity in iron pnictides: analysis of the five-orbital hubbard-holstein model, *Phys. Rev. Lett.* **2010**, 104, 157001 (4 pp).

Kou, S. P.; Li, T.; Weng, Z. Y.; Coexistence of itinerant electrons and local moments in iron-based superconductors, *Europhys. Lett.* **2009**, *88*, 17010 (6 pp).

Kresin, V. Z.; Wolf, S. A. Electron-lattice interaction and its impact on high T_C superconductivity, *Rev. Mod. Phys.* **2009**, *81*,481-501.

Kunzler, J. E.; Wernick, J. H.; Hsu, F. S. L.; Buehler, E. Superconductivity in Nb_3Sn at high current density in a magnetic field of 88 kgauss, *Phys. Rev. Lett.* **1961**, *6*, 89-91.

Lai, K.T.; Kwong, F. L.; Dickon, H. L. N. Superconductivity in fluorine and yttrium co-doped SmFeAsO, *J. Appl. Phys.* **2012**, *111*, 093912 (5 pp).

Landau, L. D. `Theory of phase transformations. II, *Zh. Eksp. Teor. Fiz. (Russ.)* **1937**, *7*, 627-.

Larkin, A. I., Ovchinnikov, Y. N. Pinning in type II superconductors, *J. Low Temp. Phys.* **1979,** *34*, 409-428.

Lee(a), C. H.; Iyo, A.; Eisaki, H.; Kito, H.; Fernandezdiaz, M. T.; Ito, T.; Kihou, K.; Matsuhata, H.; Braden, M.; Yamada, K. Effect of structural parameters on superconductivity in fluorine-free $LnFeAsO_{1-y}$ (Ln = La, Nd), *J. Phys. Soc. Japan* **2008** *77*, 083704 (4 pp).

Lee(b), P.; Lee, P. J. Encyclopedia of Materials: Science and Technology: Superconductor: Wires and Cables: Materials and Processes; Elsevier: Netherlands, **2004**, 1-11.

Lee(c), S.; Jiang, J.; Weiss, J. D.; Folkman, C. M.; Bark, C. W.; Tarantini, C.; Xu, A.; Abraimov, D.; Polyanskii, A.; Nelson, C. T.; Zhang, Y.; Baek, S. H.; Jang, H. W.; Yamamoto, A; Kametani, F; Pan, X, Q; Hellstrom, E. E.; Gurevich, A.; Eom, C. B.; Larbalestier, D. C. Weak-link behavior of grain boundaries in superconducting $Ba(Fe_{1-x}Co_x)_2As_2$ bicrystals, *Appl. Phys. Lett.* **2009**, *95*, 212505 (3 pp).

Lei, H.; Hu, R.; Choi, E. S.; Warren, J. B.; Petrovic, C. Pauli-limited upper critical field of $Fe_{1+y}Te_{1-x}Se_x$, *Phys. Rev. B* **2010**, *81*, 094518 (7 pp).

Liang C. Y.; Che, R. C.; Yang, H. X.; Tian, H. F.; Xiao, R. J.; Lu, J. B.; Li, R.; Li, J. Q. Synthesis and structural characterization of LaOFeP superconductors, *Supercond. Sci. Technol.* **2007**, *20*, 687-690.

Liu(a), C. Three- to two-dimensional transition of the electronic structure in $CaFe_2As_2$: A parent compound for an iron arsenic high-temperature superconductor, *Phys. Rev. Lett.* **2009**, *102*, 167004 (4 pp).

Liu(b), R. H.; Wu, G.; Wu, T.; Fang, D. F.; Chen, H.; Li, S.Y.; Liu, K.; Xie, Y. L.; Wang, X. F.; Yang, R. L.; Ding, L.; He, C.; Feng, D. L.; Chen, X. H. Anomalous transport properties and phase diagram of the FeAs-based $SmFeAsO_{1-x}F_x$ superconductors, *Phys. Rev. Lett.* **2008**, *101*, 087001 (4pp).

London, F.; London, H. Superconductivity and diamagnetism, *Physica* **1935a**, *2*, 341-354.

London, F.; London, H. The electromagnetic equations of the supraconductor, *Proc. Roy. Soc. A* **1935b**, *149*, 71-88.

Lu, W.; Shen, X. L.; Yang, J.; Li, Z. C.; Yi, W.; Ren, Z. A.; Dong, X. L.; Che, G. C.; Sun, L. L.; Zhou, F.; Zhao, Z. X. Superconductivity at 41.0 K in the F-doped $LaFeAsO_{1-x}F_x$, *Solid State Commun.* **2008**, *148*, 168-170.

Ma(a), F.; Ji, W.; Hu, J.; Lu, Z. Y.; Xiang, T. First-principles calculations of the electronic structure of tetragonal α-FeTe and α-FeSe crystals: evidence for a bicollinear antiferromagnetic order, *Phys. Rev. Lett.* **2009**, *102*, 177003 (4 pp).

Ma(a), F.; Lu, Z. Y. Iron-based layered compound LaFeAsO is an antiferromagnetic semimetal, *Phys. Rev. B* **2008**, *78*, 033111 (4pp).

Ma(b), Y. Progress in wire fabrication of iron-based superconductors, *Supercond. Sci. Technol.* **2012**, *25*, 113001 (24pp).

Ma(b), Y.; Gao, Z. S.; Wang, L.; Qi, Y. P.; Wang, D. L.; Zhang, X. P. Simple One-Step Synthesis and Superconducting Properties of $SmFeAsO_{1-x}F_x$, *Chin. Phys. Lett.* **2009a**, *26*, 037401 (4 pp).

Ma(b), Y.; Gao, Z.; Qi, Y.; Zhang, X.; Wang, L.; Zhang, Z.; Wang, D. Fabrication and characterization of iron pnictide wires and bulk materials through the powder-in-tube method, *Physica C* **2009b**, *469*, 651–656.

Ma(b), Y.; Wang, L.; Qi, Y.; Gao, Z.; Wang, D.; Zhang X. Development of powder-in-tube processed iron pnictide wires and tapes, *IEEE T. Appl. Supercon.* **2011**, *21*, 2878-2881.

Margadonna, S.; Takabayashi, Y.; McDonald, M. T.; Brunelli, M.; Wu, G.; Liu, R. H.; Chen, X. H.; Prassides, K. Crystal structure and phase transitions across the metal-superconductor boundary in the $SmFeAsO_{1-x}F_x$ ($0 \leq x \leq 0.20$) family, *Phys. Rev. B* **2009**, *79*, 014503 (7pp).

Martinelli, A.; Ferretti, M.; Manfrinetti, P.; Palenzona, A.; Tropeano, M.; Cimberle, M. R.; Ferdeghini, C.; Valle, R.; Bernini, C.; Putti, M.; Siri, A. S. Synthesis, crystal structure, microstructure, transport and magnetic properties of SmFeAsO and SmFeAs($O_{0.93}F_{0.07}$), *Supercond. Sci. Technol.* 2008, *21*, 095017 (7pp).

Matsuhita, T. Flux pinning in superconductors; Springer: Berlin, **2007**.

Matsumoto, K. High temperature superconductors: General theory of High T_C superconductors; Wiley-VCH: Weinheim, **2010**, 1–47.

Mazin, I. I. Superconductivity gets an iron boost, *Nature* **2010**, *464*, 183-186.

Mazin, I. I.; Schmalian, J. Pairing symmetry and pairing state in ferropnictides: Theoretical overview, *Physica C* **2009**, *469*, 614-627.

McQueen, T. M.; Huang, Q.; Ksenofontov, V.; Felser, C.; Xu, Q.; Zandbergen, H.; Hor, Y. S.; Allred, J.; Williams, A. J.; Qu, D.; Checkelsky, J.; Ong, N. P.; Cava, R. J. *Phys. Rev. B* **2009**, *79*, 014522 (7 pp).

Meissner, W.; Oschenfeld, R. A new effect upon the occurrence of superconductivity, *Naturwissenschaften* **1933**, *21*, 787-788.

Min, Z. A.; Ming, Z. Q. Electron-phonon coupling in cuprate and iron-based superconductors revealed by Raman scattering, *Chin. Phys. B* **2013**, 22, 087103 (12 pp).

Mizuguchi, Y.; Hara, Y.; Deguchi, L.; Tsuda, S.; Yamaguchi, T.; Takeda, K.; Kotegawa, H.; Tou, H.; Takano, Y. Anion height dependence of T_C for the Fe-based superconductor, *Supercond. Sci. Technol.* **2010**, *23*, 054013 (5 pp).

Moon, C. Y.; Park, S. Y.; Choi, H. J. Dominant role of local-moment interactions in the magnetic ordering of iron pnictide superconductors: a comparative study of arsenides and antimonides from first principles, *Phys. Rev. B* **2009**, *80*, 054522 (6 pp).

Müller, K. H. Frequency dependence of AC susceptibility in high-temperature superconductors: Flux creep and critical state at grain boundaries, *Physica C* **1990**, *168*, 585-590.

Nagamatsu, J.; Nakagawa, N.; Muranaka, T.; Zenitani, Y.; Akimitsu, J. Superconductivity at 39 K in magnesium diboride, *Nature* **2001**, *410*, 63-64.

Narduzzo, A.; Grbić, M. S.; Požek, M.; Dulčić, A.; Paar, D.; Kondrat, A.; Hess, C.; Hellmann, I.; Klingeler, R.; Werner, J.; Köhler, A.; Behr, G.; Büchner, B. Upper critical field, penetration depth, and depinning frequency of the high-temperature superconductor LaFeAsO0.9F0.1 studied by microwave surface impedance, *Phys. Rev. B* **2008**, *78*, 012507 (4 pp).

Nikolo, M.; Goldfarb, R. B. Flux creep and activation energies at the grain boundaries of Y-Ba-Cu-O superconductors, *Phys. Rev. B* **1989**, *39*, 6615-6618.

Nomura, T.; Kim, S. W.; Kamihara, Y.; Hirano, M.; Sushko, P. V.; Kato, K.; Takata, M.; Shluger, A. L.; Hosono, H. Crystallographic phase transition and high-T_C superconductivity in LaFeAsO:F, *Supercond. Sci. Technol.* **2008**, *21*, 125028 (9pp).

Oh, H.; Moon, J.; Shin, D.; Moon, C. Y.; Choi H. J. Brief review on iron-based superconductors: are there clues for unconventional superconductivity, *Progress in Superconductivity* **2011,** *13*, 65-84.

Okada, H.; Igawa, K.; Takahashi, H.; Kamihara, Y.; Hirano, M.; Hosono, H.; Matsubayashi, K.; Uwatoko, Y. Superconductivity under high pressure in LaFeAsO, *J. Phys. Soc. Jpn.* **2008**, *77*, 113712 (4 pp).

Onnes, H. K. *Leiden Commun.*, **1911**, *124*, 1226-.

Otabea, E. S.; Kiuchia, M.; Kawaia, S.; Moritab, Y.; Geb, J.; Nib, B.; Gaoc, Z.; Wangc, L.; Qic, Y.; Zhangc, X.; Mac, Y. Global and local critical current density in superconducting $SmFeAsO_{1-x}F_x$ measured by two methods, *Physica C* **2009**, *469*, 1940-1944.

Parker, D. R.; Pitcher, M. J.; Baker, P. J.; Franke, I.; Lancaster, T.; Blundell, S. J.; Clarke, S. J. Structure, antiferromagnetism and superconductivity of the layered iron arsenide NaFeAs, *Chem. Commun.* **2009**, *16*, 2189-2191.

Polichetti, M.; Adesso, M. G.; Zola, D.; Luo, J. L.; Chen, G. F.; Li, Z.; Wang, N. L.; Noce, C.; Pace, S. Granularity and vortex dynamics in $LaFeAsO_{0.92}F_{0.08}$ probed by harmonics of the ac magnetic susceptibility, *Phys. Rev. B* **2008**, *78*, 224523 (10pp).

Prakash, J.; Singh, S. J.; Banerjee, A.; Patnaik, S.; Ganguli, A. K. Enhancement in transition temperature and upper critical field of $CeO_{0.8}F_{0.2}FeAs$ by yttrium doping, *Appl. Phys. Lett.* **2009**, *95*, 262507 (3 pp).

Pratt, D. K.; Tian, W.; Kreyssig, A.; Zarestky, J. L.; Nandi, S.; Ni, N.; Bud’ko, S. L.; Canfield, P. C.; Goldman, A. I.; McQueeney, R. J. Coexistence of competing antiferromagnetic and superconducting phases in the under doped

$Ba(Fe_{0.953}Co_{0.047})_2As_2$ compound using X-ray and neutron scattering techniques, *Phys. Rev. Lett.* **2009**, *103*, 087001 (4 pp).

Putti, M.; Pallecchi, I.; Bellingeri, E.; Cimberle, M. R.; Tropeano, M.; Ferdeghini, C.; Palenzona, A.; Tarantini, C.; Yamamoto, A.; Jiang, J.; Jaroszynski, J.; Kametani, F.; Abraimov, D.; Polyanskii, A.; Weiss, J. D.; Hellstrom, E. E.; Gurevich, A.; Larbalestier, D. C.; Jin, R.; Sales, B. C.; Sefat, A. S.; McGuire, M. A.; Mandrus, D.; Cheng, P.; Jia, Y.; Wen, H. H.; Lee S.; Eom C. B. New Fe-based superconductors: properties relevant for applications, *Supercond. Sci. Technol*. **2010**, *23*, 034003 (10pp).

Ren(a), Z. A.; Che, G. C.; Dong, X. L.; Yang, J.; Lu, W.; Yi, W.; Shen, X. L.; Li, Z. C.; Sun, L. L.; Zhou, F.; Zhao, Z. X. Superconductivity and phase diagram in iron-based arsenic-oxides $ReFeAsO_{1-\delta}$ (Re = rare-earth metal) without fluorine doping, *Europhys. Lett.* **2008a**, *83*, 17002 (4 pp).

Ren(a), Z. A.; Lu, W.; Yang, J.; Yi, W.; Shen, X. L.; Li, Z. C.; Che, G. C.; Dong, X. L.; Sun, L. L.; Zhou, F.; Zhao, Z. X. Superconductivity at 55K in iron-based F-doped layered quaternary compound $Sm[O_{1-x}F_x]FeAs$, *Chin. Phys. Lett.* **2008b**, *25*, 2215-2216.

Ren(a), Z. A.; Zhao, Z. X. Research and prospects of iron-based superconductors, *Adv. Mater.* **2009**, *21*, 4584-4592.

Ren(b), Z.; Tao, Q.; Jiang, S.; Feng, C.; Wang, C.; Dai, J.; Cao, G.; Xu, Z. Superconductivity induced by phosphorus doping and its coexistence with ferromagnetism in $EuFe_2(As_{0.7}P_{0.3})_2$, *Phys. Rev. Lett*. **2009**, *102*, 137002 (4 pp).

Riggs, S. C.; McDonald, R. D.; Kemper, J. B.; Stegen, Z.; Boebinger, G. S.; Balakirev, F. F.; Kohama, Y.; Migliori, A.; Chen, H.; Liu, R. H.; Chen, X. H. Doping dependent nonlinear Hall effect in $SmFeAsO_{1-x}F_x$, *J. Phys.: Condens. Matter*. **2009**, *21*, 412201 (5pp).

Rotter, M.; Tegel, M.; Johrendt, D. Superconductivity at 38 K in the iron arsenide $(Ba_{1-x}K_x)Fe_2As_2$, *Phys. Rev. Lett.* **2008**, 101, 107006 (4pp).

Salamati, H.; Kameli, P. AC susceptibility study of YBCO thin film and BSCCO bulk superconductors, *J. Magn. Magn. Mater*. **2004**, *278*, 237-243.

Savvides, N.; Katsaros, A.; Andrikidis, C.; Muller, K. H. Temperature, field and frequency dependence of intergranular AC loss in high-temperature superconductors, *Physica C* **1992**, 197, 267-273.

Schrieer, J. R. Theory of superconductivity; Advanced book program, Perseus books, **1964**.

Schrieffer, J. R.; Tinkham, M.; Superconductivity, *Rev. Mod. Phys*., **1999**, *71*, S313-S317.

Sefat, A. S. Bulk synthesis of iron-based superconductors, *Curr. Opin. Solid State Mater. Sci.* **2013**, *17*, 59–64.

Sefat, A. S. Pressure effects on two superconducting iron-based families, *Rep.Prog.Phys.* **2011**, *74*, 124502 (14 pp).

Sefat, A. S.; Huq, A.; McGuire, M. A.; Jin, R.; Sales, B. C.; Mandrus, D. Superconductivity in $LaFe_{1-x}Co_xAsO$, *Phys. Rev. B* **2008a**, *78*, 104505 (9 pp).

Sefat, A. S.; Jin, R.; Mcguire, M. M.; Sales, B. C.; Singh, D. J.; Mandrus, D. Superconductivity at 22 K in Co-Doped $BaFe_2As_2$ Crystals, *Phys. Rev. Lett*. **2008b**, *101*, 117004 (4 pp).

Sefat, A. S.; McGuire, M. A.; Sales, B. C.; Jin, R.; Howe, J. Y.; Mandrus, D. Electronic correlations in the superconductor $LaFeAsO_{0.89}F_{0.11}$ with low carrier density, *Phys. Rev. B* **2008c**, *77*, 174503 (6 pp).

Senatore, C.; Wu, G.; Liu, R. H.; Chen, X. H.; Flukiger, R. Upper critical fields well above 100 T for the superconductor $SmFeAsO_{0.85}F_{0.15}$ with T_C=46 K, *Phys. Rev. B* **2008**, *78*, 054514 (7pp).

Seuntjens, J. M.; Larbalestier, D. C. On the improvement of $DyBa_2Cu_3O_{7-\delta}$ properties through better sintering, *J. Appl. Phys*. **1990**, *67*, 2007-2016.

Shekhar, C.; Singh, S.; Siwach, P. K.; Singh, H. K.; Srivastava, O. N. Synthesis and microstructural studies of iron oxypnictide $LaO_{1-x}F_xFeAs$ superconductors, *Supercond. Sci. Technol.* **2008**, *22*, 015005 (5 pp).

Shi, S. L.; Fang, A. H.; Xie, X. M.; Huang, F. Q.; Jiang, M. H. MgF_2 doping of SmFeAsO superconductors prepared by mechanical alloying and rapid annealing, *Chem. Mater.* **2011**, *23*, 3039-3044.

Shirage, P. M.; Miyazawa, K.; Kito, H.; Eisaki, H.; Iyo, A. Superconductivity at 43 K at ambient pressure in the iron-based layered compound $La_{1-x}Y_xFeAsO_y$, *Phys. Rev. B* **2008**, *78*, 172503 (4 pp).

Shuba, R.; Chen, I. W. Effect of seeding on the microstructure and mechanical properties of α-SiAlON: II, Ca-α-SiAlON, *J. Am. Ceram. Soc.* **2002**, *85*, 1260-1267.

Shubnikov, L.V.; Khotkevich, V.I.; Shepelev, Y. D.; Riabinin, Y. N. Magnetic properties of superconducting metals and alloys, *Zh. Exp. Teor. Fiz. (USSR)* **1937**, *7*, 221-237.

Singh, D. J.; Du, M. H. Density functional study of $LaFeAsO_{1-x}F_x$: A low carrier density superconductor near itinerant magnetism, *Phys. Rev. Lett.* **2008**, *100*, 237003 (4 pp).

Solov’ev, A. L.; Dmitriev, V. M. Fluctuation conductivity and pseudogap in YBCO high-temperature superconductors, *Low Temp. Phys.* **2009**, *35*, 169-197.

Solovjov, A. L.; Svetlov, V. N.; Stepanov, V. B.; Sidorov, S. L.; Tarenkov, V. Y.; D’yachenko, A. I.; Agafonov, A. B. Possibility of local pair existence in optimally doped $SmFeAsO_{1-x}$ in pseudogap regime, *Low Temp. Phys.* **2011**, *37*, 557-560.

Steglich, F.; Aarts, J.; Bredl, C. D.; Lieke, W.; Meschede, D.; Franz, W.; Schäfer, H. Superconductivity in the presence of strong Pauli paramagnetism: $CeCu_2Si_2$, *Phys. Rev. Lett.* **1979**, *43*, 1892 -1896.

Sun, Y.; Ding, Y.; Zhuang, J. C.; Cui, L. J.; Yuan, X. P.; Shi, Z. X.; Ren, Z. A. An anomalous tail effect in the resistivity transition and weak-link behavior of superconducting $NdFeAsO_{0.88}F_{0.12}$, *Supercond. Sci. Technol*. **2011**, *24*, 085011 (5 pp).

Superconductivity Present and Future Applications 2009 CCAS: Coalition for the Commercial Application of Superconductors http://ccas-web.org/pdf/ccas_brochure_web.pdf

Takabayashi, Y.; McDonald, M. T.; Papanikolaou, D.; Margadonna, S.; Wu, G.; Liu, R. H.; Chen, X. H.; Prassides, K. Doping dependence of the pressure response of T_C in the $SmO_{1-x}F_xFeAs$ superconductors, *J. Am. Chem. Soc.* **2008**, *130*, 9242–9243.

Takada, Y. S- and p-wave pairings in the dilute electron gas: Superconductivity mediated by the Coulomb hole in the vicinity of the Wigner-crystal phase, *Phys. Rev. B* **1993**, *47*, 5202-5211.

Takahashi, H.; Igawa, K.; Arii, K.; Kamihara, Y.; Hirano, M.; Hosono, H. Superconductivity at 43 K in an iron-based layered compound $LaO_{1-x}F_xFeAs$, *Nature* **2008**, *453*, 376-378.

Tani, T.; Itahara, H.; Kadoura, H.; Asahi, R. Crystallographic orientation analysis on calcium cobaltite ceramic grains textured by reactive- templated grain growth, *Int. J. Appl. Ceram. Technol.* **2007**, *4*, 318-325.

Tanigaki, K.; Ebbesen, T. W.; Saito, S.; Mizuki, J.; Tsai, J. S.; Kubo, Y.; Kuroshima, S. Superconductivity at 33 K in CsxRbyC60, *Nature* **1991**, *352*, 222-223.

Tarantini, C.; Gurevich, A. High-field properties of pure and doped MgB_2 and Fe-based superconductors, *MRS Bulletin* 2011, *36*, 626-630.

Tarantini, C.; Gurevich, A.; Larbalestier, D. C.; Ren, Z. A.; Dong, X. L.; Lu, W.; Zhao, Z. X. Superconductivity and antiferromagnetic ordering in the high-field paramagnetic oxypnictide $NdFeAsO_{0.94}F_{0.06}$, *Phys. Rev. B* **2008**, *78*, 184501(5pp).

Tesanovic, Z. Viewpoint: Are iron pnictides new cuprates, *Physics* **2009**, *2*, 60.

Tropeano, M.; Fanciulli, C.; Canepa, F.; Cimberle, M. R.; Ferdeghini, C.; Lamura, G.; Martinelli, A.; Putti, M.; Vignolo, M.; Palenzona, A. Effect of chemical pressure on spin density wave and superconductivity in undoped and 15% F-doped $La_{1-y}Y_yFeAsO$ compounds, *Phys. Rev. B* **2009**, *79*, 174523 (6 pp).

Varghese, N.; Vinod, K.; Abhilash Kumar, R. G. ; Syamaprasad, U. Influence of reactivity of sheath materials with Mg/B on superconducting properties of MgB_2, *J. Appl. Phys.***2007**, *102*, 043914 (4 pp).

Vegard, L. The constitution of the mixed crystals and the room filling the atoms, *J. Phys.* **1921**, *5*, 17-26.

Vinu, S.; Sarun, P. M.; Shabna, R.; Syamaprasad, U. Refinement of microstructure and highly improved electrical properties of $Bi_{1.6}Pb_{0.5}Sr_{1.925}Ho_{0.075}Ca_{1.1}Cu_{2.1}O_{8+\delta}$ superconductor, *J. Appl. Phys.* **2009**, *106*, 063920 (6pp).

Vonsovsky, S. V.; Izyumov, Y. A.; Kurmaev, E. Z. Superconductivity in transition metals; Springer: New York, **1982**.

Wang(a), C.; Li, L.; Chi, S.; Zhu, Z.; Ren, Z.; Li, Y.; Wang, Y.; Lin, X.; Luo, Y.; Jiang, S.; Xu, X.; Cao, G.; Xu, Z. Thorium-doping–induced superconductivity up to 56 K in $Gd_{1-x}Th_xFeAsO$, *Europhys. Lett.* **2008**, *83*, 67006 (4pp).

Wang(a), C.; Yao, C.; Lin, H.; Zhang, X.; Zhang, Q.; Wang, D.; Ma, Y.; waji, S. A.; Watanabe, K;. Tsuchiya, Y.; Sun, Y.; Tamegai, T. Large transport J_C in Sn-added $SmFeAsO_{1-x}F_x$ tapes repared by an ex situ PIT method, *Supercond. Sci. Technol.* **2013**, *26*, 075017 (6pp).

Wang(a), C.; Yao, C.; Zhang, X. P.; Gao, Z. S.; Wang, D. L.; Wang, C. D.; Lin, H.; Ma, Y. W.; Awaji, S.; Watanabe, K. Effect of starting materials on the superconducting properties of $SmFeAsO_{1-x}F_x$ tapes, *Supercond. Sci. Technol.* **2012**, *25*, 035013 (4 pp).

Wang(b), L.; Qi, Y.; Wang, D.; Gao, Z.; Zhang, X.; Zhang, Z.; Wang, C.; Ma, Y. Low-temperature synthesis of $SmFeAsO_{0.7}F_{0.3-\delta}$ wires with a high transport critical current density, *Supercond. Sci. Technol.* **2010**, *23*, 075005 (4 pp).

Wang(c), X. C.; Liu, Q. Q.; Lv, Y. X.; Gao, W. B.; Yang, L. X.; Yu, R. C.; ,Li, F. Y.; Jin, C. Q. The superconductivity at 18 K in LiFeAs system, *Solid State Commun.* **2008**, *148*, 538-540.

Wang(d), X. L.; Ghorbani, S. R.; Peleckis, G.; Dou, S. Very high critical field and superior J_C-field performance in $NdFeAsO_{0.82}F_{0.18}$ with T_C of 51 K, *Adv. Mater.* **2009**, *21*, 236-239.

Wei, Z.; Li, H. O.; Hong, W. L.; Lv, Z. M.; Wu, H. Y.; Guo, X. F.; Ruan, K. Q. Superconductivity at 57.3 K in La-Doped iron-based layered compound $Sm_{0.95}La_{0.05}O_{0.85}F_{0.15}FeAs$, *J. Supercond. Novel Magn.* **2008**, 21, 213-215.

Wen, H. H.; Mu, G.; Fang, L.; Yang, H.; Zhu, X. Y. Superconductivity at 25 K in hole-doped $(La_{1-x}Sr_x)OFeAs$, *Europhys. Lett.* **2008**, *82*, 17009 (5pp).

Williamson, G. K.; Hall, W. H. X-ray line broadening from filed aluminium and wolfram, *Acta Metall.* **1953**, *1*, 22-31.

Wu, M. K.; Ashburn, J. R.; Torng, C. J.; Hor, P. H.; Meng, R. L.; Gao, L.; Huang, Z. J.; Wang, Y. Q.; Chu, C. W. Superconductivity at 93 K in a new mixed-phase Y-Ba-Cu-O compound system at ambient pressure, *Phys. Rev. Lett.* **1987**, *58*, 908-910.

Yamamoto, A.; Jiang, J.; Kametani, F.; Polyanskii, A.; Hellstrom, E.; Larbalestier, D.; Martinelli, A.; Palenzona, A.; Tropeano, M.; Putti M. Evidence for electromagnetic granularity in polycrystalline Sm1111 iron-pnictides with enhanced phase purity, *Supercond. Sci. Technol.* **2011**, *24*, 045010 (7pp).

Yamamoto, A.; Jiang, J.; Tarantini, C., Craig, N.; Polyanskii, A.A.; Kametani, F.; Hunte, F.; Jaroszynski, J.; Hellstrom, E. E.; Larbalestier, D. C.; Jin, R.; Sefat, A. S.; McGuire, M. A.; Sales, B. C.; Christen, D. K.; Mandrus, D. Evidence for electromagnetic granularity in the polycrystalline iron-based superconductor $LaO_{0.89}F_{0.11}FeAs$, *Appl. Phys. Lett.* **2008a**, *92*, 252501 (3 pp).

Yamamoto, A.; Polyanskii, A. A.; Jiang, J.; Kametani, F.; Tarantini, C.; Hunte, F.; Jaroszynski, J.; Hellstrom, E. E.; Lee, P. J.; Gurevich, A.; Larbalestier, D. C.; Ren, Z. A.; Yang, J.; Dong, X. L.; Lu, W.; Zhao, Z. X. Evidence for two distinct scales of current flow in polycrystalline Sm and Nd iron oxypnictides, *Supercond. Sci. Technol.* **2008b**, *21*, 095008 (11pp).

Yan, J. Q.; Nandi, S.; Zarestky, J. L.; Tian, W.; Kreyssig, A.; Jensen, B.; Kracher, A.; Dennis, K. W.; McQueeney, R. J.; Goldman, A. I.; McCallum, R. W.; Lograsso, T. A. Flux growth at ambient pressure of millimeter-sized single crystals of LaFeAsO, $LaFeAsO_{1-x}F_x$, and $LaFe_{1-x}Co_xAsO$, *Appl.Phys. Lett.* **2009**, *95*, 222504 (3 pp).

Yang(a), J. L.; Ren, W. J.; Li, D.; Hu, W. J.; Li, B.; Zhang, Z. D. Superconductivity modulated by internal pressure in $Ce_{1-x}Gd_xFeAsO_{0.84}F_{0.16}$ compounds, *Supercond. Sci. Technol.* **2008**, *23*, 025003 (pp).

Yang(a), J. L.; Ren, W. J.; Li, D.; Zhang, Z. D. Structural evolution of $Ce_{1-x}Gd_xFeAsO_{0.84}F_{0.16}$ superconductors, *J. Appl. Phys*. **2011**, *109*, 07E154 (3 pp).

Yang(b), J.; Ren, Z. A.; Che, G. C.; Lu, W.; Shen, X. L.; Li, Z. C.; Yi, W.; Dong, X. L.; Sun, L. L.; Zhou, F.; Zhao, Z. X. The role of F-doping and oxygen vacancies on the superconductivity in SmFeAsO compounds, *Supercond. Sci. Technol*. **2009**, *22*, 025004 (5pp).

Yang(c), L. X.; Xie, B.; Zhang, Y.; He, C.; Ge, Q. Q.; Wang, X. F.; Chen, X. H.; Arita, M.; Jiang, J.; Shimada, K.; Taniguchi, M.; Vobornik, I.; Rossi, G.; Hu, J. P.; Lu, D. H.; Shen, Z. X.; Lu, Z. Y.; Feng, D. L. Surface and bulk electronic structures of LaFeAsO studied by angle-resolved photoemission spectroscopy, *Phys. Rev. B* **2010**, *82*, 104519 (9 pp).

Yi, W.; Sun, L.; Ren, Z.; Lu, W.; Dong, X.; Zhang, H. J.; Dai, X.; Fang, Z.; Li, Z.; Che, G.; Yang, J.; Shen, X.; Zhou, F.; Zhao, Z. Pressure effect on superconductivity of iron-based arsenic-oxide $ReFeAsO_{0.85}$ (Re=Sm and Nd), *Eur. Phys. Lett.* **2008a**, *83*, 57002 (4 pp).

Yi, W.; Yang, J.; Shen, X. L.; Lu, W.; Li, Z. C.; Ren, Z. A.; Che, G. C.; Dong, X. L.; Zhou, F.; Sun, L. L.; Zhao, Z. X. Superconductivity in the mixed rare earth iron oxyarsenide $La_{1-x}Sm_xFeAsO_{0.85}$, *Supercond. Sci. Technol.* **2008b**, *21*, 125022 (3 pp).

Yi, W.; Zhang, C.; Sun, L.; Ren, Z.; Lu, W.; Dong, X.; Li, Z.; Che, G.; Yang, J.; Shen, X.; Dai, X.; Fang, Z.; Zhou, F.; Zhao, Z. High-pressure study on $LaFeAs(O_{1-x}F_x)$ and $LaFeAsO_\delta$ with different T_C, *Europhys. Lett.* **2008c**, 84, 67009 (4 pp).

Yildirim, T. Origin of the 150-K anomaly in LaFeAsO: competing antiferromagnetic interactions, frustration, and a structural phase transition, *Phys. Rev. Lett.* **2008**, *101*, 057010 (4 pp).

Yin, Z. P.; Lebègue, S.; Han, M. J.; Neal, B. P.; Savrasov, S. Y.; Pickett, W. E. Electron-hole symmetry and magnetic coupling in antiferromagnetic LaFeAsO, *Phys. Rev. Lett.* **2008**, *101*, 047001 (4 pp).

Yuan ,H. Q.; Singleton, J.; Balakirev, F. F.; Baily, S. A.; Chen, G. F.; Luo, J. L.; Wang, N. L. Nearly isotropic superconductivity in $(Ba,K)Fe_2As_2$, *Nature* **2009**, *457*, 565-568.

Zhang(a), L.; Leng, X.; Ding, S. Y.; Zhu, X. B.; Sun, Y. P. AC susceptibility in an inhomogeneous superconductor, *Supercond. Sci. Technol.* **2010**, *23,* 065020 (6pp).

Zhang(b), X.; Wang, L.; Qi, Y.; Wang, D.; Gao, Z.; Zhang, Z.; Ma, Y. Effect of sheath materials on the microstructure and superconducting properties of $SmO_{0.7}F_{0.3}FeAs$ wires, *Physica C* **2010**, *470*, 104-108.

Zhang(c), Y.; Chen, F.; He, C.; Zhou, B.; Xie, B. P.; Fang, C.; Tsai, W. F.; Chen, X. H.; Hayashi, H.; Jiang, J.; Iwasawa, H.; Shimada, K.; Namatame, H.; Taniguchi, M.; Hu, J. P.; Feng, D. L. Orbital characters of bands in the iron-based superconductor $BaFe_{1.85}Co_{0.15}As_2$, *Phys. Rev. B* **2011a**, *83*, 054510 (9 pp).

Zhang(c), Y.; Chen, Y. L.; Cui, Y. J.; Cheng, C. H.; Zhang, H.; Zhao, Y. A. Study of the Fe-based superconductor $SmFeAsO_{1-x}F_x$ by x-ray photoelectron spectroscopy, *Supercond. Sci. Technol.* **2009**, *22*, 015007 (6pp).

Zhang(c), Y.; Nelson, C. T.; Lee, S.; Jiang, J.; Bark, C. W.; Weiss, J. D.; Tarantini, C.; Folkman, C. M.; Baek, S. H.; Hellstrom, E. E.; Larbalestier, D. C.; Eom, C. B.; Pan, X. Self-assembled oxide nanopillars in $BaFe_2As_2$ epitaxial thin films for vortex pinning, *Appl. Phys. Lett*. **2011b**, *98*, 042509 (3 pp).

Zhao(a), J.; Huang, Q.; Cruz, C.;, Li, S.; Lynn, J. W.; Chen, Y.; Green, M. A.; Chen, G. F.; Li, G.; Li, Z.; Luo, J. L.; Wang, N. L.; Dai, P. Structural and magnetic phase diagram of $CeFeAsO_{1-x}F_x$ and its relation to high-temperature superconductivity, *Nat. Mater.* **2008**, *7*, 953-959.

Zhao(b), L. D.; Berardana, D.; Dragoea, N. Electrical transport properties of F-doped LaFeAsO oxypnictide, *J. Alloys. Compd.* **2010**, *508*, 606-609.

Zhigadlo, N. D.; Katrych, S.; Bukowski, Z.; Weyeneth, S.; Puzniak, R.; Karpinski, J. Single crystals of superconducting $SmFeAsO_{1-x}F_y$ grown at high pressure, *J. Phys.: Condens. Matter* **2008**, *20*, 342202.

Zhigadlo, N. D.; Katrych, S.; Weyeneth, S.; Puzniak, R.; Moll, P. J. W.; Bukowski, Z.; Karpinski, J.; Keller, H.; Batlogg, B. Th-substituted SmFeAsO: Structural details and superconductivity with T_C above 50 K, *Phys. Rev. B* **2010**, *82*, 064517 (11 pp).

Zhu, X.; Yang, H.; Fang, L.; Mu, G.; Wen, H. Upper critical field, Hall effect and magnetoresistance in the iron-based layered superconductor $LaFeAsO_{0.9}F_{0.1-\delta}$, *Supercond. Sci. Technol.* **2008**, *21*, 105001 (5 pp).